

Search for the decay $K_L \rightarrow \pi^0 \nu \bar{\nu}$

DISSERTATION
Presented in Partial Fulfillment of the Requirements
for the Degree of Doctor of Science
in the Graduate School of Osaka University

Department of Physics at Osaka University
YAMANAKA TAKU Group

by

Ken SAKASHITA

February, 2006

Abstract

We report on the first dedicated search for the $K_L \rightarrow \pi^0 \nu \bar{\nu}$ decay in E391a experiment at the 12 GeV Proton Synchrotron in High Energy Accelerator Research Organization (KEK). The $K_L \rightarrow \pi^0 \nu \bar{\nu}$ decay is one of the best probe to study the CP violation. In the Standard Model of elementary particle physics, the branching ratio of the $K_L \rightarrow \pi^0 \nu \bar{\nu}$ decay determines the CP violation parameter within the theoretical uncertainty of $O(1\%)$. We analyzed 10 % of data taken in the first period of the E391a experiment. No signal candidate events were observed. We set a new upper limit:

$$Br(K_L \rightarrow \pi^0 \nu \bar{\nu}) < 2.10 \times 10^{-7} ,$$

at the 90 % confidence level. This represents an improvement of a factor 2.8 over the current limit.

Acknowledgment

This thesis could not have been produced without the enormous efforts of many people. I would like to take this time to thank them.

First and foremost, I would like to express my deepest gratitude to my supervisor, Prof. Taku Yamanaka, for giving me an opportunity for the research in the wonderful world of high energy physics and for his support and guidance for my research activity. I have also been very lucky to have the opportunity to learn from him. Things learnt from him in these past six years are great assets for me.

My special thanks go to Prof. T. Inagaki, who is the spokesperson of E391a experiment. He has been giving me a number of interesting ideas about high energy experiment. I would like to thank all of the E391a collaborators. I greatly appreciate the help of H. Okuno, T. Sato, G.Y. Lim and T.K. Komatsubara, who gave me invaluable advice on analysis and experimental technique. In particular, I enjoyed the discussion on physics with T.K. Komatsubara.

I have worked on the DAQ system for E391a experiment. I am deeply thankful to Y. Sugaya and M. Yamaga, who taught me from basic knowledge to technical things on DAQ. I would also like to thank the KEK electronics group: M. Tanaka and S. Simazaki for their support on the equipment of the electronics, in particular on the development of “AmpDiscr” module. I also appreciate the kindness of peoples from KEK experimental support group, and REPIC Co., Ltd. for their support.

I am also grateful for the help of M. Yamaga, H. Nanjo, H. Watanabe and T. Sumida, who were the members of software development in E391a. I would also like to thank the members of KEK Computing Center. My special thanks go to T. Miyashita, who was one of the support members of KEKCC system from IBM, and G. Iisaka, who established a PC farm used for analysis in E391a.

My warmest gratitude goes to Y.B. Hsiung, T. Nakano, T. Nomura, N. Sasao and Y.W. Wah for their help and advice in $K_L \rightarrow \pi^0 \nu \bar{\nu}$ analysis. I really enjoyed discussions with them on physics and analysis. I would like to thank M. Doroshenko, H. Ishii, H.S. Lee, H. Morii, J. Nix and G.N. Perdue for their kindness and friendship. I am sure that this thesis did not exist without their help and encouragement.

I have stayed and performed my research at KEK in the past four years. I especially enjoyed my research life with H. Watanabe and T. Sumida. I would like to thank H. Watanabe, who taught me many things related to particle detectors, physics, data analysis and human life. I would also like to thank T. Sumida. It was great fortune for me to work with him. I enjoyed having many chats with them in my research life.

I would like to thank all the other graduate students in E391a collaboration for their

friendship and help in the life at KEK.

I would like to thank all of the members of the Yamanaka-Taku Group at Osaka University. My special thanks go to T. Hara and H. Miyake who gave me invaluable advice on physics and computing. I would like to thank K. Kotera. I really enjoyed discussions with him on physics and other topics. Even for a short period of my stay at Osaka University, I also enjoyed my Osaka life with all of the students of the High Energy Physics Group at Osaka University.

I would like to express my sincere gratitude to the secretaries of the KEK-PS group: N. Kimura and H. Ohata. I am also deeply thankful to the secretaries of the Yamanaka-Taku Group: S. Tsuzuki, S. Sugimoto and M. Kawaguchi for their help and enjoyable conversations.

I would like to express the special appreciation to my old friends and friends in my home town for cheering me up all the time. Although during my hard days, I have enjoyed meeting them. I never forget their encouragement.

Finally, I would like to thank my family who have supported and encouraged me for a long time. My parents, Kimio and Midori Sakashita, have been continuously supporting me since I was born. My brothers, Yosuke and Masahiro, also supported me in various ways. Although we are living apart from each other, I believe we are always connected as a family.

Ken Sakashita
at Osaka
February 2006

Contents

1	Introduction	1
1.1	Phenomenology of CP violation in Neutral Kaon	2
1.1.1	Indirect CP Violation	3
1.1.2	Direct CP Violation	4
1.2	CP violation in the Standard Model	5
1.2.1	CKM matrix and unitarity triangle	5
1.2.2	Current status of CKM parameters	7
1.3	$K_L \rightarrow \pi^0 \nu \bar{\nu}$ decay in the Standard Model	8
1.4	$K_L \rightarrow \pi^0 \nu \bar{\nu}$ decay beyond the Standard Model	10
1.4.1	Grossman-Nir limit	10
1.4.2	$K_L \rightarrow \pi^0 \nu \bar{\nu}$ for probing physics beyond the Standard Model	11
1.5	History of the $K_L \rightarrow \pi^0 \nu \bar{\nu}$ search	12
1.6	KEK-PS E391a Experiment	13
1.7	Outline of this thesis	14
2	Experimental method	15
2.1	Overview	15
2.2	Single Event Sensitivity	15
2.3	Detection method	16
2.4	Background	16
2.5	Features of the E391a experiment	18
2.5.1	Ideas to catch all the photons	18
2.5.2	Ideas to reduce beam neutron interactions	19
2.6	Summary	19
3	Apparatus and run	21
3.1	K_L beam	22
3.1.1	Primary proton beam and K_L production target	22
3.1.2	Neutral beam line	22
3.2	Detector element	25
3.2.1	Overview	25
3.2.2	Electromagnetic calorimeter	25
3.2.3	Charged veto	30

3.2.4	Main barrel	31
3.2.5	Front barrel	34
3.2.6	Collar counters	37
3.2.7	Back anti and Beam hole charged veto	39
3.3	Vacuum system	42
3.4	Trigger	46
3.4.1	Physics trigger	46
3.4.2	Other trigger	48
3.5	Data acquisition system	48
3.5.1	Detail description of the E391a DAQ	49
3.6	Run	50
3.6.1	Physics Run	50
3.6.2	Special Run	50
4	Monte Carlo simulation	53
4.1	Event generation	53
4.1.1	Parent particle generation	53
4.1.2	Decay	55
4.2	Detector response	56
4.3	Accidental activity	57
5	Event reconstruction	59
5.1	Photon finding	60
5.1.1	Cluster finding	60
5.1.2	A criterion to reject non-isolated clusters	60
5.1.3	Photon identification	62
5.1.4	Energy and position calculation	62
5.2	π^0 reconstruction	66
6	Event selection	69
6.1	Background sources	69
6.1.1	Background from beam interactions	69
6.1.2	Background from K_L decay	72
6.2	Event Selection Cuts	74
6.2.1	Photon veto cuts	74
6.2.2	Charged particle veto cuts	80
6.2.3	Shower shape cut	81
6.2.4	Photon energy cut	82
6.2.5	Time difference cut	84
6.2.6	Hit position cuts	84
6.2.7	Acoplanarity angle cut	84
6.2.8	Kinematic cuts for the core neutron background	84
6.2.9	Vertex cut	86
6.2.10	$P_T - Z_{\text{vtx}}$ correlation cut	86

6.2.11	P_T cut	88
6.3	Acceptance	91
6.4	Normalization	92
7	Background Estimation	97
7.1	Background from K_L decay	97
7.1.1	$K_L \rightarrow \pi^0 \pi^0$ background	97
7.1.2	$K_L \rightarrow \gamma \gamma$ background	99
7.1.3	Other K_L backgrounds	100
7.2	Backgrounds associated with the neutron interaction	103
7.2.1	Core neutron multiple π^0	103
7.2.2	Other backgrounds associated with neutron interactions	107
7.3	Summary of background estimation	107
7.4	The number of background events outside the signal region	108
8	Systematic Errors	111
8.1	Branching ratio	111
8.2	Acceptance ratio	111
8.2.1	Different reconstruction methods	112
8.2.2	Discrepancy in Γ_{00}/Γ_{000}	113
8.2.3	The energy measurement by the CsI calorimeter	114
8.3	Statistical uncertainty	114
8.4	Summary	114
9	Result and Discussion	117
9.1	Data with all event selection cuts	117
9.2	Result	117
9.3	Discussion on physics	119
9.4	Discussion on the model in Monte Carlo simulation	119
9.5	Discussion from experimental point of view	119
9.5.1	Detection method	120
9.5.2	Background	120
9.5.3	Hermetic photon veto	121
9.6	Further $K_L \rightarrow \pi^0 \nu \bar{\nu}$ search	123
10	Conclusion	125
A	Identification of photon cluster	127
A.1	Cluster size	127
A.2	Cluster shape	128
A.3	Energy dispersion	129
A.4	Timing dispersion	130
A.5	Summary	132
B	$K_L \rightarrow \pi^0 \pi^0 \pi^0$ ($\pi^0 \pi^0$) reconstruction	135

C Upper limit with another statistics model

141

List of Figures

1.1	The box diagrams of the $K^0 - \overline{K}^0$ mixing. The K^0 and \overline{K}^0 oscillate via $\Delta S = 2$ transition.	4
1.2	The feynman diagrams of semi-leptonic decays in neutral kaons, where $l = (e, \mu)$. The K^0 decay involves positive lepton and \overline{K}^0 decay involves negative one. . .	4
1.3	The unitarity triangle. (a) Representation of the triangle formed by the CKM matrix element in the complex plane. (b) Rescaled triangle with vertices A,B and C at $(\bar{\rho}, \bar{\eta})$, $(1, 0)$ and $(0, 0)$, respectively. In this context, $\bar{\rho} = \rho(1 - \lambda^2/2)$ and $\bar{\eta} = \eta(1 - \lambda^2/2)$. As will be described in later, the branching ratio of the $K_L \rightarrow \pi^0 \nu \bar{\nu}$ decay determines the height of the unitarity triangle.	7
1.4	Constraints in the $(\bar{\rho}, \bar{\eta})$ plane with recent experimental measurements. In this figure, $ \epsilon $ denotes as ϵ_K	8
1.5	The Feynman diagrams of the $K_L \rightarrow \pi^0 \nu \bar{\nu}$ decay. The decay is dominated by the second order electroweak interactions by the (a) penguin diagram and (b) box diagram.	9
1.6	A history plot of the search for the $K_L \rightarrow \pi^0 \nu \bar{\nu}$ decay. In this figure, $(\gamma\gamma)$ and $(e^+e^-\gamma)$ denote the experimental approach with the $\pi^0 \rightarrow \gamma\gamma$ decay and $\pi^0 \rightarrow e^+e^-\gamma$ decay, respectively.	13
1.7	The distribution of the transverse momentum for the final remaining events in the search for $K_L \rightarrow \pi^0 \nu \bar{\nu}$ decay with $\pi^0 \rightarrow \gamma\gamma$ decay by the KTeV collaboration [24]. The arrow shows the signal region: $160 \leq P_T(\text{MeV}/c) \leq 260$	14
2.1	The distribution of the transverse momentum of two photons' system for $K_L \rightarrow \pi^0 \nu \bar{\nu}$ (solid), $K_L \rightarrow \pi^0 \pi^0$ (yellow hatched) and $K_L \rightarrow \gamma\gamma$ decays (green hatched) obtained by a Monte Carlo simulation.	17
2.2	A conceptual view of the hermetic detector. The K_L decay region is surrounded with the detector in order to detect all photons from K_L decay.	19
3.1	Schematic view of the E391a experiment. The E391a experiment consists of the neutral beam line and the detector system. The proton beam was delivered from KEK 12 GeV Proton Synchrotron.	21
3.2	Plan view of the neutral beam line. The neutral beam line consists of a pair of sweeping magnets, and six sets of collimators (C1 - C6).	24

3.3	Beam profiles at the exit of the C6 obtained by a Monte Carlo simulation without absorber. The triangles and circles indicate those for γ 's and neutrons with energies above 1 MeV, respectively.	24
3.4	K_L momentum distribution at the exit of the beam line (C6) obtained by a Monte Carlo simulation which will be described in Chapter 4. The average momentum of K_L beam is 2.6 GeV/c.	24
3.5	An overview of the E391a detector. K_L 's enter from the left side.	25
3.6	An overview of the electromagnetic calorimeter. It consists of 576 CsI crystals and 24 Sandwich modules.	27
3.7	Schematic drawing of CsI crystal and associated equipments.	27
3.8	Edge CsI crystals. There were seven different shapes.	29
3.9	Sandwich module. There were three different types of modules. Type-A, type-B, and type-C modules consisted of four, five and two pairs of the lead / scintillator layer, respectively.	29
3.10	Schematic view of the Xenon gain monitoring system.	30
3.11	The gain stability of CsI's PMT as a function of the operation days.	30
3.12	The energy resolution as a function of the incident energy as measured with a positron beam with 25 Normal CsI crystals.	31
3.13	Schematic drawings of CV. Right drawing shows a detail structure of the outer CV.	31
3.14	The light yield of the outer CV as a function of the distance from the PMT [32].	32
3.15	An overview of the detectors in the middle section. Main barrel (MB) and Barrel charged veto (BCV) are supported by the vacuum vessel.	32
3.16	Schematic drawing of MB module. We call the first 15 layers from the bottom as "inner module" and the remaining 30 layers as "outer module".	32
3.17	Readout scheme of MB module. Two PMTs were attached at each end of MB module.	33
3.18	A prism-shape photo-cathode (a) vs. a normal photo-cathode (b) [33].	33
3.19	The light yield of MB module as a function of the distance from the PMT. We attached four PMTs on one MB module: downstream outer (red triangle), downstream inner (black square), upstream outer (blue triangle), and upstream inner (open circle) [36].	35
3.20	Timing resolution of MB module as a function of the distance from the PMT [36].	35
3.21	Schematic drawing of BCV. The green circles show the WLS fibers.	35
3.22	An overview of the upstream detectors.	36
3.23	FB module, which consists of 59 lead (1.5 mm) and scintillator (5 mm) sandwich layers.	36
3.24	Schematic drawing of CC02. Left drawing shows a view from the downstream. Right drawing shows details of CC02 module.	37
3.25	Schematic drawing of CC04 and CC05.	38
3.26	Front view of CC06 and CC07. CC06 and CC07 had the same dimensions and consisted of 10 lead glass crystals.	39
3.27	Back Anti (BA), which consists of six lead / scintillator modules and six Quartz modules.	40

3.28	Front view of BHCV, which consists of four plastic scintillators.	41
3.29	The E391a vacuum system. Region-2 corresponds to the high vacuum decay region, and Region-1 corresponds to the region in which all the detector components were located. There are two sets of the Rotary-pump and the Roots-pump systems, and four Turbo Molecular pumps (TMP).	44
3.30	Cross section of the film, “Membrane”, used to separate the high vacuum region and the low vacuum region.	45
3.31	The vacuum pressure for the low vacuum region and the high vacuum region as a function of the evacuation time. First, we turned on the Rotary pump and evacuate gas from the whole area down to 10 Pa level. Next we turned on the Roots pump. After the pressure reached to 1 Pa, we closed the gate valve (A) in order to separate the low vacuum region and the high vacuum region and then turned on the all TMPs.	45
3.32	The discharge voltage as a function of the vacuum pressure. Typical HV value in the actual operation was 1.0 kV – 1.6 kV.	45
3.33	Schematic view of CsI crystals with 72 regions for the Hardware cluster counter.	47
3.34	The distribution of the hardware clusters from the real data. Since there were large amount of $N_{\text{HC}} = 1$ events due to beam associated events, we required $N_{\text{HC}} \geq 2$ in the physics trigger.	47
3.35	Schematic view of the E391a DAQ system.	49
4.1	The distribution of the momentum (left) and the beam density (right) for the halo neutron beam at the z position of the C6.	54
4.2	The distribution of the momentum (left) and the beam density (right) for the core neutron beam at the z position of the C6.	54
4.3	The relative energy detected at the phototube for MB as a function of the distance from the phototube, which is expressed as Equation 4.7. The measured distribution is shown in Fig. 3.19	57
5.1	A flow chart of the event reconstruction for the $K_L \rightarrow \pi^0 \nu \bar{\nu}$ signal.	59
5.2	An example of a $K_L \rightarrow \pi^0 \pi^0 \pi^0$ decay in which each π^0 decays into two photons, producing six photons hitting the CsI calorimeter. Hatched boxes are the CsI crystals which have energy deposit above 1 MeV.	60
5.3	The diagram of the cluster finding algorithm. First, we sorted the cluster seeds by their energy deposit in descending order. We then grouped the neighboring cluster seeds to form clusters according to the procedures (2) through (5). The neighboring crystals are defined as crystals sharing an edge.	61
5.4	The fraction of the energy leakage as a function of the energy deposit (E_{dep}). The fraction of the energy leakage was expressed as $F = p1 + p2/\sqrt{E_{dep}(\text{GeV})}$	63
5.5	The distributions of the difference between the incident and reconstructed energy for photons from π^0 produced at the Al target before (white) and after (dashed) the energy leakage correction, as studied with MC.	63

5.6	A schematic view of the $E_0^{x(y)}$, $E_+^{x(y)}$ and $E_-^{x(y)}$. Colored squares show the CsI crystals with a finite energy deposit and those crystals make a cluster. The red square shows the crystal with a maximum energy deposit among the neighboring crystals. The $E_0^{x(y)}$, $E_+^{x(y)}$ and $E_-^{x(y)}$ were defined as the total energy in the column: center column, left column and right column, respectively.	64
5.7	The distribution of the value, q , for the photons with the energies greater than 550 MeV.	64
5.8	A schematic view of the position correction. Taking the shower length (L) into account, the incident position (P_{inc}) was calculated from the reconstructed position (P_{rec}) and the incident angle.	65
5.9	The shower length(L) as a function of the energy of photon obtained by the MC study.	66
5.10	The distributions of the difference between the incident and the reconstructed positions for both before and after the position correction. The standard deviation of the position was observed to be 0.5 cm. In this analysis, we used this value as the position resolution, σ_x and σ_y without any energy and incident angle dependences.	66
5.11	The distributions of the invariant mass of two photons ($M_{\gamma\gamma}$) for before (solid) and after (dashed) applying the energy and position corrections. The peak of $M_{\gamma\gamma}$ after the corrections is 0.135 ± 0.004 GeV/ c^2 , which is consistent with the π^0 mass, as measured with the π^0 run data.	67
5.12	The mean of $M_{\gamma\gamma}$ does not depend on the minimum photon energy after applying the energy and position corrections (blue dot) in contrast to before applying the corrections (black square), as measured with the π^0 run data.	67
5.13	A schematic view of parameters used to reconstruct the π^0 vertex.	68
6.1	The distribution of P_T versus Z_{vtx} of the reconstructed π^0 after online trigger requirements for the real data.	70
6.2	The distribution of P_T versus Z_{vtx} for the signal MC (upper left), the background caused by $K_L \rightarrow \pi^0\pi^0$ (upper right), core neutron interactions (lower left) and halo neutron interactions (lower right).	71
6.3	Overview of the core neutron background.	73
6.4	The distribution of the reconstructed vertex, Z_{vtx} , of the core neutron background studied with the MC. The events were categorized into the core neutron single π^0 events (cross hatched) and the core neutron multiple π^0 events (dashed).	74
6.5	The top plot shows the distribution of the decay vertex reconstructed with assuming the π^0 mass. The bottom plot shows the distribution of the decay vertex reconstructed with assuming that the two photons came from an $\eta \rightarrow \gamma\gamma$ decay. A clear peak at $z = 550$ cm was observed.	74
6.6	The distribution of the relative hit timing difference between the MB (T_{MB}) and the CsI (T_{CsI}) versus the hit position for (a) inner module and (b) outer module.	76

6.7	The distribution of energy in the inner MB module (a) and the outer MB module (b). The red dashed histogram consists of events from $K_L \rightarrow \pi^0\pi^0\pi^0$ decays where four photons hitting the CsI calorimeter and some of photons hitting the MB. The blue dashed histogram consists of events from $K_L \rightarrow \pi^0\pi^0$ decays in which the MB signal consisting of photons in the shower-splash-back.	77
6.8	The left plots show the correlation between the total light yield in the quartz layer (E_Q) and the total energy deposit in the scintillator layer (E_S) of BA for photons and neutrons studied with the MC. The right plots show the distributions of the ratio of the total light yield in the quartz layer to the total energy deposit in the scintillator layer.	78
6.9	The distribution of the invariant mass of four photons without the photon veto cuts (solid) and with the photon veto cuts (hatched). The events in the lower mass region (B) were $K_L \rightarrow \pi^0\pi^0\pi^0$ where two photons were missed.	80
6.10	The distribution of energy deposit in the CV for a minimum ionization particle collected during the calibration (muon) run. We required the energy deposit in the CV to be less than 0.5 MeV.	81
6.11	The distribution of energy deposit in the BHCV. We required that all the four BHCV counters have less than 0.1 MeV energy deposit.	81
6.12	Four-photon event samples contained $K_L \rightarrow \pi^0\pi^0$, and $K_L \rightarrow \pi^0\pi^0\pi^0$ with one or more fused clusters.	82
6.13	The distributions of the maximum RMS among the photons measured with the real data (four-photon event samples). The top left through the bottom right figures correspond to the distribution for the number of cluster size of 3 through 11. The solid and dashed histograms show the distributions for the $K_L \rightarrow \pi^0\pi^0\pi^0$ and $K_L \rightarrow \pi^0\pi^0$ events, respectively.	83
6.14	Top figure shows distributions of the smaller energy of the two photons for the signal (solid) and the “core neutron multiple π^0 ” background MC (dashed). Bottom figure shows the distribution for the real data.	85
6.15	The distribution of the photon’s hit position closer to the beam hole. The hit position was centered on the CsI calorimeter. Top plot shows the distributions between two photons for the signal (solid) and the “core neutron multiple π^0 ” backgrounds MC (dashed). Bottom figure shows the distribution for the real data.	85
6.16	The distribution of the hit timing difference between two photons as measured with the real data.	86
6.17	The MC distribution of the transverse momentum of the reconstructed 2γ from $K_L \rightarrow \gamma\gamma$ versus the larger ΔE_γ between two photons, where ΔE_γ is the difference between the incident and reconstructed energy. The P_T tends to be larger for larger ΔE_γ	87
6.18	The MC distribution of the acoplanarity angle of 2γ from $K_L \rightarrow \gamma\gamma$ versus the larger ΔE_γ between two photons, where ΔE_γ is the difference between the incident and reconstructed energy. The acoplanarity angle tends to be smaller for larger ΔE_γ	87
6.19	A schematic view of the acoplanarity angle. The beam goes into the page.	87

6.20	The MC distribution of the acoplanarity angle for the $K_L \rightarrow \pi^0 \nu \bar{\nu}$ signal (solid) and $K_L \rightarrow \gamma \gamma$ background (dashed).	87
6.21	The correlation between the vertices reconstructed by assuming that the two photons came from the π^0 and the η . Most of these events are η 's produced by the core neutron at the membrane in the beam.	88
6.22	The distribution of the decay vertex (Z_η) in the data, reconstructed assuming that the two photons came from an η decay. If Z_η is in the range: $530 \leq Z_\eta(\text{cm}) \leq 575$, the event was identified as the η produced at the membrane in the beam.	88
6.23	A schematic view of the definition of the π^0 projection length R_{π^0}	89
6.24	The MC distribution of R_{π^0} for both the $K_L \rightarrow \pi^0 \nu \bar{\nu}$ signal (solid) and the core neutron background (dashed), in which events in the fiducial region.	89
6.25	The distribution of the Z_{vtx} for the real data with loose photon veto cuts.	89
6.26	The distribution of the Z_{vtx} for the signal MC with loose photon veto cuts.	89
6.27	The distribution of the parameter $\alpha \equiv P_T(\text{GeV}/c) - 8.0 \times 10^{-4}(\text{GeV}/c \cdot \text{cm}) \times Z_{\text{vtx}}(\text{cm})$ for both the $K_L \rightarrow \pi^0 \nu \bar{\nu}$ signal (solid) and the core neutron background (dashed) for the events in $300 \leq Z_{\text{vtx}}(\text{cm}) \leq 500$	90
6.28	Z_{vtx} versus P_T for the $K_L \rightarrow \pi^0 \nu \bar{\nu}$ signal from MC with all selection cuts except for the photon veto cuts. The blue box shows the signal region.	90
6.29	Z_{vtx} versus P_T for the core neutron background from MC with all the selection cuts except for the photon veto cuts. The blue shows the signal region.	90
6.30	The distribution of the invariant mass (left) and the decay vertex (right) for the $K_L \rightarrow \pi^0 \pi^0$. In the top plot, the dots show the data and the histogram shows the MC. The bottom plot shows the ratio of the data to the MC.	94
6.31	The distribution of the invariant mass (left) and the decay vertex (right) for the $K_L \rightarrow \pi^0 \pi^0 \pi^0$. In the top plot, the dots show the data and the histogram shows the MC. The bottom plot shows the ratio of the data to the MC.	94
7.1	Top: The distribution of the invariant mass of the four photons ($M_{4\gamma}$) with only the cuts on the photon veto detectors except the BA. The dots show data, the solid histogram shows total MC, the blue hatched histogram shows the $K_L \rightarrow \pi^0 \pi^0$ MC and the red hatched histogram shows the $K_L \rightarrow \pi^0 \pi^0 \pi^0$ MC. Bottom: The ratio of the data to the MC.	98
7.2	Top: The distribution of the energy deposit in the MB inner module for the data (dots), the MC $K_L \rightarrow \pi^0 \pi^0$ (blue hatched) and the MC $K_L \rightarrow \pi^0 \pi^0 \pi^0$ (red hatched). Bottom: The ratio of the data to the MC.	99
7.3	Top: The distribution of the energy deposit in the MB outer module for the data (dots), the MC $K_L \rightarrow \pi^0 \pi^0$ (blue hatched) and the MC $K_L \rightarrow \pi^0 \pi^0 \pi^0$ (red hatched). Bottom: The ratio of the data to the MC.	99
7.4	Top: $M_{4\gamma}$ with the cuts on the photon veto detectors and after applying the rejection power of BA. The dots show data, the solid histogram shows total MC, the blue hatched shows the $K_L \rightarrow \pi^0 \pi^0$ MC and the red hatched shows the $K_L \rightarrow \pi^0 \pi^0 \pi^0$ MC. Bottom: The ratio of the data to the MC.	100

7.5	Top: $M_{4\gamma}$ with the cuts on the photon identification and the shower shape in addition to the cuts on the photon veto detectors. The dots show data, the solid histogram shows total MC, the blue hatched shows the $K_L \rightarrow \pi^0\pi^0$ MC and the red hatched shows the $K_L \rightarrow \pi^0\pi^0\pi^0$ MC. Bottom: The ratio of the data to the MC.	101
7.6	The distribution of Z_{vtx} versus P_T for the $K_L \rightarrow \pi^0\pi^0$ MC with all the event selection cuts.	101
7.7	The distribution of energy deposit in the BHCV collected during the calibration (muon) run. The curve shows the fitted asymmetric-gaussian.	102
7.8	The distribution of energy deposit in the CV collected during the calibration (muon) run. The curve shows the fitted asymmetric-gaussian.	102
7.9	Z_{vtx} versus P_T with all the event selection cuts. The region with $300 \leq Z_{\text{vtx}}(\text{cm}) \leq 525$ and $0.05 \leq P_T(\text{GeV}/c) \leq 0.4$ was masked, and divided into eight regions for a background study.	104
7.10	An illustration of the four cut combinations.	106
7.11	The distributions of the photon energy (left) and the hit position (right). Solid (dashed) shows the distribution before (after) the PV cut. The shape of both distributions did not depend on the PV cut.	106
7.12	The Z_{vtx} distribution for the ‘‘core neutron single π^0 ’’ events and the ‘‘halo neutron CV’’ events where the Z_{vtx} was properly reconstructed. The contamination in the signal region was estimated by assuming a Gaussian shape.	108
7.13	The distribution of the decay vertex assuming the η mass. Events in the region: $530 \leq Z_\eta(\text{cm}) \leq 575$ were removed by the η cut.	108
7.14	The distribution of the reconstructed vertex, Z_{vtx} , (left) and the transverse momentum, P_T (right) measured in the π^0 run with the Al target. We estimated the fraction of the event contamination in the fiducial region to be 3.5 ± 0.4 %.	109
7.15	The Z_{vtx} versus P_T with all the event selection cuts. The number of events observed ($N_{\text{obs.}}$) and expected (in bracket) for the all the regions except for the signal region are shown.	110
8.1	Top: The distribution of the vertex χ^2 of $K_L \rightarrow \pi^0\pi^0\pi^0$ decays. Dots show data and histogram shows MC. Bottom: The ratio of data and MC.	112
9.1	The 2-dimensional plot between Z_{vtx} and P_T with all the event selection cuts.	118
9.2	Top : The distribution of π^0 energy in MC when we assumed V–A interaction in $K_L \rightarrow \pi^0\nu\bar{\nu}$ decay. The blue line shows Equation 4.3. Bottom : The distribution of π^0 energy in MC when we did not assume V–A interaction. The π^0 energy is according to three body phase space.	120
9.3	The distribution of the reconstructed decay vertex (Z_{vtx}) after online requirements for data taken in the first period (solid) and taken in the second period (dashed). The distributions are normalized by the expected number of K_L decay.	121

9.4	The MC distribution of the distance between a missed photon and the nearest photon cluster for two photon-cluster event samples in $K_L \rightarrow \pi^0\pi^0$ decays. The histograms show the events without any cuts (solid), with the photon veto cut on CsI (blue solid), and with the shower shape cut, “RMS cut”, (blue dashed).	122
A.1	A schematic drawing of the csize-5 and the csize-1.	128
A.2	The distribution of the csize-5 (horizontal axis) versus the cluster energy (vertical axis) for the $K_L \rightarrow \pi^0\pi^0\pi^0$ decays in data.	129
A.3	The distribution of the csize-1 (horizontal axis) versus the cluster energy (vertical axis) for the $K_L \rightarrow \pi^0\pi^0\pi^0$ decays in data.	129
A.4	The distribution of the csize-5 (horizontal axis) versus the cluster energy (vertical axis) for events collected with the trigger requiring at least one hardware cluster.	130
A.5	The distribution of the csize-1 (horizontal axis) versus the cluster energy (vertical axis) for events collected with the trigger requiring at least one hardware cluster.	130
A.6	A sketch of the cluster-shape. The red square indicates the crystal which had the maximum energy deposit in the cluster. Cluster-shape is the number of crystals sharing the edge with the crystal shown in red.	132
A.7	The distribution of the cluster-shape versus the csize-1.	132
A.8	The distribution of the energy dispersion versus the csize-1.	133
A.9	The distribution of the timing dispersion for the $K_L \rightarrow \pi^0\pi^0\pi^0$ data.	133
B.1	The distribution of the smallest vertex χ^2 for the six-photon-event samples. In the top plot, the dots show the real data and the histogram shows the MC. The bottom plot shows the ratio of the data to the MC.	138
B.2	The 2-dimensional distribution of the $M_{6\gamma-2\text{nd.}-\chi^2}$ versus $\Delta\chi^2$ for the six-photon-event samples measured with the real data. The events in the red box: $0.47 \leq M_{6\gamma-2\text{nd.}-\chi^2}(\text{GeV}/c^2) \leq 0.54$ and $\Delta\chi^2 < 15$ had a potential to be mis-reconstructed K_L , and thus were rejected.	138
B.3	The distribution of the difference between the smallest vertex χ^2 and the next smallest χ^2 for the six-photon-event samples. In the top plot, the dots show the real data and the histogram shows the MC. The bottom plot shows the ratio of the data to the MC.	139
B.4	The distribution of the invariant mass ($M_{6\gamma}$) for the best χ^2 combination without any χ^2 cut (black histogram), with only best χ^2 cut (light blue), and with both χ^2 cuts (blue dashed), for data.	139

List of Tables

1.1	A list of the models beyond the Standard Model and the predicted branching ratio of the $K_L \rightarrow \pi^0 \nu \bar{\nu}$ decay.	12
3.1	Specifications of the KEK-PS accelerator and the neutral beam in the E391a experiment.	23
3.2	Positions, dimensions, brief configurations and the number of readouts of the detector elements.	26
3.3	Total volume and surface area for the fiducial region and the outside region as shown in Fig. 3.29.	42
3.4	Requirements for CV and each photon veto detector. E_{cls} is a summed energy in each eight channel in the detector. E_{tot} is the total energy deposit in the detector.	48
3.5	Summary of the condition of the physics data taking.	50
6.1	The list of the thresholds applied to the photon veto detectors. The signal efficiency for each cut, ε_A , was defined as Equation 6.2 and estimated with the MC.	79
6.2	The rejection power of photon veto cuts measured with the real data as described in the text. The photon veto using the CC02, CC03, CC04, CC05, CC06, CC07 and FB were combined.	80
6.3	The acceptance for the $K_L \rightarrow \pi^0 \nu \bar{\nu}$ signal estimated by the MC. The survival probability for each selection cut is also listed. We used 6.8×10^5 K_L decays in the acceptance estimation. Each number is normalized by the number of events with two clusters on the CsI calorimeter.	92
6.4	The lists of the survival probabilities for each background source studied with the MC. The numbers in this table were based on the order of cuts actually applied in the analysis.	95
6.5	The lists of the survival probabilities for each background source studied with the MC. The numbers in this table were based on the order of cuts actually applied in the analysis. The ratio of the number of K_L decays between MC and data were 9.16, 1.45, 0.81, 0.65 for $K_L \rightarrow \pi^0 \pi^0$, $K_L \rightarrow \gamma \gamma$, $K_L \rightarrow \pi^- e^+ \nu$ and $K_L \rightarrow \pi^+ \pi^- \pi^0$ decay, respectively.	96

7.1	The list of the number of events in each cut combinations measured by the real data.	107
7.2	The list of the estimated number of background events in each region.	109
8.1	The shift in the Γ_{00}/Γ_{000} due to the energy fluctuation of MB detector.	113
8.2	The list of the statistical uncertainty in the acceptance estimation and the observed number of normalization mode, $K_L \rightarrow \pi^0\pi^0$ decay. A detailed description of the acceptance estimation is given in Section 6.3.	115
8.3	The systematic and statistical uncertainties in the SES.	115
9.1	Summary of the E391a experiment. Run-I, Run-II and Run-III are the first, second and third period of the data taking, respectively. "abs." means a short of the absorber. We fixed the membrane before stating the Run-II.	123
A.1	The list of the requirements on the csize-5 and the csize-1 to identify clusters as photons.	128
A.2	The list of the requirements on the cluster size: csize-5 and csize-1 to identify clusters as photons.	131
A.3	The list of the requirements on the energy dispersion, E_R , to identify clusters as photons.	131
A.4	The summary of the cut efficiency for each photon identification cut except for the cut on the TDI. The number for each cut in the upper two columns is the ratio: $N(\text{all cuts})/N(\text{all cuts except for the specific cut})$ for $K_L \rightarrow \pi^0\pi^0\pi^0$ events. The numbers in the column " $K_L \rightarrow \pi^0\nu\bar{\nu}$ MC" are the ratio for $K_L \rightarrow \pi^0\nu\bar{\nu}$ MC events. The numbers in the last column show the ratio for two photon event samples in the region, $300 \leq Z_{\text{vtx}}(\text{cm}) \leq 500$	133
B.1	The fifteen possible photon pairings to form three π^0 's from six photons. In the table, $[i, j]$ means that a π^0 is formed with two photons with indices, i and j	137
B.2	The three possible photon pairings to form two π^0 's from four photons. In the table, $[i, j]$ means that a π^0 is formed with two photons with indices, i and j	137
C.1	90 % confidence level intervals for the Poisson signal mean, $[\mu_1, \mu_2]$, for the observed number of events, n_0 , with 1.9 expected background events.	142

Chapter 1

Introduction

Symmetries and invariances have always played important role in physics. The Noether's theorems introduces the connection between continuous symmetries and the conserved quantities, e.g. the translational and rotational invariance lead the conservation of the momentum and angular momentum. As well as the continuous symmetries, discrete symmetries have formed an important part of our understanding of physics.

We know that nature is mostly invariant under the following three discrete transformations:

- Parity(P) – inverting the space,
- Charge conjugation(C) – exchanging particles and anti-particles, and
- Time reversal(T) – changing the time coordinate t into $-t$.

One of important symmetry arises from the combined transformation of C, P and T: i.e. CPT symmetry. This CPT symmetry predicts the equality of masses, lifetimes and the magnitude of electric charge of particles and anti-particles.

An asymmetry under the Parity transformation was observed in the β decay of Co^{60} by C. S. Wu *et al.* in 1956 [1]. This phenomena helped us to find out the mechanism of the weak interaction. In 1964, J. H. Chistenson, J. W. Cronin, V. L. Fitch and R. Turley discovered the violation of the symmetry under the combination of the P and C transformations, CP, in long-lived neutral kaons [2]. The CP violation is interesting because it implies T violation with CPT symmetry and it also relates to one of the requirements for the matter-dominant universe [3].

Today, the Standard Model in particle physics consistently describes the nature. The CP violation could also be explained by the Kobayashi-Maskawa model which is a part of the Standard Model. However, the magnitude of the CP violation in the Kobayashi-Maskawa model is too small to explain the matter-dominant universe [4]. A new source of CP violation can be a breakthrough to solve this issue. Recently, there are several models to introduce a new origin of the CP violation.

This thesis describes a search for $K_L \rightarrow \pi^0 \nu \bar{\nu}$ decay, which is one of the best probes to understand the origin of the CP violation. In the following sections, we will describe a potential of the $K_L \rightarrow \pi^0 \nu \bar{\nu}$ decay to the CP violation in the Standard Model and beyond the Standard

Model. Section 1.1 explains the phenomenology of CP violation in neutral kaon system. The CKM matrix and the relation between the complex phase in the CKM matrix and the CP violation is explained in Section 1.2. Section 1.3 describes how the $K_L \rightarrow \pi^0 \nu \bar{\nu}$ decay plays a role in the Standard Model. Section 1.4 describes several theories for the $K_L \rightarrow \pi^0 \nu \bar{\nu}$ decay beyond the Standard Model and a new sources of the CP violation in those theories. Section 1.5 explains a history of the $K_L \rightarrow \pi^0 \nu \bar{\nu}$ decay search. In the experimental viewpoint, Section 1.6 explains the first dedicated experiment to search for $K_L \rightarrow \pi^0 \nu \bar{\nu}$ decay, E391a Experiment, and the importance of this experiment. An outline of this thesis is given in Section 1.7.

1.1 Phenomenology of CP violation in Neutral Kaon

In order to understand the theoretical interest in $K_L \rightarrow \pi^0 \nu \bar{\nu}$ decay, one needs to know the basics about the CP violation in neutral kaon system. To explain the CP violation, we will start with the kaon phenomenology.

The K^0 and \bar{K}^0 mesons are strangeness eigenstates:

$$K^0 = \begin{pmatrix} d \\ \bar{s} \end{pmatrix} \quad (S = +1), \quad (1.1)$$

$$\bar{K}^0 = \begin{pmatrix} \bar{d} \\ s \end{pmatrix} \quad (S = -1), \quad (1.2)$$

where S denotes the strangeness quantum number. They are produced through strong interactions, such as:

$$\pi^- + p \rightarrow K^0 + \Lambda, \quad (1.3)$$

$$K^- + p \rightarrow \bar{K}^0 + n \quad (1.4)$$

with conserving the strangeness.

However, they are not simultaneously eigenstates of CP, since

$$\text{CP}|K^0\rangle = |\bar{K}^0\rangle, \quad (1.5)$$

$$\text{CP}|\bar{K}^0\rangle = |K^0\rangle. \quad (1.6)$$

Although there is an ambiguity on the phase between these two states, we can choose the phase as the above because the phase is physically unobservable. Since our interest is a CP violation, we need to introduce CP eigenstates instead of K^0 and \bar{K}^0 .

The CP eigenstates K_1 and K_2 can be defined as a linear combination of the K^0 and \bar{K}^0 :

$$|K_1\rangle = \frac{1}{\sqrt{2}}(|K^0\rangle + |\bar{K}^0\rangle), \quad (1.7)$$

$$|K_2\rangle = \frac{1}{\sqrt{2}}(|K^0\rangle - |\bar{K}^0\rangle). \quad (1.8)$$

As shown in the equations:

$$\text{CP}|K_1\rangle = \frac{1}{\sqrt{2}}(|\bar{K}^0\rangle + |K^0\rangle) = +|K_1\rangle \quad (CP = +1), \quad (1.9)$$

$$\text{CP}|K_2\rangle = \frac{1}{\sqrt{2}}(|\bar{K}^0\rangle - |K^0\rangle) = -|K_2\rangle \quad (CP = -1), \quad (1.10)$$

where the CP eigenvalue is +1 for K_1 , and -1 for K_2 . Since the two pion final states ($\pi^0\pi^0$ or $\pi^+\pi^-$) have CP eigenvalue of +1 and the three pion final states ($\pi^0\pi^0\pi^0$ or $\pi^+\pi^-\pi^0$) have CP eigenvalue of -1, if CP conserves, K_1 can decay to the two pion final states, and K_2 can decay to the three pion final states, but not vice versa. Therefore, until CP violation was observed in 1964, it had been believed that the short lived kaon (K_S) should correspond to the K_1 and the long lived kaon (K_L) to the K_2 , in which difference in lifetimes arose from the amount of phase space available.

There are two kinds of CP violations in the neutral kaon system, one is called “indirect CP violation” and another is called “direct CP violation”. The following two subsections briefly describe these two phenomena.

1.1.1 Indirect CP Violation

The “indirect CP violation” arises from the $K^0 - \bar{K}^0$ mixing (Fig. 1.1). In 1964, CP violation was first observed in the decay $K_L \rightarrow \pi^+\pi^-$. To explain this process, K_L and K_S were interpreted as a superposition of the K_1 and K_2 ,

$$\begin{aligned} |K_S\rangle &= \frac{1}{\sqrt{1+|\epsilon|^2}}(|K_1\rangle + \epsilon|K_2\rangle) \\ &= \frac{1}{\sqrt{1+|\epsilon|^2}}((1+\epsilon)|K^0\rangle + (1-\epsilon)|\bar{K}^0\rangle) \end{aligned} \quad (1.11)$$

$$\begin{aligned} |K_L\rangle &= \frac{1}{\sqrt{1+|\epsilon|^2}}(|K_2\rangle + \epsilon|K_1\rangle) \\ &= \frac{1}{\sqrt{1+|\epsilon|^2}}((1+\epsilon)|K^0\rangle - (1-\epsilon)|\bar{K}^0\rangle) \end{aligned} \quad (1.12)$$

where ϵ determines the size of $K_1(K_2)$ contamination to $K_L(K_S)$, and the first coefficient are for normalization. They imply that the $K^0 - \bar{K}^0$ mixing is asymmetric by $|\epsilon|$. The K_1 component in the K_L is considered to decay into the two pion final state. Therefore, decay processes do not contribute to the CP violation, and the small contamination of the K_1 caused the CP violation.

We can evaluate the mixing parameter $|\epsilon|$ by using the semi-leptonic decay, $K^0 \rightarrow \pi^-l^+\nu_l$ and $\bar{K}^0 \rightarrow \pi^+l^-\bar{\nu}_l$ ($l = e, \mu$), as shown in Fig. 1.2. The $|\epsilon|$ is obtained from the charge asymmetry, δ , in semi-leptonic decay of K_L , defined as :

$$\delta = \frac{\Gamma(K_L \rightarrow \pi^-l^+\nu_l) - \Gamma(K_L \rightarrow \pi^+l^-\bar{\nu}_l)}{\Gamma(K_L \rightarrow \pi^-l^+\nu_l) + \Gamma(K_L \rightarrow \pi^+l^-\bar{\nu}_l)}. \quad (1.13)$$

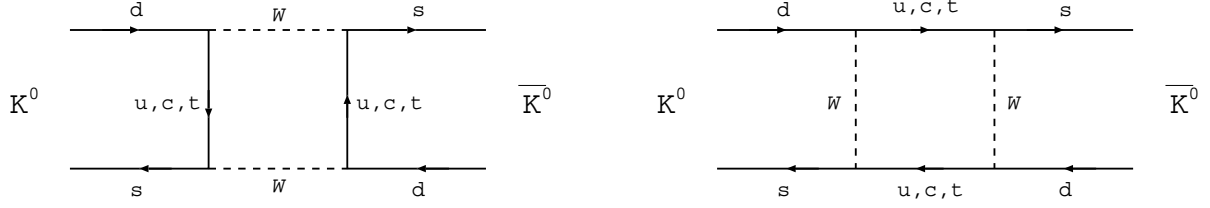


Figure 1.1: The box diagrams of the $K^0 - \bar{K}^0$ mixing. The K^0 and \bar{K}^0 oscillate via $\Delta S = 2$ transition.

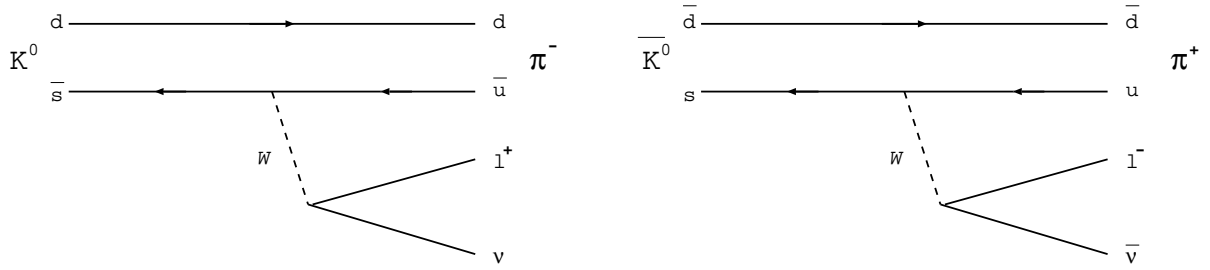


Figure 1.2: The feynman diagrams of semi-leptonic decays in neutral kaons, where $l = (e, \mu)$. The K^0 decay involves positive lepton and \bar{K}^0 decay involves negative one.

Substituting Equation 1.12 into Equation 1.13 yields

$$\delta \approx 2\text{Re}(\epsilon) . \quad (1.14)$$

Experimentally, the current world average for the charge asymmetry is [5]

$$\delta = (3.27 \pm 0.12) \times 10^{-3} . \quad (1.15)$$

The ϵ can be evaluated by taking the phase of ϵ , $\phi_\epsilon = 43.51^\circ \pm 0.05^\circ$ [5], into account;

$$|\epsilon| = (2.284 \pm 0.014) \times 10^{-3} . \quad (1.16)$$

It implies that the CP violation observed in $K_L \rightarrow \pi\pi$ decay is explained with the indirect CP violation where asymmetric $K^0 - \bar{K}^0$ mixing results in small contamination of K_1 component in K_L .

1.1.2 Direct CP Violation

The ‘‘direct CP violation’’ arises in the decay process. In this context, it means that a CP eigenstate of one type is allowed to decay into another CP eigenstate. Examples of direct CP violation are the decay of the K_2 to two pion final state or the K_1 to three pion final state. An evidence for direct CP violation in the neutral kaon system was reported in the measurement

of a parameter $\text{Re}(\epsilon'/\epsilon)$. The $\text{Re}(\epsilon'/\epsilon)$ is obtained from the double ratio of the decay widths of the $K_{L(S)} \rightarrow \pi^+\pi^-$ and $K_{L(S)} \rightarrow \pi^0\pi^0$ decays:

$$\frac{\Gamma(K_L \rightarrow \pi^+\pi^-)/\Gamma(K_S \rightarrow \pi^+\pi^-)}{\Gamma(K_L \rightarrow \pi^0\pi^0)/\Gamma(K_S \rightarrow \pi^0\pi^0)} \approx 1 + 6\text{Re}(\epsilon'/\epsilon). \quad (1.17)$$

A non-zero value of $\text{Re}(\epsilon'/\epsilon)$ indicates an existence of the direct CP violation. The world average listed in the PDG [5] is

$$\text{Re}(\epsilon'/\epsilon) = (1.67 \pm 0.26) \times 10^{-3}. \quad (1.18)$$

Therefore, the direct CP violation exists.

The origin of CP violation in the $K_L \rightarrow \pi^0\nu\bar{\nu}$ decay is the direct CP violation, as will be described later. In the next section, we will describe a theory which explains why CP does not conserve in the $K^0 - \bar{K}^0$ mixing and in the decay process within the Standard Model framework.

1.2 CP violation in the Standard Model

In the Standard Model, the Lagrangian of the charged current in the weak interaction is given by:

$$L_{CC} = \frac{g}{\sqrt{2}} [\bar{u}_i V_{ij} d_j W^- + \bar{d}_j V_{ij}^* u_i W^+] \quad (1.19)$$

where $u_i = (u, c, t)$ are left-handed up-type quarks and $d_i = (d, s, b)$ are left-handed down-type quarks, and W^\pm denote the weak bosons. V_{ij} is the 3×3 unitary CKM (Cabibbo-Kobayashi-Maskawa) matrix which connects the up-type quarks with the down-type quarks:

$$V = \begin{pmatrix} V_{ud} & V_{us} & V_{ub} \\ V_{cd} & V_{cs} & V_{cb} \\ V_{td} & V_{ts} & V_{tb} \end{pmatrix}. \quad (1.20)$$

The Lagrangian changes under CP transformation as follows:

$$L_{CC} \xrightarrow{\text{CP}} \frac{g}{\sqrt{2}} [\bar{d}_j V_{ij} u_i W^+ + \bar{u}_i V_{ij}^* d_j W^-] \quad (1.21)$$

Therefore, the interaction is invariant under CP transformation if $V_{ij} = V_{ij}^*$. In fact, the CKM matrix elements are complex so that the interaction is not invariant under the CP transformation.

1.2.1 CKM matrix and unitarity triangle

The CKM matrix was first introduced by Kobayashi and Maskawa [6], based on the concept of flavor mixing originally introduced by Cabibbo [7]. V has 9 free parameters but the number of

these parameters is reduced to 4 by the redefinition of the phase of quark fields. A convenient parameterization of V with three angles $\theta_{12}, \theta_{23}, \theta_{13}$ and a phase δ is

$$V = \begin{pmatrix} c_{12}c_{13} & s_{12}c_{13} & s_{13}e^{i\delta} \\ -s_{12}c_{23} - c_{12}s_{23}s_{13}e^{i\delta} & c_{12}c_{23} - s_{12}s_{23}s_{13}e^{i\delta} & s_{23}c_{13} \\ s_{12}c_{23} - c_{12}s_{23}s_{13}e^{i\delta} & -c_{12}c_{23} - s_{12}s_{23}s_{13}e^{i\delta} & c_{23}c_{13} \end{pmatrix}. \quad (1.22)$$

where $c_{ij} = \cos \theta_{ij}$ and $s_{ij} = \sin \theta_{ij}$.

As shown in Equation 1.19 and 1.20, the matrix elements of V express the coupling strength at the vertex of W^\pm and up-type and down-type quarks. Wolfenstein [8] parameterized the CKM matrix through an expansion in powers of $\lambda = |V_{us}| = 0.22$:

$$V = \begin{pmatrix} 1 - \frac{\lambda^2}{2} & \lambda & A\lambda^3(\rho - i\eta) \\ -\lambda & 1 - \frac{\lambda^2}{2} & A\lambda^2 \\ A\lambda^3(1 - \rho - i\eta) & -A\lambda^2 & 1 \end{pmatrix} + \mathcal{O}(\lambda^4), \quad (1.23)$$

where η is the CP violation phase. In this parameterization, V is CP invariant to the order of λ^2 , and CP violation shows up first in the order of λ^3 . Numerical values of these parameters are determined from experiments as discussed in the later subsection.

All the CP violating observables are proportional to a quantity J [9], which is independent of the choice of phase parameterization:

$$J = \text{Im}[V_{ij}V_{ik}V_{ik}^*V_{ij}^*] \quad (i \neq l, j \neq k) \quad (1.24)$$

where l and k denote up-type and down-type quarks, respectively. In terms of explicit parameterizations given above, J becomes

$$J = c_{12}c_{23}c_{13}^2s_{12}s_{23}s_{13} \sin \delta \simeq \lambda^6 A^2 \eta. \quad (1.25)$$

Imposing the unitarity condition to the first and third columns in the CKM matrix, we obtain

$$V_{ub}^*V_{ud} + V_{cb}^*V_{cd} + V_{tb}^*V_{td} = 0. \quad (1.26)$$

This relation can be expressed as a triangle in the complex plane, which is called the unitarity triangle. We can take $V_{ud} \approx 1$ to the first order in λ , and the unitarity condition becomes

$$V_{ub}^* + V_{td} = A\lambda^3. \quad (1.27)$$

Figure 1.3 shows the triangle obtained from Equation 1.26. The area of the triangle is proportional to the measure of CP violation, J . This means that, in the Standard Model, a measurement of the CP violating magnitude is equivalent to evaluating the area of the unitarity triangle in Fig. 1.3.

Therefore, a measurement of an amplitude of the imaginary parameter η , is the essence of CP violation in the Standard Model. In Equations 1.22, 1.23, such amplitudes are introduced with the $|V_{td}|$ or $|V_{ub}|$ component in the diagrams of CP violating processes.

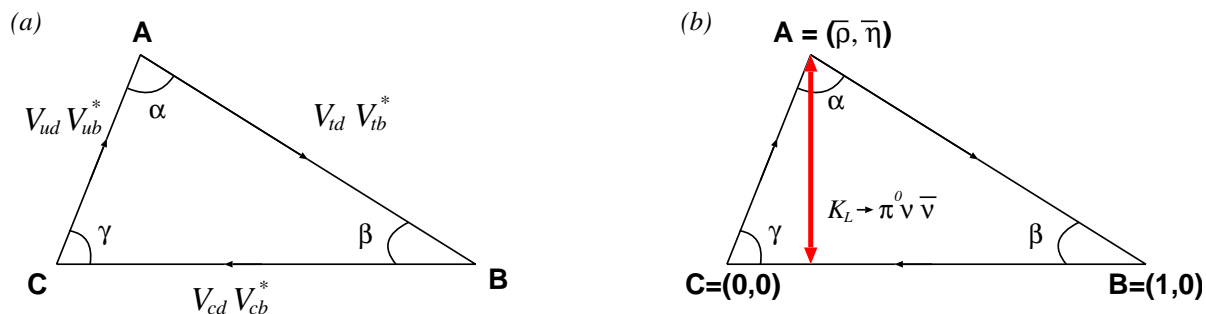


Figure 1.3: The unitarity triangle. (a) Representation of the triangle formed by the CKM matrix element in the complex plane. (b) Rescaled triangle with vertices A, B and C at $(\bar{\rho}, \bar{\eta})$, $(1, 0)$ and $(0, 0)$, respectively. In this context, $\bar{\rho} = \rho(1 - \lambda^2/2)$ and $\bar{\eta} = \eta(1 - \lambda^2/2)$. As will be described in later, the branching ratio of the $K_L \rightarrow \pi^0 \nu \bar{\nu}$ decay determines the height of the unitarity triangle.

1.2.2 Current status of CKM parameters

As shown in Equation 1.25, A , λ and η determine the size of CP violation in the Standard Model. They are also used in theoretical calculations to predict the branching ratio of $K_L \rightarrow \pi^0 \nu \bar{\nu}$ decay, as will be discussed in the next section. Therefore, we briefly summarize the current status of constraints on the CKM parameters, which are imposed from a combination of various experiments.

The $\lambda = |V_{us}|$ is determined by the decay rates of strange particles. The current average value is reported to be $|V_{us}| = 0.2200 \pm 0.0026$ [5]. The A can be determined with the λ and the measurement of the $|V_{cb}|$ as shown in Equation 1.20 and 1.23. The $|V_{cb}|$ is obtained from the semi-leptonic decays in B mesons to be $|V_{cb}| = (41.3 \pm 1.5) \times 10^{-3}$ [5].

The constraints on $(\bar{\rho}, \bar{\eta})$ plane, where $\bar{\rho} = \rho(1 - \lambda^2/2)$ and $\bar{\eta} = \eta(1 - \lambda^2/2)$, respectively, are imposed from several experimental measurements. A detailed description can be found in ref. [5]. The $|\epsilon|$ and $\sin 2\beta$ are typical parameters in the K and B meson systems, respectively.

The $|\epsilon|$ is connected to $(\bar{\rho}, \bar{\eta})$ through the relation [10]:

$$\epsilon = \bar{\eta} A^2 B_K \left[1.248(1 - \bar{\rho}) A^2 \left(\frac{m_t}{170(\text{GeV})} \right)^{1.52} + 0.31 \right], \quad (1.28)$$

where B_K is the ratio of the true matrix element to that obtained using vacuum insertion, and it is estimated to be 0.85 ± 0.15 [11].

The decay processes of $b \rightarrow c \bar{c} s$ give, in the time-dependent CP violation, an important parameter $\sin 2\beta$, where β is an angle of the unitary triangle in the $(\bar{\rho}, \bar{\eta})$ plane as shown in Fig. 1.3 (b). The present experimental results from BELLE and BaBar experiments determine it to be [5]:

$$\sin 2\beta = 0.736 \pm 0.049. \quad (1.29)$$

All the constraints on the $(\bar{\rho}, \bar{\eta})$ nicely overlap in one region as shown in Fig. 1.4. The measurement in the K meson system, $|\epsilon|$, and the measurement in the B meson system, $\sin 2\beta$,

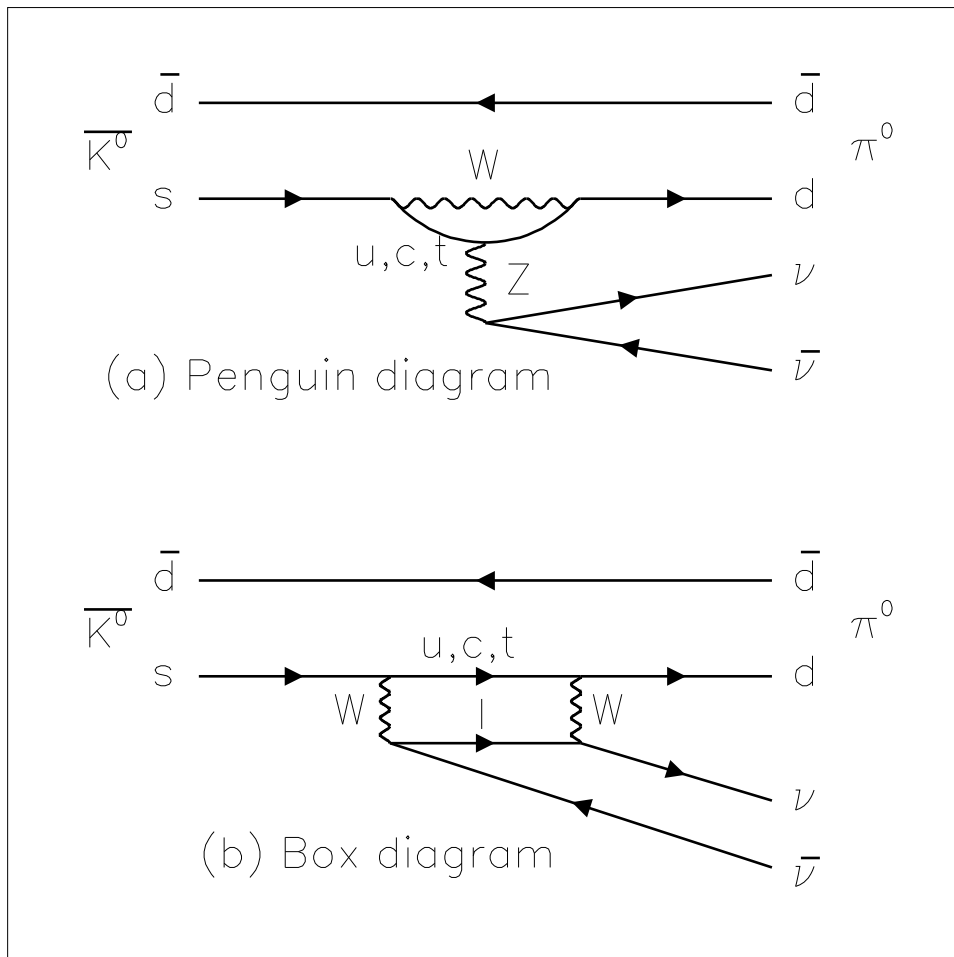


Figure 1.5: The Feynman diagrams of the $K_L \rightarrow \pi^0 \nu \bar{\nu}$ decay. The decay is dominated by the second order electroweak interactions by the (a) penguin diagram and (b) box diagram.

The $Br(K_L \rightarrow \pi^0 \nu \bar{\nu})$ is represented in the Standard Model as [15]:

$$Br(K_L \rightarrow \pi^0 \nu \bar{\nu}) = 6.87 \times 10^{-4} \times Br(K^+ \rightarrow \pi^0 e^+ \nu) \times A^4 \lambda^8 \eta^2 X^2(x_t) \quad (1.34)$$

where $Br(K^+ \rightarrow \pi^0 e^+ \nu)$ is the branching ratio of the $K^+ \rightarrow \pi^0 e^+ \nu$ decay, x_t is the square of the ratio of the top to the W masses, $x_t = m_t^2/m_W^2$, and $X(x_t)$ is the Inami-Lim loop function [16] with QCD higher order corrections, respectively. We can compute $Br(K_L \rightarrow \pi^0 \nu \bar{\nu})$ to an exceptionally high degree of precision that is not matched by any other decays of mesons. The reasons are the facts that (1) long-distance contributions are negligible and (2) the hadronic matrix elements are extracted directly from experimental measurements of the $Br(K^+ \rightarrow \pi^0 e^+ \nu)$. The theoretical uncertainty in $Br(K_L \rightarrow \pi^0 \nu \bar{\nu})$ is only 1 – 2 %.

Using experimental inputs of the CKM parameters, the $Br(K_L \rightarrow \pi^0 \nu \bar{\nu})$ is predicted in the Standard Model to be $Br(K_L \rightarrow \pi^0 \nu \bar{\nu}) = (3.0 \pm 0.6) \times 10^{-11}$. The 20 % of uncertainty comes from uncertainties on the CKM parameters and the quark masses.

Because of the theoretical cleanness, the measurement of the $K_L \rightarrow \pi^0 \nu \bar{\nu}$ branching ratio can be directly translated into precise information on the magnitude of the CP violation in the Standard Model. Assuming that the branching ratio is measured within ± 5 %, we can determine the CP violation phase, η , within ± 3 %. On the other hand, the measurement of the CP asymmetry in the B meson system, $B \rightarrow J/\psi K_S$, also can determine the CP violation phase in the Standard Model with a small theoretical uncertainty. The magnitude of the CP violation determined by both measurements should be the same in the Standard Model.

$$(\text{size of CPV})_{\pi\nu\nu} = (\text{size of CPV})_{J/\psi K_S} \quad (1.35)$$

This relation is not only a very powerful tool to check the Standard Model, but also a useful handle to discriminate among different new physics, which will be described in the next.

1.4 $K_L \rightarrow \pi^0 \nu \bar{\nu}$ decay beyond the Standard Model

In this section, we describe a role of the $K_L \rightarrow \pi^0 \nu \bar{\nu}$ decay beyond the Standard Model, in particular, concerning possible new sources of CP violation. First, we describe a model independent limit on the $Br(K_L \rightarrow \pi^0 \nu \bar{\nu})$, so-called the Grossman-Nir limit. After the description of the Grossman-Nir limit, we will describe an overview of the $K_L \rightarrow \pi^0 \nu \bar{\nu}$ decay in the physics beyond the Standard Model.

1.4.1 Grossman-Nir limit

A charged kaon decay $K^+ \rightarrow \pi^+ \nu \bar{\nu}$ is closely related to the $K_L \rightarrow \pi^0 \nu \bar{\nu}$ decay. The $K^+ \rightarrow \pi^+ \nu \bar{\nu}$ decay can be illustrated by replacing the d quark with the u quark in the $K^0 \rightarrow \pi^0 \nu \bar{\nu}$. A stringent constraint on the branching ratio of $K_L \rightarrow \pi^0 \nu \bar{\nu}$ decay can be derived using the information on the charged mode and the isospin symmetry, as was suggested by Y. Grossman and Y. Nir [12]. The model independent limit on the branching ratio of $K_L \rightarrow \pi^0 \nu \bar{\nu}$ decay, the Grossman-Nir limit, can be expressed as¹:

$$Br(K_L \rightarrow \pi^0 \nu \bar{\nu}) < 4.4 \times Br(K^+ \rightarrow \pi^+ \nu \bar{\nu}). \quad (1.38)$$

¹Let define θ to be the relative CP violation phase between $K^0 - \bar{K}^0$ mixing (indirect CP violation) and $s \rightarrow d \nu \bar{\nu}$ decay (direct CP violation) for $K_L \rightarrow \pi^0 \nu \bar{\nu}$ decay, and consider the isospin symmetry relation,

The AGS E949 collaboration at Brookhaven National Laboratory observed 3 $K^+ \rightarrow \pi^+ \nu \bar{\nu}$ decay events so far [14]. The measured branching ratio of $K^+ \rightarrow \pi^+ \nu \bar{\nu}$ is $[1.47_{-0.89}^{+1.30}] \times 10^{-10}$, and its upper limit is $Br(K^+ \rightarrow \pi^+ \nu \bar{\nu}) < 3.2 \times 10^{-10}$ at the 90 % confidence level. Therefore,

$$Br(K_L \rightarrow \pi^0 \nu \bar{\nu}) < 1.4 \times 10^{-9} \quad (90 \% \text{ C.L.}) . \quad (1.39)$$

Since this is a fundamental requirement, this bound is valid in virtually any extensions of the Standard Model. Therefore, most of models for new physics beyond the Standard Model predict $Br(K_L \rightarrow \pi^0 \nu \bar{\nu})$ below the Grossman-Nir limit as will be described below.

1.4.2 $K_L \rightarrow \pi^0 \nu \bar{\nu}$ for probing physics beyond the Standard Model

The $K_L \rightarrow \pi^0 \nu \bar{\nu}$ decay plays a special role in the investigation of new physics beyond the Standard Model. The clean theoretical character of $K_L \rightarrow \pi^0 \nu \bar{\nu}$ decay remains valid in essentially all extensions of the Standard Model. Also the $K_L \rightarrow \pi^0 \nu \bar{\nu}$ decay can determine the new origin of CP violation with small theoretical uncertainties. In contrast to the $K_L \rightarrow \pi^0 \nu \bar{\nu}$ decay, the measurement of CP violation in the B meson system, such as non-leptonic two-body B decay ($B \rightarrow \pi\pi$, $B \rightarrow K\pi$, etc.) are vulnerable to the hadronic uncertainties in the relevant observables. Moreover, the $K_L \rightarrow \pi^0 \nu \bar{\nu}$ decay process is dominated by the second order processes of the electroweak interactions, hence it is sensitive to new flavor interactions and/or CP violation phases in the intermediate state.

An explicit example was pointed out in references [17, 18]. Buras *et al.* predict a large phase of the new origin of CP violation, which leads to an enhancement of the electroweak penguin process (“Enhanced EW penguin”). They assume this effect can be implemented in both K and B meson system universally. It would provide a much better fit of recent $B \rightarrow \pi K$ data from B factories.

Table 1.1 lists the recently considered models beyond the Standard Model and the predicted branching ratio of the $K_L \rightarrow \pi^0 \nu \bar{\nu}$ decay. In the Minimal Flavor Violation (MFV) hypothesis, there are no additional CP violation phases, and the flavor mixing can be explained only by the CKM matrix in the Standard Model. Therefore, deviations from the Standard Model amplitudes rarely exceed the $O(20)\%$ level. Moreover, since there are no additional CP violation phases, the relation between the magnitude of the CP violation in the $K_L \rightarrow \pi^0 \nu \bar{\nu}$ decay and the CP asymmetry measured in $B \rightarrow J/\psi K_S$, Equation 1.35, must be satisfied. On the other hand, in general Minimal Supersymmetric Standard Model (MSSM), it is possible to implement new CP violation phases. In the general MSSM, the branching ratio of $K_L \rightarrow \pi^0 \nu \bar{\nu}$ decay can

$A(K^0 \rightarrow \pi^0 \nu \bar{\nu})/A(K^+ \rightarrow \pi^+ \nu \bar{\nu}) = 1/\sqrt{2}$. A relation between two decay widths $K_L \rightarrow \pi^0 \nu \bar{\nu}$ decay and $K^+ \rightarrow \pi^+ \nu \bar{\nu}$ decay is:

$$r_{is} \times \frac{\Gamma(K_L \rightarrow \pi^0 \nu \bar{\nu})}{\Gamma(K^+ \rightarrow \pi^+ \nu \bar{\nu})} = \sin^2 \theta , \quad (1.36)$$

where $r_{is} = 0.954$ is the isospin breaking factor [13]. With this relation and $\sin^2 \theta \leq 1$, the model independent limit on the ratio of two branching ratio is :

$$\frac{Br(K_L \rightarrow \pi^0 \nu \bar{\nu})}{Br(K^+ \rightarrow \pi^+ \nu \bar{\nu})} < \frac{\tau_{K_L}}{\tau_{K^+}} \times \frac{1}{r_{is}} \simeq 4.4 , \quad (1.37)$$

where $\tau_{K_L}/\tau_{K^+} = 4.17$.

Table 1.1: A list of the models beyond the Standard Model and the predicted branching ratio of the $K_L \rightarrow \pi^0 \nu \bar{\nu}$ decay.

model	ref.	$Br(K_L \rightarrow \pi^0 \nu \bar{\nu})/10^{-11}$
Minimal Flavor Violation	[15]	$\sim 20 \%$
General MSSM	[19]	$< \text{a few} \times 10$
Enhanced EW penguin	[17, 18]	31 ± 10

be as large as a few times 10^{-10} . The effect of new CP violation phase to $K_L \rightarrow \pi^0 \nu \bar{\nu}$ is different from that of $\Delta F = 2$ processes, e.g. $K^0 - \bar{K}^0$ and $B^0 - \bar{B}^0$ mixing. This implies that the relationship, Equation 1.35, is naturally broken, hence some differences would appear between the magnitude of the CP violation in the $K_L \rightarrow \pi^0 \nu \bar{\nu}$ decay and the CP asymmetry measurement from the $B \rightarrow J/\psi K_S$ decay.

1.5 History of the $K_L \rightarrow \pi^0 \nu \bar{\nu}$ search

Although the $K_L \rightarrow \pi^0 \nu \bar{\nu}$ decay offers a window for the study of CP violation, the present upper limit on the branching ratio of the $K_L \rightarrow \pi^0 \nu \bar{\nu}$ decay is

$$Br(K_L \rightarrow \pi^0 \nu \bar{\nu}) < 5.9 \times 10^{-7} \quad (90 \% \text{ C.L.}) \quad (1.40)$$

by the KTeV experiment [20]. This is still a few orders of magnitude higher than the SM prediction. In this section, we describe the past experimental searches for the $K_L \rightarrow \pi^0 \nu \bar{\nu}$ decay from an experimental viewpoint. There are five measurements on the $K_L \rightarrow \pi^0 \nu \bar{\nu}$ decay in the past as shown in Fig. 1.6.

The first search was performed by Littenberg [21]. He extracted a limit from the experiment of Cronin *et. al.* [22, 23] for the $K_L \rightarrow \pi^0 \pi^0$ decay. The limit was

$$Br(K_L \rightarrow \pi^0 \nu \bar{\nu}) < 7.6 \times 10^{-3} \quad (90 \% \text{ C.L.}) . \quad (1.41)$$

The following experimental studies on the $K_L \rightarrow \pi^0 \nu \bar{\nu}$ decay were carried out in two different approaches.

The first approach used $\pi^0 \rightarrow e^+ e^- \gamma$ decay to identify $K_L \rightarrow \pi^0 \nu \bar{\nu}$ decay. The current upper limit was set by the search using this approach. The advantage of using the $\pi^0 \rightarrow e^+ e^- \gamma$ is that the decay vertex can be reconstructed with $e^+ e^-$ tracks. Therefore, one can reconstruct the invariant mass of $e^+ e^- \gamma$ and require it to be m_{π^0} . On the other hand, a disadvantage is that the branching ratio of the $\pi^0 \rightarrow e^+ e^- \gamma$ decay is so small ($\sim 1\%$) that one needs a larger number of K_L 's.

Another approach used $\pi^0 \rightarrow \gamma \gamma$ decay. KTeV experiment set a limit on the branching ratio [24]:

$$Br(K_L \rightarrow \pi^0 \nu \bar{\nu}) < 1.6 \times 10^{-6} \quad (90 \% \text{ C.L.}) , \quad (1.42)$$

based on a special run taken in one day. As shown in Fig. 1.7, one event was observed in the signal region while 3.5 ± 0.9 background events were expected. The advantage of using the

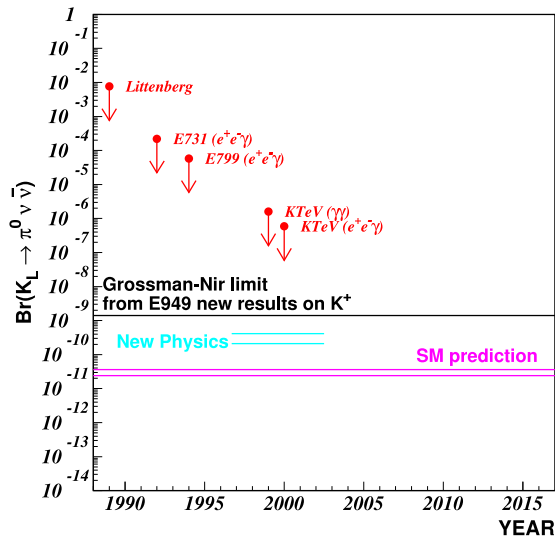


Figure 1.6: A history plot of the search for the $K_L \rightarrow \pi^0 \nu \bar{\nu}$ decay. In this figure, $(\gamma\gamma)$ and $(e^+e^-\gamma)$ denote the experimental approach with the $\pi^0 \rightarrow \gamma\gamma$ decay and $\pi^0 \rightarrow e^+e^-\gamma$ decay, respectively.

$\pi^0 \rightarrow \gamma\gamma$ decay is that since the branching ratio of the $\pi^0 \rightarrow \gamma\gamma$ is $\sim 99\%$, thus $O(10^2) \sim O(10^3)$ times higher sensitivity than using the $\pi^0 \rightarrow e^+e^-\gamma$ decay is achievable. However, the search for $K_L \rightarrow \pi^0 \nu \bar{\nu}$ using the $\pi^0 \rightarrow \gamma\gamma$ decay was already contaminated by the background. The main backgrounds were

- Other K_L decays such as $K_L \rightarrow \pi^0 \pi^0$ where two photons were missed, and
- Beam-associated backgrounds such as $\Lambda \rightarrow n \pi^0$ decay and π^0 production by the neutron interaction with detector materials.

The expected number of background, 3.5 ± 0.9 , was dominated by the background from neutron interactions.

If one wants to search for $K_L \rightarrow \pi^0 \nu \bar{\nu}$ decay with the $\pi^0 \rightarrow \gamma\gamma$ decay, one needs to improve the detector system in order to catch all the extra photons, and improve the neutral beam in order to reduce the number of Λ 's and neutrons. In addition, it is important to reduce the amount of detector materials in the beam in order to avoid neutron interactions.

1.6 KEK-PS E391a Experiment

In order to discover $K_L \rightarrow \pi^0 \nu \bar{\nu}$ decay and explore new origin of the CP violation, we started a series of experiments. We first carried out the first dedicated experiment, E391a experiment, at the 12 GeV proton synchrotron in High Energy Accelerator Research Organization (KEK). The E391a experiment started in February 2004 and had three data taking runs until December 2005. The purpose of E391a experiment is to establish a new experimental method. In E391a experiment, we identified $K_L \rightarrow \pi^0 \nu \bar{\nu}$ decay using $\pi^0 \rightarrow \gamma\gamma$ decay and introduced several new approaches to suppress the number of background events.

To achieve the goal, we should understand background sources and analysis techniques in our new experimental method. Based on the experience in E391a experiment, we plan to

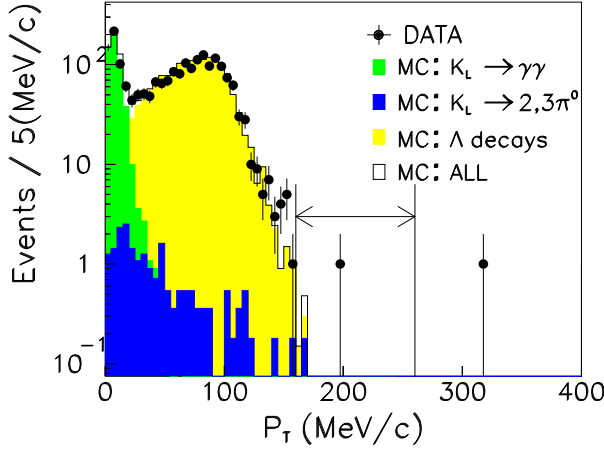


Figure 1.7: The distribution of the transverse momentum for the final remaining events in the search for $K_L \rightarrow \pi^0 \nu \bar{\nu}$ decay with $\pi^0 \rightarrow \gamma\gamma$ decay by the KTeV collaboration [24]. The arrow shows the signal region: $160 \leq P_T(\text{MeV}/c) \leq 260$.

search for $K_L \rightarrow \pi^0 \nu \bar{\nu}$ decay with a sensitivity of $O(10^{-13})$ at a high intensity 50 GeV/c proton synchrotron in J-Parc in the future.

In this thesis, we will describe a new result of the search for $K_L \rightarrow \pi^0 \nu \bar{\nu}$ using 10 % data taken in the first period of E391a experiment. This is the first step of our long road to the goal and this result led to a new understanding on background sources and analysis techniques in the new experimental method.

1.7 Outline of this thesis

We will first describe the experimental technique in Chapter 2. Chapter 3 describes the experimental apparatus and run. The Monte Carlo simulation of the kaon beams and detector is described in Chapter 4. Chapter 5 explains the event reconstruction method. Chapter 6 describes the event selection to suppress the number of background events. The background estimation is given in Chapter 7. Chapter 8 describes a discussion of systematic uncertainties to a sensitivity of $K_L \rightarrow \pi^0 \nu \bar{\nu}$ decay in this search. Chapter 9 presents the result of this search. Finally, we will conclude this thesis in Chapter 10.

Chapter 2

Experimental method

E391a experiment is the first dedicated experiment in the world to search for $K_L \rightarrow \pi^0 \nu \bar{\nu}$ decay. In this chapter, we give a conceptual description of the E391a experiment.

2.1 Overview

$K_L \rightarrow \pi^0 \nu \bar{\nu}$ decay has been searched for in several experiments as a by-product of their physics themes. We carried out the first dedicated experiment in the world, E391a experiment, to search for $K_L \rightarrow \pi^0 \nu \bar{\nu}$ decay.

The purpose of E391a experiment is to establish the experimental method of the measurement of $K_L \rightarrow \pi^0 \nu \bar{\nu}$ decays. The past experimental result is $Br(K_L \rightarrow \pi^0 \nu \bar{\nu}) < 5.9 \times 10^{-7}$, at the 90 % C.L. which is still a few orders of magnitude higher than the Standard Model prediction. Therefore, the primary physics motivation of the E391a is to explore $K_L \rightarrow \pi^0 \nu \bar{\nu}$ decays by improving the sensitivity down to the Grossman-Nir limit, 1.4×10^{-9} . In order to improve the sensitivity to the $K_L \rightarrow \pi^0 \nu \bar{\nu}$ decay, we need to increase both the number of K_L decays and the signal acceptance. At the same time, we should keep the number of background events small enough. In the following sections, we first introduce a parameter in an experiment. We then describe a detection method, considered background sources, and features of the E391a experiment.

2.2 Single Event Sensitivity

Here, we introduce a parameter used often in rare decay experiments, called “Single Event Sensitivity”. For example, if we observe some $K_L \rightarrow \pi^0 \nu \bar{\nu}$ decays, the branching ratio of the $K_L \rightarrow \pi^0 \nu \bar{\nu}$ decay would be:

$$Br(K_L \rightarrow \pi^0 \nu \bar{\nu}) = \frac{n_{sig}^{obs}}{N_{decay} \times A_{sig}} \quad (2.1)$$

where n_{sig}^{obs} is the observed number of $K_L \rightarrow \pi^0 \nu \bar{\nu}$ decays, N_{decay} is the total number of K_L decays, and A_{sig} is the signal acceptance, which is the probability to observe the signal decay.

Single Event Sensitivity (SES) is expressed as:

$$\text{SES} = \frac{1}{N_{decay} \times A_{sig}} . \quad (2.2)$$

It means that, in an experiment with a SES, we expect to observe $Br(K_L \rightarrow \pi^0 \nu \bar{\nu})/\text{SES}$ signal events on average.

The number of K_L decays can be measured by using other K_L decay mode. We call such a K_L decay mode as ‘‘normalization mode’’. The number of K_L decays, N_{decay} , is :

$$N_{decay} = \frac{n_{norm}^{obs}}{A_{norm} \times Br(norm)} , \quad (2.3)$$

where n_{norm}^{obs} is the observed number of events, A_{norm} and $Br(norm)$ are the acceptance and the branching ratio of the normalization mode, respectively.

Substituting Equation 2.3 into Equation 2.2, the SES is :

$$\text{SES} = Br(norm) \times \frac{A_{norm}}{A_{sig}} \times \frac{1}{n_{norm}^{obs}} . \quad (2.4)$$

Considering Equation 2.2, we should increase both the number of K_L decays and the signal acceptance in order to improve the sensitivity to the $K_L \rightarrow \pi^0 \nu \bar{\nu}$ decay.

2.3 Detection method

In E391a experiment, K_L 's were produced by striking protons from the 12 GeV proton synchrotron (KEK-PS) on a target. The signal for $K_L \rightarrow \pi^0 \nu \bar{\nu}$ decay is two photons from π^0 decay and no other particles detected in the final state.

The only K_L decay modes that have only two photons in the final state are $K_L \rightarrow \pi^0 \nu \bar{\nu}$ and $K_L \rightarrow \gamma \gamma$ decays. All other decay modes include at least two charged particles or at least four photons, and these decays can be removed by requiring that there are only two photons in the final state. We can discriminate $K_L \rightarrow \pi^0 \nu \bar{\nu}$ decay from $K_L \rightarrow \gamma \gamma$ decay by requiring a finite transverse momentum of the detected two photons' system.

By detecting $\pi^0 \rightarrow \gamma \gamma$, instead of $\pi^0 \rightarrow e^+ e^- \gamma$ used in previous search [20], we can get better sensitivity because the $Br(\pi^0 \rightarrow \gamma \gamma)$ is ~ 80 times larger than the $Br(\pi^0 \rightarrow e^+ e^- \gamma)$. In the experiment, we measure two photon energies and positions with an electromagnetic calorimeter and reconstruct π^0 . In order to make the signal acceptance large, we set the electromagnetic calorimeter at the downstream end of the decay region because two photons from π^0 decay are boosted in the K_L direction.

2.4 Background

One of the key issues in the $K_L \rightarrow \pi^0 \nu \bar{\nu}$ experiment is how to suppress the number of background events. Here, we describe several background sources that we considered in the E391a experiment.

Background due to photon inefficiency

If we lose some photons from a K_L decay or other reactions, it becomes a background event. One example is $K_L \rightarrow \pi^0\pi^0$ decay where two photons are missed. Figure 2.1 shows the distribution of the transverse momentum of two photons' system. We can discriminate between the signal and the background event by requiring a large transverse momentum. However, if the number of $K_L \rightarrow \pi^0\pi^0$ background events increases, they contaminate the signal region. Therefore, we should reduce such background events as much as possible.

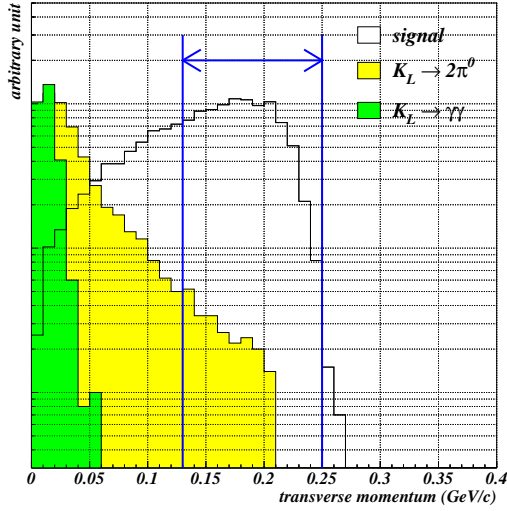


Figure 2.1: The distribution of the transverse momentum of two photons' system for $K_L \rightarrow \pi^0\nu\bar{\nu}$ (solid), $K_L \rightarrow \pi^0\pi^0$ (yellow hatched) and $K_L \rightarrow \gamma\gamma$ decays (green hatched) obtained by a Monte Carlo simulation.

One of the sources to miss photons is a so-called “fusion” where two nearby photons in the electromagnetic calorimeter are misidentified as one photon. It mainly depends on the size of segmentation of the electromagnetic calorimeter because almost the electromagnetic shower lies within one Molière radius. Also it depends on a method for finding photons.

Another sources is a detection inefficiency. There are two major mechanisms that cause the detection inefficiency.

1. *Electro-magnetic interaction*

There are two effects.

- (a) Punch through effect, where a photon passes through the detector without interacting with the detector material. The inefficiency for this effect is described by

$$\text{Inefficiency} = e^{-\sigma \cdot \rho \cdot l} \quad (2.5)$$

where l is a length of the detector, σ is a normalized cross section(cm^2/g) and ρ is a density(g/cm^3). As described in Equation (2.5), with a longer detector length, the inefficiency is reduced.

- (b) Sampling effect. For a sampling calorimeter such as a lead / scintillator sandwich, there is a sampling effect in which the energy deposit in the scintillator is below a detection threshold due to a fluctuation.

2. Photo-nuclear interaction

The photo-nuclear interaction is a reaction that an incident photon is absorbed by the nucleus and this nucleus emits protons, neutrons or photons. If only neutrons are released, the incident photon will not be detected.

The photon inefficiency depends on the incident photon energy and the type of detector. The photon inefficiency including the effect of the photo-nuclear interaction was measured for both a lead / scintillator sandwich detector and a CsI crystal for photons with the energies below 1 GeV [25], and above 1 GeV [26].

Background due to beam interaction

Many neutrons were also produced by the hadronic interaction at the target. If a neutron in the beam interacts with a detector material or with residual air, and one or more π^0 's are produced, it can become a background event.

Background due to charged particle inefficiency

Most K_L particles decay into at least two charged particles such as $K_L \rightarrow \pi^\pm e^\mp \nu$, $K_L \rightarrow \pi^\pm \mu^\mp \nu$ and $K_L \rightarrow \pi^+ \pi^- \pi^0$. In the experiment, we reject them by detecting charged particles with a scintillator. However, the charged particle inefficiency of such detector causes additional background sources.

2.5 Features of the E391a experiment

We designed an experiment to search for $K_L \rightarrow \pi^0 \nu \bar{\nu}$ decay with a high sensitivity while suppressing the backgrounds described above. Here, we describe the ideas for our detector system and K_L beam. These ideas are also meant to be applied to high sensitivity experiments in the future. In chapter 3 we will describe each detector component in detail.

2.5.1 Ideas to catch all the photons

We built a hermetic detector system to detect all the particles from K_L decays and other reactions. Figure 2.2 shows a conceptual view of the hermetic detector. All detector components are located in such a way that there are no insensitive regions. We used CsI crystals as the electromagnetic calorimeter and several sandwich type detectors to detect extra particles. In order to suppress events that decayed upstream of the detector surrounding the K_L decay regions, we built additional detector at the upstream of the hermetic detector system.

On the other hand, we still should make a beam hole in such a hermetic detector system in order to avoid any beam interactions with the detector materials. This allows some photons to escape down the beam hole. We put a detector at the end of the beam to catch such photons, but its detection efficiency is lowered by the high beam flux in the detector. This increases the overall photon inefficiency of the detector system. Therefore, the K_L beam has to be as narrow as possible to reduce such an inefficiency.

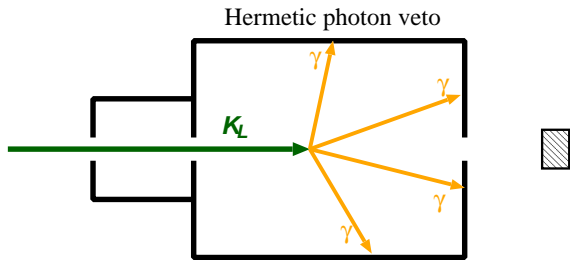


Figure 2.2: A conceptual view of the hermetic detector. The K_L decay region is surrounded with the detector in order to detect all photons from K_L decay.

2.5.2 Ideas to reduce beam neutron interactions

In order to reduce beam neutron interactions producing π^0 's, we took two approaches. First, we evacuate gas from the decay region down to 10^{-4} Pa to avoid interactions between neutrons in the beam and the gas. With this pressure, the number of background events will be negligible (≤ 0.1 events) for an experiment searching for $K_L \rightarrow \pi^0 \nu \bar{\nu}$ decay with the branching ratio of $O(10^{-10})$ [28]. However, such high vacuum is difficult with the detector components inside, because of large amount of out-gassing from detector materials. In order to avoid this problem, we put the detector components in a low vacuum region (~ 0.1 Pa). These different vacuum region can be separated by a thin film. We will describe details of the vacuum system in Section 3.3.

Second, we reduced the beam halo component as low as possible to minimize their interactions with the detector materials. In the E391a experiment, the rate of the beam halo is 5 orders of magnitude lower than the rate of the beam core.

2.6 Summary

We summarize key issues of the our experimental method as below.

- We detect $K_L \rightarrow \pi^0 \nu \bar{\nu}$ requiring two photons from π^0 decay ($\pi^0 \rightarrow \gamma \gamma$) and no other signal detected in the final state.
- We suppress the backgrounds, such as $K_L \rightarrow \pi^0 \pi^0$ decays with two missing photons and beam neutron interactions producing one or more π^0 , by following experimental approaches.
 1. We detect all the extra particles in the final state using the hermetic detector.
 2. To reduce beam neutron interactions, we evacuate gas from the decay region down to 10^{-5} . Also we reduce the beam halo components as low as possible to minimize their interactions with the detector materials.

In the next chapter, we will explain details of the experimental apparatus which were constructed to satisfy these purposes.

Chapter 3

Apparatus and run

In this chapter, we will describe the experimental apparatus of the E391a experiment. The E391a experiment was proposed to search for $K_L \rightarrow \pi^0 \nu \bar{\nu}$ decay at KEK and was approved in 2001. As shown in Fig. 3.1, the experimental apparatus consists of the 12 GeV Proton Synchrotron in KEK (KEK-PS), a neutral beam line and a detector system. Neutral beam line and detectors were constructed at the East Counter Hall in KEK.

Section 3.1 describes the neutral beam line. Section 3.2 explains the detector system. The details of the vacuum system is given in Section 3.3. Section 3.4 describes the trigger system. Section 3.4 describes the data acquisition system. Finally, we explain the run conditions in Section 3.6.

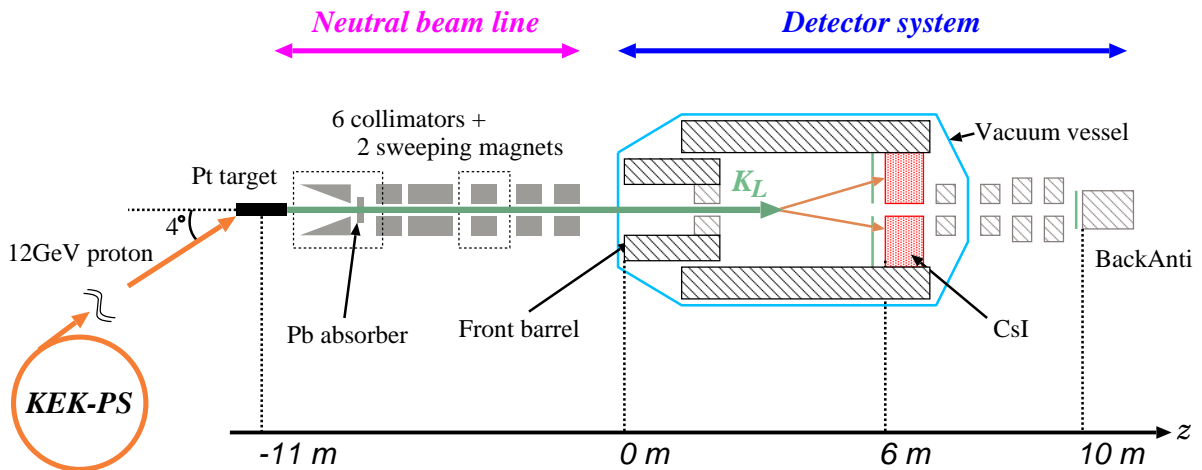


Figure 3.1: Schematic view of the E391a experiment. The E391a experiment consists of the neutral beam line and the detector system. The proton beam was delivered from KEK 12 GeV Proton Synchrotron.

3.1 K_L beam

Figure 3.2 shows an overview of the neutral beam line including the production target. Protons from the KEK-PS hit a production target and then produced K_L particles. K_L 's went to the detector system through the neutral beam line.

In the following subsections, we will describe the primary proton beam, the K_L production target and the neutral beam line.

3.1.1 Primary proton beam and K_L production target

Protons were accelerated up to the kinetic energy of 12 GeV in 2 seconds, and then extracted slowly to the East counter Hall going through the EP2-C beam line. The extraction took 2 second (Slow Extraction mode). We call the extracted protons during the 4 second cycle as “spill”. The protons hit the production target and produced secondary particles. Typical beam intensity at the target was 2.5×10^{12} protons per a spill. The profile of the primary proton beam was an ellipse with $\sigma = 1.1$ mm in vertical and $\sigma = 3.3$ mm in horizontal directions [27].

The production target was made of platinum(Pt) with 60 mm in length ($0.68\lambda_I$, $20X_0$, where λ_I and X_0 are the interaction length and the radiation length, respectively) and 8 mm in diameter. The target and the neutral beam line set on a same axis in order to minimize the source point of the secondary particles viewed from the detector system. The primary proton beam struck the target with 4° horizontally with respect to the neutral beam line. Hence, the secondary particles went through the neutral beam line with the extraction angle of 4° . This extraction angle was chosen in order to reduce the number of neutrons compared to the number of K_L 's because the beam neutron interaction with the residual gas could be a background source in the $K_L \rightarrow \pi^0\nu\bar{\nu}$ decay. The neutron/ K_L ratio was ~ 60 at the target.

3.1.2 Neutral beam line

The neutral beam line in the E391a experiment was constructed to satisfy following conditions.

1. *Pencil beam*

“*Pencil beam*” means a narrow beam. There were two reasons. One reason was to reduce the uncertainty of the transverse momentum of the π^0 , since it is used to discriminate between the signal and the background, as mentioned in Section 2.3. Since we reconstructed the transverse momentum of π^0 assuming that the π^0 decay vertex was on the beam axis, large beam size would increase the transverse momentum resolution.

Another reason was to reduce a probability that photons went through the beam hole without being detected. With the pencil beam, we could make the beam hole smaller.

2. *Clean beam*

“*Clean beam*” means that halo component in the neutral beam is small. If a neutron in the halo interacted with the detector materials, it could become a background event.

As shown in Fig. 3.2, the neutral beam line consisted of a pair of sweeping magnets, two stages of collimation using six sets of collimators (C1 – C6), lead(Pb) and beryllium(Be) absorbers and a vacuum pipe. Total length from the target to the exit of last collimator (C6) was

Table 3.1: Specifications of the KEK-PS accelerator and the neutral beam in the E391a experiment.

parameter	value
<u>KEK-PS accelerator</u>	
Proton energy	12 GeV (in kinetic energy)
Typical intensity / pulse	2.5×10^{12}
Repetition cycle	4 sec
Flat top	2 sec (Slow extraction mode)
Duty factor	0.5
<u>Neutral beam line</u>	
Target	Pt rod (60 mm ($0.68\lambda_I$) long, 8 mm in diameter)
Targeting angle	4°
Beam profile	2 mrad of a half cone angle
neutron / K_L ratio	60
Average K_L momentum at C6	2.6 GeV

11 m in order to reduce the number of muons punching through the materials in the beam line. Also, this distance helped to reduce backgrounds from some hyperon decays, such as $\Lambda \rightarrow n\pi^0$. The total length of the collimators corresponded to approximately $47\lambda_I$.

The lead and beryllium absorbers reduced γ 's and neutrons in the beam, respectively. The first three collimators, C1, C2 and C3, were used to define the beam profile in an aperture of 2 mrad of a half cone angle. The last two collimators, C5 and C6, were used to trim the beam halo. A part of halo neutrons were produced at the C6 by secondary neutrons and by charged pions from K_L decays. In order to reject the background events due to the neutrons produced at the C6, plastic scintillator rings with a thickness of 1 cm were installed as an active detection element between tungsten disks in the downstream half of the C6. Scintillation light was read out through wavelength-shifting fibers arranged at the outer periphery of the scintillator disks.

The fourth collimator, C4, was used to reduce thermal neutrons which were one of the sources of accidental hits in the detector region. C4 consisted of the thin gadolinium-oxide (Gd_2O_3) sheets. Our measurement confirmed that C4 reduced the thermal neutron flux by one order of magnitude [27].

Figure 3.3 shows the beam profiles for γ 's and neutrons at the exit of C6, obtained by Monte Carlo simulation. The neutral beam was sharply collimated, and the flux ratio of halo to core was lower than 10^{-5} . Figure 3.4 shows the K_L momentum spectrum at exit of the C6 reproduced by the Monte Carlo simulation. The average momentum of K_L beam was 2.6 GeV/c at C6.

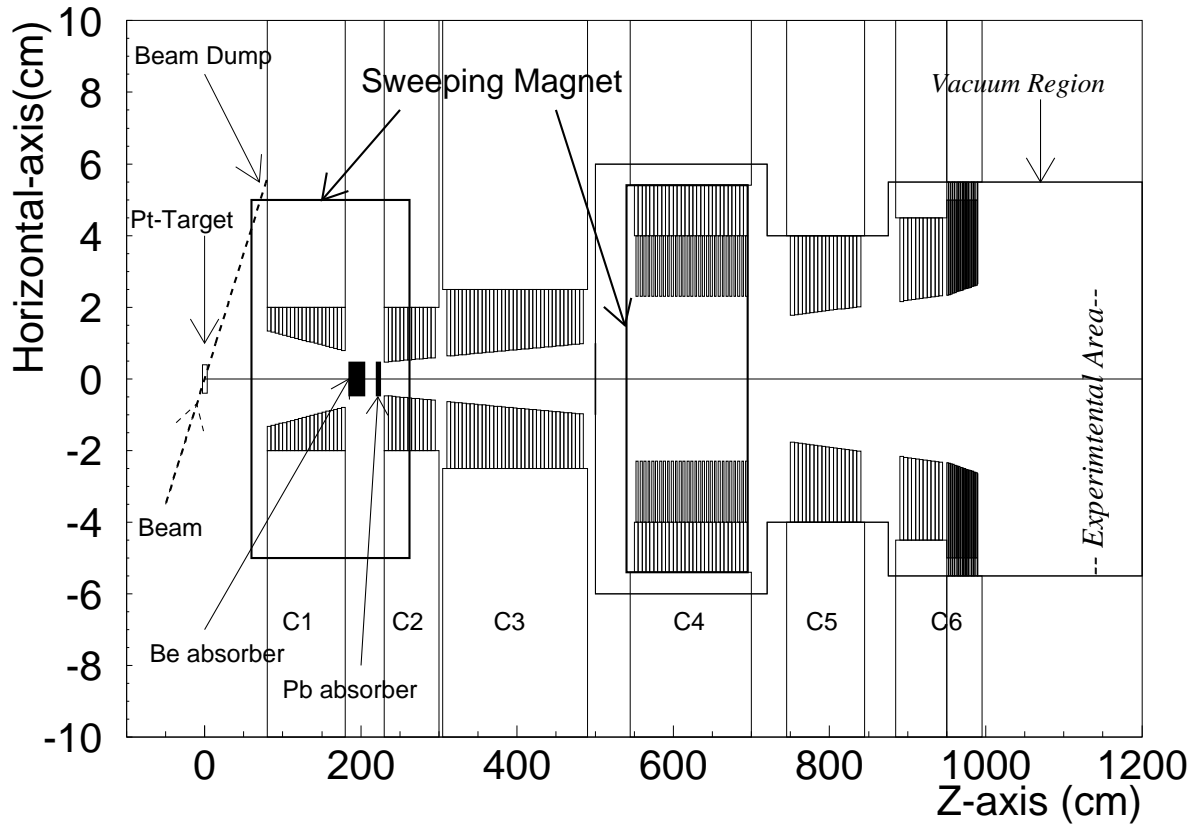


Figure 3.2: Plan view of the neutral beam line. The neutral beam line consists of a pair of sweeping magnets, and six sets of collimators (C1 – C6).

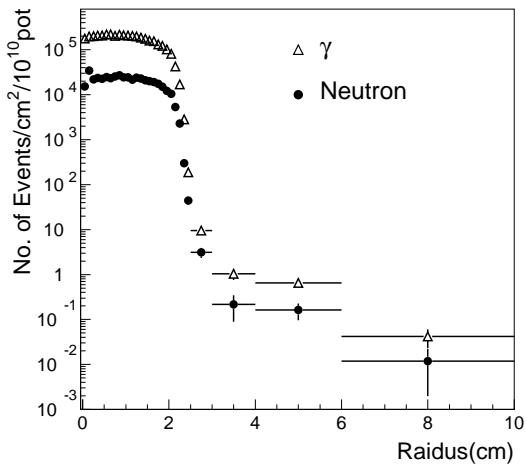


Figure 3.3: Beam profiles at the exit of the C6 obtained by a Monte Carlo simulation without absorber. The triangles and circles indicate those for γ 's and neutrons with energies above 1 MeV, respectively.

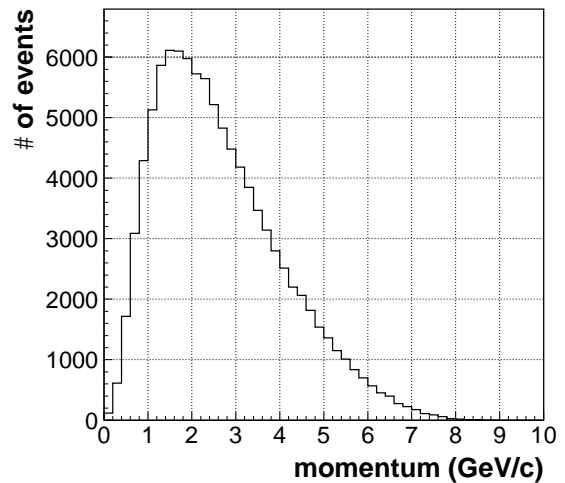


Figure 3.4: K_L momentum distribution at the exit of the beam line (C6) obtained by a Monte Carlo simulation which will be described in Chapter 4. The average momentum of K_L beam is 2.6 GeV/c.

3.2 Detector element

3.2.1 Overview

As mentioned in Section 2.3, we measured photon energies and positions by an electromagnetic calorimeter and detected all the extra particles by a hermetic detector system.

Figure 3.5 shows an overview of the E391a detector. K_L 's decayed in the vacuum decay region of 10^{-5} Pa. We put most of the detector components inside a vacuum vessel to avoid any absorption of photons and charged particles.

The electromagnetic calorimeter was placed at the downstream end of the decay region to detect two photon energies and positions. Other detector components were used to detect photons that did not hit the calorimeter. The decay region was covered by Main Barrel (MB). The upstream of the decay region was covered by Front Barrel (FB) and Collar-Counter-02 (CC02) to suppress background events from K_L 's decaying upstream of the decay region. To detect photons going parallel to the beam and through the beam hole, we placed CC03, CC04, CC05, CC06 and CC07 perpendicular to the beam axis. These detectors were surrounding the beam holes. Back Anti (BA) was placed at the end of beam in order to detect photons going through the beam hole and undetected by other detectors. To detect charged particles, three charged veto detectors: CV, BCV and BHCV were set.

Total length of the detector system was 10 m. Table 3.2 lists positions, dimensions, brief configurations and the number of readouts of each detector element.

We defined the E391a coordinate system. The \vec{z} was according to the beam direction. Our reference point in the z -axis was the front surface of FB. The \vec{y} was the vertically upward direction of the system. The \vec{x} satisfied the relation of the right-hand system, i.e. $\vec{x} = \vec{y} \times \vec{z}$.

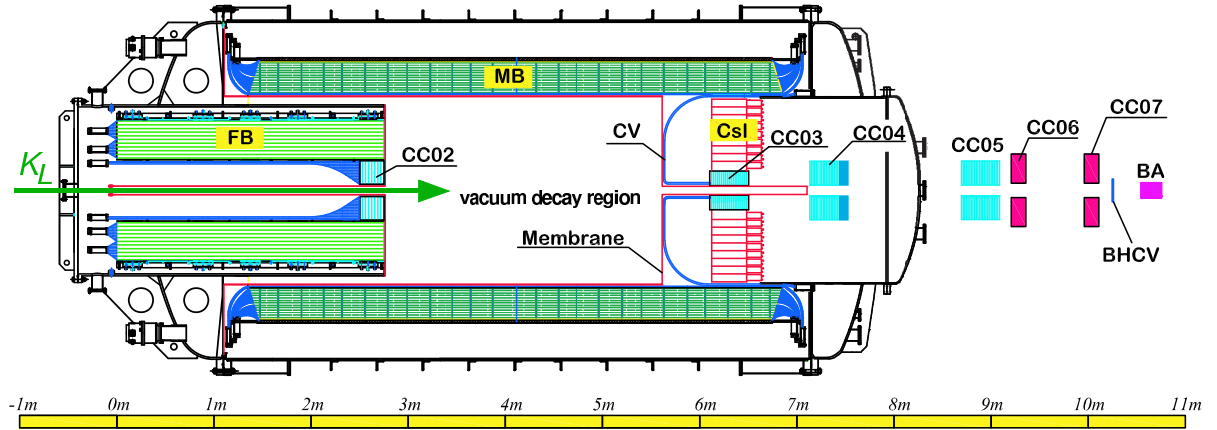


Figure 3.5: An overview of the E391a detector. K_L 's enter from the left side.

3.2.2 Electromagnetic calorimeter

We used an array of CsI crystals as an electromagnetic calorimeter. As shown in Fig. 3.6, the electromagnetic calorimeter was in a circular shape and 1.9 m in diameter. There was

Table 3.2: Positions, dimensions, brief configurations and the number of readouts of the detector elements.

detector	z position (cm)	transverse size (cm)	configuration	# of readouts
FB	0.0	outer diameter: 145.0 inner diameter: 62.0	lead/scint.	32
MB	134.8	outer diameter: 276.0 inner diameter: 200.0	lead/scint.	128
BCV	134.8	outer diameter: 200.0 inner diameter: 199.0	plastic scint.	32
CC02	239.1	outer diameter: 62.0 inner diameter: 15.8	lead/scint.	8
CV	554.8	outer diameter: 190.6 inner: 12.0 (square)	plastic scint.	32+4
CsI	614.8	outer diameter: 190.6 inner: 25.0 (square)	CsI(pure)	576
CC03	609.8	outer: 25.0 (square) inner: 12.0 (square)	tungsten/scint.	6
Sandwich	614.8	(outside of CsI calorimeter)	lead/scint.	24
CC04	710.3	outer: 50.0 (square) inner: 12.6 (square)	lead/scint.	4
CC05	874.1	outer: 50.0 (square) inner: 12.6 (square)	lead/scint.	6
CC06	925.6	outer: 30.0 (square) inner: 15.0 (square)	lead glass	10
CC07	1000.6	outer: 30.0 (square) inner: 15.0 (square)	lead glass	10
BHCV	1029.3	20.0 (square)	plastic scint.	4
BA	1059.3	24.5 (square)	lead/scint. Quartz	36 42

CC03 inside of the calorimeter with 12 cm \times 12 cm hole. The electromagnetic calorimeter was located on $z = 614.8$ cm. It consisted of 576 pure CsI crystals locating on a cylindrical support structure. Most of them were square shape CsI crystals. In order to fit the calorimeter inside the support structure, we used no-square shape CsI crystals, “Edge CsI”, and lead / scintillator sandwich, “Sandwich module”, at the outer edge of electromagnetic calorimeter.

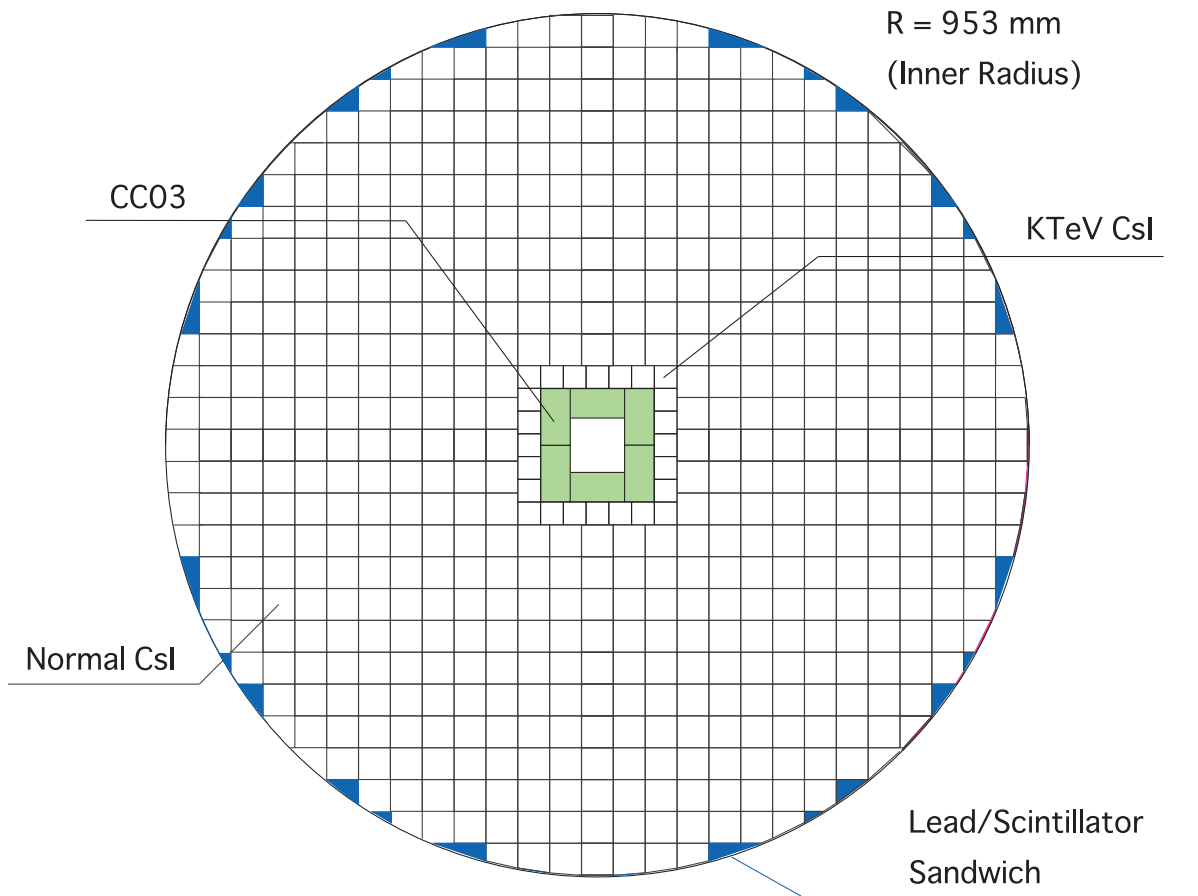


Figure 3.6: An overview of the electromagnetic calorimeter. It consists of 576 CsI crystals and 24 Sandwich modules.

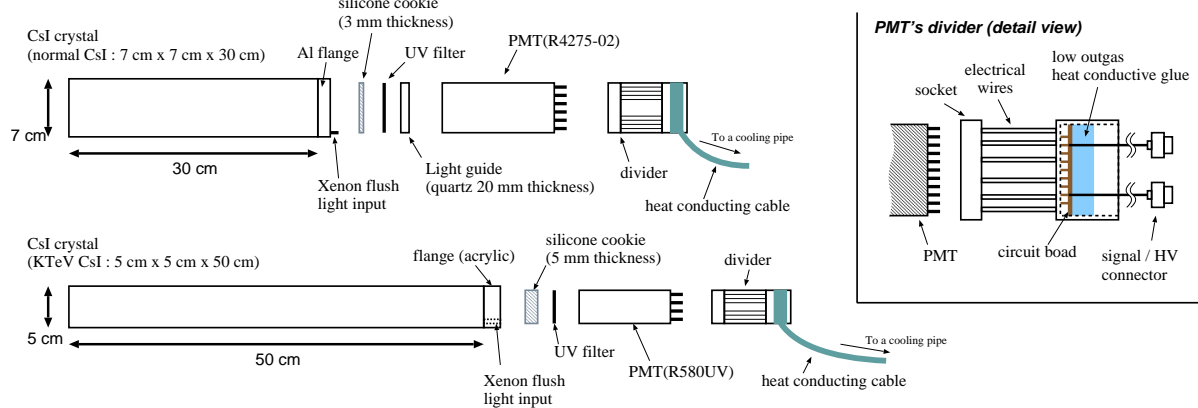


Figure 3.7: Schematic drawing of CsI crystal and associated equipments.

CsI crystal and Sandwich module

CsI crystal

We used two different sizes of CsI crystals. One of them was $7\text{ cm} \times 7\text{ cm} \times 30\text{cm}(= 16X_0)$ crystals. We call them “Normal CsI”, and there were 496 of them. The other was $5\text{cm} \times 5\text{cm} \times 50\text{cm}(= 27X_0)$ crystals. Since we borrowed them from KTeV experiment, we call them “KTeV CsI”, and there were 24 of them.

For Normal CsI, we wrapped each crystal with a $100\ \mu\text{m}$ thick Teflon sheet and then wrapped with a $20\ \mu\text{m}$ thick Aluminized mylar in order to optically isolate each crystal and to make the light collection effective. The Normal CsI crystal yielded typically 15 photoelectrons per MeV of the energy deposit. The scintillation light produced by the electromagnetic showers in the CsI crystal was detected by the photo-multiplier tube (PMT) mounted on the back of each crystal. As shown in Fig. 3.7, each crystal was viewed by a 2 inch Hamamatsu R4275-02 PMT through a 3 mm thick silicone cookie, and a UV transmitting filter to reduce the emission spectrum of the slow component of the scintillation light from CsI crystal. Since these modules were operated in vacuum, we modified the PMT divider to reduce heat dissipation and heat conduction from the divider to the PMT. This was achieved by decreasing the divider current and taking a larger gap between the PMT and the divider circuit board as shown in Fig. 3.7. We also filled the PMT divider with a 5 mm thick heat conductive glue (METACAST 5448). The PMT divider was connected to a cooling water pipe. The cooling water system is described in Section 3.3.

We put 24 KTeV CsI crystals at the inner edge of the calorimeter. Each KTeV CsI was wrapped with a $13\ \mu\text{m}$ thick mylar. The KTeV CsI yielded typically 20 photoelectrons per MeV of the energy deposit. Each KTeV CsI was viewed by a 1.5 inch Hamamatsu R580-UV PMT through a 5 mm thick silicone cookie and a UV transmitting filter, as shown in Fig. 3.7. We used the PMT divider with same the structure as the ones for the Normal CsI crystals. We filled the PMT divider with a heat conductive glue (EN11) and connected the divider to a cooling water pipe.

Edge CsI

For the outside edge, we cut $7\text{ cm} \times 7\text{ cm} \times 30\text{cm}(= 16X_0)$ crystals to fit the calorimeter inside the support structure. There were 56 such crystals in seven different shapes as shown in Fig. 3.8. The optical treatment and its light yield was almost the same as the Normal CsI. We used $1\frac{1}{8}$ inch Photonis XP 2978 PMTs for smaller 32 crystals and 2 inch Hamamatsu R4275-02 PMTs for the rest. These PMTs were directly attached to the crystal.

Sandwich module

In order to fill gaps between CsI calorimeter and the support structure, we used lead / scintillator sandwich, so-called “Sandwich module”. There were 24 Sandwich modules. The Sandwich modules consisted of the 1 mm thick lead and 5 mm thick plastic-scintillator layers. As shown in Fig. 3.9, there were three different types: type-A, type-B and type-C, according to the number of layers. The scintillation light produced by the electromagnetic shower in the Sandwich module was absorbed by wavelength-shifting (WLS) fibers. WLS fibers were 1mm

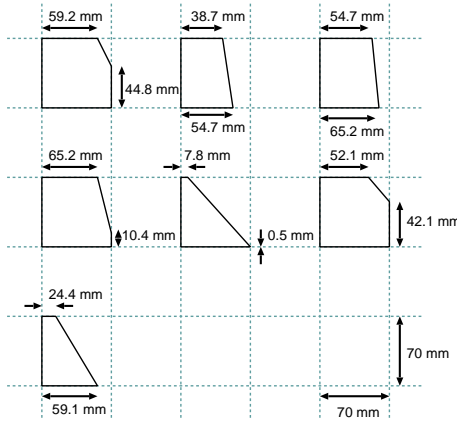


Figure 3.8: Edge CsI crystals. There were seven different shapes.

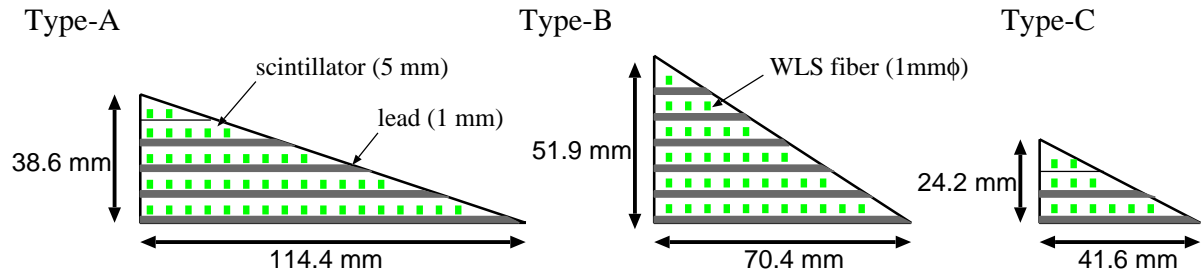


Figure 3.9: Sandwich module. There were three different types of modules. Type-A, type-B, and type-C modules consisted of four, five and two pairs of the lead / scintillator layer, respectively.

in diameter with a multi-cladding(KURARAY Y-11) and were glued to grooves on the surface of the scintillator plate. The light from the WLS fiber was detected by a $1\frac{1}{8}$ inch Hamamatsu H1398 PMT. The other end of the fiber was polished and treated with an aluminum coating. Typical light yield was 10–20 photoelectrons per MeV energy deposit.

Xenon gain monitoring system

Figure 3.10 shows a schematic view of the calibration system to monitor the stability of the PMT's gain. A Xenon lamp flashing at 1.1 Hz was located in the constant temperature box. The light from the Xenon lamp was distributed into the PMT of CsI crystals through a clear fiber. In the constant temperature box, there were seven monitor PMTs for monitoring. One of them was used for triggering. Three of them were used to monitor the light yield of the Xenon lamp distributed to CsI crystals. Other three PMTs were used to monitor the light yield of the Xenon lamp itself by directly connecting clear fibers from the Xenon lamp. We checked a stability of each monitor PMT with a stable light source attached at the front surface of the PMT.

Figure 3.11 shows the average gain of PMT as a function of the operation days, monitored

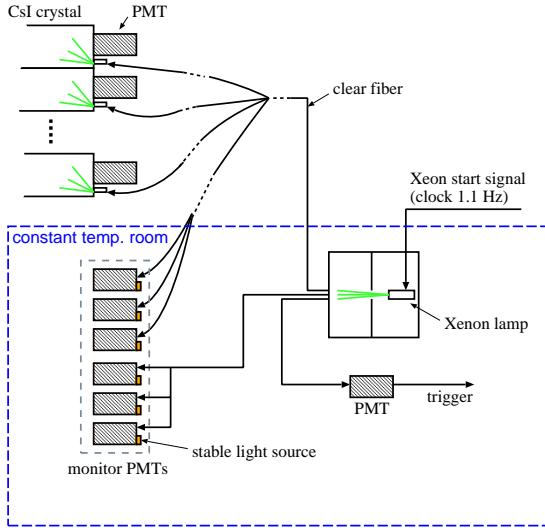


Figure 3.10: Schematic view of the Xenon gain monitoring system.

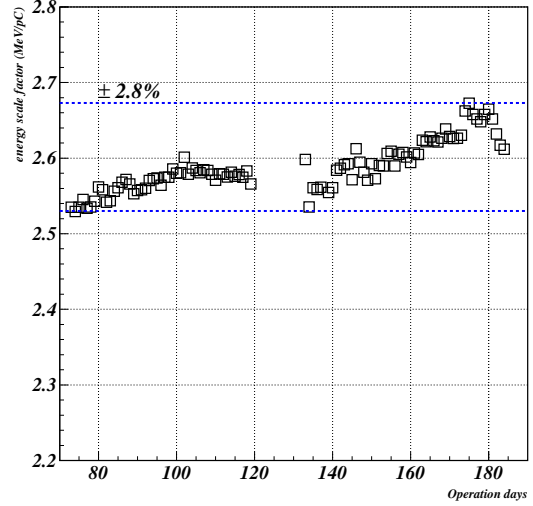


Figure 3.11: The gain stability of CsI's PMT as a function of the operation days.

by the Xenon system. The fluctuation of the gain was within $\pm 2.8\%$.

Performance of the electro-magnetic calorimeter

We measured the energy resolution of the electromagnetic calorimeter using a positron beam. Figure 3.12 shows the energy resolution as a function of the incident energy, E , as measured with 25 Normal CsI crystals. As a result, we obtained the energy resolution:

$$\frac{\sigma_E}{E(\text{GeV})} \simeq \frac{1\%}{\sqrt{E(\text{GeV})}} \oplus 1\%. \quad (3.1)$$

We continually calibrated the energy scale factor using cosmic ray muons and minimum ionization particles in the beam during the operation [29, 30]. We also studied the energy scale factor using the data as described in Chapter 5.

3.2.3 Charged veto

Most K_L particles decay into at least two charged particles such as $K_L \rightarrow \pi^\pm e^\mp \nu$, $K_L \rightarrow \pi^\pm \mu^\mp \nu$ and $K_L \rightarrow \pi^+ \pi^- \pi^0$. In order to reject these decays, we installed the ‘‘Charged Veto’’ (CV) detector in the front of CsI calorimeter.

We grouped CV into the outer CV and the inner CV as shown in Fig. 3.13. The outer CV consisted of 32 plastic scintillator plates with a thickness of 6 mm. They were 50 cm away from CsI surface and bent at outside of the calorimeter, and extended to phototubes. The inner CV consisted of 4 plastic scintillator plates with a thickness of 6 mm. They were located parallel to the beam axis. We used 2 inch Hamamatsu R329 PMT for all the CV counters.

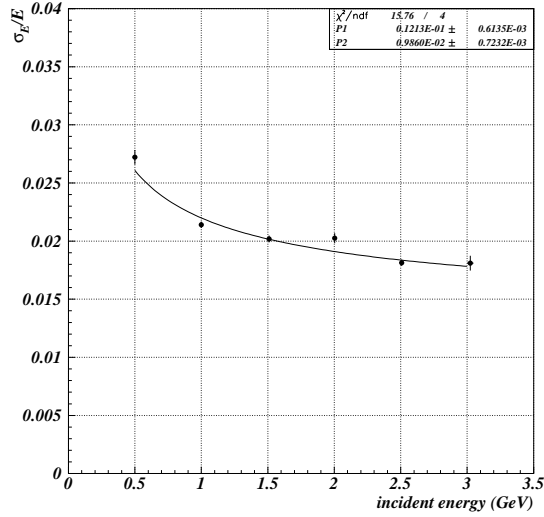


Figure 3.12: The energy resolution as a function of the incident energy as measured with a positron beam with 25 Normal CsI crystals.

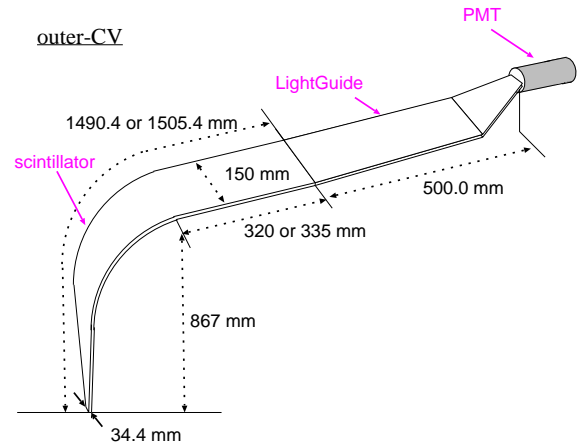
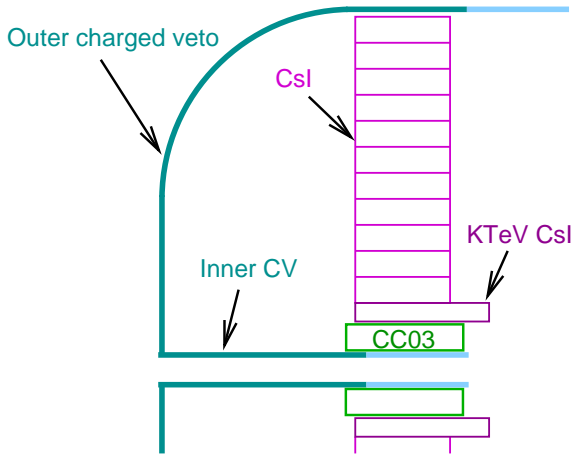


Figure 3.13: Schematic drawings of CV. Right drawing shows a detail structure of the outer CV.

Figure 3.14 shows the light yield as a function of the distance from the PMT, which was measured with a β source [32]. The light yield increases at the far end due to the scintillator's wedge like shape.

3.2.4 Main barrel

Main barrel(MB) surrounded the K_L decay region to detect photons from the K_L decay and other reactions. MB consisted of 32 modules as shown in Fig. 3.15. The overall size of MB was 2.76 m in the outer diameter, 2.00 m in the inner diameter and 5.5 m in the longitudinal

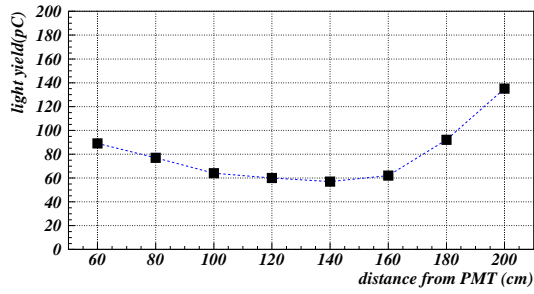


Figure 3.14: The light yield of the outer CV as a function of the distance from the PMT [32].

length.

Each module was in a trapezoid shape as shown in Fig. 3.16. It consisted of 45 pairs of a 5 mm thick plastic-scintillator plate and a lead sheet. For inner 15 layers, each lead sheet was 1 mm in thickness. For the rest of 30 layers, each lead sheet was 2 mm in thickness. Each scintillator plate was sandwiched by white reflecting sheets. Total thickness of the module was 317.9 mm which corresponds to $13.5X_0$. These layers were compressed between a 3 mm thick steel plate at the inside and a 28.6 mm thick steel backbone plate at the outside with 52 screw bolts.

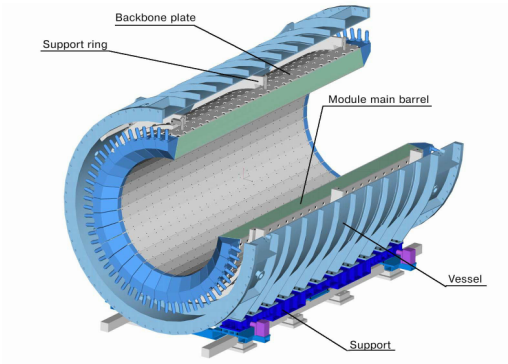


Figure 3.15: An overview of the detectors in the middle section. Main barrel (MB) and Barrel charged veto (BCV) are supported by the vacuum vessel.

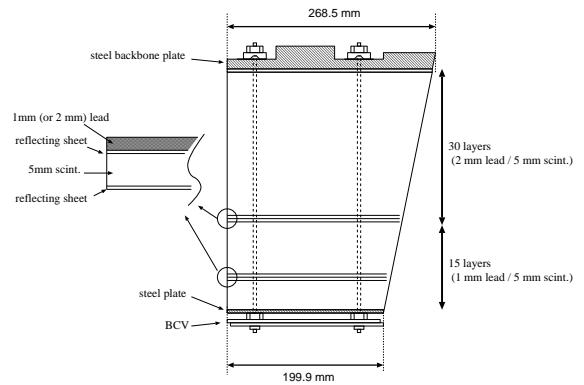


Figure 3.16: Schematic drawing of MB module. We call the first 15 layers from the bottom as “inner module” and the remaining 30 layers as “outer module”.

Scintillator plate

Scintillator plates were made of a MS resin (a copolymer of methylmethacrylate and styrene) infused with the fluors PPO(1 %) and POPOP(0.02 %). In order to increase a strength of

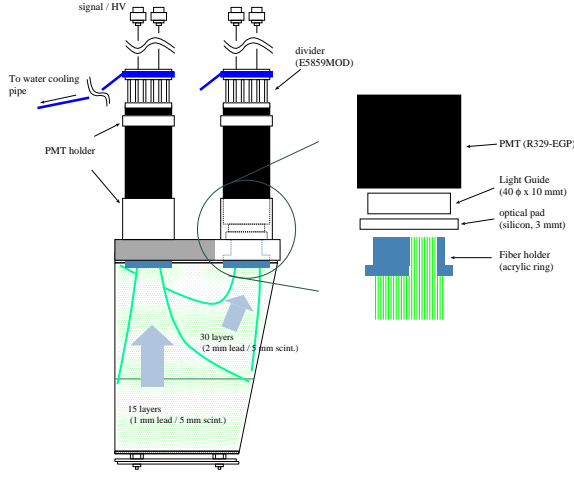


Figure 3.17: Readout scheme of MB module. Two PMTs were attached at each end of MB module.

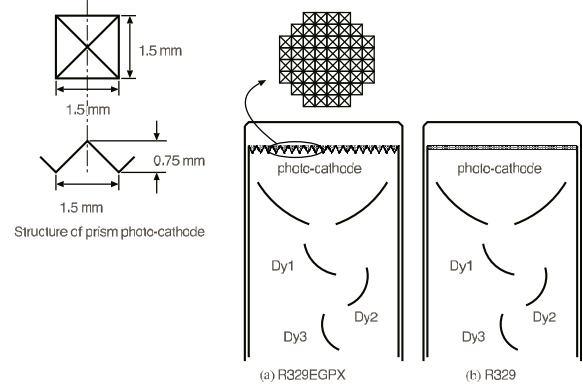


Figure 3.18: A prism-shape photo-cathode (a) vs. a normal photo-cathode (b) [33].

the scintillator plate to sustain its long detector length, we used the MS resin instead of usual polystyrene. The scintillator plate had 1.3 mm deep grooves at a 10 mm interval to insert wavelength shifting fibers described in the next paragraph.

Wavelength shifting fiber

In order to reduce attenuation loss of the scintillation light, we used wavelength-shifting(WLS) fibers glued in grooves of the scintillator plate. The WLS fiber was 1 mm in diameter with a multi-cladding structure(KURARAY Y-11). The scintillation light produced by the electromagnetic shower in MB module was absorbed in the WLS fibers. The WLS fiber has an absorption peak at $\lambda = 430$ nm and emission peak at $\lambda = 476$ nm.

Connection between fibers and PMT

At both edges of fibers, we grouped the fibers from the layers with the same lead thickness. We call the inner 15 layers as “inner module” and the outer 30 layers as “outer module”. We attached four PMTs on each MB module: two PMTs at the farthest side from CsI calorimeter, and two PMTs at the nearest side from CsI calorimeter. A schematic view of the fiber readout for MB module is shown in Fig. 3.17. The WLS fibers were glued with a optical cement (BICRON BC-600) in the acrylic ring and fibers were cut and polished. The light from the fibers was guided to the PMT through a 3 mm thick silicone cookie and a 10 mm thick light guide.

PMT / divider

We used 2 inch Hamamatsu R329-EGP PMT, which we newly developed with Hamamatsu Photonics K.K. [33]. In order to increase the quantum efficiency for the WLS emission light, we established a prism-shape photo-cathode (Fig. 3.18) and modified the material of the photo-cathode to be sensitive to a green light region to match the emission spectrum of the WLS fiber. The R329-EGP was 1.8 times more sensitive to the WLS emission light than a standard PMT, R329.

In order to reduce heat dissipation and heat conduction from the PMT divider to the PMT, we connected the divider with a cooling water pipe, and used a new PMT divider which was similar to the ones for the CsI crystals described in Section 3.2.2.

Gain monitoring system

To check the detector stability, we monitored the PMT gain by using a LED calibration system. A blue LED at the outside of the vacuum vessel was flashed with 1.1 Hz, and its light was guided through an acrylic flange and clear fibers to each PMT.

The gain shift between the on-beam period and the off-beam period was less than 1 %.

Performance

Performance of MB was measured using cosmic ray muons both before and after its installation. Typical pulse width (FWHM) was 16 nsec [36]. Figure 3.19 shows the distribution of the light yield of MB module as a function of the distance from PMT. Typical light yield was 35 (10) photo-electrons per MeV energy deposited at the nearest (farthest) point from the PMT. As shown in Fig. 3.20, the timing resolution was 0.6 nsec for 15 MeV energy deposit (inner module) and 0.5 nsec for 30 MeV energy deposit (outer module), respectively.

Barrel Charged Veto

In order to identify charged particles, a plastic scintillator plate was placed in front of MB. Figure 3.21 shows a schematic view of Barrel Charged Veto(BCV) detector. BCV was made of two 5 mm thick scintillator plates glued together with optical cement. Properties of the scintillator plate were the same as MB. Total size was 550 cm in longitudinal length, 1 cm in total thickness and 20 cm in width. WLS fibers(KURARY Y-11) were sandwiched between the scintillator plates. The scintillator light was read out by the 1 inch Hamamatsu R7899-EGP PMT with a prism photo-cathode optimized for the WLS emission light.

3.2.5 Front barrel

Front barrel (FB) had a similar structure with MB. It was surrounding upstream of the K_L decay region. As shown in Fig. 3.22, FB consisted of 16 modules. The overall size of FB was 1.45 m in outer diameter, 0.62 m in inner diameter and 2.75 m in longitudinal length.

A schematic drawing of FB module is shown in Fig. 3.23. It consisted of 59 pairs of a 5 mm thick scintillator plate and a 1.5 mm thick lead sheet. Total thickness of the module was

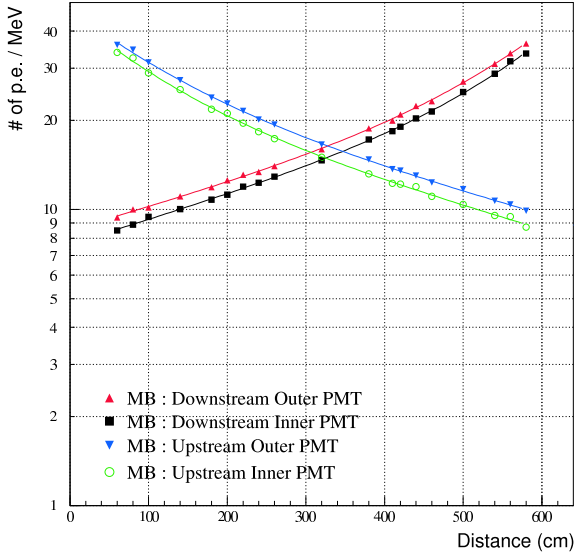


Figure 3.19: The light yield of MB module as a function of the distance from the PMT. We attached four PMTs on one MB module: downstream outer (red triangle), downstream inner (black square), upstream outer (blue triangle), and upstream inner (open circle) [36].

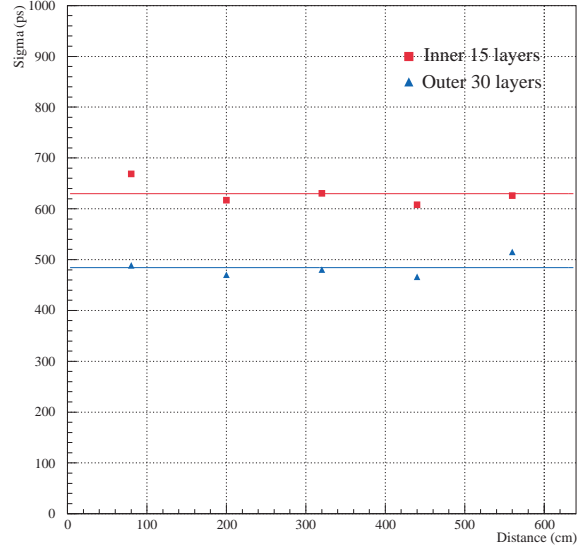


Figure 3.20: Timing resolution of MB module as a function of the distance from the PMT [36].

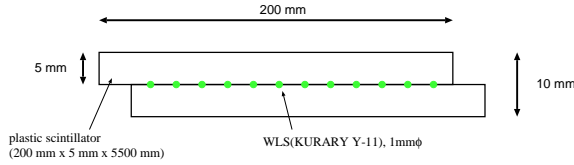


Figure 3.21: Schematic drawing of BCV. The green circles show the WLS fibers.

413 mm which corresponds to $17.2X_0$. These layers were compressed by five steel belts (100 μm in thickness) with six screw bolts.

In FB, we used a different WLS fiber: 1 mm in diameter with a multi-cladding structure (BICRON BCF-91a). At edge of the fibers, we grouped the fibers into two bundles: the inner 27 layers and the rest of 32 layers, and attached 2 inch Hamamatsu R329-EGP PMT to each bundle. Opposite edge of the fibers was covered by an Aluminized mylar to reflect light.

Performance of FB was measured using cosmic ray muons both before and after installation. Typical light yield was 20 (10) photo-electrons per MeV energy deposit at the nearest (farthest) point from the PMT.

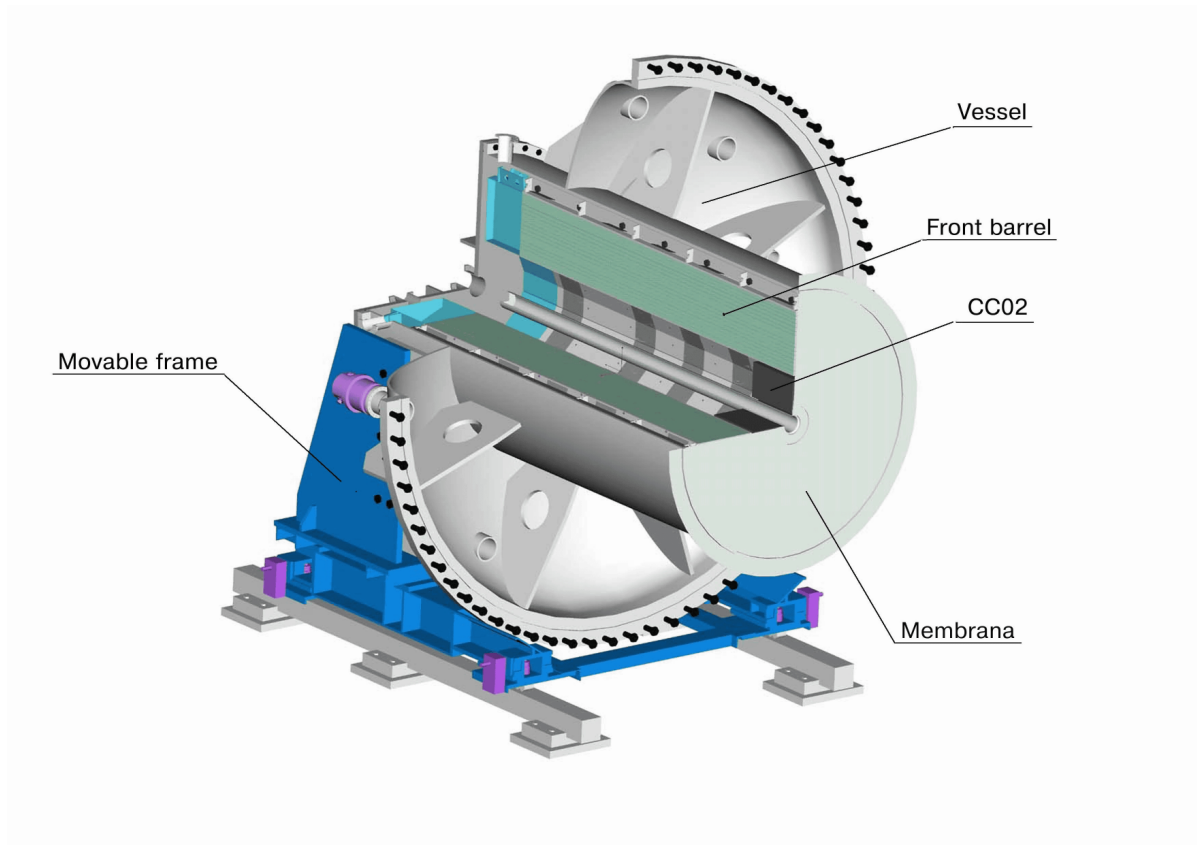


Figure 3.22: An overview of the upstream detectors.

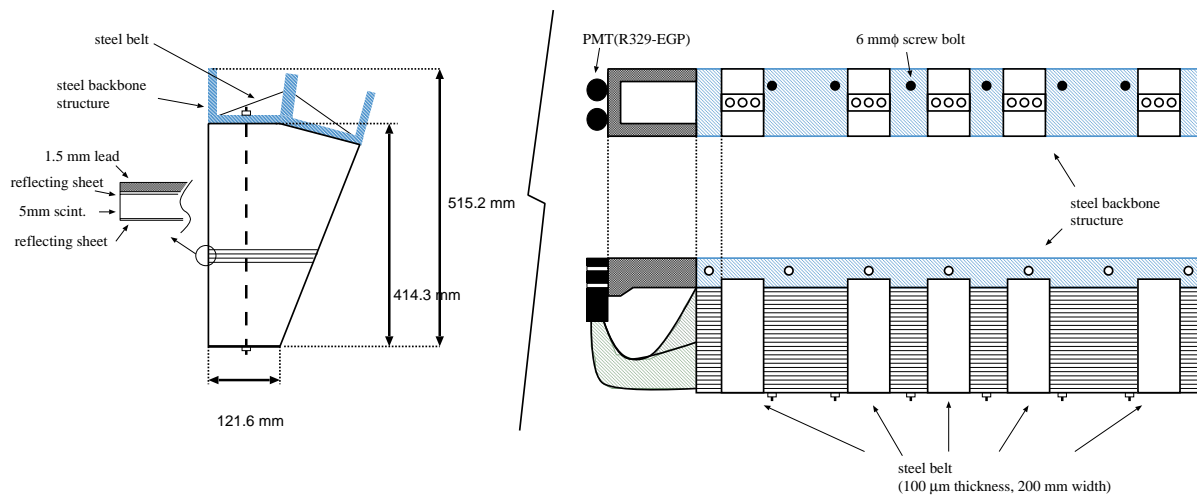


Figure 3.23: FB module, which consists of 59 lead (1.5 mm) and scintillator (5 mm) sandwich layers.

3.2.6 Collar counters

In order to detect photons going parallel to the beam, we placed a series of photon veto detectors perpendicular to the beam axis. These detectors were surrounding the beam holes (so-called ‘‘Collar Counter’’). There were six collar counters: CC02, CC03, CC04, CC05, CC06 and CC07. (There was no CC01 for historical reasons.) Here, we describe the structure and performance of these detectors.

CC02

CC02 was located at the downstream edge and inside the cylinder formed by FB and surrounding the beam hole as shown in Fig. 3.22. Figure 3.24 is a schematic drawing of CC02. CC02 consisted of 8 modules and forms an octagonal shape. Inner beam hole was 158.4 mm in diameter. To detect photons coming along the beam axis, CC02 had a shashlik structure in which radiators were set perpendicularly to the beam axis. Each module consisted of 43 pairs of a 5 mm thick scintillator plate and a lead sheet. For middle 29 layers, each lead sheet was 2 mm in thickness. For the rest of 14 layers, each lead sheet was 1 mm in thickness. Total radiation length was $15.73X_0$. These layers were compressed between 1.5 cm thick aluminum plates.

We used the same type of WLS fibers as FB to read out the scintillation light. The WLS fibers were 2.5 m long, and attached to phototubes through a 5 mm thick silicone cookie. We used 2 inch Hamamatsu R329-EGP PMT.

Typical light yield was 10 photo-electrons per MeV energy deposit.

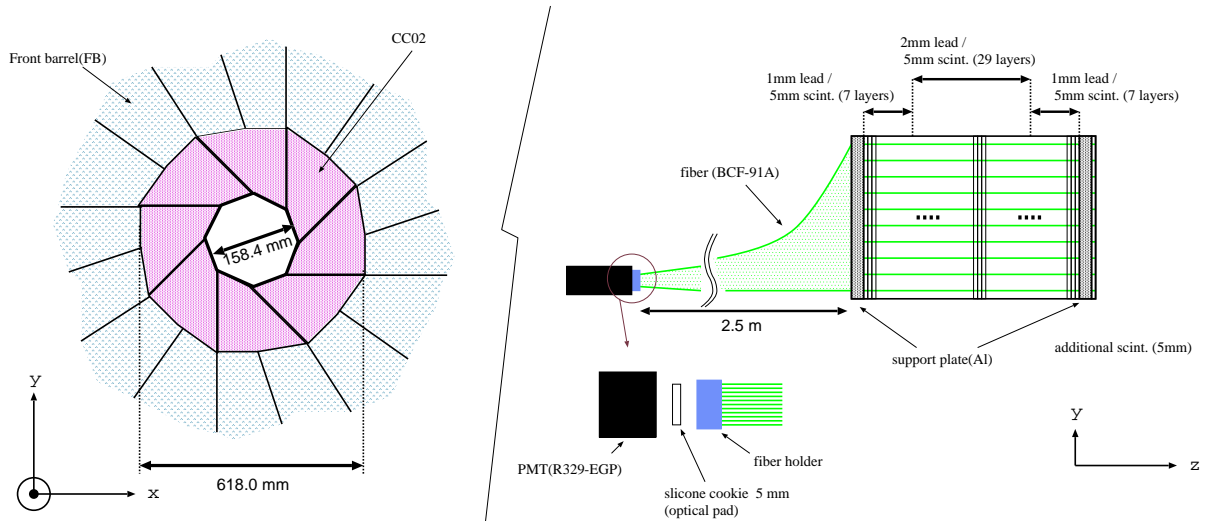


Figure 3.24: Schematic drawing of CC02. Left drawing shows a view from the downstream. Right drawing shows details of CC02 module.

CC03

CC03 was located at the center of the electromagnetic calorimeter. CC03 detected photons coming from K_L decays near the electromagnetic calorimeter. The size was $250 \text{ mm} \times 250 \text{ mm} \times 400 \text{ mm}$ with a $120 \text{ mm} \times 120 \text{ mm}$ beam hole. The detector consisted of six modules. Each module consisted of 26 pairs of a 3.4 mm thick scintillator and a 1 mm thick tungsten plate. These plates were parallel to the beam direction.

CC04 and CC05

CC04 and CC05 were located downstream the electromagnetic calorimeter in order to detect photons escaping from the decay region. Both CC04 and CC05 were $500 \text{ mm} \times 500 \text{ mm}$ in cross section with a $126 \text{ mm} \times 126 \text{ mm}$ beam hole.

CC04 consisted of 32 pairs of a 5 mm thick scintillator and a 2 mm thick lead plate. In front of the first lead / scintillator layer, there were two additional scintillator plates with higher PMT gains in order to detect charged particles effectively. The total thickness was $11.4X_0$.

CC05 consisted of 32 pairs of a 5 mm thick scintillator and a 2 mm thick lead plate. There were two additional scintillator plates with higher PMT gains, at downstream side of CC05 in order to detect charged particles effectively. The total thickness was the same as CC04.

For both detectors, we used WLS fibers to read out scintillation light. The light from the fibers was viewed by 2 inch Hamamatsu H1161 PMT's directly.

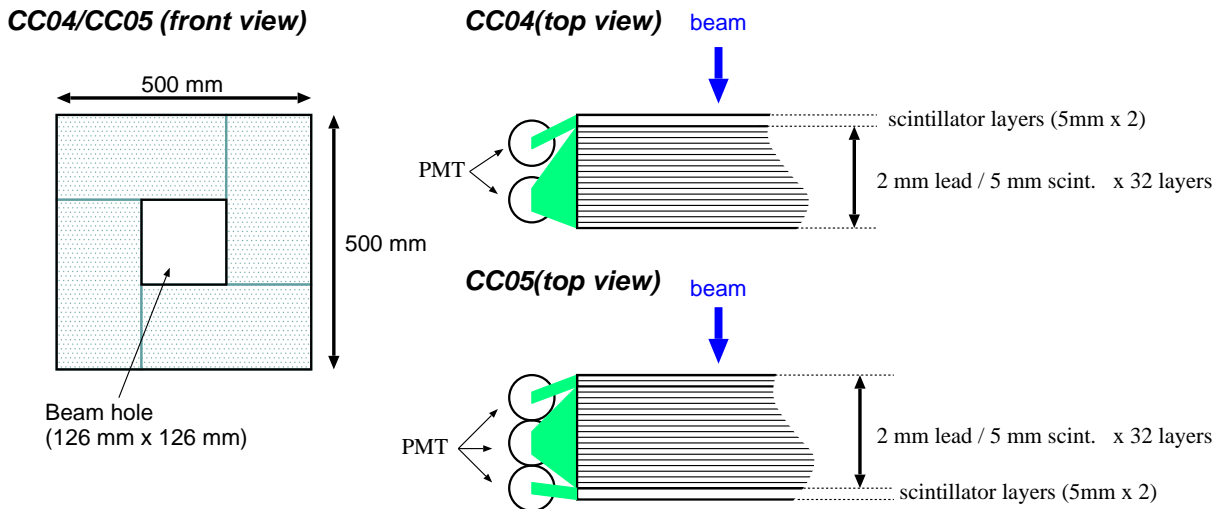


Figure 3.25: Schematic drawing of CC04 and CC05.

CC06 and CC07

CC06 and CC07 were located downstream of CC05. These detectors also detected photons escaping from the decay region. They had the same structure and consisted of 10 lead glass

blocks as shown in Fig. 3.26. Each lead glass block was 300 mm \times 150 mm in cross section and 150 mm long. The chemical composition of each lead glass was 55 % of PbO, 4 % of K₂O, 39 % of SiO₂ and 2 % of Na₂O. Its density was 4.08 g/cm³ and the refractive index was 1.7. Total radiation length was 6.3X₀. Electrons and positrons which were produced by an electromagnetic shower in CC06 / CC07 emitted a Cherenkov light, which was detected by a 5 inch Hamamatsu R1250 PMT which was directly attached to the lead glass with a optical cement.

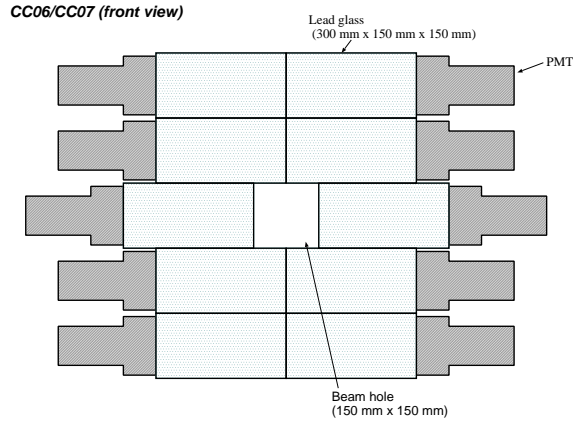


Figure 3.26: Front view of CC06 and CC07. CC06 and CC07 had the same dimensions and consisted of 10 lead glass crystals.

3.2.7 Back anti and Beam hole charged veto

Back anti

Back anti (BA) was located at the end of the neutral beam. BA covered the beam core region. The purpose of BA was to detect photons going through the beam hole.

There were many neutrons in the beam hit BA. If we mis-identified them as photons, it caused some signal loss. Therefore, we should discriminate photons and neutrons hitting BA. We also had to make BA tolerant to its high rate.

In order to satisfy these requirements, BA was constructed as shown in Fig. 3.27. It consisted of six lead / scintillator modules and six quartz layers. Each lead / scintillator module consisted of six pairs of a 5 mm thick plastic-scintillator and a 2 mm thick lead plate. Each quartz layer consisted of seven quartz crystals which were 35 mm \times 245 mm in cross section and 30 mm thick. Total radiation length was 14X₀. Cherenkov light was emitted in the quartz crystal with the refractive index of 1.46. Since most of secondary particles from neutron interactions in BA had a momentum lower than the Cherenkov light threshold ($\beta_t = 1/n$ where n denotes the refractive index), there were no signal in the quartz crystals. On the other hand, secondary particles from both photon and neutron interactions deposited their energy in the scintillator. Therefore, we would discriminate between photons and neutrons by comparing signals in the lead / scintillator layers and in the quartz layers.

Scintillation light in each scintillator plate was transmitted along WLS fibers glued on the scintillator plate. The WLS fiber was 1 mm in diameter and with multi-cladding (KURARY

Y-11). The WLS fibers from each plate were viewed by a $1\frac{1}{8}$ inch Photonis XP 2978 PMT. Cherenkov light in each quartz crystal was directly detected by the PMT. We used an active PMT dividers (Photonis VD109/T : transistor-based divider) for all the read out channels in BA in order to reduce gain shift due to the high rate.

In actual operation, the typical rate was 3 MHz per channel. It causes a 10 % gain shift between beam on and off periods.

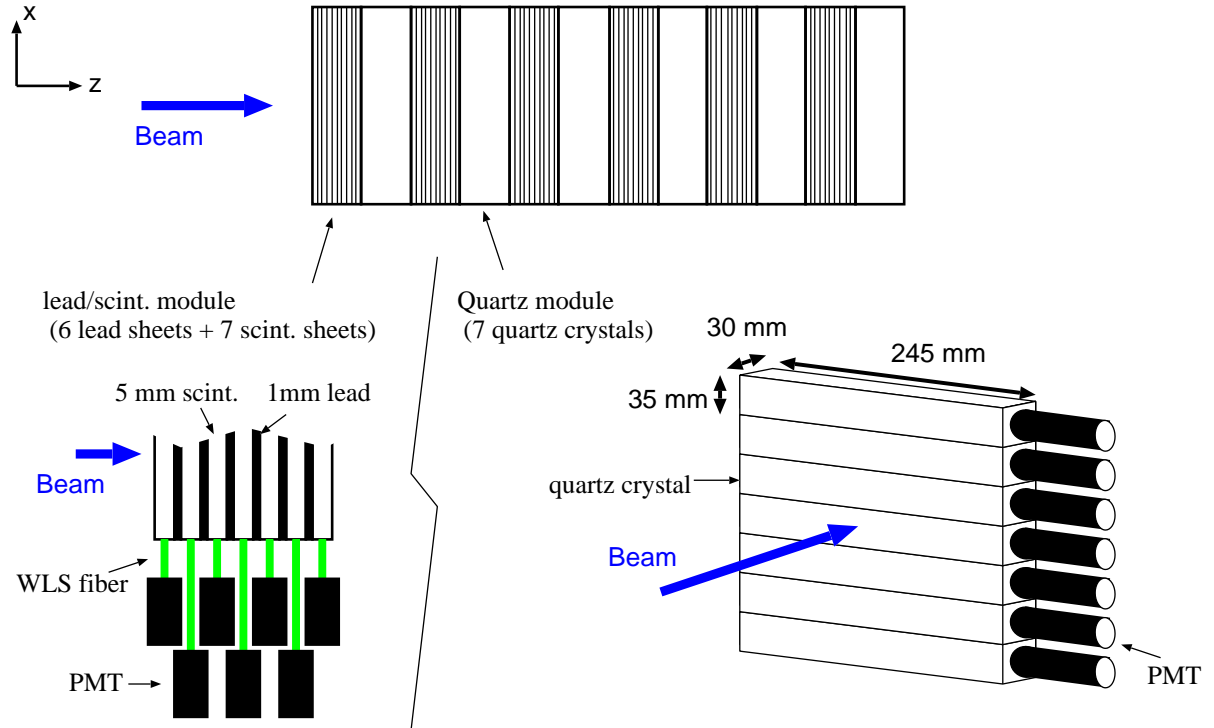


Figure 3.27: Back Anti (BA), which consists of six lead / scintillator modules and six Quartz modules.

Beam hole charged veto

The purpose of Beam hole charged veto is to detect charged particles from $K_L \rightarrow \pi^+\pi^-\pi^0$ decays, which was one of the background sources as described in Section 2.4.

BHCV consisted of four plastic scintillators with a thickness of 1 mm. The scintillator light was directly detected by the PMTs from the both edges. The PMT was EMI 9954B and the PMT divider was an active PMT divider which was developed by FNAL KTeV experiment.

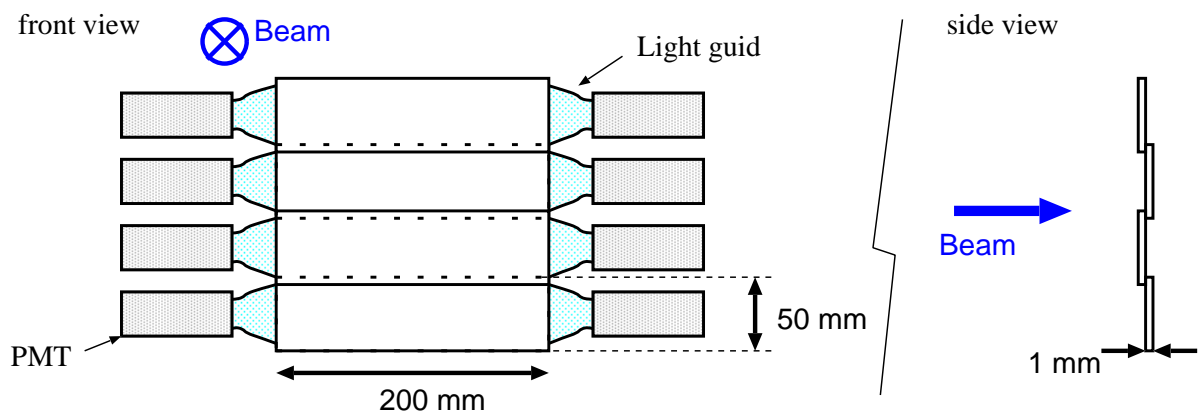


Figure 3.28: Front view of BHCV, which consists of four plastic scintillators.

3.3 Vacuum system

One of background sources was events where neutrons in the beam interacts with residual air in the decay region and then produces one or more π^0 . As described in Chapter 2, we need 10^{-4} Pa to suppress such backgrounds to ≤ 0.1 events level [28].

For this purpose, we built a vacuum system. Except for CC05, CC06, CC07, BHCV and BA, all the detector components were located in the vacuum.

Overview

It is difficult to evacuate gas down to 10^{-5} Pa level with the detector components inside, because of large amount of out-gassing from detector materials. In order to avoid this problem, we separated the vacuum region into two, and placed the detector components in a low vacuum region. Hereafter, we define the high vacuum decay region as Region-2, and the region with detector components as Region-1.

Figure 3.29 shows an overview of the vacuum system. Total volume and surface area for both regions are summarized in Table 3.3. We evacuated gas from the Region-2 down to 10^{-5} Pa, and the Region-1 down to 0.1 Pa. Therefore, the pressure difference between two vacuume regions was $\Delta P \simeq 0.1$ Pa.

Table 3.3: Total volume and surface area for the fiducial region and the outside region as shown in Fig. 3.29.

	Volume	Surface area	Pressure in the operation
Region-1(outside region)	100 m ³	220 m ²	0.1 Pa
Region-2(fiducial region)	10 m ³	40 m ²	10^{-5} Pa

We used a thin film to separate two vacuum regions. Requirements for such film were:

- the film should be thin as much as possible in order to avoid any absorption of photons and charged particles, and
- the film should be made of a low out-gassing material in order to achieve 10^{-5} Pa for the 40 m² surface area.

For these requirements, we used a multi-structure film. Figure 3.30 shows a schematic drawing of the film which is usually used for blimps. We call this film as “membrane”. Total thickness was 190 μm which corresponds to $4 \times 10^{-4} X_0$. The membrane consisted of a low-density polyethylene with a thickness of 80 μm , a Aluminized EVAL film with a thickness of 15 μm , a nylon film with a thickens of 15 μm and a low-density polyethylene with a thickness of 80 μm .

We fixed the membrane to the inner surface of detectors surrounding the decay region using a support structure, which was a combination of aluminum pipes.

Pumping system and their performance

Two sets of the Rotary-pump and the Roots-pump system were used to evacuate gases to 0.1 Pa level. They were attached to a large manifold (10 m long, 30 cm in diameter). The manifold was connected to the vacuum vessel with eight pipes (10 cm in diameter). Throughput of the Roots pump was 0.27 m³/s. For high vacuum, we used four Turbo Molecular pumps (TMPs), which were able to evacuate gas down to a high vacuum (10⁻² to 10⁻⁶ Pa level). Operation of the TMP should start from at least 1 Pa level. Throughput was 3200 m³/s using all the TMPs.

Figure 3.31 shows the pressure level for both low vacuum region and high vacuum region as a function of the evacuation time. It took a half day to reach 10⁻⁴ Pa and two weeks to reach 10⁻⁵ Pa.

Operation of the PMT in the vacuum

Since we operated PMTs in the vacuum, we were unable to not use convection to cool the PMT bases. For CsI calorimeter, this was a serious problem since the light yield of CsI has a temperature dependence of -1.3 %/°C. In order to cool the bases, we installed a water cooling system. Cold water with a temperature of 10 °C flowed in a cooper pipe behind the CsI crystals. Heat conducting cables made of copper were attached between the PMT dividers and the cooper pipe. The temperature for both the CsI crystal and its divider was approximately 20°C during the operation. In addition, we also used the water cooling for FB, MB and BCV.

The electric discharge in the vacuum depends on the arrangement of the HV terminals in the PMT divider. Figure 3.32 shows the discharge voltage as a function of the vacuum pressure. In order to avoid the discharge, we applied the HV only after the pressure was ≤ 1 Pa.

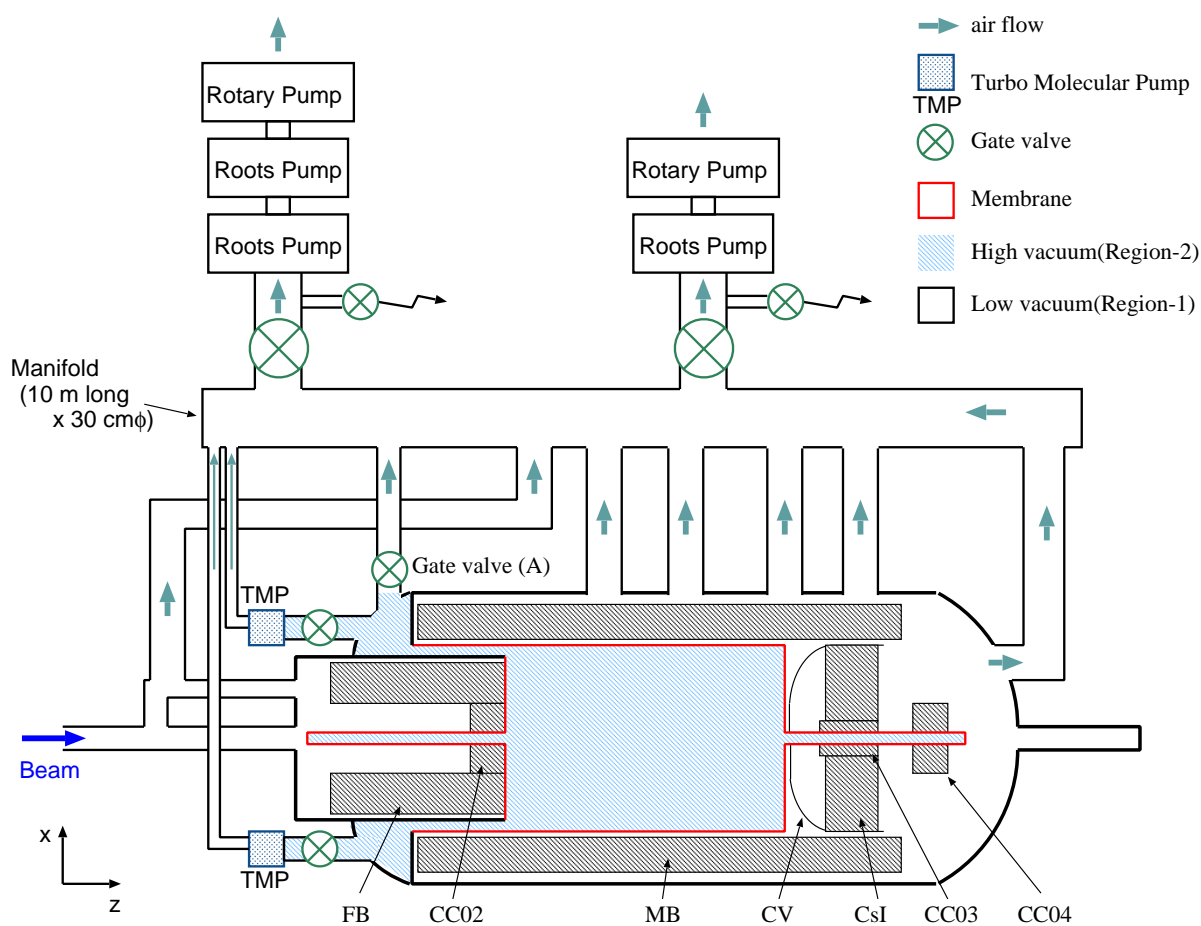


Figure 3.29: The E391a vacuum system. Region-2 corresponds to the high vacuum decay region, and Region-1 corresponds to the region in which all the detector components were located. There are two sets of the Rotary-pump and the Roots-pump systems, and four Turbo Molecular pumps (TMP).

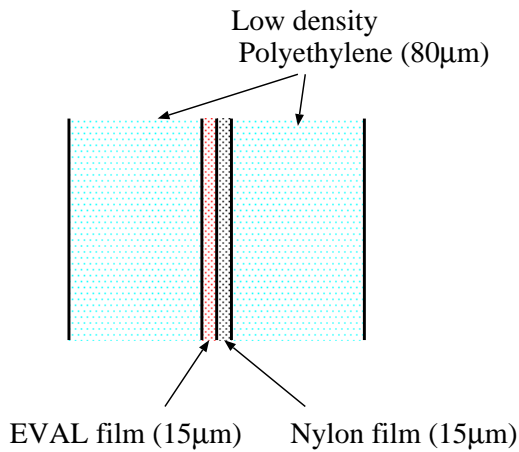


Figure 3.30: Cross section of the film, “Membrane”, used to separate the high vacuum region and the low vacuum region.

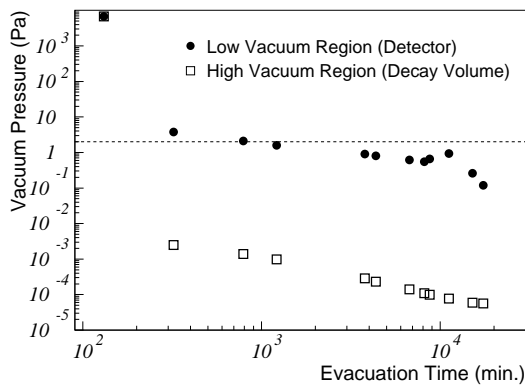


Figure 3.31: The vacuum pressure for the low vacuum region and the high vacuum region as a function of the evacuation time. First, we turned on the Rotary pump and evacuate gas from the whole area down to 10 Pa level. Next we turned on the Roots pump. After the pressure reached to 1 Pa, we closed the gate valve (A) in order to separate the low vacuum region and the high vacuum region and then turned on the all TMPs.

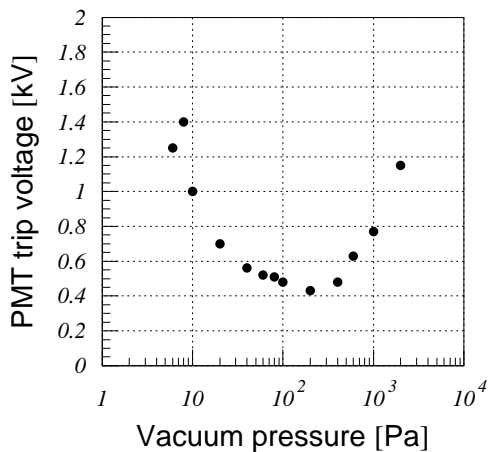


Figure 3.32: The discharge voltage as a function of the vacuum pressure. Typical HV value in the actual operation was 1.0 kV – 1.6 kV.

3.4 Trigger

We used a single-level trigger system. There were four kinds of triggers for specific purposes. In the following subsections, we will describe detailed of each trigger decision.

3.4.1 Physics trigger

As mentioned in Section 2.3, the signal for $K_L \rightarrow \pi^0 \nu \bar{\nu}$ decay is two photons from a π^0 decay and no other particles detected in the final state. Physics trigger was designed to select such final state while rejecting most of the background events. To decide the physics trigger, we counted the number of photons hitting CsI calorimeter using “Hardware cluster counter”, and rejected events involving extra particles requiring no energy deposit in CV and several photon veto detectors.

In these processes, we used a module named “AmpDiscr (AD)”. In the following paragraphs, we will describe the AD module, the “Hardware cluster counter” and the requirements of the physics trigger.

AmpDiscr (AD) module

We developed a new module, “AmpDiscr (AD)”, which was a multi purposes NIM module for the front-end system, with the help of the KEK Electronics Online Group. This module was used for all the detector readout. The purposes of the AD module were:

- to make a sum of PMT signals to be used in the trigger decision, and
- to discriminate PMT signals with a low threshold to make TDC signals without any electronic noise.

Eight PMT signals from the same detector entered the AD module. The AD module provided:

1. analog output (through) signal for each PMT signal,
2. two outputs of the analog sum of eight PMT signals, and
3. discriminated (ECL level) pulse for each PMT signal.

The analog outputs were used to measure charge (ADC) and the discriminated pulses were used to measure timing (TDC). In order to avoid any electronic noise during signal transfer, we placed the AD modules right behind the detector system. In reality, since there were no serious noise, we applied 1 mV threshold for CsI.

The analog sum signals were used for the “Hardware cluster counter” of the calorimeter and for vetoes the other detectors.

Hardware cluster counter (HCC)

We made a hardware cluster counter (HCC) in order to count the number of photons in CsI calorimeter. We grouped eight neighboring CsI crystals and made 72 regions in total as shown in Fig. 3.33. The analog sum of signals from each region was formed by an AD module. We counted the number of regions whose analog sum exceeded 30 mV^1 and defined the number as N_{HC} .

Figure 3.34 shows the distribution of N_{HC} from the real data. Since there were many events with $N_{\text{HC}} = 1$ due to beam associated events, we required $N_{\text{HC}} \geq 2$ in the trigger.

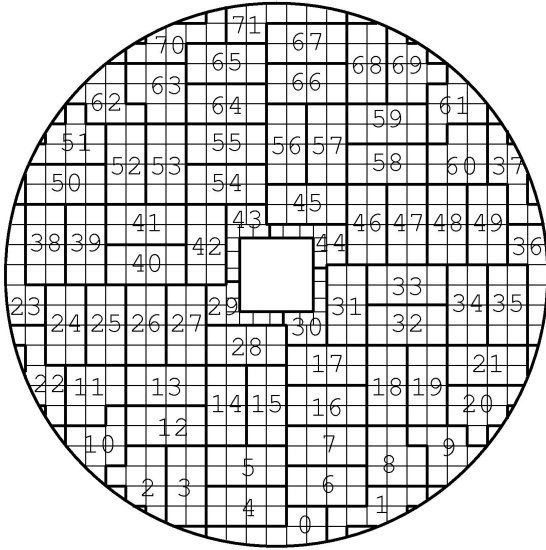


Figure 3.33: Schematic view of CsI crystals with 72 regions for the Hardware cluster counter.

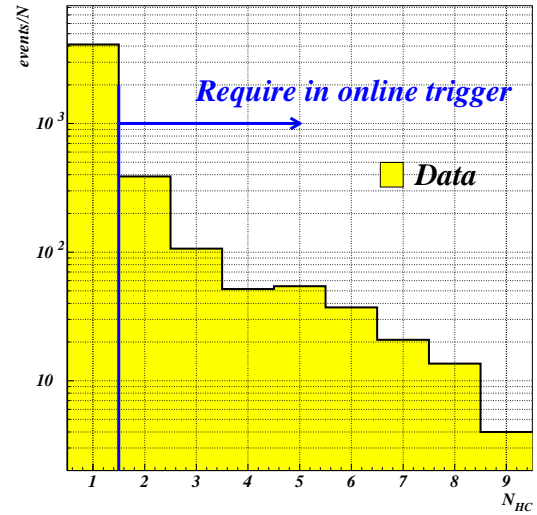


Figure 3.34: The distribution of the hardware clusters from the real data. Since there were large amount of $N_{\text{HC}} = 1$ events due to beam associated events, we required $N_{\text{HC}} \geq 2$ in the physics trigger.

Requirements of the Physics trigger

To select events where two photons and no other particles detected in the final state, we required energies deposited in CV and each photon veto to be less than the threshold shown in Table 3.4.

The K_L decay rate in the decay region was approximately 2.8×10^5 events per 2 second spill with typical intensity of 2.5×10^{12} protons on the target. After requirements described above, the trigger rate was reduced to 800 events per 2 second spill.

¹It corresponds to approximately 60 MeV energy deposited in CsI calorimeter.

Table 3.4: Requirements for CV and each photon veto detector. E_{cls} is a summed energy in each eight channel in the detector. E_{tot} is the total energy deposit in the detector.

Detector	Requirement	Detector	Requirement
CV	$E_{cls} \leq 1.5\text{MeV}$	MB	$E_{tot} \leq 15\text{MeV}$
FB	$E_{cls} \leq 30\text{MeV}$	CC02	$E_{tot} \leq 15\text{MeV}$
CC03	$E_{tot} \leq 15\text{MeV}$	CC04	$E_{tot} \leq 45\text{MeV}$
CC05	$E_{tot} \leq 25\text{MeV}$		

3.4.2 Other trigger

Besides the physics trigger, there were following triggers.

- *Calibration triggers* : Xenon trigger was used to flash the Xenon lamp with a 1.1 Hz clock, for gain monitoring of CsI calorimeter as described in Section 3.2.2. LED trigger was used to flash the LED with a 1.1 Hz clock, for gain monitoring of MB as described in Section 3.2.4. The frequency of 1.1 Hz was chosen not to synchronize with the spill to check the gain of these detector during whole protons delivering period.

Cosmic trigger and Muon trigger collected muons passing through the detector vertically and horizontally, respectively, to calibrate each detector system.

- *Minimum bias triggers* : In order to check the performance of the physics trigger, we formed a set of triggers with relaxed conditions. One of them was a trigger requiring $N_{\text{HC}} \geq 1$ without any vetoes. Another was a trigger requiring $N_{\text{HC}} \geq 2$ without any vetoes.
- *Accidental trigger* : In order to collect events to monitor the detector's accidental activities, the accidental trigger was formed. Since the accidental activities depended on the beam intensity, we used a signal from a counter which was located nearby the production target.

3.5 Data acquisition system

The data acquisition (DAQ) system in the E391a experiment was built to collect data with a high efficiency. Figure 3.35 shows an overview of the E391a DAQ system. The total number of detector channels was approximately 1000. Charge and timing information of each detector channel were recorded every event.

We used a network distributed system with multiple CPUs. Three CPUs were used to read out two Fastbus-VME systems and a TKO-VME system. The dead time of the DAQ system was $600 \mu\text{s}/\text{event}$, which was dominated by a processing time of the Fastbus-VME. Therefore, it corresponded to 78 % live time with 800 events/spill ($\sim 400 \text{ Hz}$) trigger request. In such a trigger rate, typical data size was 10 Mbyte/spill.

In the following paragraphs, detail of the DAQ system is described.

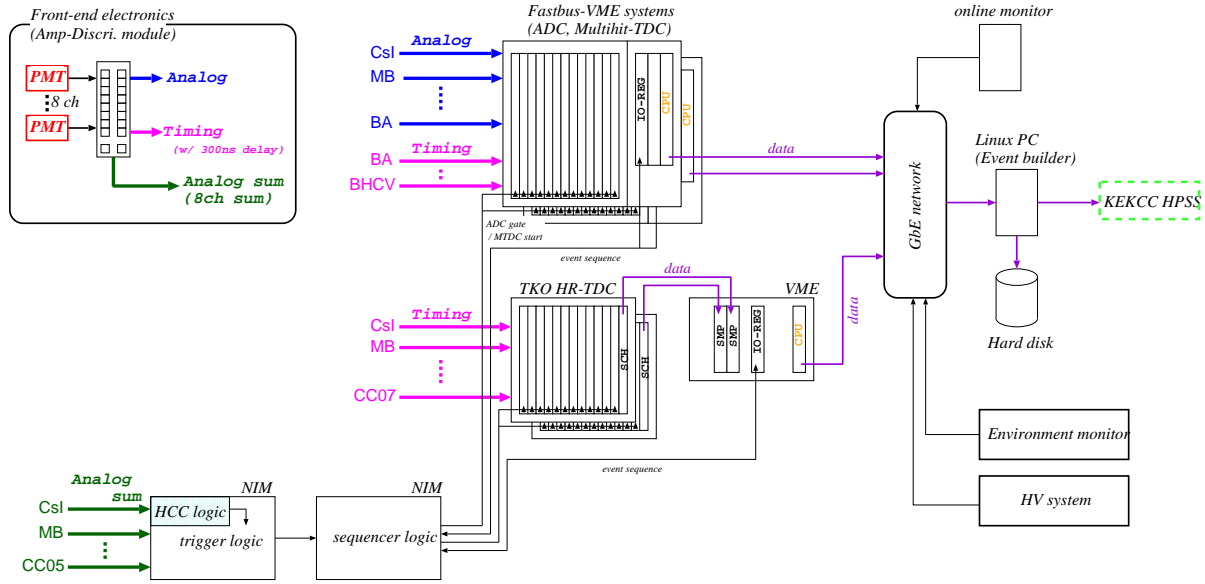


Figure 3.35: Schematic view of the E391a DAQ system.

3.5.1 Detail description of the E391a DAQ

The E391a DAQ system consisted of two Fastbus-VME systems, one TKO-VME system and one Linux PC for the event-building. In addition, it consisted of several Linux PCs for an online monitoring, an environment monitor and a HV control. All the CPUs and the PCs were connected each other through the GbE network.

The charge information (analog signal) from each detector channel was transmitted from the AD module to the 1885F ADC through a 90 m coaxial cable. For BA and BHCV, the timing information (ECL signal) was transmitted from the AD module to the 1877 MTDC through a 30 m twist-pair cable. The 1885F and 1877 modules were mounted in two Fastbus crates. Their data was read out by the two Fastbus-VME system. We used two sets of a Fastbus-VME interface (SIS4100 NGF) and a VME CPU (FORCE54 UltraSPARCH 500 MHz boards). After waiting for the 1885F conversion time of $256 \mu\text{s}$ which was started by the gate signal with a width of 200 nsec, an event sequence signal started the data transfer both from the 1885F and the 1877 to NGF's FIFO buffer (2 kbyte) in a DMA block transfer mode. The data in the FIFO was moved to the CPU's memory every event. The data in the CPU's memory was transferred to the Linux PC for the event-building every spill. Total processing time was $600 \mu\text{s}/\text{event}$.

The timing information (ECL signal) except for the BA and BHCV was transmitted from the AD module to the TKO HR-TDC through a 30 m twist-pair cable. The data of the HR-TDC was read out by the TKO-VME system. It consisted of two TKO-SCH controllers with the TKO crates and one VME CPU. The HR-TDC operated with a common-start mode and a full range was 100 ns. After waiting for the HR-TDC conversion time of $100 \mu\text{s}$, an event sequence signal started the data transfer. The TKO-SCH module controlled the data transfer from the HR-TDC to the VME memory module (SMP) every event. The data in the SMP was

transferred to the Linux PC for the event-building every spill. Total processing time was 500 $\mu\text{s}/\text{event}$.

In order to confirm that partial data in the three data buffers were from the same event, we sent 8 bit event ID to each buffer.

The data from the Fastbus-VME systems and the TKO-VME system were combined and written in the local Hard-Disk-Drive(HDD). The data in the local HDD was transferred to a large storage system in the KEK Computing Center (HPSS system) through the KEK Giga-bit network every run. Typical data size per a day was 90 Gbyte. We checked the event consistency of the combined data in the beginning of the offline analysis.

3.6 Run

We carried out the first data taking (E391a Run-I) from February 2004 to June 2004. We took the physics runs for sixty days. In addition, there were some special runs mainly for a calibration purpose. In this section, we will describe the running conditions for both the physics runs and the special runs.

3.6.1 Physics Run

The running condition in the physics runs is summarized in Table 3.5. During the physics run, we monitored the number of reconstructed $K_L \rightarrow \pi^0\pi^0\pi^0$ events every spill. This number depended on the proton intensity, the detector stability, etc.. Hence, we were able to monitor a data quality at the online stage. There were also other online monitoring for the beam profile, and the trigger quality.

Table 3.5: Summary of the condition of the physics data taking.

Typical proton intensity	2.5×10^{12}
Beryllium absorber	OUT
Lead absorber	IN
HCC threshold	30 mV
Physics trigger rate	750 events/spill
High vacuum	1×10^{-5} Pa
Low vacuum	≤ 0.1 Pa

3.6.2 Special Run

We carried out several special runs. In the followings, we will describe their purposes and running conditions.

π^0 run

The purpose of the π^0 run is to calibrate the electromagnetic calorimeter.

An aluminum(Al) target with a thickness of 5 mm was inserted in the beam at $z = 280.5$ cm (behind CC02) in order to produce π^0 by neutrons in the beam.

Since we know that the π^0 decay vertex is at the Al target, we were able to measure the invariant mass of the two photons from the π^0 decay. By requiring the invariant mass to be the π^0 's mass, we adjusted the gain of each CsI crystal. This data was also used to check our event reconstruction performance.

We had the π^0 run for one week in the last period.

Other calibration run

Other calibration run was mainly a muon run using muons coming from the production target by turning off the sweeping magnet in the neutral beam line. These muons were used to calibrate the energy scale in each detector.

Air run

As shown in Table 3.5, we carried out the physics runs with 10^{-5} Pa in the fiducial region. In order to check the rate of the neutron interaction with the air, we took data at an atmospheric pressure (10^5 Pa).

High intensity run

Accidental activities in the detector depended on the instantaneous beam intensity. In order to check this dependence, we carried out the high intensity run. To increase the instantaneous beam intensity, we carried out short spill runs with 1.0 sec, 0.5 sec and 0.2 sec on-beam period instead of 2 sec. It means that the instantaneous beam intensity is 2, 4 and 10 times larger than the normal instantaneous beam intensity, respectively.

Chapter 4

Monte Carlo simulation

In order to calculate our signal sensitivity, we need to know the acceptances of both the signal and the normalization mode. We used a Monte Carlo simulation, MC, to estimate these acceptances. The MC was also used to study background sources. For these purposes, the MC should reproduce events by simulating the parent particles' production, the decays of particles, the interactions with the detector materials and the detectors' response. We used the GEANT3 package [34] as a framework of the MC. As mentioned in Section 2.4, we considered several background sources. In order to study the background due to the hadronic interactions of the neutron in the beam, we use the GFULKA code [34].

In the MC, we obtained an energy deposited in the detector and a timing of particles hitting the detector, and converted them to quantities which had the same definition with the real data. It enables us to analyze both the real data and the MC using the same analysis routines and applying the same event selection criteria (cuts).

In this chapter, we will describe the MC in detail. We will describe the event generation in Section 4.1. A study of the detector response is described in Section 4.2. Since the detector has many accidental activities in the real data, we simulated this effect in the MC. We will explain how the effect is included in the MC in Section 4.3.

4.1 Event generation

In the MC, we generate a parent particle (K_L or neutron) with an initial momentum vector and a position, and then let it propagate and decay. In this section, we will describe the generation of the parent particle and the decay.

4.1.1 Parent particle generation

Initial position and momentum vector of K_L 's and neutrons were obtained from an independent Monte Carlo simulation ("beam line simulation"). In the beam line simulation, we struck a proton with 12 GeV in kinematic energy on a platinum(Pt) target, 60 mm in long and 8 mm in diameter. We set the collimator C1 through C6 downstream of the target and the Pb absorber according to the correct relative positions. The interactions of the secondary particles in those collimators were simulated. The profile for K_L 's and neutrons were collected at the z position

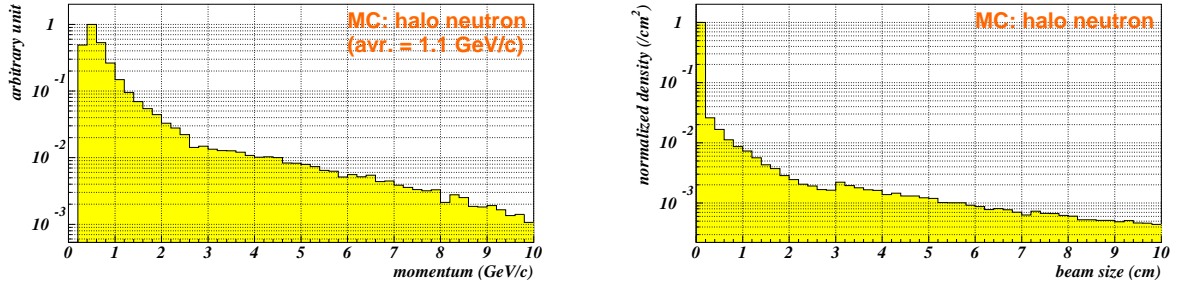


Figure 4.1: The distribution of the momentum (left) and the beam density (right) for the halo neutron beam at the z position of the C6.

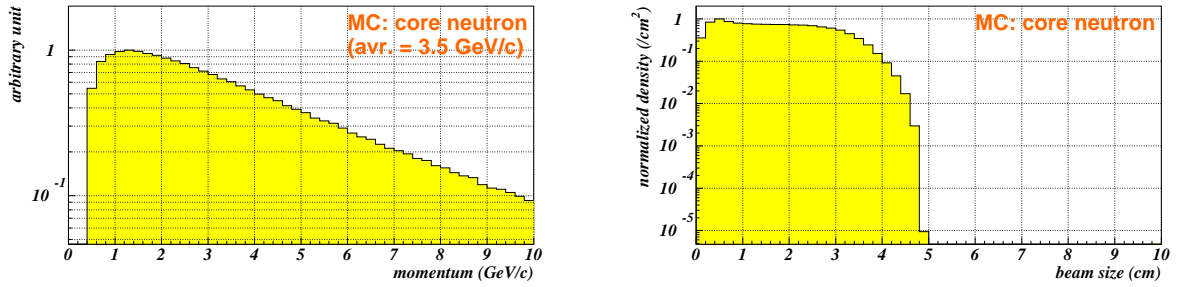


Figure 4.2: The distribution of the momentum (left) and the beam density (right) for the core neutron beam at the z position of the C6.

of the last collimator, C6. At the same time, we collected the profile of the neutron's in order to study background sources associated with the beam neutron interactions. Further information of the beam line simulation can be found in ref. [27, 28].

The profiles of the K_L and the neutron beam were measured by past experiments. As a result, the ratio of the halo to the core beam was 10^{-5} , and the momentum distribution of neutrons in the beam was consistent with the result from the beam line simulation. Furthermore, we had an engineering run using same the electromagnetic calorimeter to measure the K_L beam profile. We fed the measured K_L momentum and the beam size into our Monte Carlo simulation.

The momentum distribution of the K_L beam is shown in Fig. 3.4. For further analysis, we defined neutrons going through the beam hole of the electromagnetic calorimeter as core neutrons and anything else as halo neutrons. Figure 4.1 and 4.2 show the distribution of the momentum and the beam density at the C6 for the halo neutron and the core neutron, respectively.

4.1.2 Decay

To generate a decay, we first picked its initial momentum and position according to the distributions obtained with the beamline simulation. The decay vertex was determined according to the K_L proper time, τ , and its Lorentz factor. The distribution of the decay vertex, z , with a momentum, p_{K_L} , is expressed:

$$f(z) \propto \exp\left(-\frac{z}{\Delta z}\right), \quad (4.1)$$

where

$$\Delta z = c\tau\beta\gamma = c\tau \times \frac{p_{K_L}[\text{GeV}/c]}{m_{K_L}[\text{GeV}/c^2]}. \quad (4.2)$$

At the decay vertex, the parent particle was forced to decay into secondary particles of a specific decay mode. Except for $K_L \rightarrow \pi^0\nu\bar{\nu}$ decay, we used the GDECAY routine in the GEANT3 in order to calculate a four-momentum vector for each secondary particle and boosted them in the K_L direction. The secondary particles decayed according to their life times and branching ratios which were defined in the GEANT3 package.

$K_L \rightarrow \pi^0\nu\bar{\nu}$ decay

The distribution of the π^0 momentum in the $K_L \rightarrow \pi^0\nu\bar{\nu}$ decay was calculated as follows [35, 21]. Here, we assumed V–A interaction at the decay vertex. From the Standard Model calculation, the differential decay rate can be represented as

$$\frac{d\Gamma}{dE_\pi} \sim \lambda f_+^2 [(m_K^2 - m_\pi^2 - q^2)^2 - \frac{2}{q^2} (\frac{q^2\lambda^2}{3} + m_\pi^2 q^4)], \quad (4.3)$$

where m_K is the mass of the K_L , and E_π and m_π are the energy and the mass of the π^0 , respectively,

$$q^2 \equiv m_K^2 + m_\pi^2 - 2m_K E_\pi, \text{ and} \quad (4.4)$$

$$\lambda \equiv [(m_K^2 + m_\pi^2 - q^2)^2 - 4m_K^2 m_\pi^2]^{1/2}. \quad (4.5)$$

The form factor, f_+ , was parameterized as $f_+ = 1 + \lambda_+ q^2/m_\pi^2$ with $\lambda_+ = 0.032$, which was measured by experiments [5]. The kinematical constraint,

$$m_\pi \leq E_\pi \leq (m_K^2 + m_\pi^2)/2m_K, \quad (4.6)$$

is also required.

Once the π^0 's energy was chosen, following the spectrum expressed in Equation 4.3, its direction was determined isotropically in the K_L rest frame. The π^0 was then boosted in the K_L direction and it immediately decayed into two photons with a branching ratio of 98.8%.

4.2 Detector response

We simulated the detector response using GEANT except for BA. For BA, we used data to study its response, because hadronic interaction took too long CPU time to simulate.

For other detectors, we simulated particles' interactions with the detector material, such as pair production, multiple scattering, etc., according to their cross sections. We traced their interactions until particle's energy was below a cut off energy. The cut off energy was set at 0.05 MeV for electrons, positrons and photons, and 0.1 MeV for hadrons and muons. We summed energy deposits in the sensitive detector material for each detector channel. The hit "timing" was simulated as the time when the summed energies exceeded the discriminator threshold used in the data taking. The summed energy deposit in each detector channel was defined as "energy" in the detector except for MB and CV. For MB and CV, we simulated their light propagation and attenuation in the plastic-scintillator. In the following paragraphs, we describe how we simulated the light propagation and attenuation in the MB and the CV.

MB

Since MB detector was 5 m long, the attenuation of scintillation light in MB should be taken into account. The scintillation light from MB was transmitted through WLS fibers and detected by phototubes at the edge of the fibers. When a particle hits MB at a distance l from the phototubes, the energy measured by the phototubes is expressed as

$$E = E_0(a_1 e^{-\frac{l}{\lambda_1}} + a_2 e^{-\frac{l}{\lambda_2}}) \quad (4.7)$$

where E_0 is the energy deposit at the incident position, $\lambda_1(\lambda_2)$ is the attenuation length and $a_1(a_2)$ is a normalization factor for the long (short) term component. Using cosmic ray muons, we measured the attenuation lengths: $\lambda_1 = (6.08 \pm 0.56)$ m, $\lambda_2 = (1.13 \pm 0.15)$ m and $a_1/a_2 = 1.11 \pm 0.02$ [36]. We used these parameters for all the MB modules.

We defined the energy detected at the phototubes for a minimum ionization particle passing through the center of MB to be 15 MeV for the inner module and 30 MeV for the outer module. Figure 4.3 shows the relative energy detected at the phototubes as a function of the distance from the phototube, which is normalized by the energy at the center of MB.

In addition, we simulated the hit timing of the incident particle at the phototubes by taking the light propagation into account. In the MC, we used the speed of the light propagation, (17.7 ± 0.1) cm/nsec, as measured with cosmic ray muons [36].

CV

As mentioned in Section 3.2.3, the scintillation light in outer CV was affected by its odd shape. We corrected the effective light yield of the outer CV by using the relative light yield as a function of the hit position, as shown in Fig. 3.14.

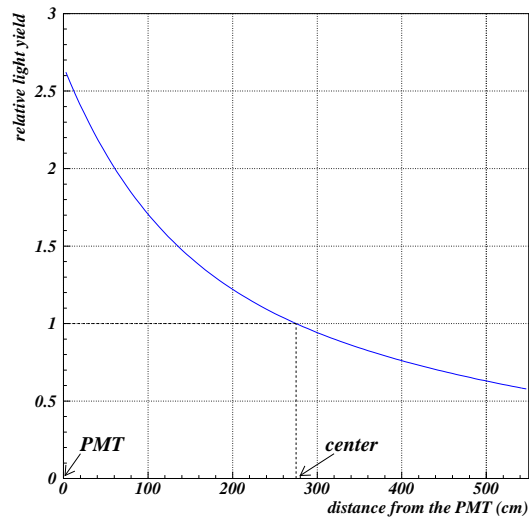


Figure 4.3: The relative energy detected at the phototube for MB as a function of the distance from the phototube, which is expressed as Equation 4.7. The measured distribution is shown in Fig. 3.19

4.3 Accidental activity

In the actual experiment, detector had many accidental activities, which were caused by particles coming either from the target or from other reactions. These accidental activities caused additional energy deposit in the detector, and it affects the acceptance. Also, a coincidence of two accidental hits on the electromagnetic calorimeter is an additional background source.

In order to simulate the effect of the accidental activity, we overlaid the data collected by the accidental trigger on the generated MC events. The energy deposit was simply added together channel by channel. As for the timing information, we kept the earlier hit of the hits among the accidental data and the MC.

Chapter 5

Event reconstruction

The signal of $K_L \rightarrow \pi^0 \nu \bar{\nu}$ decay is two photons with no other particles detected in the final state. The events were reconstructed in the following two processes.

1. find two photons in the CsI calorimeter (**photon finding**), and
2. reconstruct the π^0 decay vertex by assuming the π^0 mass (**π^0 reconstruction**).

Figure 5.1 shows a flow chart of the event reconstruction. In this chapter, first, the method of the photon finding is given in Section 5.1. The reconstruction method of the π^0 decay vertex is described in Section 5.2.

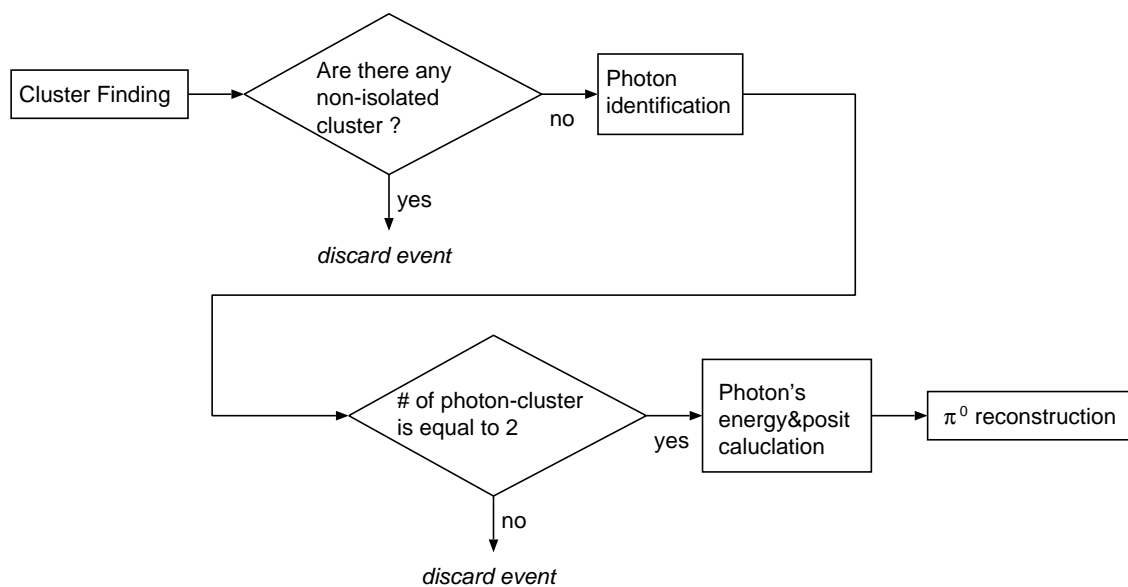


Figure 5.1: A flow chart of the event reconstruction for the $K_L \rightarrow \pi^0 \nu \bar{\nu}$ signal.

5.1 Photon finding

When a photon hits the CsI calorimeter, it generates an electromagnetic shower and its energy is spread over multiple CsI crystals. Figure 5.2 shows an example of $K_L \rightarrow \pi^0 \pi^0 \pi^0$ decay in which each π^0 decays into two photons, producing six photons hitting the CsI calorimeter.

The task of the photon finding is to reconstruct photons from the energy deposit in CsI crystals. It is important to reconstruct all the photons hitting the calorimeter because, if we miss some of them, it causes additional photon detection inefficiency. In particular, we should distinguish two photons hitting close to each other in the calorimeter. Therefore, we first find clusters, which are contiguous groups of the CsI crystals with energy deposit exceeding a threshold. We then required that each cluster shape is consistent with a single photon.

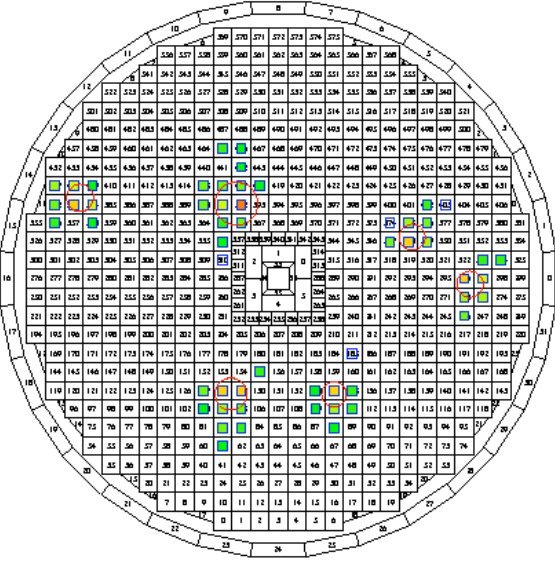


Figure 5.2: An example of a $K_L \rightarrow \pi^0 \pi^0 \pi^0$ decay in which each π^0 decays into two photons, producing six photons hitting the CsI calorimeter. Hatched boxes are the CsI crystals which have energy deposit above 1 MeV.

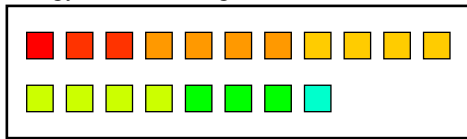
5.1.1 Cluster finding

We defined cluster as a group of neighboring CsI crystals with finite energy deposit. First, we picked CsI crystals with energy deposit exceeding 5 MeV and defined them as “cluster seeds”. We then grouped the neighboring cluster seeds to form clusters. The neighboring crystals are defined as crystals sharing an edge. An example of forming a cluster is shown in Fig. 5.3. We started the cluster growth from the CsI crystal which has a maximum energy deposit among the cluster seeds, because such a crystal is generally at the center of an electromagnetic shower generated by a photon. This algorithm was run over until all cluster seeds were used.

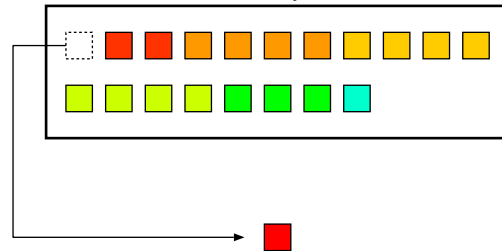
5.1.2 A criterion to reject non-isolated clusters

After the cluster finding, the number of local maxima in each cluster was counted. A local maximum was defined as a crystal whose energy was greater than any of the neighboring crystals. If a cluster had two or more local maxima, it was defined as a non-isolated cluster.

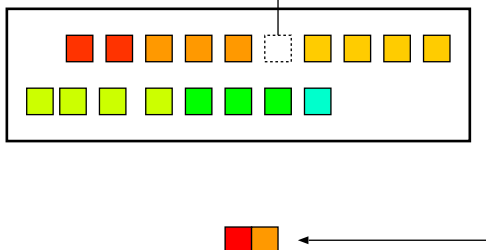
- (1) sort cluster seeds by the size of the deposit energy in descending order



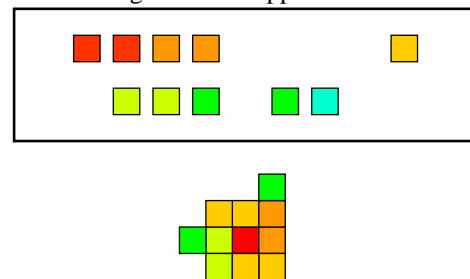
- (2) start cluster growth with a first crystal in the cluster seeds, i.e. crystal with max. energy



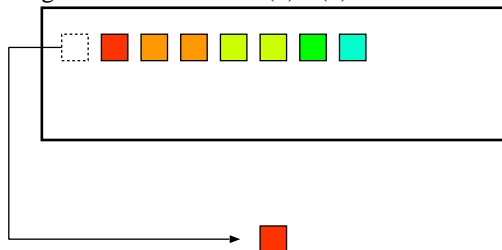
- (3) look for neighboring crystals which are sharing an side with the cluster



- (4) if there are no more neighboring crystals, the cluster growth is stopped



- (5) sort cluster seeds again, and start next cluster growth and continue (3) - (4)



- (6) continue the procedures until all cluster seeds are used up.

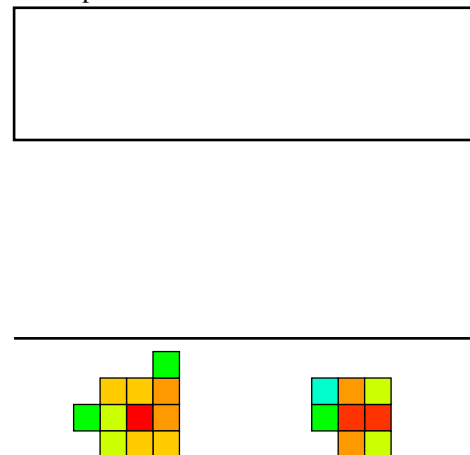


Figure 5.3: The diagram of the cluster finding algorithm. First, we sorted the cluster seeds by their energy deposit in descending order. We then grouped the neighboring cluster seeds to form clusters according to the procedures (2) through (5). The neighboring crystals are defined as crystals sharing an edge.

In this step, we rejected events with indistinguishable clusters, because those clusters had a potential to have more than one photons. On the other hand, even a single photon can produce a cluster with multiple local maxima due to a fluctuation of the electromagnetic shower. This caused some acceptance loss. A MC study found that the acceptance loss was 5 % for the $K_L \rightarrow \pi^0 \nu \bar{\nu}$ decay, 15 % and 8 % for the $K_L \rightarrow \pi^0 \pi^0 \pi^0$ (6γ on the calorimeter) and $K_L \rightarrow \pi^0 \pi^0$ (4γ), respectively.

5.1.3 Photon identification

Next procedure was to identify clusters consistent with photon showers. In order to identify photon-clusters, we compared the number of CsI crystals in the cluster, a connection pattern, a timing dispersion and an energy dispersion of the cluster, against actual photon hits of the $K_L \rightarrow \pi^0 \pi^0 \pi^0$ decays in the real data. A detailed description of the requirement of the photon-cluster is given in Appendix A. In particular, we required each cluster to have two or more CsI crystals in the photon identification.

5.1.4 Energy and position calculation

Energy

The energy deposit of the photon was defined as the sum of energies in the cluster:

$$E_{dep} \equiv \sum_{i=1}^n e_i, \quad (e_i \geq 5\text{MeV}) \quad (5.1)$$

where e_i is the energy deposit in each crystal and n is the number of the crystals in the cluster. However, E_{dep} was not the true energy of the photon because some energies of the photon leaked out of the cluster.

The fraction of the energy leakage was evaluated with a MC study. Figure 5.4 shows the fraction of the energy leakage as a function of the energy deposit (E_{dep}). The fraction of the energy leakage was defined as the mean of reconstructed energy deposit. In order to get the true incident energy of the photon, we applied an energy leakage correction to the E_{dep} . The energy of photon was calculated as :

$$E_{inc} = (1 + F) \cdot E_{dep} \quad (5.2)$$

where $F = 0.034 + 0.023/\sqrt{E_{dep}(\text{GeV})}$ is the fraction of the energy leakage obtained from the MC. After applying the energy leakage correction, the average of the difference between the incident energy and the reconstructed energy is zero as shown in Fig. 5.5.

Position

The position of the photon in the calorimeter was calculated in two steps. First, we reconstructed the position of the photon, $P_{rec} = (x_r, y_r, z_r)$, where z_r is the position at the front of the CsI calorimeter, $z_r = 614.8$ cm. The x_r and y_r were reconstructed independently using a same method. In the position reconstruction, we used the energy deposit in the CsI crystals

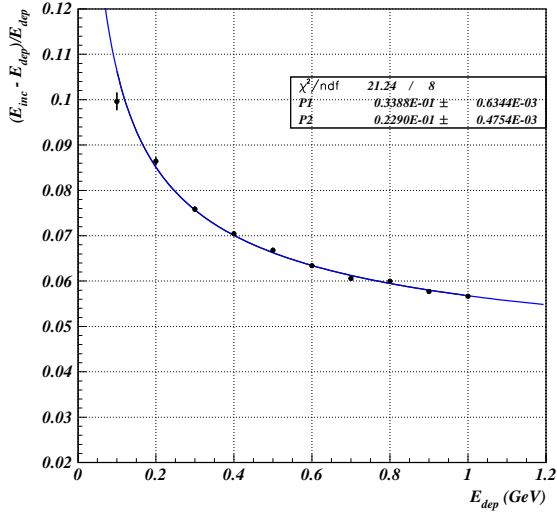


Figure 5.4: The fraction of the energy leakage as a function of the energy deposit (E_{dep}). The fraction of the energy leakage was expressed as $F = p1 + p2/\sqrt{E_{dep}(\text{GeV})}$.

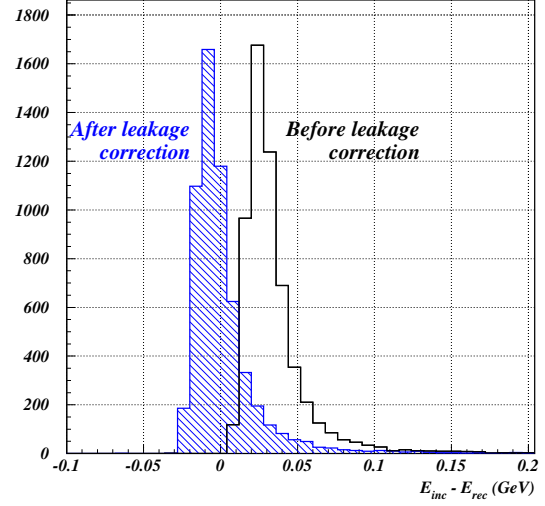


Figure 5.5: The distributions of the difference between the incident and reconstructed energy for photons from π^0 produced at the Al target before (white) and after (dashed) the energy leakage correction, as studied with MC.

in each cluster. We looked for the CsI crystals with a maximum energy deposit among the neighboring crystals. We defined a center column consisting of the crystals, in which x (y) position was same of the crystal with the maximum energy deposit. Energy sums, $E_0^{x(y)}$, $E_+^{x(y)}$ and $E_-^{x(y)}$, were defined as the total energy deposit in the center column, the left side column and the right side column, respectively, for x_r (y_r) as shown in Fig. 5.6. A ratio, q , was defined as:

$$q \equiv \frac{\max(E_+^{x(y)}, E_-^{x(y)})}{E_0^{x(y)}}. \quad (5.3)$$

The distribution of q was measured by the real data¹. Moreover, we measured six different distributions depending on the total energy deposit in the cluster. One example is shown in Fig. 5.7. The most likely values of q were small corresponding to events in which the central part of the shower was mostly contained within the center column.

¹We studied $K_L \rightarrow \pi^0 \pi^0 \pi^0$ decays in the real data with six photons. These samples had no background contamination so that clusters on the CsI calorimeter were actual photons from K_L decay.

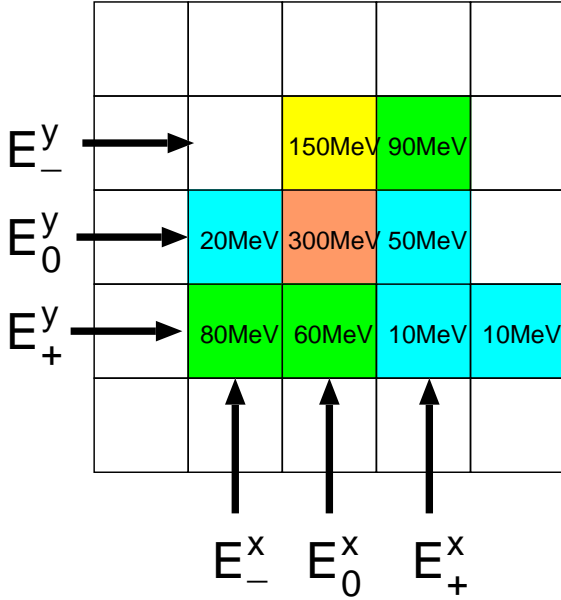


Figure 5.6: A schematic view of the $E_0^{x(y)}$, $E_+^{x(y)}$ and $E_-^{x(y)}$. Colored squares show the CsI crystals with a finite energy deposit and those crystals make a cluster. The red square shows the crystal with a maximum energy deposit among the neighboring crystals. The $E_0^{x(y)}$, $E_+^{x(y)}$ and $E_-^{x(y)}$ were defined as the total energy in the column: center column, left column and right column, respectively.

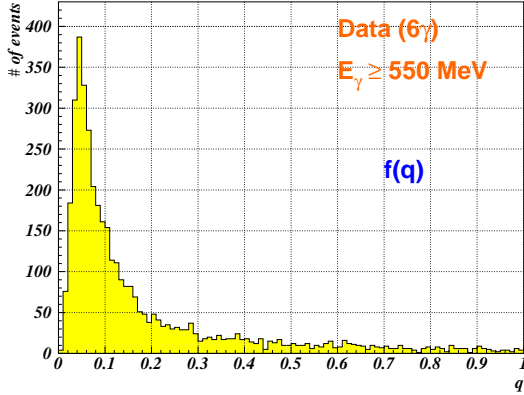


Figure 5.7: The distribution of the value, q , for the photons with the energies greater than 550 MeV.

The hit position, $x_{rec}(y_{rec})$, was calculated:

$$x_{rec} = \frac{h}{2} \frac{\int_0^q f(q') dq'}{\int_0^1 f(q') dq'}, \quad (5.4)$$

where h is the size of the CsI crystal with the maximum energy deposit and $f(q)$ is the distribution of the ratio, q , as shown in Fig. 5.7. Based on the MC simulation where we injected photons in perpendicular to the CsI crystals at the random position of the surface, the reconstructed position with Equation 5.4 was consistent with the incident position within ± 0.7 cm. However, a finite difference would arise when photons injected with an angle.

Second, we corrected this difference between the reconstructed position and the incident

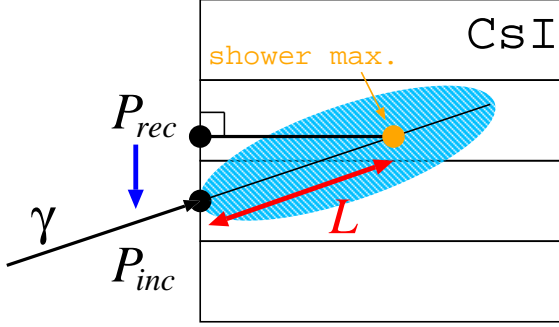


Figure 5.8: A schematic view of the position correction. Taking the shower length (L) into account, the incident position (P_{inc}) was calculated from the reconstructed position (P_{rec}) and the incident angle.

position. We calculated the incident position of the photon at the upstream surface of the CsI calorimeter, $P_{inc} = (x_{in}, y_{in}, z_{in})$, where z_{in} is the position of the CsI calorimeter, $z_{in} = 614.8$ cm. As shown in Fig. 5.8, the incident position was calculated as a function of the shower length(L):

$$x_{in} = x_r - L \cdot \sin \theta \cdot \cos \phi, \quad (5.5)$$

$$y_{in} = y_r - L \cdot \sin \theta \cdot \sin \phi, \quad (5.6)$$

where θ is the polar angle of the photon from the z -axis and ϕ is the azimuth angle of the photon around the z -axis. In order to estimate the incident angle of the photon, we temporarily reconstructed a π^0 decay vertex from a combination of two photons according to the π^0 reconstruction as will be described in Section 5.2. For this purpose, we used the position of the photon, P_{rec} . Once we obtained the direction of the photon, from the decay vertex to the photon position P_{rec} , we calculated the θ and ϕ . The shower length L is expressed as:

$$L(\text{cm}/X_0) \equiv \frac{|P_{inc} - P_{rec}|}{X_0} = p_1 + p_2 \cdot \ln(E(\text{GeV})) \quad (5.7)$$

where X_0 is the radiation length of the CsI (1.85 cm), E is the incident energy, and p_1, p_2 are free parameters. Using MC, we estimated p_1 and p_2 to be 6.22 and 0.98, respectively (Fig. 5.9). After applying the position correction, the hit position of the photon was reconstructed correctly within 0.5 cm in a standard deviation as shown in Fig. 5.10.

Performance of photon reconstruction

We checked the performance of the photon reconstruction by using the data collected in the π^0 run with an Al plate inserted in the beam. The invariant mass of the two photons from the π^0 decay was calculated with the known vertex and the reconstructed energy and position of the photons.

The peak position of the invariant mass, $M_{\gamma\gamma}$, is correctly on the π^0 mass after applying both the energy and position corrections as shown in Fig. 5.11. Also as shown in Fig. 5.12, the peak position of $M_{\gamma\gamma}$ does not depend on the minimum photon's energy after the energy and position corrections. These facts indicate that the energies and the positions were correctly reconstructed.

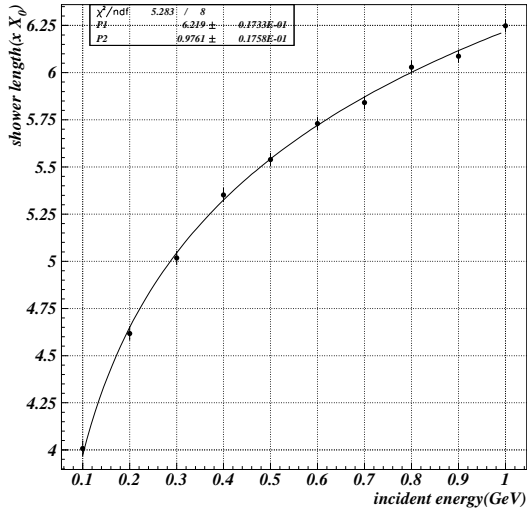


Figure 5.9: The shower length(L) as a function of the energy of photon obtained by the MC study.

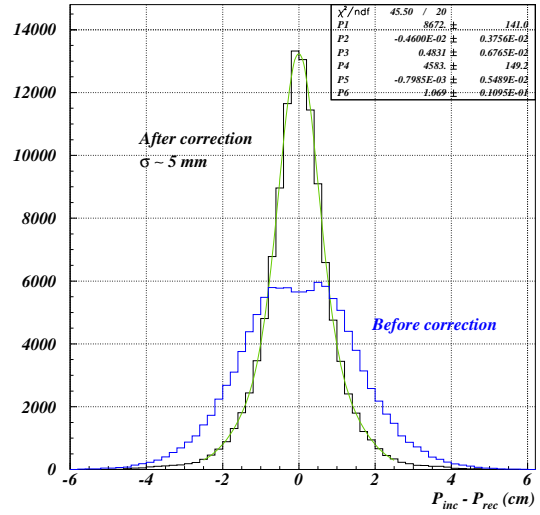


Figure 5.10: The distributions of the difference between the incident and the reconstructed positions for both before and after the position correction. The standard deviation of the position was observed to be 0.5 cm. In this analysis, we used this value as the position resolution, σ_x and σ_y without any energy and incident angle dependences.

5.2 π^0 reconstruction

Once we obtained two photon-clusters, we calculated a π^0 decay vertex, Z_{vtx} , by assuming the π^0 mass. In this calculation, we also assumed that the vertex is on the z -axis, $(0, 0, Z_{\text{vtx}})$. Figure 5.13 shows the relation between several measured quantities and $dz \equiv Z_{\text{CsI}} - Z_{\text{vtx}}$.

From the geometric conditions, there are following relations:

$$r_{12}^2 = d_1^2 + d_2^2 - 2d_1d_2 \cos \theta, \quad (5.8)$$

$$d_1 = \sqrt{r_1^2 + (dz)^2}, \text{ and} \quad (5.9)$$

$$d_2 = \sqrt{r_2^2 + (dz)^2}, \quad (5.10)$$

where r_{12} is the distance between the two photons, θ is the angle between the two photons' directions, d_1 , d_2 are the distances between the decay vertex and the hit positions, r_1 , r_2 are the distances of the hit positions from the z -axis. In addition, assuming that the invariant

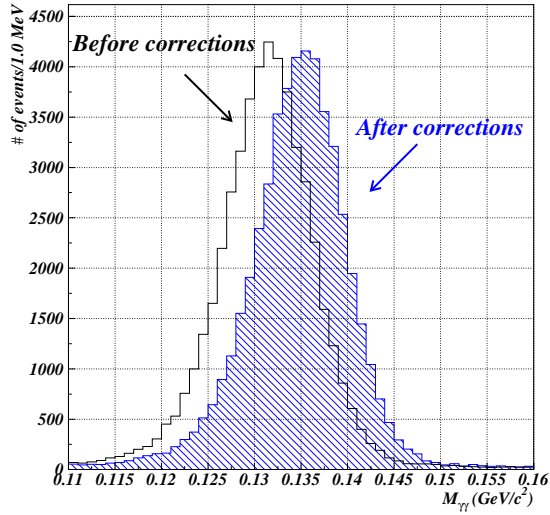


Figure 5.11: The distributions of the invariant mass of two photons ($M_{\gamma\gamma}$) for before (solid) and after (dashed) applying the energy and position corrections. The peak of $M_{\gamma\gamma}$ after the corrections is 0.135 ± 0.004 GeV/c^2 , which is consistent with the π^0 mass, as measured with the π^0 run data.

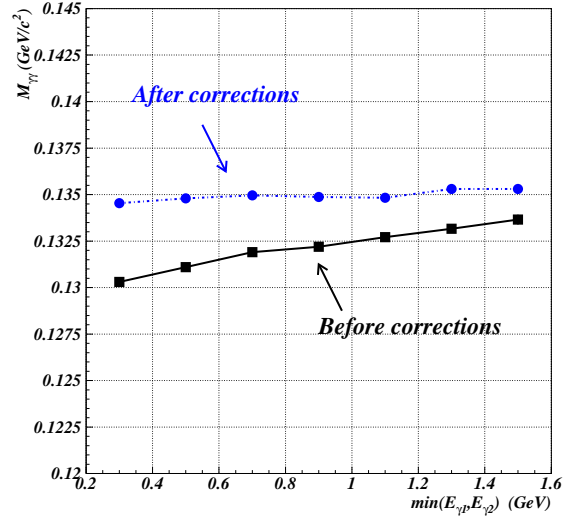


Figure 5.12: The mean of $M_{\gamma\gamma}$ does not depend on the minimum photon energy after applying the energy and position corrections (blue dot) in contrast to before applying the corrections (black square), as measured with the π^0 run data.

mass of the two photons is the π^0 mass (M_{π^0}), we get:

$$\cos\theta = 1 - \frac{M_{\pi^0}^2}{2E_1E_2}, \quad (5.11)$$

where E_1 and E_2 are the energies of the photons. Therefore, the decay vertex, Z_{vtx} , was calculated from the Equation 5.8, 5.9, 5.10 and 5.11. Also the standard deviation of the decay vertex, σ_{vtx} , was calculated from the standard deviation of the measured quantities: σ_{E_i} , σ_{x_i} and σ_{y_i} for each photon ($i = 1, 2$), using the error propagation from these equations.

After reconstructing the vertex $(0, 0, Z_{\text{vtx}})$, the momentum vector of the π^0 was calculated as the sum of two photon momenta. The transverse momentum of the π^0 , P_T , is expressed as

$$P_T = \sqrt{(P_x^{\pi^0})^2 + (P_y^{\pi^0})^2}, \quad (5.12)$$

where $P_x^{\pi^0}$ and $P_y^{\pi^0}$ are x and y components of the π^0 momentum, respectively. The P_T is independent of the reference frame, and stays within a kinematical limit. This feature played an important role in background suppression as will be discussed in Chapter 7.

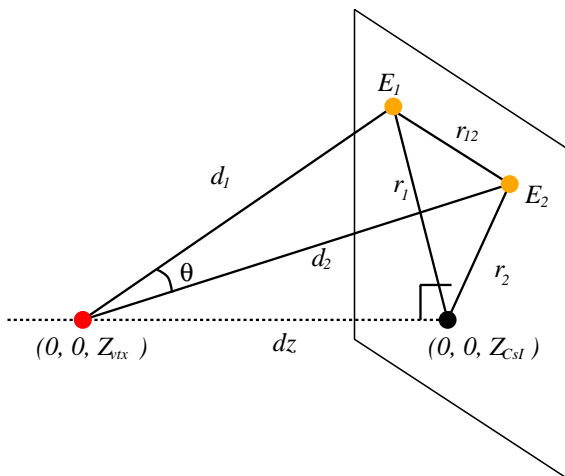


Figure 5.13: A schematic view of parameters used to reconstruct the π^0 vertex.

Chapter 6

Event selection

As discussed in Chapter 2, one of the important steps in the analysis is to suppress backgrounds. In this chapter, we will describe the event selection criteria in detail.

Before starting the discussion on the event selection, in Fig. 6.1, we show the distribution of the Z_{vtx} versus P_T of the reconstructed π^0 after online trigger requirements. Unexpectedly, a large number of events are clustered at $Z_{\text{vtx}} = 550$ cm. We later found that the membrane, which is a thin separator between low and high vacuum regions, was partially hanging in the beam at $z = 550$ cm. The neutrons hitting the membrane were producing secondary particles including π^0 's.

Even though there were many background events caused by the membrane problem, we developed the event selection cuts to suppress total background events to be less than 1 event while keeping a reasonable signal acceptance. For developing the selection cuts, we temporary defined a signal region in the Z_{vtx} and P_T : $300 < Z_{\text{vtx}}(\text{cm}) < 500$ and $0.12 < P_T(\text{GeV}/c) < 0.24$. The selection cuts were tuned by monitoring the number of background events outside the signal region.

Section 6.1 describes several background sources including the background from the membrane problem. Section 6.2 explains event selection cuts in order to suppress those background events. Section 6.3 summarizes a signal acceptance which was estimated using the MC. Section 6.4 describes the analysis of the normalization mode.

6.1 Background sources

Figure 6.2 shows the MC distribution of the Z_{vtx} versus the P_T for $K_L \rightarrow \pi^0 \nu \bar{\nu}$ decay and several background sources after the online trigger requirements. In this section, we will explain the characteristics of each background source.

6.1.1 Background from beam interactions

Here, we will describe two types of backgrounds caused by neutrons.

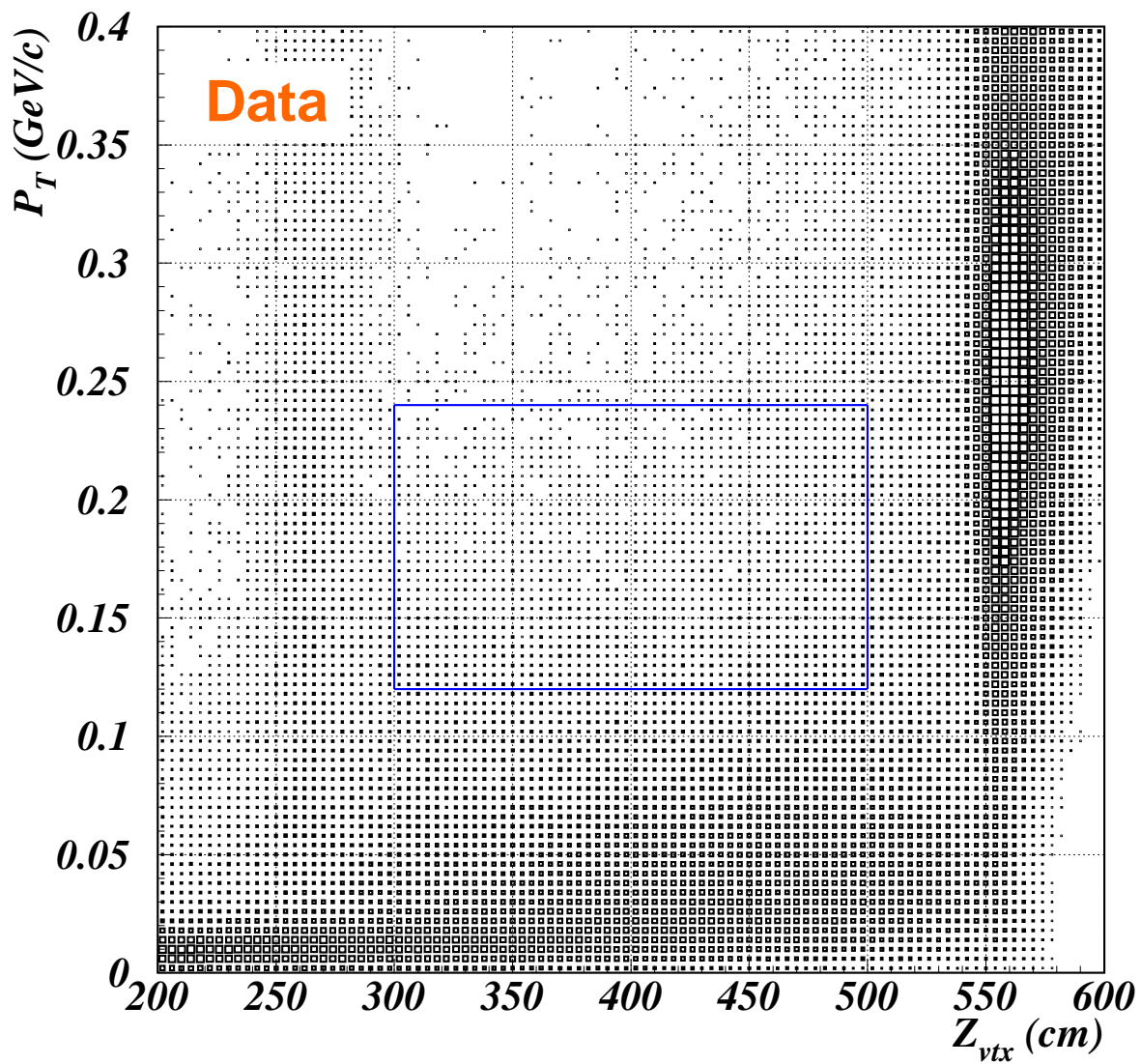


Figure 6.1: The distribution of P_T versus Z_{vtx} of the reconstructed π^0 after online trigger requirements for the real data.

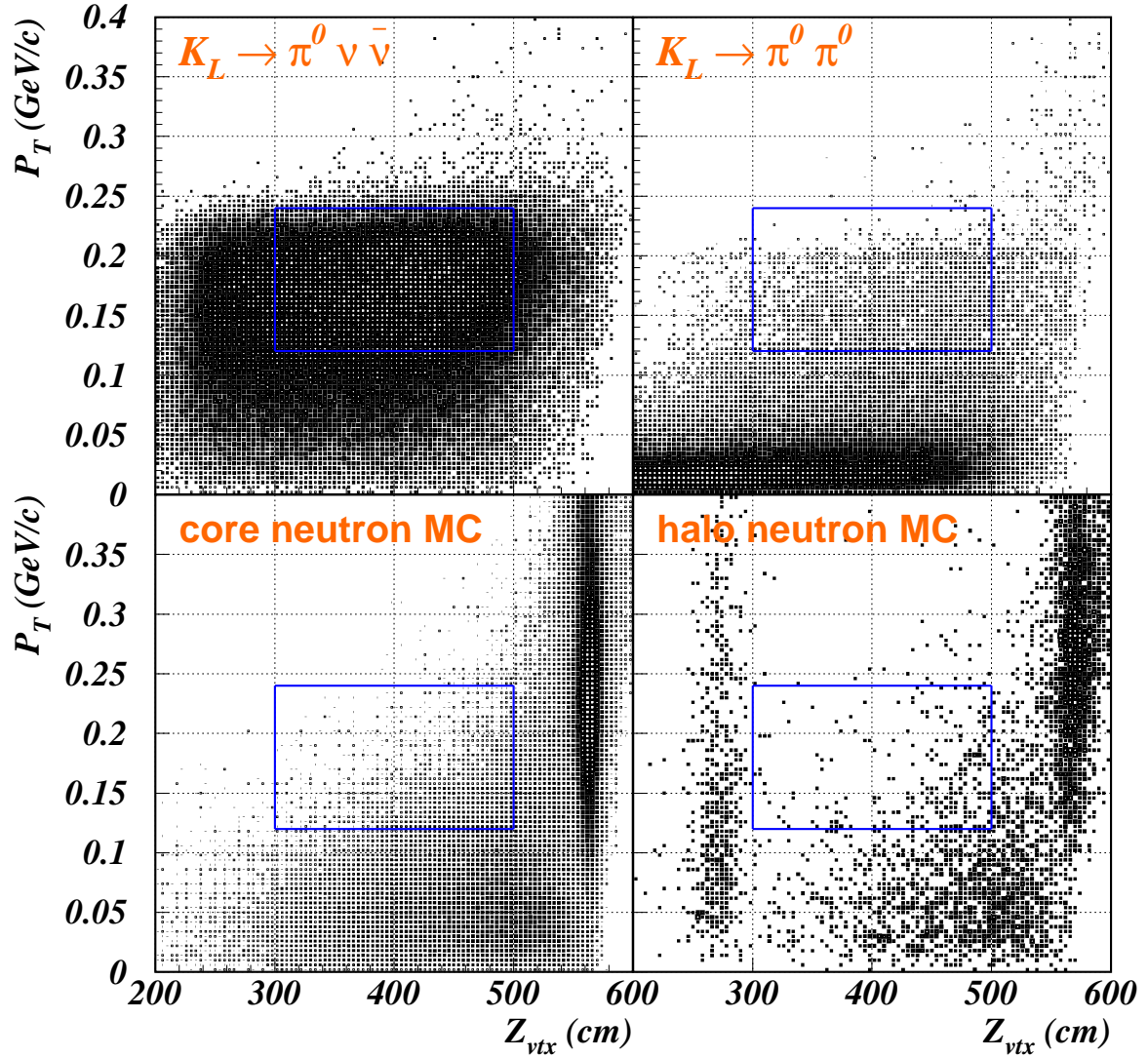


Figure 6.2: The distribution of P_T versus Z_{vtx} for the signal MC (upper left), the background caused by $K_L \rightarrow \pi^0 \pi^0$ (upper right), core neutron interactions (lower left) and halo neutron interactions (lower right).

Core neutron background

The “core neutron background” was caused by neutrons in the beam core striking the membrane at $z = 550$ cm and producing secondary particles. In order to understand the phenomena of the core neutron background, we ran a Monte Carlo simulation with a hypothetical material: 1 g/cm³ in density and 0.2 mm in thickness, in the front of the CV at $z = 550$ cm. The core neutron was simulated according to the momentum spectrum and the profile as shown in Fig. 4.2. The core neutron background was categorized into three sources as shown in Fig. 6.3.

The first source was events in which two photons from a single π^0 were detected. Hereafter, we call it the “core neutron single π^0 ” event. In this case, we could reconstruct the decay vertex, Z_{vtx} , correctly at the position of the membrane in the beam ($Z_{\text{vtx}} = 550$ cm).

The second source was events in which the two photons from multiple π^0 's were detected (“core neutron multiple π^0 ” event). In this case, we could not reconstruct the decay vertex correctly by assuming π^0 mass, and these events were distributed in the fiducial region ($300 < Z_{\text{vtx}}(\text{cm}) < 500$), as shown in Fig. 6.4. On the other hand, these events had extra photons in the final state, and thus can be suppressed by detecting those extra photons.

The third background source was events in which the η -mesons were produced at the membrane and the two photons from the η were detected (“core neutron η ” event). Since we reconstruct Z_{vtx} assuming that the two photons came from π^0 , the Z_{vtx} is shifted upstream. However, if we reconstruct the vertex assuming the η mass, there is a clear peak at $z = 550$ cm in data as shown in Fig. 6.5. In the core neutron MC, these background events were not reproduced, because GEANT-3 package did not generate η in the neutron interaction.

Halo neutron background

The “halo neutron background” was caused by the neutrons in the beam halo interacting with CC02 and CV. In order to understand the phenomena of the halo neutron background, we ran a Monte Carlo simulation for halo neutrons with the momentum spectrum and the profile shown in Fig. 4.1. The bottom right plot in Fig. 6.2 shows the reconstructed P_T versus Z_{vtx} for these background events.

Similarly to the core neutron background, the events at $z = 550$ cm and 280 cm were the single π^0 background events produced at CV and CC02, respectively. We call them as “halo neutron CV” event and “halo neutron CC02” event. The events in the fiducial region were multiple π^0 background events, in which the π^0 's were mainly produced at CV.

6.1.2 Background from K_L decay

The background from $K_L \rightarrow \pi^0\pi^0$ decay was caused by missing photons from the decay. The photons were missed due to two effects: (i) photon detection inefficiency, and (ii) overlapping photons that were not resolved (fused cluster). As described in Chapter 2, the $K_L \rightarrow \pi^0\pi^0$ background could remain even after applying a kinematical constraint, such as a P_T cut. Therefore, the probability of the missing photons determined the size of the $K_L \rightarrow \pi^0\pi^0$ background.

$K_L \rightarrow \gamma\gamma$ decay was the only other decay with two photons in the final state. However, the $K_L \rightarrow \gamma\gamma$ decay could be isolated from the $K_L \rightarrow \pi^0\nu\bar{\nu}$ decay by kinematical constraints

because the P_T of the two-photon system is zero.

Other background sources were charged decay modes. The $K_L \rightarrow \pi^- e^+ \nu$ decay mode was a possible source if the following three things happened in CV:

1. the π^- went through $\pi^- + p \rightarrow \pi^0 + n$ and two photons decayed from the π^0 overlapped in the electromagnetic calorimeter,
2. the e^+ went through a pair annihilation ($e^+ + e^- \rightarrow \gamma + \gamma$), and these two photons also overlapped, and

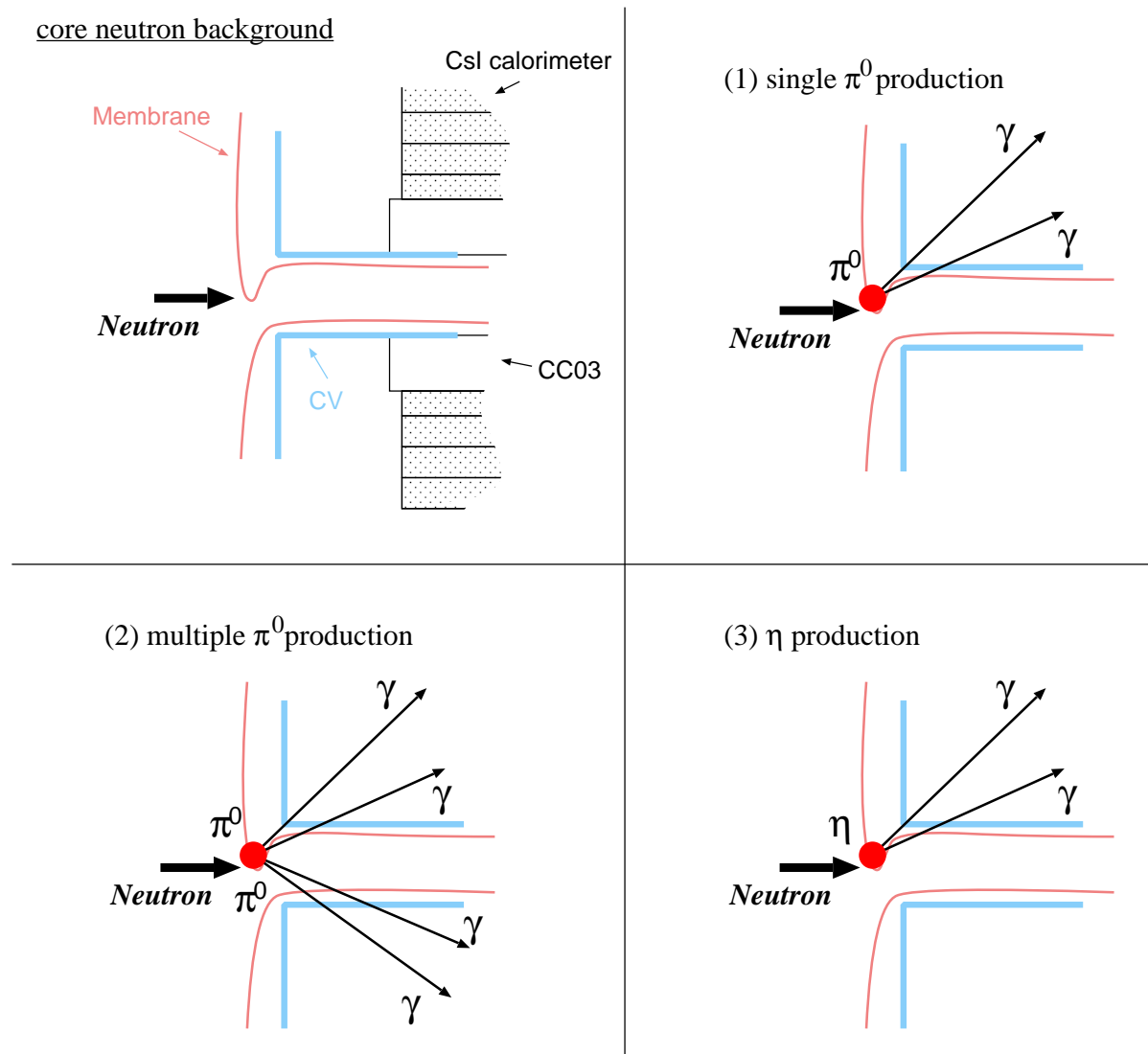


Figure 6.3: Overview of the core neutron background.

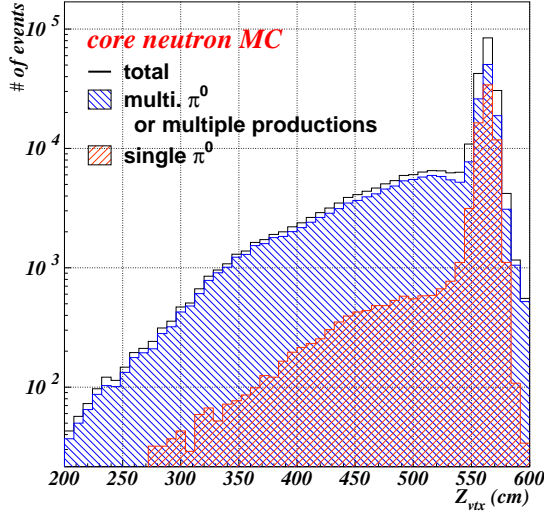


Figure 6.4: The distribution of the reconstructed vertex, Z_{vtx} , of the core neutron background studied with the MC. The events were categorized into the core neutron single π^0 events (cross hatched) and the core neutron multiple π^0 events (dashed).

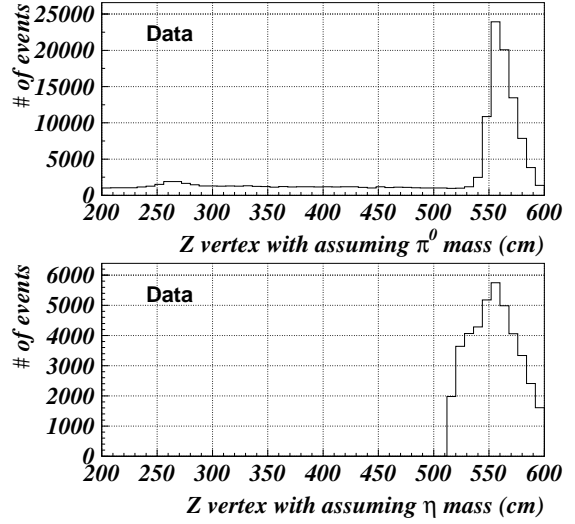


Figure 6.5: The top plot shows the distribution of the decay vertex reconstructed with assuming the π^0 mass. The bottom plot shows the distribution of the decay vertex reconstructed with assuming that the two photons came from an $\eta \rightarrow \gamma\gamma$ decay. A clear peak at $z = 550$ cm was observed.

3. the energy deposit in CV was too low to be detected.

In addition, $K_L \rightarrow \pi^+\pi^-\pi^0$ decays with the π^+ and π^- going through the beam hole without being detected by the BHCV, were another source of background.

6.2 Event Selection Cuts

Of these backgrounds described above, the core neutron backgrounds was dominant in the first data taking of E391a experiment. In the following subsections, we will describe the details of the event selection cuts to suppress the backgrounds.

6.2.1 Photon veto cuts

The backgrounds involving extra photons were suppressed by applying cuts to all the photon veto detectors. In the following paragraphs, we will describe the cut on each photon veto detector. The performance of these cuts is given in the last subsection.

CsI

We used the CsI calorimeter also as a photon veto. For signal events, we required only two photon clusters with energies more than 10 MeV each. In order to make sure that there are no other photons in the calorimeter, we applied the following three requirements.

- We required that all the CsI crystals which do not belong to the clusters have energies less than 3 MeV. Here, we also required that such CsI crystals should be 35 cm away from the nearest photon cluster to be insensitive to the fluctuation of the tail of the photon cluster.
- In photon identification, we required each photon cluster to have two or more crystals. Therefore, some of clusters consisting of only one CsI crystal with a finite energy deposit (so-called a “single-box-cluster”) were lost. We required that single-box-clusters have energies less than 10 MeV.
- Some photons hitting near the outside edge of the calorimeter were lost because its shower leaked out of the calorimeter depositing only small energy in the calorimeter. In order to veto such photons, we required the energy deposit in the CsI crystals near the outer edge of the calorimeter (> 80 cm from the center) to be less than 1.5 MeV, and less than 1 MeV for the non-square CsI crystals.

MB

In order to make the effect of the cut on MB detector independent of the photon’s hit position, we defined the energy in MB as¹:

$$\begin{aligned}
 E_{MB} &= c[E_{\text{PMT-dn}} \times E_{\text{PMT-up}}]^{1/2} \\
 &= c \left[(E_0 e^{-\frac{z_{hit}}{\lambda}}) \times (E_0 e^{-\frac{L-z_{hit}}{\lambda}}) \right]^{1/2} \\
 &= c E_0 e^{-\frac{L}{\lambda}}, \tag{6.1}
 \end{aligned}$$

where c is a calibration factor, $E_{\text{PMT-dn(up)}}$ is the size of the signal from the PMT at the nearest (farthest) side from the CsI calorimeter. E_0 is the incident photon’s energy, z_{hit} is the hit position, λ is the light attenuation length and L is the length of the MB (~ 500 cm). The last formula does not depend on the photon’s hit position, z_{hit} . We calibrated the energy scale of MB with cosmic ray muons passing the module perpendicularly, which deposit 15 MeV (30 MeV) in the scintillators of inner (outer) MB module.

We found that some particles in the electromagnetic shower in the CsI calorimeter went back to the MB. We will call this phenomenon as “shower-splash-back”.

We studied the shower-splash-back with four-photon event samples from $K_L \rightarrow \pi^0 \pi^0 \rightarrow 4\gamma$ decays, and $K_L \rightarrow \pi^0 \pi^0 \pi^0 \rightarrow 6\gamma$ decays with two missing photons in data. Figure 6.6(a) shows the distribution of the relative timing difference between the photon hitting the CsI

¹Here, we approximately expressed the signal from the phototubes of the MB as: $E_{\text{PMT}} = E_0 e^{-\frac{z}{\lambda}}$.

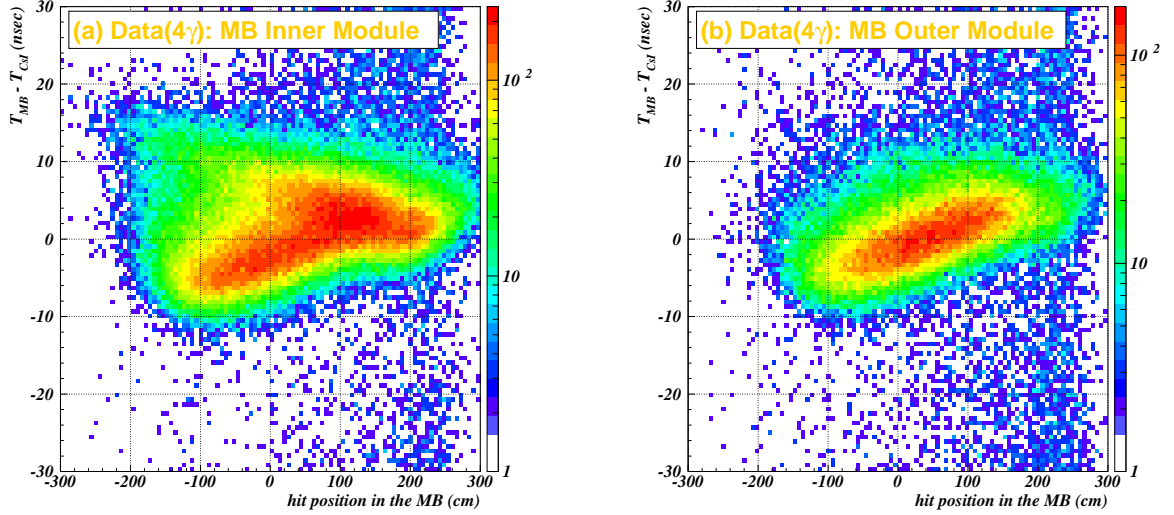


Figure 6.6: The distribution of the relative hit timing difference between the MB (T_{MB}) and the CsI (T_{CsI}) versus the hit position for (a) inner module and (b) outer module.

calorimeter and the photon hitting the MB, $\Delta T = T_{MB} - T_{CsI}$, versus the hit position in the inner MB module. There are two components. First component consists of photons from the $K_L \rightarrow \pi^0\pi^0\pi^0$ decays where some of photons hitting the MB. Since the photons from the K_L decays in the fiducial region usually hit the MB earlier than the photons hitting the CsI calorimeter, the ΔT was negative. Second component consists of photons which were in the “shower-splash-back” from the CsI calorimeter. In this case, the photons flew from the CsI calorimeter to the MB, thus the ΔT was positive. The slope of this component was approximately equal to the speed of light. The $K_L \rightarrow \pi^0\nu\bar{\nu}$ signal would also produce the shower-splash-back. Figure 6.6(b) shows the same distribution for the outer MB module. Unlike the inner MB module, there was only one component, which corresponds to the photons from the K_L decays. This was because the photons of the “shower-splash-back” had smaller energy than the photons from the K_L decays and deposited most of its energy in the inner MB module.

Figure 6.7 shows the distributions of E_{MB} in the inner and outer MB module for the four-photon event samples in data. We required timing of the PMT at the either end was within 200 nsec from the timing of photons hitting the CsI calorimeter. The E_{MB} for $K_L \rightarrow \pi^0\pi^0$ decays in which four photons were detected in the CsI calorimeter comes from the shower-splash-back. The E_{MB} for $K_L \rightarrow \pi^0\pi^0\pi^0$ decays with two missing photons comes from photons hitting MB. We discriminated between the two decays with the invariant mass of four photons. We required that energy deposit to be less than 1 MeV and 0.5 MeV in the inner and outer MB modules, respectively. The threshold on the inner module was set higher, to be less sensitive to the shower-splash-back.

In addition, to detect photons hitting the outside edge of the CsI calorimeter, we also used

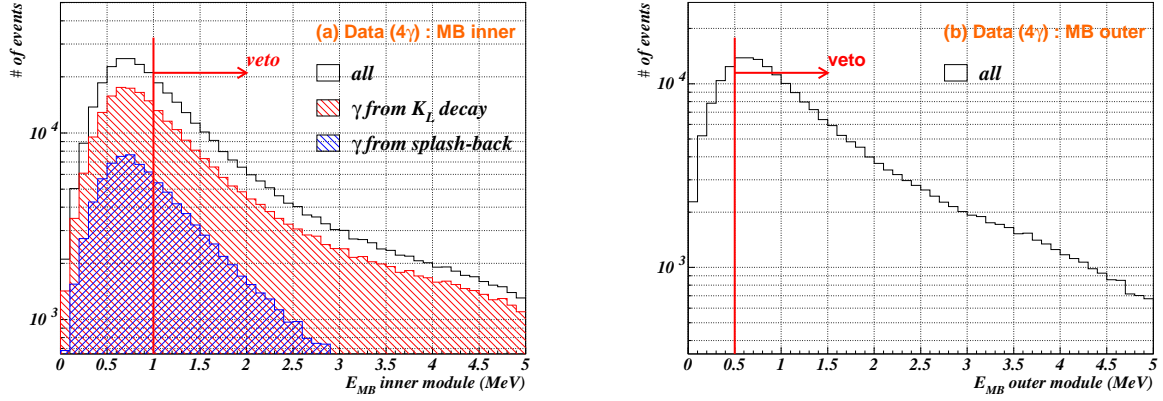


Figure 6.7: The distribution of energy in the inner MB module (a) and the outer MB module (b). The red dashed histogram consists of events from $K_L \rightarrow \pi^0\pi^0\pi^0$ decays where four photons hitting the CsI calorimeter and some of photons hitting the MB. The blue dashed histogram consists of events from $K_L \rightarrow \pi^0\pi^0$ decays in which the MB signal consisting of photons in the shower-splash-back.

MB. Since MB surrounded the CsI calorimeter, some shower leaked into MB. If a photon hits near the outside edge of CsI calorimeter (> 70 cm from the center), we required that total energy deposited in the MB module nearest to the photon hit position in the CsI calorimeter and the neighboring two modules, to be less than 0.5 MeV.

BA

To minimize the signal acceptance loss, we should not veto events with neutrons hitting BA. The signal from the quartz layer and the scintillator layer in the BA enables us to discriminate between photons and neutrons.

We first defined “hit” as a layer having a TDC value within ± 10 nsec of prompt timing. The TDC threshold for quartz layers and scintillator layers were 0.1 MIP² and 0.5 MeV, respectively. The total light yield in the quartz layer, E_Q , was defined as the summed light yield for all the quartz layers having the hit. The total energy deposited in the scintillator layer, E_S , was defined as the summed energies for all the scintillator layers having the hit. Figure 6.8 shows a correlation between the E_Q and E_S for photons and neutrons studied with the MC. We identified the hit as a photon if $E_Q \geq 0.5$ MIP and $E_Q/E_S \geq 10$.

However, if there was an earlier hit within 80 nsec, the hit with the prompt timing was not registered in the Multihit TDC because the TDC stop signal was 80 nsec long. In order to avoid losing photons due to this problem, we did the following:

- Re-define “hit” as a layer having energy deposit exceeding a threshold, where the threshold was 0.5 MIP for quartz layers, and 1.0 MeV for scintillator layers.

²The light yield in the quartz layer was normalized by the light yield from minimum ionization particle(MIP).

- Find six or more hits in continuous layers, and calculate E_Q^{cls} (the sum of energies in the continuous hit quartz layers), and E_S^{cls} (the sum of energies in the continuous hit scintillator layers). If there were two or more such continuous hits, we only used the one having the maximum E_Q^{cls} among them.
- Identify the continuous hits as a photon if they satisfy $E_Q^{cls}/E_S^{cls} \geq 30$.

If the hit was identified as a photon, we rejected this event.

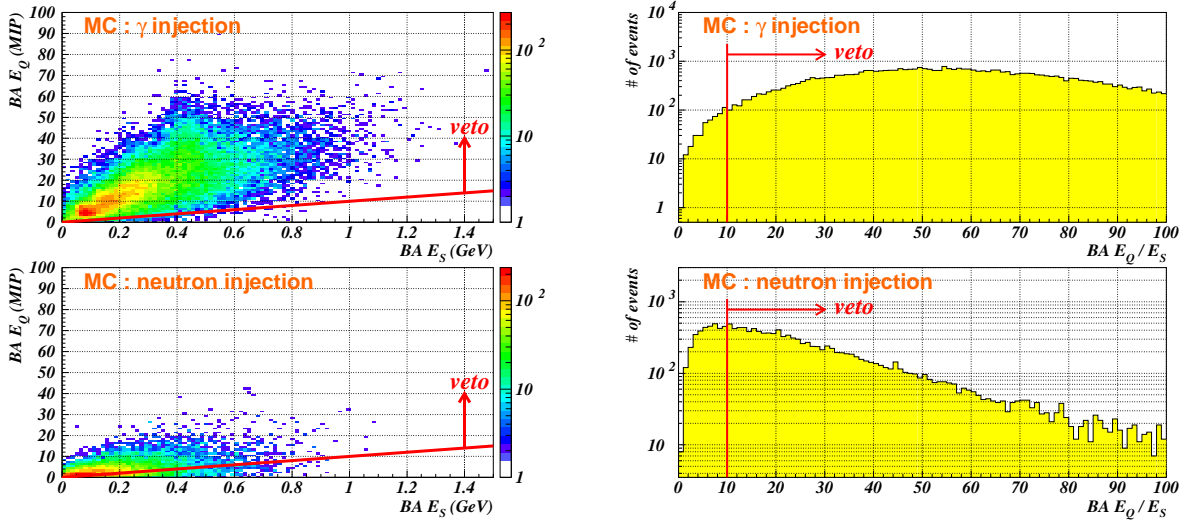


Figure 6.8: The left plots show the correlation between the total light yield in the quartz layer (E_Q) and the total energy deposit in the scintillator layer (E_S) of BA for photons and neutrons studied with the MC. The right plots show the distributions of the ratio of the total light yield in the quartz layer to the total energy deposit in the scintillator layer.

Other detectors

We applied a cut on energy deposits in other photon veto detectors: FB, CC02, CC03, CC04, CC05, CC06 and CC07. The cuts on the CC02, CC04, CC06 and CC07 were performed with a ± 15 nsec timing window. For each detector, the energy deposit was calibrated with minimum ionization particles³. Each threshold value is listed in Table 6.1.

³In particular, for FB, we used minimum ionization particles passing through the farthest point from the PMT.

Performance

We studied what fraction of $K_L \rightarrow \pi^0 \nu \bar{\nu}$ signal events could pass each cut. The signal efficiency of the photon veto cut A was defined:

$$\varepsilon_A \equiv \frac{(\# \text{ of events with all the cuts})}{(\# \text{ of events with all the cuts except for the cut } A)}. \quad (6.2)$$

Table 6.1 lists ε_A for each photon veto cut, studied with MC. The signal efficiency of the MB cut (ε_{MB}) was lower than the others because of accidental activities in the MB and the shower-splash-back from the CsI calorimeter. For the BA photon veto, we used data to estimate the signal efficiency (ε_{BA}). The signal loss was mainly caused by the neutrons accidentally hitting the BA. We will discuss the effect of the cut in section 6.3.

Table 6.1: The list of the thresholds applied to the photon veto detectors. The signal efficiency for each cut, ε_A , was defined as Equation 6.2 and estimated with the MC.

Detector	threshold	ε_A
CC02	4 MeV	1.0
CC03	1.5 MeV	0.98
CC04	3 MeV	0.98
CC06	5 MeV	0.98
CC07	50 MeV	0.99
FB	2 MeV	0.91
CsI	3 MeV	0.78
MB	1 MeV for the inner modules, and 0.5 MeV for the outer modules	0.60
BA	0.5 MIP for E_Q , and $E_Q/E_S \geq 10$	–

The rejection power of the photon veto cuts was studied with four-photon event samples from $K_L \rightarrow \pi^0 \pi^0 \rightarrow 4\gamma$ decays, and $K_L \rightarrow \pi^0 \pi^0 \pi^0 \rightarrow 6\gamma$ decays with two missing photons. Similarly to the $K_L \rightarrow \pi^0 \pi^0$ background to the $K_L \rightarrow \pi^0 \nu \bar{\nu}$ decay, the sources of missing photons in the $K_L \rightarrow \pi^0 \pi^0 \pi^0$ were the photon detection inefficiency and fused clusters. As shown in Fig. 6.9, we identified the events with the invariant mass $M_{4\gamma}$, in the range: $0.45 \leq M_{4\gamma}(\text{GeV}/c^2) \leq 0.55$ as $K_L \rightarrow \pi^0 \pi^0$ events, and $M_{4\gamma}(\text{GeV}/c^2) \leq 0.45$ as $K_L \rightarrow \pi^0 \pi^0 \pi^0$ events. The rejection power of each photon veto cut was measured with the reduction factor for $K_L \rightarrow \pi^0 \pi^0 \pi^0$ events in the selected mass region. Table 6.2 lists the rejection power of each photon veto cut. With all the photon veto cuts, the ratio of the number of $K_L \rightarrow \pi^0 \pi^0$ signal to the number of $K_L \rightarrow \pi^0 \pi^0 \pi^0$ background improved by a factor 11, which was consistent with the MC expectation within 18 %.

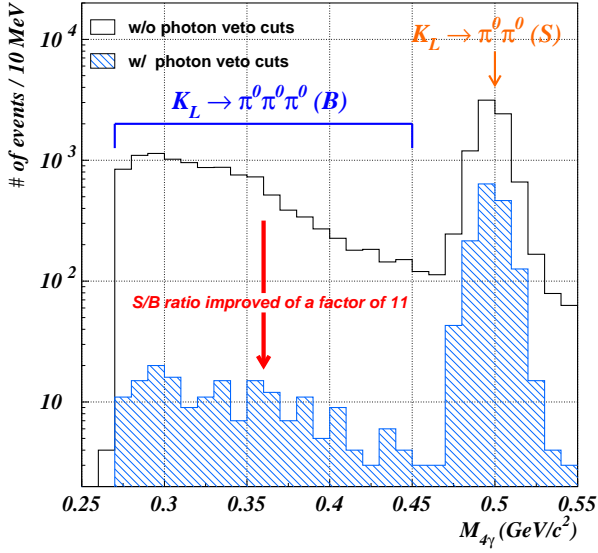


Figure 6.9: The distribution of the invariant mass of four photons without the photon veto cuts (solid) and with the photon veto cuts (hatched). The events in the lower mass region (B) were $K_L \rightarrow \pi^0 \pi^0 \pi^0$ where two photons were missed.

Table 6.2: The rejection power of photon veto cuts measured with the real data as described in the text. The photon veto using the CC02, CC03, CC04, CC05, CC06, CC07 and FB were combined.

photon veto	rejection power
CC02–CC07, FB	2.96 ± 0.25
CsI photon veto	5.54 ± 0.45
MB veto	3.76 ± 0.32
BA veto	3.56 ± 0.30

6.2.2 Charged particle veto cuts

A cut on the energy deposit in the CV was applied to reject events involving charged particles. In particular, the $K_L \rightarrow \pi^- e^+ \nu$ decay with the π^- and the e^+ depositing only small energies was a possible background source, as described in Section 6.1. Figure 6.10 shows the distribution of the energy deposit in the CV for minimum ionization particles collected during the calibration (muon) run. We required the energy deposit in each CV counter to be less than 0.5 MeV by applying a cut on the ADC counts⁴. However, according to the MC, the lower threshold on the CV induced 9 % additional loss to the $K_L \rightarrow \pi^0 \nu \bar{\nu}$ signal because sometimes particles

⁴Since we are cutting on the ADC counts, we are actually cutting on the light yield. We defined the light yield of the CV counter as 1.2 MeV if a minimum ionization particle passed through the farthest point from the PMT.

splashed back from the electromagnetic calorimeter and deposited a finite energy in the CV. For confirmation, we evaluated the acceptance loss due to the cut on CV for $K_L \rightarrow \pi^0\pi^0\pi^0$ and $K_L \rightarrow \pi^0\pi^0$ decays. It was 10 % (8.5 %) for $K_L \rightarrow \pi^0\pi^0\pi^0$ ($K_L \rightarrow \pi^0\pi^0$) and was consistent with the MC within 2.6 % (1.7 %).

A cut on the energy deposit in the BHCV was also important for suppressing the background from $K_L \rightarrow \pi^+\pi^-\pi^0$ decay, where π^+ and π^- went through the beam hole. Figure 6.11 shows the distribution of the maximum signal⁵ among four plastic scintillator plates in the BHCV for minimum ionization particles collected during the calibration (muon) run. We required that all the four BHCV counters have less than 0.1 MeV energy deposit by applying a cut on the ADC counts. This caused a 9 % signal loss as estimated with the MC.

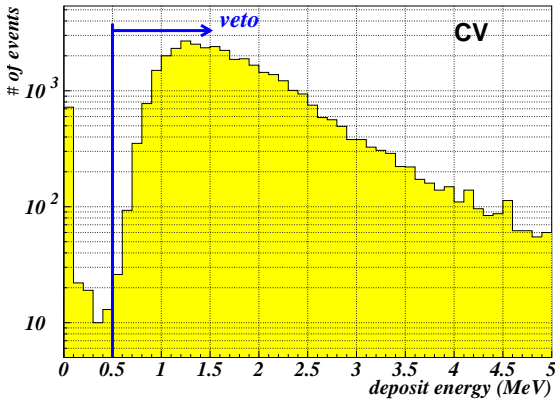


Figure 6.10: The distribution of energy deposit in the CV for a minimum ionization particle collected during the calibration (muon) run. We required the energy deposit in the CV to be less than 0.5 MeV.

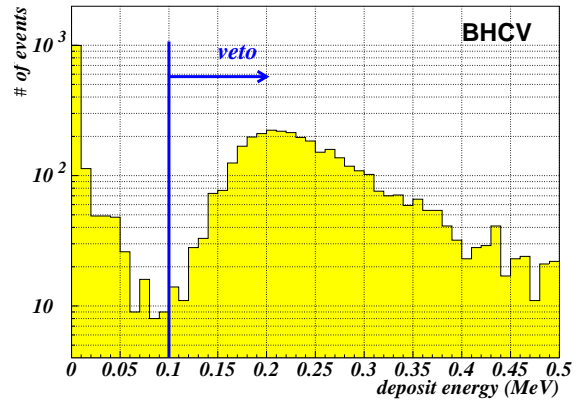


Figure 6.11: The distribution of energy deposit in the BHCV. We required that all the four BHCV counters have less than 0.1 MeV energy deposit.

6.2.3 Shower shape cut

The background involving fused clusters, where two nearby photons were misidentified as one photon, could be suppressed by a cut on the transverse shower shape. To represent the transverse shower shape of photon clusters, we introduced a quantity:

$$\text{RMS} = \sqrt{\frac{\sum_{i=1}^n e_i r_i^2}{E_{dep}}}, \quad (6.3)$$

⁵We defined the signal from the BHCV in each plastic scintillator plate as a summed signal from PMTs at the both edges.

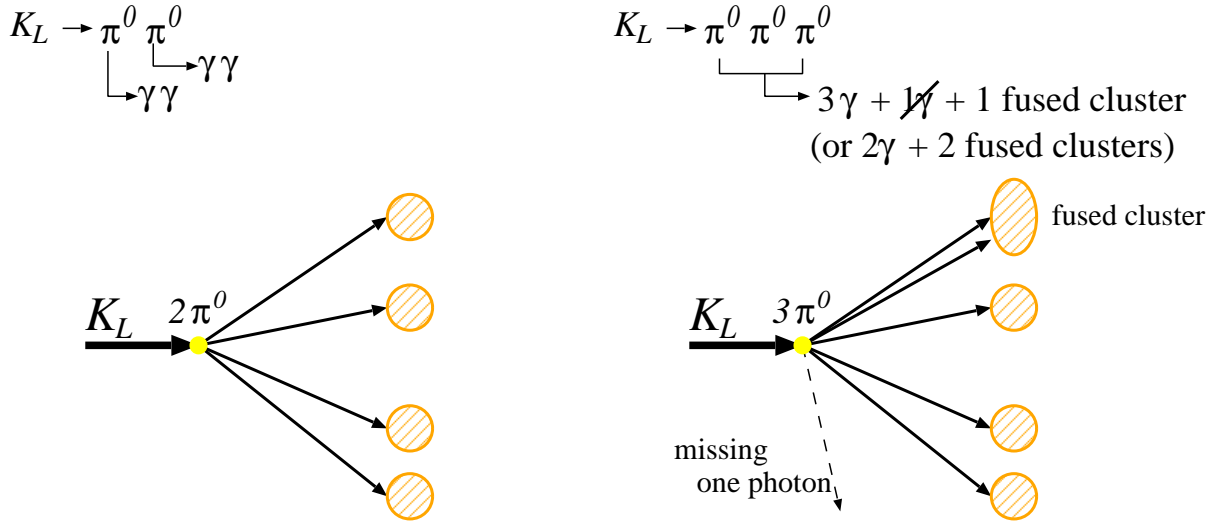


Figure 6.12: Four-photon event samples contained $K_L \rightarrow \pi^0 \pi^0$, and $K_L \rightarrow \pi^0 \pi^0 \pi^0$ with one or more fused clusters.

where e_i is the energy deposit in the CsI crystal, n is the number of crystals which has energy deposit exceeding 5 MeV associated with the photon cluster, and r_i is the relative distance between each CsI crystal and the center ($=P_{inc}$) of the photon cluster.

We studied the RMS using four-photon event samples. Some of the events in $M_{4\gamma}(\text{GeV}/c^2) \leq 0.45$ were $K_L \rightarrow \pi^0 \pi^0 \pi^0$ with one or two fused clusters, as shown in Fig. 6.12. Figure 6.13 shows the distributions of the maximum RMS among the clusters in the four-photon event samples in data. The $K_L \rightarrow \pi^0 \pi^0 \pi^0$ decays with two missing photons contained clusters with larger RMS than clusters from the $K_L \rightarrow \pi^0 \pi^0$ signal. Therefore, we rejected photons having large RMS. The distributions of the RMS for photons from the $K_L \rightarrow \pi^0 \pi^0$ signal and $K_L \rightarrow \pi^0 \pi^0 \pi^0$ background depended on the number of crystals in the cluster, n . Therefore, cut on the maximum RMS depended on the number crystals in each cluster. The shower shape cut reduced the $K_L \rightarrow \pi^0 \pi^0 \pi^0$ background by a factor 2.6 as measured with the real data, which was consistent with the MC expectation within 20 %. On the other hand, the shower shape cut rejected 16 % of the $K_L \rightarrow \pi^0 \nu \bar{\nu}$ signal events as estimated with the MC.

6.2.4 Photon energy cut

We also applied a cut on the energy of the photons. Some photons that were associated with the “core neutron multiple π^0 ” background had slightly smaller energy than the $K_L \rightarrow \pi^0 \nu \bar{\nu}$ signal, as shown in Fig. 6.14. Figure 6.14 also shows the distribution for the real data. In order to suppress the contamination of the core neutron background, we required each photon in the calorimeter to have more than 200 MeV. Furthermore, this cut suppressed background events with photons which traveled back from the downstream of the calorimeter, because such photons had small energies. MC studies showed that the cut on the photon energy rejected 39 % of the “core neutron multiple π^0 ” background and 27 % of $K_L \rightarrow \pi^0 \nu \bar{\nu}$ signal.

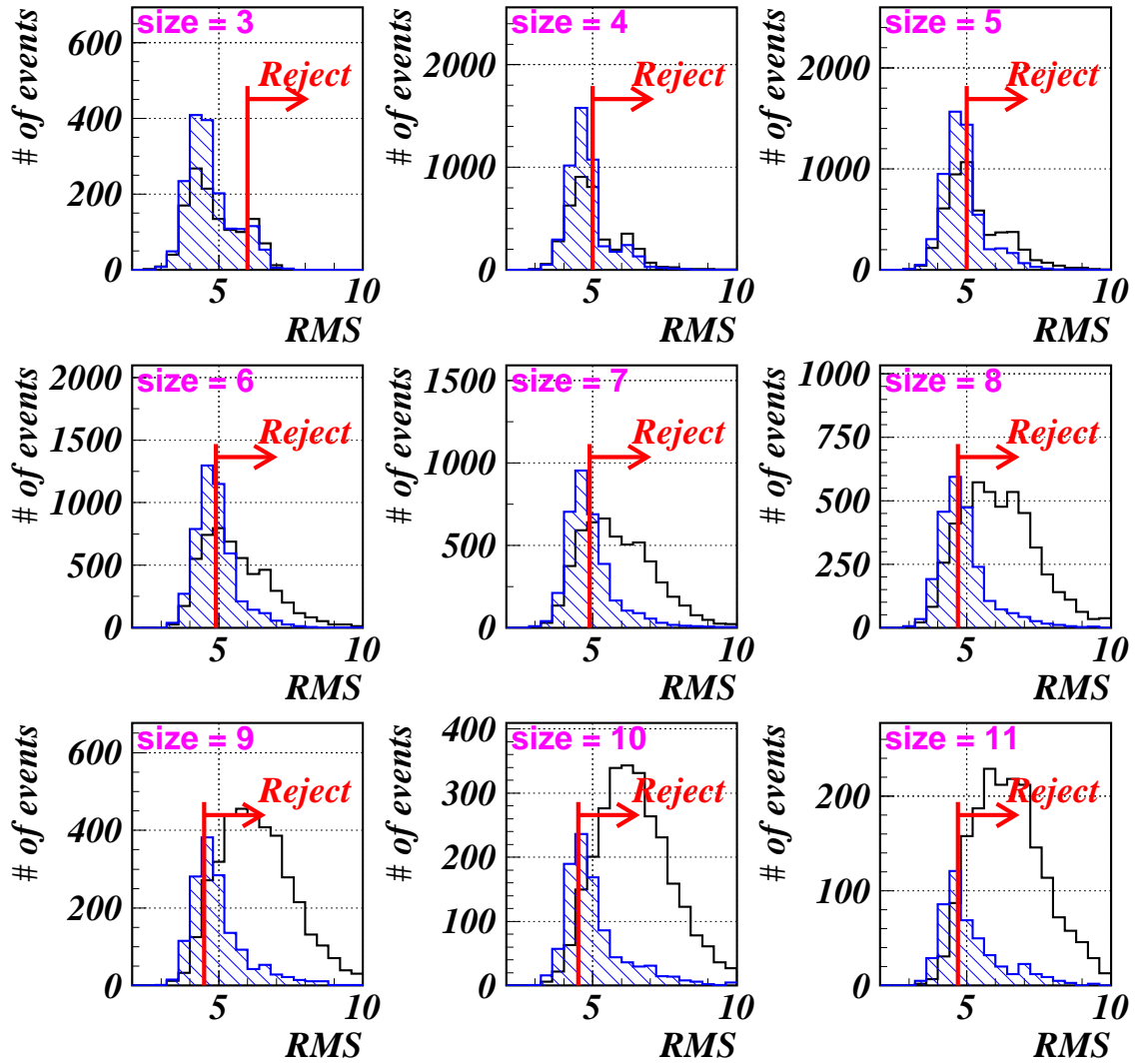


Figure 6.13: The distributions of the maximum RMS among the photons measured with the real data (four-photon event samples). The top left through the bottom right figures correspond to the distribution for the number of cluster size of 3 through 11. The solid and dashed histograms show the distributions for the $K_L \rightarrow \pi^0 \pi^0 \pi^0$ and $K_L \rightarrow \pi^0 \pi^0$ events, respectively.

6.2.5 Time difference cut

We required that the difference between two photon hit timings to be in ± 4 nsec in order to suppress additional background contamination caused by the accidental activity. For example, two accidental photon clusters on the CsI calorimeter could become a background event.

Figure 6.16 shows the distribution of the difference between the two photon hit timings as measured with the real data. The signal survival probability was estimated to be $0.971 \pm 0.005_{(\text{stat.})}$.

6.2.6 Hit position cuts

We required that photons hit outside the $17.5 \text{ cm} \times 17.5 \text{ cm}$ square area centered on the CsI calorimeter. This is because, as shown in Fig. 6.15, the photons produced by the core neutron hitting the membrane made hits closer to the beam hole than the $K_L \rightarrow \pi^0 \nu \bar{\nu}$ signal.

We also required that all the photons on the calorimeter to be within 80 cm from the center of the CsI calorimeter. This was to reject photons with energy leaking out of the calorimeter.

The cut on the hit position rejected 26 % of the “core neutron multiple π^0 ” background, and 23 % of $K_L \rightarrow \pi^0 \nu \bar{\nu}$ signal.

6.2.7 Acoplanarity angle cut

The transverse momentum of the two photons from $K_L \rightarrow \gamma\gamma$ decays basically balanced while it did not in the $K_L \rightarrow \pi^0 \nu \bar{\nu}$ decay. Therefore, we suppressed the $K_L \rightarrow \gamma\gamma$ decay by requiring large transverse momentum, $P_T \geq 0.12 \text{ GeV}/c$, as described later. However, if the energy of a photon is mis-measured, the transverse momentum of the reconstructed 2γ will have a larger transverse momentum as shown in Fig. 6.17. Since the probability that the transverse momentum exceeds the cut point is small, $K_L \rightarrow \gamma\gamma$ could not be a serious background in this analysis, but it would be serious in the future analysis.

In order to suppress events having such large transverse momentum, we introduced a quantity, “acoplanarity angle”. The acoplanarity angle was defined as a supplement of the angle spanned by the momentum vectors projected on the plane perpendicular to the beam axis (Fig. 6.19), and this does not use photon energies. Figure 6.18 shows that, in contrast to the transverse momentum, the acoplanarity angle is small even if the photon’s energy is mis-measured.

The acoplanarity angle distributions are different between $K_L \rightarrow \pi^0 \nu \bar{\nu}$ signal and $K_L \rightarrow \gamma\gamma$ background, as shown in Fig. 6.20. We required the acoplanarity angle to be larger than 30° . Even without the P_T cut, it rejected 99.93 % of $K_L \rightarrow \gamma\gamma$ decays while 89 % of $K_L \rightarrow \pi^0 \nu \bar{\nu}$ signal passed this requirement.

6.2.8 Kinematic cuts for the core neutron background

The following two kinematic cuts were additionally applied in order to suppress the core neutron background.

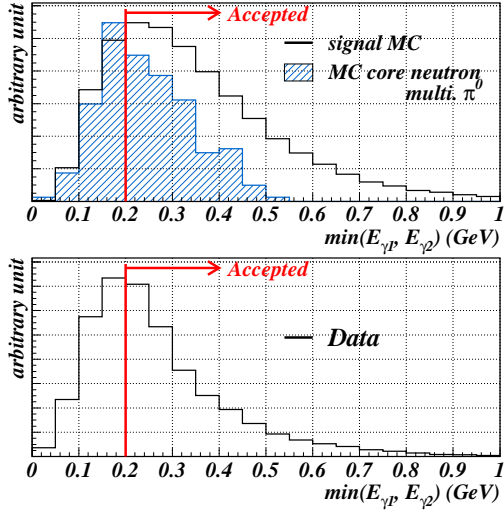


Figure 6.14: Top figure shows distributions of the smaller energy of the two photons for the signal (solid) and the “core neutron multiple π^0 ” background MC (dashed). Bottom figure shows the distribution for the real data.

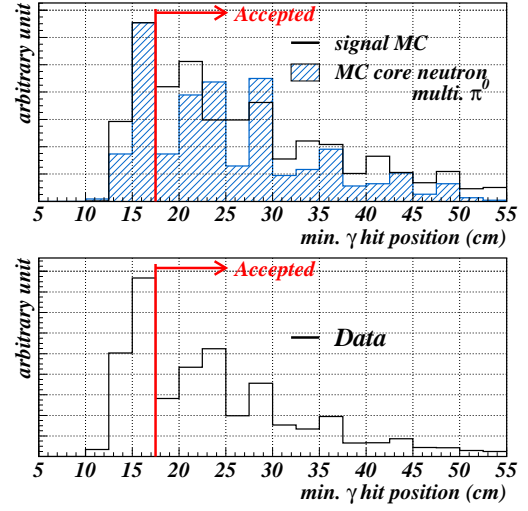


Figure 6.15: The distribution of the photon’s hit position closer to the beam hole. The hit position was centered on the CsI calorimeter. Top plot shows the distributions between two photons for the signal (solid) and the “core neutron multiple π^0 ” backgrounds MC (dashed). Bottom figure shows the distribution for the real data.

η cut

We rejected η -mesons produced at the membrane in the beam. For all the two photon events, we assumed that the two photons came from the η decay and reconstructed the decay vertex, Z_η . The Z_η and Z_{vtx} (reconstructed with assuming the π^0 mass) were correlated as shown in Fig. 6.21. We rejected the events which had $525 \leq Z_\eta(\text{cm}) \leq 575$, as shown in Fig. 6.22. The η cut, however, rejected 25 % of the $K_L \rightarrow \pi^0 \nu \bar{\nu}$ signal because their Z_η were in the cut region.

π^0 projection length cut

In order to reject the “core neutron multiple π^0 ” background events, we applied another kinematical cut. The π^0 projection length (R_{π^0}) was defined as the distance between the beam axis and the projection of the π^0 momentum vector on the CsI calorimeter, as shown in Fig. 6.23. Figure 6.24 shows the MC distribution of R_{π^0} for the core neutron background and the signal. We required $R_{\pi^0} > 21$ cm. It rejected 60 % of the core neutron background, while the 78 % of the signal passed this requirement.

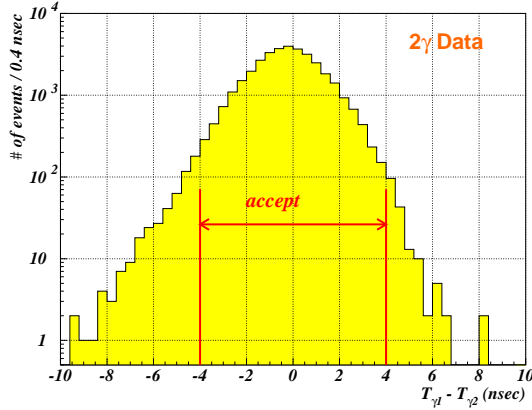


Figure 6.16: The distribution of the hit timing difference between two photons as measured with the real data.

6.2.9 Vertex cut

Figure 6.25 shows the distribution of the Z_{vtx} with the loose photon veto cuts⁶ for the real data. The “core neutron single π^0 ” background events and “halo neutron single π^0 ” background events correspond to the events at $Z_{\text{vtx}} = 550$ cm and 280 cm, respectively. We required the reconstructed π^0 vertex to be in $300 \leq Z_{\text{vtx}}(\text{cm}) \leq 500$ to reject both background events. The cut positions were chosen to suppress the number of each background events to be less than 0.1 events. The distribution of the Z_{vtx} for the signal MC is shown in 6.26. The 90 % of signal passed this requirement.

6.2.10 $P_T - Z_{\text{vtx}}$ correlation cut

In order to further suppress the “core neutron multiple π^0 ” background, we applied a cut on the correlation between P_T and Z_{vtx} . As shown in Fig. 6.2, the “core neutron multiple π^0 ” backgrounds are populated at low P_T – downstream region. If energetic photons from the membrane hit the calorimeter, the decay vertex is reconstructed at the upstream of the membrane, and the reconstructed P_T becomes smaller, according to Equation 5.11. On the other hand, if soft photons from the membrane are detected by the calorimeter, the decay vertex will be reconstructed downstream with a large opening angle, and the P_T will be large.

Therefore, we used this characteristics to suppress the “core neutron multiple π^0 ” background. A parameter α was defined as:

$$\alpha \equiv P_T(\text{GeV}/c) - 8.0 \times 10^{-4}(\text{GeV}/c \cdot \text{cm}) \times Z_{\text{vtx}}(\text{cm}) \quad (Z_{\text{vtx}} < 525\text{cm}), \quad (6.4)$$

where the coefficient, 8.0×10^{-4} was obtained by fitting the P_T distribution from the “core neutron multiple π^0 ” background as a function of the Z_{vtx} using the core neutron MC. Figure 6.27 shows the parameter α for the core neutron background and the $K_L \rightarrow \pi^0 \nu \bar{\nu}$ signal. The lower

⁶The energy threshold on the photon veto detectors were set slightly higher than the photon veto cuts as described in Section 6.2.1.

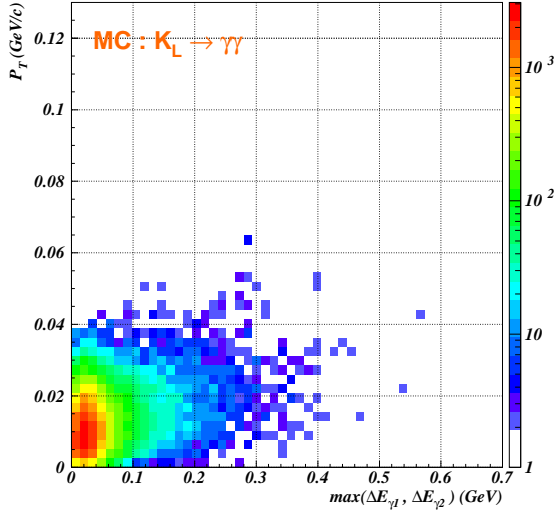


Figure 6.17: The MC distribution of the transverse momentum of the reconstructed 2γ from $K_L \rightarrow \gamma\gamma$ versus the larger ΔE_γ between two photons, where ΔE_γ is the difference between the incident and reconstructed energy. The P_T tends to be larger for larger ΔE_γ .

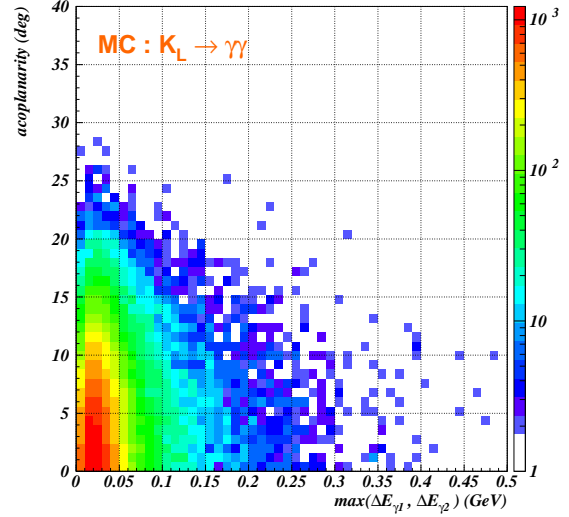


Figure 6.18: The MC distribution of the acoplanarity angle of 2γ from $K_L \rightarrow \gamma\gamma$ versus the larger ΔE_γ between two photons, where ΔE_γ is the difference between the incident and reconstructed energy. The acoplanarity angle tends to be smaller for larger ΔE_γ .

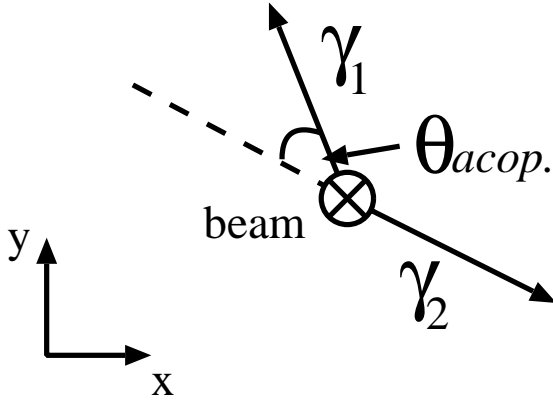


Figure 6.19: A schematic view of the acoplanarity angle. The beam goes into the page.

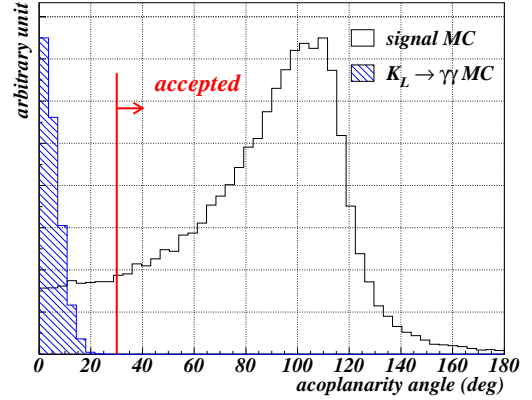


Figure 6.20: The MC distribution of the acoplanarity angle for the $K_L \rightarrow \pi^0 \nu \bar{\nu}$ signal (solid) and $K_L \rightarrow \gamma\gamma$ background (dashed).

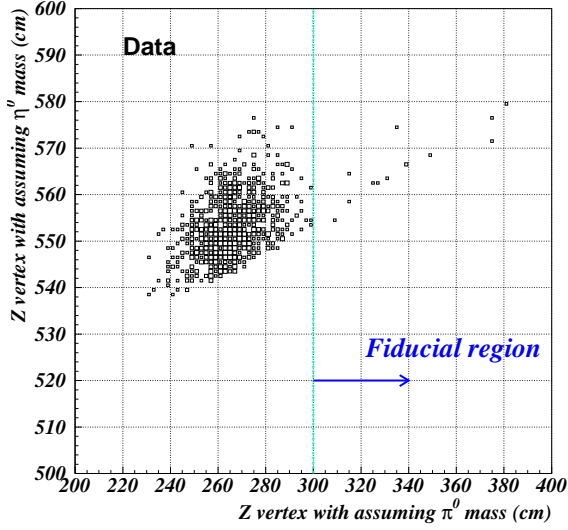


Figure 6.21: The correlation between the vertices reconstructed by assuming that the two photons came from the π^0 and the η . Most of these events are η 's produced by the core neutron at the membrane in the beam.

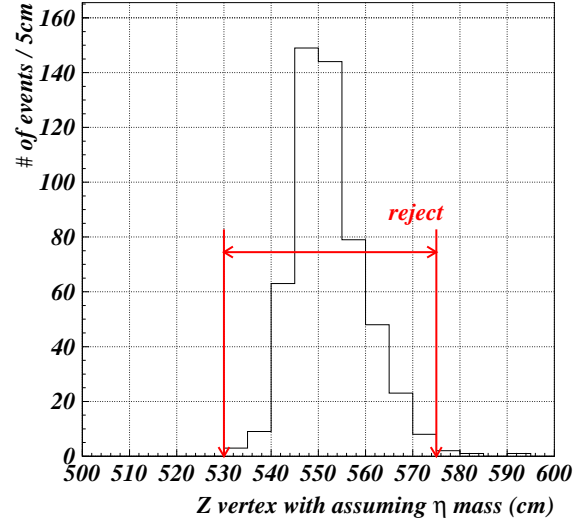


Figure 6.22: The distribution of the decay vertex (Z_η) in the data, reconstructed assuming that the two photons came from an η decay. If Z_η is in the range: $530 \leq Z_\eta(\text{cm}) \leq 575$, the event was identified as the η produced at the membrane in the beam.

boundary for the $\alpha \geq -0.225$ GeV/c was determined by minimizing the contamination of the “core neutron multiple π^0 ” background while keeping a reasonable signal acceptance.

6.2.11 P_T cut

Another cut, $P_T \geq 0.12$ GeV/c, was applied to suppress π^0 from Λ decay ($\Lambda \rightarrow \pi^0 n$) whose maximum P_T is 109 MeV/c. This decay was not a serious background in this analysis, but it would be serious in the future experiments. On the other hand, the upper boundary on P_T was determined to be $P_T \leq 0.24$ GeV/c from the kinematical limit on the $K_L \rightarrow \pi^0 \nu \bar{\nu}$ decay ($P_{max} = 0.231$ GeV/c), allowing for the smearing effect due to detector resolutions.

Finally, Fig.6.28 and Fig.6.29 show the MC distribution of Z_{vtx} versus P_T for the $K_L \rightarrow \pi^0 \nu \bar{\nu}$ signal and the core neutron background, respectively, with the signal box overlaid on top of them.

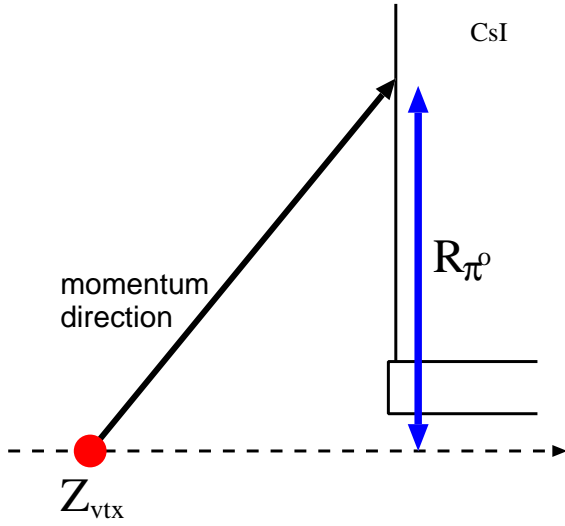


Figure 6.23: A schematic view of the definition of the π^0 projection length R_{π^0} .

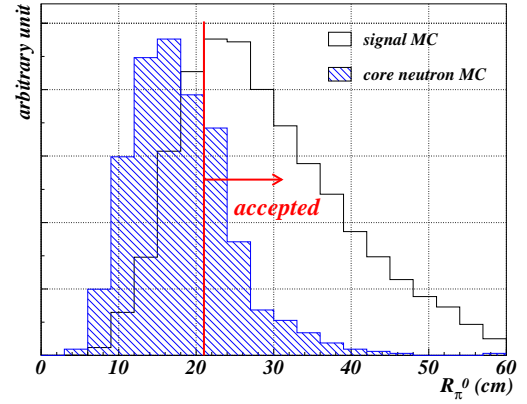


Figure 6.24: The MC distribution of R_{π^0} for both the $K_L \rightarrow \pi^0 \nu \bar{\nu}$ signal (solid) and the core neutron background (dashed), in which events in the fiducial region.

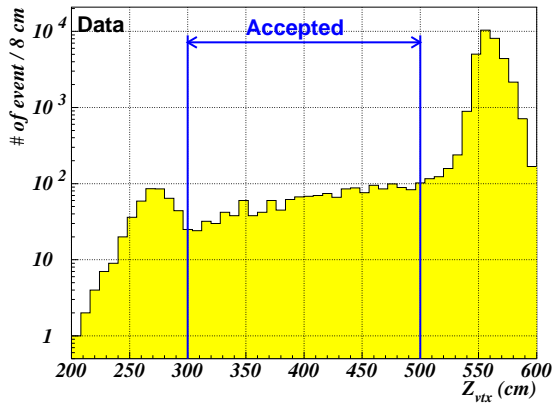


Figure 6.25: The distribution of the Z_{vtx} for the real data with loose photon veto cuts.

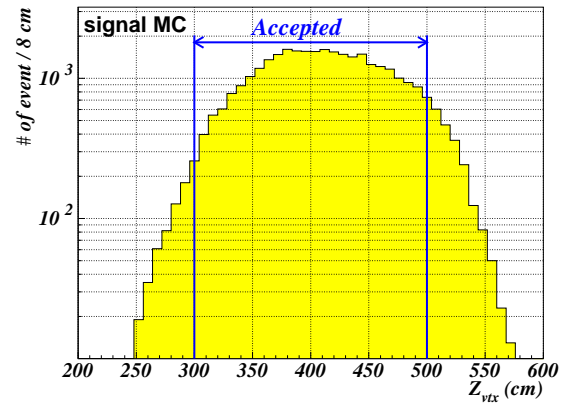


Figure 6.26: The distribution of the Z_{vtx} for the signal MC with loose photon veto cuts.

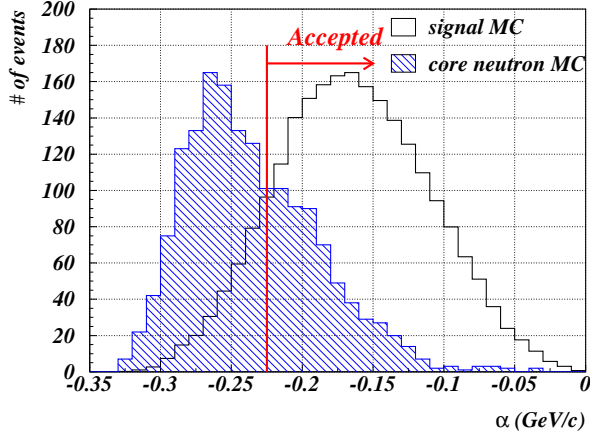


Figure 6.27: The distribution of the parameter $\alpha \equiv P_T(\text{GeV}/c) - 8.0 \times 10^{-4}(\text{GeV}/c\cdot\text{cm}) \times Z_{\text{vtx}}(\text{cm})$ for both the $K_L \rightarrow \pi^0 \nu \bar{\nu}$ signal (solid) and the core neutron background (dashed) for the events in $300 \leq Z_{\text{vtx}}(\text{cm}) \leq 500$.

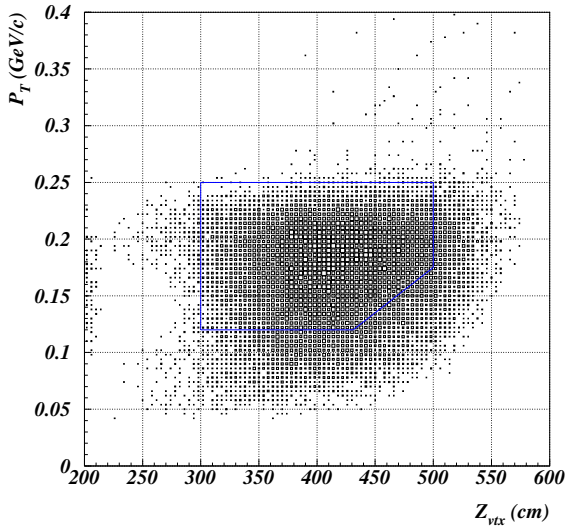


Figure 6.28: Z_{vtx} versus P_T for the $K_L \rightarrow \pi^0 \nu \bar{\nu}$ signal from MC with all selection cuts except for the photon veto cuts. The blue box shows the signal region.

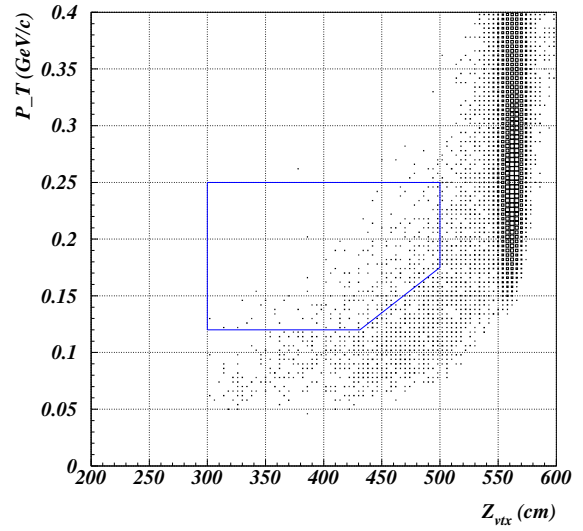


Figure 6.29: Z_{vtx} versus P_T for the core neutron background from MC with all the selection cuts except for the photon veto cuts. The blue shows the signal region.

6.3 Acceptance

All the event selection cuts have been determined. In this section, we summarize the signal acceptance and a survival probability of each selection cut. We define the survival probability for the cut A :

$$\epsilon_A = \frac{(\# \text{ of events after cut } A)}{(\# \text{ of events before cut } A)}. \quad (6.5)$$

We used MC to estimate the survival probabilities for each cut, except for⁷,

- (a) cut on the timing dispersion of the photons,
- (b) cut on the hit timing difference between two photons, and
- (c) photon veto cut on the BA,

because it was difficult to accurately measure their effect with the MC. The total signal acceptance was defined as:

$$A_{sig} \equiv \frac{N_{rec}}{N_{decay}} \cdot \epsilon_{(a)} \cdot \epsilon_{(b)} \cdot \epsilon_{(c)}, \quad (6.6)$$

where the N_{rec} is the number of reconstructed MC events after applying all the event selection cuts except for the cuts (a), (b) and (c), and N_{decay} is the number of K_L decays in the MC.

Table 6.3 lists the survival probability and acceptance for each selection cut studied with the 6.8×10^5 K_L decays in the MC. Applying all the selection cuts except for the cuts (a), (b) and (c), we obtained the ratio: $N_{rec}/N_{decay} = [1.08 \pm 0.01_{(MC \text{ stat.})}] \times 10^{-2}$. The main component of the acceptance loss was the photon veto cuts.

The survival probability for the timing dispersion cut, $\epsilon_{(a)}$, was evaluated by using the $K_L \rightarrow \pi^0\pi^0$ and $K_L \rightarrow \pi^0\pi^0\pi^0$ data. The survival probability in the $K_L \rightarrow \pi^0\pi^0$ and $K_L \rightarrow \pi^0\pi^0\pi^0$ was 0.896 ± 0.008 and 0.937 ± 0.028 , respectively. Taking the number of photons into account, we obtained $\epsilon_{(a)}$ to be $0.966 \pm 0.008_{(stat.)}$ for the $K_L \rightarrow \pi^0\nu\bar{\nu}$ decay.

The survival probability for the hit timing difference cut, $\epsilon_{(b)}$, was evaluated by using the two photon event samples, as described in subsection 6.2.5. We estimated $\epsilon_{(a)}$ to be $0.971 \pm 0.005_{(stat.)}$.

The survival probability for the BA photon veto cut, $\epsilon_{(c)}$, was evaluated by using the $K_L \rightarrow \pi^0\pi^0$ and $K_L \rightarrow \pi^0\pi^0\pi^0$ data. In the $K_L \rightarrow \pi^0\pi^0$ and the $K_L \rightarrow \pi^0\pi^0\pi^0$ analyses⁸, we compared the number of reconstructed K_L 's with and without the cut (c). The acceptance loss in the $K_L \rightarrow \pi^0\pi^0$ and $K_L \rightarrow \pi^0\pi^0\pi^0$ was 0.638 ± 0.022 and 0.658 ± 0.022 , respectively. Taking the average of them, we estimated $\epsilon_{(c)}$ to be $0.648 \pm 0.012_{(stat.)}$.

Finally, we obtained the signal acceptance:

$$A_{sig} = [0.657 \pm 0.016] \times 10^{-2}. \quad (6.7)$$

We will consider the error on A_{sig} as a source of a systematic error on the single event sensitivity, as will be discussed in Chapter 8.

⁷The cut on the timing dispersion was one of the selection cuts in the photon identification described in Section 5.1, and Appendix A

⁸A detailed description is given in Appendix B.

Table 6.3: The acceptance for the $K_L \rightarrow \pi^0 \nu \bar{\nu}$ signal estimated by the MC. The survival probability for each selection cut is also listed. We used 6.8×10^5 K_L decays in the acceptance estimation. Each number is normalized by the number of events with two clusters on the CsI calorimeter.

Cut	survival prob.	acceptance
Cluster finding	0.67	6.70×10^{-1}
Online Trigger	0.51	3.40×10^{-1}
Photon finding	0.78	2.65×10^{-1}
π^0 reconstruction	0.97	2.57×10^{-1}
vertex cut	0.67	1.71×10^{-1}
Photon veto cuts except BA	0.36	6.22×10^{-2}
Charged veto cuts	0.82	5.09×10^{-2}
Shower shape cut	0.86	4.36×10^{-2}
Photon energy cut	0.77	3.34×10^{-2}
Hit position cuts	0.77	2.57×10^{-2}
Acoplanarity angle cut	0.90	2.32×10^{-2}
η cut	0.75	1.73×10^{-2}
π^0 projection distance cut	0.80	1.39×10^{-2}
P_T cut	0.78	1.08×10^{-2}

We summarized the survival probabilities for each background source obtained by the MC study, in Table 6.4 and 6.5. The cut on the CV and BHCV (= ‘‘Charged veto cuts’’ in the table) were effective in suppressing the ‘‘core neutron single π^0 ’’ and the ‘‘core neutron multiple π^0 ’’ background because those background interactions often involved charged particles. The cut on the photon veto detectors (= ‘‘Photon veto cuts except BA’’) was effective for the background sources involving extra photons.

For the backgrounds associated the neutron interaction, i.e. the core neutron background and the halo neutron background, we did not use the MC in the background estimation, as will be described in next Chapter. The reason was that it was difficult to properly produce the rate of the neutron interaction with the detector material.

6.4 Normalization

In order to estimate the number of K_L decays in this search, we analyzed the $K_L \rightarrow \pi^0 \pi^0$ decays as the normalization mode.

As discussed in Section 2.2, the systematic uncertainties in the single event sensitivity mainly comes from the acceptance ratio between the $K_L \rightarrow \pi^0 \nu \bar{\nu}$ signal and the normalization mode. In order to reduce the systematic uncertainties, we made the selection criteria for the $K_L \rightarrow \pi^0 \pi^0$ almost the same as for the $K_L \rightarrow \pi^0 \nu \bar{\nu}$.

The invariant mass of the four photons and the reconstructed decay vertex for the $K_L \rightarrow \pi^0\pi^0$ decay are shown in Fig. 6.30. The MC correctly reproduced the real data. We defined the $K_L \rightarrow \pi^0\pi^0$ signal region: $0.47 \leq M_{4\gamma}(\text{GeV}/c^2) \leq 0.53$, and $300 \leq \text{decay vertex (cm)} \leq 500$. The contamination of the $K_L \rightarrow \pi^0\pi^0\pi^0$ background in the $K_L \rightarrow \pi^0\pi^0$ signal region was estimated by extrapolating the side band to the invariant mass range. We estimated 30 $K_L \rightarrow \pi^0\pi^0\pi^0$ background events in the 2111 events observed in the $K_L \rightarrow \pi^0\pi^0$ signal region. Based on the MC study, we estimated that the acceptance for the $K_L \rightarrow \pi^0\pi^0$ decay is 1.41×10^{-3} . By subtracting the $K_L \rightarrow \pi^0\pi^0\pi^0$ background, we obtained the number of K_L decays:

$$N_{decay} = [1.67 \pm 0.04_{(\text{stat.})}] \times 10^9 . \quad (6.8)$$

Furthermore, the expected number of K_L decays was confirmed by checking the consistency between $K_L \rightarrow \pi^0\pi^0$ decay and $K_L \rightarrow \pi^0\pi^0\pi^0$ decay samples, where the same selection cuts were applied on both decay modes except for the requirement of the number of photons. Figure 6.31 shows the distribution of the invariant mass and the decay vertex for the $K_L \rightarrow \pi^0\pi^0\pi^0$ decay. We observed 2.55×10^4 $K_L \rightarrow \pi^0\pi^0\pi^0$ decays in the same invariant mass region with the acceptance of 7.19×10^{-5} . The ratio of the decay widths of $K_L \rightarrow \pi^0\pi^0$ decay to $K_L \rightarrow \pi^0\pi^0\pi^0$ decay was measured as:

$$\begin{aligned} \frac{\Gamma_{00}}{\Gamma_{000}} &= \frac{n_{2\pi^0}^{obs}}{n_{3\pi^0}^{obs}} \times \frac{A_{3\pi^0}}{A_{2\pi^0}} \quad (6.9) \\ &= \frac{2081}{25521} \times \frac{7.19 \times 10^{-5}}{1.41 \times 10^{-3}} \\ &= [4.16 \pm 0.09_{(\text{stat.})} \pm 0.04_{(\text{MC stat.})}] \times 10^{-3} \end{aligned}$$

where $n_{2\pi^0}^{obs}$ ($n_{3\pi^0}^{obs}$) is the number of observed decays, and $A_{2\pi^0}$ ($A_{3\pi^0}$) is the acceptance for the $K_L \rightarrow \pi^0\pi^0$ ($K_L \rightarrow \pi^0\pi^0\pi^0$) decay. This result was consistent with the PDG value, $[4.455 \pm 0.023] \times 10^{-3}$ [5], within 7 %. This difference mainly came from the mismatch between data and MC in the energy distribution in MB detector and the transverse shower shape of the photon. We assigned this difference as one of the systematic uncertainties in the single event sensitivity, as described in Chapter 8.

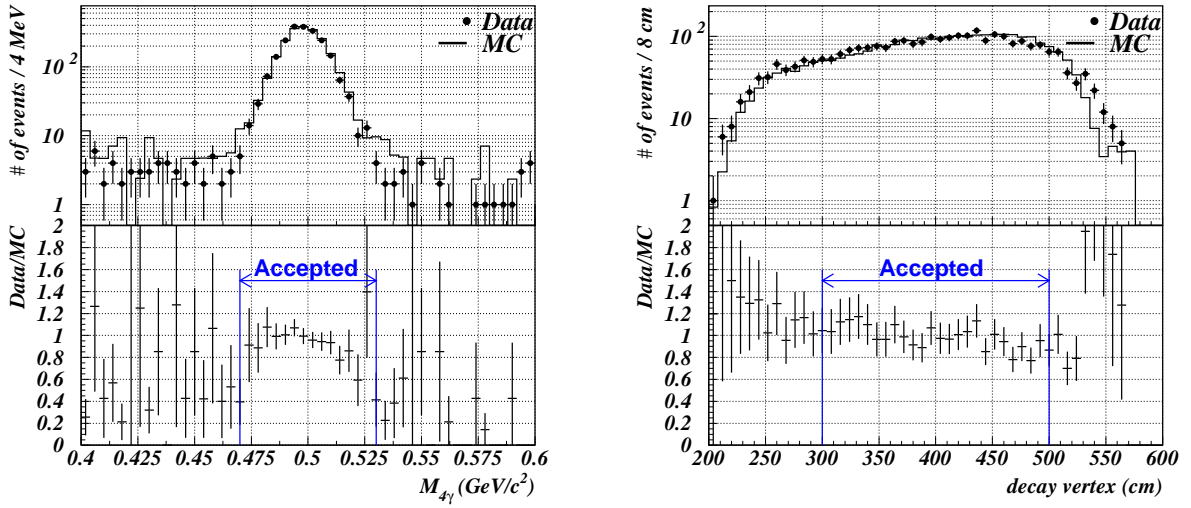


Figure 6.30: The distribution of the invariant mass (left) and the decay vertex (right) for the $K_L \rightarrow \pi^0 \pi^0$. In the top plot, the dots show the data and the histogram shows the MC. The bottom plot shows the ratio of the data to the MC.

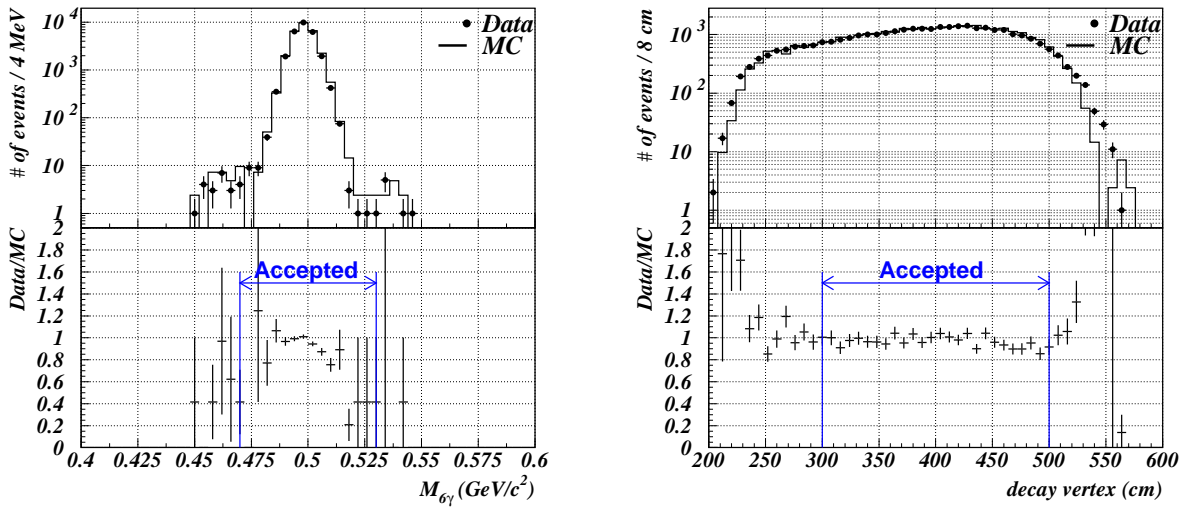


Figure 6.31: The distribution of the invariant mass (left) and the decay vertex (right) for the $K_L \rightarrow \pi^0 \pi^0 \pi^0$. In the top plot, the dots show the data and the histogram shows the MC. The bottom plot shows the ratio of the data to the MC.

Table 6.4: The lists of the survival probabilities for each background source studied with the MC. The numbers in this table were based on the order of cuts actually applied in the analysis.

Cut	core neutron single π^0		core neutron multiple π^0	
	survival prob.	# of events	survival prob.	# of events
after π^0 reconstruction	–	355500	–	834920
vertex cut	2.98×10^{-2}	10576	1.51×10^{-1}	125820
Photon veto cuts except BA	2.95×10^{-2}	312	3.06×10^{-2}	3844
Charged veto cuts	9.61×10^{-3}	3	1.20×10^{-2}	46
Shower shape cut	–	0	5.65×10^{-1}	26
Photon energy cut	–	0	6.15×10^{-1}	16
Hit position cuts	–	0	8.12×10^{-1}	13
Acoplanarity angle cut	–	0	3.08×10^{-1}	4
η cut	–	0	1.00	4
π^0 projection distance cut	–	0	5.00×10^{-1}	2
P_T cut	–	0	–	0

Cut	halo neutron single π^0		halo neutron multiple π^0	
	survival prob.	# of events	survival prob.	# of events
after π^0 reconstruction	–	4110	–	28735
vertex cut	3.33×10^{-2}	137	1.00×10^{-1}	2891
Photon veto cuts except BA	5.11×10^{-2}	7	2.32×10^{-2}	67
Charged veto cuts	–	0	2.84×10^{-1}	19
Shower shape cut	–	0	5.26×10^{-1}	10
Photon energy cut	–	0	1.00×10^{-1}	1
Hit position cuts	–	0	–	0
Acoplanarity angle cut	–	0	–	0
η cut	–	0	–	0
π^0 projection distance cut	–	0	–	0
P_T cut	–	0	–	0

Table 6.5: The lists of the survival probabilities for each background source studied with the MC. The numbers in this table were based on the order of cuts actually applied in the analysis. The ratio of the number of K_L decays between MC and data were 9.16, 1.45, 0.81, 0.65 for $K_L \rightarrow \pi^0\pi^0$, $K_L \rightarrow \gamma\gamma$, $K_L \rightarrow \pi^-e^+\nu$ and $K_L \rightarrow \pi^+\pi^-\pi^0$ decay, respectively.

Cut	$K_L \rightarrow \pi^0\pi^0$		$K_L \rightarrow \gamma\gamma$	
	survival prob.	# of events	survival prob.	# of events
after π^0 reconstruction	–	80553	–	57961
vertex cut	5.11×10^{-1}	41151	3.52×10^{-1}	20420
Photon veto cuts except BA	9.33×10^{-3}	384	3.51×10^{-1}	7163
Charged veto cuts	7.34×10^{-1}	282	7.86×10^{-1}	5628
Shower shape cut	8.23×10^{-1}	232	5.59×10^{-1}	3144
Photon energy cut	8.45×10^{-1}	196	1.00	3143
Hit position cuts	7.86×10^{-1}	154	5.43×10^{-1}	1709
Acoplanarity angle cut	3.70×10^{-1}	57	–	0
η cut	7.72×10^{-1}	44	–	0
π^0 projection distance cut	3.41×10^{-1}	15	–	0
P_T cut	1.30×10^{-1}	2	–	0

Cut	$K_L \rightarrow \pi^-e^+\nu$		$K_L \rightarrow \pi^+\pi^-\pi^0$	
	survival prob.	# of events	survival prob.	# of events
after π^0 reconstruction	–	1172300	–	99013
vertex cut	6.32×10^{-1}	741190	5.93×10^{-1}	56888
Photon veto cuts except BA	2.23×10^{-1}	165470	1.86×10^{-2}	1092
Charged veto cuts	–	0	–	0
Shower shape cut	–	0	–	0
Photon energy cut	–	0	–	0
Hit position cuts	–	0	–	0
Acoplanarity angle cut	–	0	–	0
η cut	–	0	–	0
π^0 projection distance cut	–	0	–	0
P_T cut	–	0	–	0

Chapter 7

Background Estimation

We estimated the number of remaining background events in the signal region. Furthermore, we estimated the number of background events outside the signal region and compared them with data in order to check our background understanding.

Section 7.1 describes how we used the MC to estimate the amount of background from K_L decays. Section 7.2 describes how we used the real data to estimate the number of background events associated with the neutron interaction. Section 7.3 summarizes our background estimation. Section 7.4 compares the number of background events outside the signal region with our estimation.

7.1 Background from K_L decay

7.1.1 $K_L \rightarrow \pi^0\pi^0$ background

We estimated the number of $K_L \rightarrow \pi^0\pi^0$ background events with the MC.

The $K_L \rightarrow \pi^0\pi^0$ decay became a background if two photons were undetected in the final state even though the cuts on all the photon veto detectors were applied. Therefore, the number of $K_L \rightarrow \pi^0\pi^0$ background was determined by the probability that two photons were missed.

First, we studied whether the MC reproduced the probability of missing two photons from $K_L \rightarrow \pi^0\pi^0\pi^0$ decays in the sample with four photons detected in the CsI calorimeter.

We first considered the rejection power of the cuts on the photon veto detectors. The upper plot in Fig. 7.1 shows the distribution of the invariant mass of four photons with the cuts on photon veto detectors except for the BA and without the cuts on the identification and the shower shape. Events with the invariant mass, $M_{4\gamma}$, in the range, $M_{4\gamma}(\text{GeV}/c^2) \leq 0.45$, were $K_L \rightarrow \pi^0\pi^0\pi^0$ decays missing two photons. As shown in the lower plot in Fig. 7.1, the uniform ratio of the data to the MC indicates that the MC reproduced the rejection power of the cuts on the photon veto detectors in the real data within 18 %.

We studied the distribution of the energy deposit in the MB detector, shown in Fig. 7.2 and Fig. 7.3 for confirmation. Even though the inner MB module has a discrepancies at the region below 0.5 MeV, the distributions agreed around and above the MB cut threshold (1 MeV for inner MB module, 0.5 MeV for outer MB module).

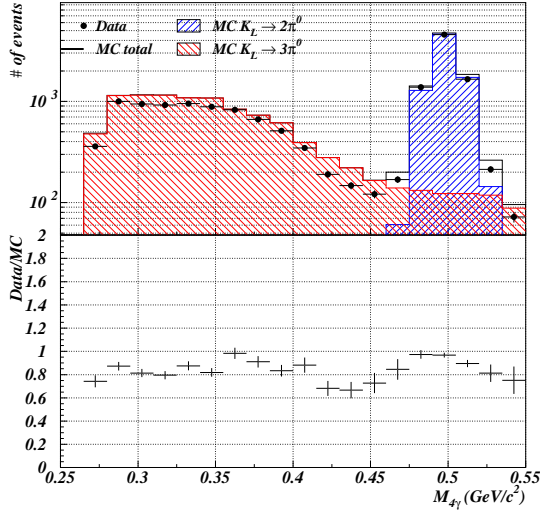


Figure 7.1: Top: The distribution of the invariant mass of the four photons ($M_{4\gamma}$) with only the cuts on the photon veto detectors except the BA. The dots show data, the solid histogram shows total MC, the blue hatched histogram shows the $K_L \rightarrow \pi^0\pi^0$ MC and the red hatched histogram shows the $K_L \rightarrow \pi^0\pi^0\pi^0$ MC. Bottom: The ratio of the data to the MC.

We studied the rejection power of the photon veto cut on the BA using the real data. Here, we assumed a constant rejection power, r , for a photon with the incident energy above a threshold at 100 MeV. As we described in Section 6.3, the signal survival probability for the BA cut was 0.65. In the MC $K_L \rightarrow \pi^0\pi^0$ background study, we applied a weight on each event depending on the number of photons entering the BA. We set the weight, w , as follows.

- if no photons above the threshold entered the BA, we used the signal survival probability, $w = 0.65$.
- if one photon above the threshold entered the BA, we assigned $w = r$.
- if n photons with an incident energy above the threshold entered the BA, we assigned $w = r^n$.

We tuned r to reproduce the number of events in the low mass region: $M_{4\gamma} \leq 0.45$, and found $r = 0.26$. Figure 7.4 shows the distribution of the invariant mass of four photons with applying the rejection power of the BA cut. The ratio of data to MC was still uniform.

Second, we considered the rejection power of the cuts on the photon identification and the shower shape. The upper plot in Fig. 7.5 shows the distribution of the invariant mass of four photons with the cuts on the photon identification and the shower shape. We also applied the cuts on the photon veto detectors and the rejection power of the BA cut. As shown in the lower plot in Fig. 7.5, the MC is about 40 % lower than data in the lower mass region, $M_{4\gamma} < 0.45$. This is because MC does not properly reproduce the transverse shower shape of the photon. Therefore, we assigned this discrepancy, 40 %, as an uncertainty in the estimated number of $K_L \rightarrow \pi^0\pi^0\pi^0$ background events in the four-photon event samples. We assumed that the uncertainty in the estimated number of $K_L \rightarrow \pi^0\pi^0$ background events for $K_L \rightarrow \pi^0\nu\bar{\nu}$ decay was also 40 % due to the mismatch between data and MC in the transverse shower shape.

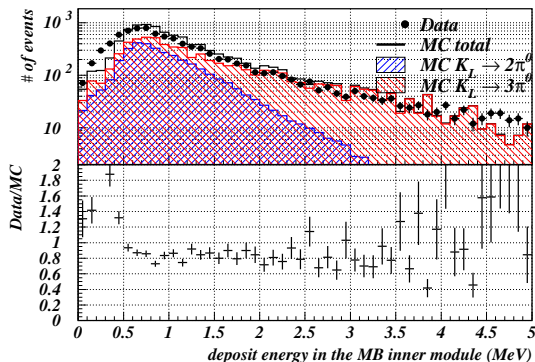


Figure 7.2: Top: The distribution of the energy deposit in the MB inner module for the data (dots), the MC $K_L \rightarrow \pi^0\pi^0$ (blue hatched) and the MC $K_L \rightarrow \pi^0\pi^0\pi^0$ (red hatched). Bottom: The ratio of the data to the MC.

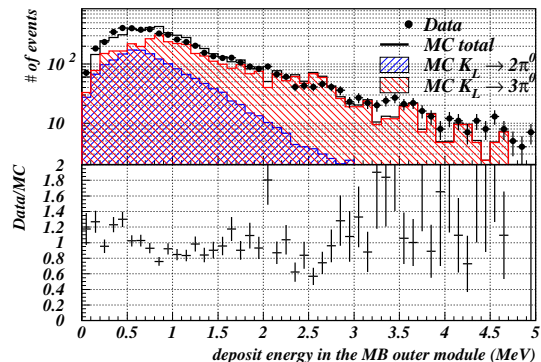


Figure 7.3: Top: The distribution of the energy deposit in the MB outer module for the data (dots), the MC $K_L \rightarrow \pi^0\pi^0$ (blue hatched) and the MC $K_L \rightarrow \pi^0\pi^0\pi^0$ (red hatched). Bottom: The ratio of the data to the MC.

The number of $K_L \rightarrow \pi^0\pi^0$ background in the search for $K_L \rightarrow \pi^0\nu\bar{\nu}$ decay was estimated using the MC with $r = 0.26$. We produced $K_L \rightarrow \pi^0\pi^0$ MC with 20 times larger statistics than the real data. Figure 7.6 shows the distribution of Z_{vtx} versus P_T for the $K_L \rightarrow \pi^0\pi^0$ MC. We observed 3 events with the total weight of 0.04 ± 0.03 events in the signal region, where the second term represents combined uncertainty on the MC statistics and the systematic uncertainty.

7.1.2 $K_L \rightarrow \gamma\gamma$ background

We considered two possibilities for the $K_L \rightarrow \gamma\gamma$ background.

The first case is where halo K_L 's decay into two photons. Since we assumed the decay vertex to be on the z axis $(0, 0, Z_{\text{vtx}})$, the halo K_L decay could be wrongly reconstructed to have a finite transverse momentum. In addition, if the K_L in the region farther than 8 cm from the beam axis decays into two photons, this event passes the acoplanarity angle cut. The number of such events was estimated as:

$$N_{\gamma\gamma}^{\text{bkg}} = N_{\text{decay}} \times P_{\text{halo}K_L} \times Br(K_L \rightarrow \gamma\gamma) \times A, \quad (7.1)$$

where $P_{\text{halo}K_L}$ is the fraction of K_L 's in the region more than 8 cm away from the beam axis, and A is an acceptance with all the selection cuts except for the P_T cut and the acoplanarity angle cut. We estimated the $P_{\text{halo}K_L}$ to be 10^{-5} from real data, and the A to be 1.2×10^{-3} from a MC study. Based on these values, the remaining number of $K_L \rightarrow \gamma\gamma$ background events due to the halo K_L is 0.01.

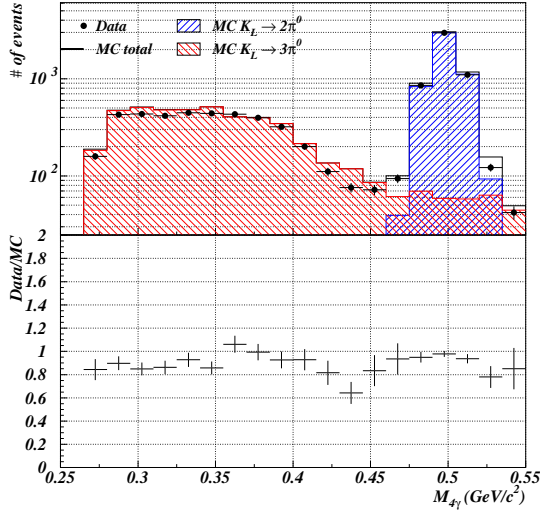


Figure 7.4: Top: $M_{4\gamma}$ with the cuts on the photon veto detectors and after applying the rejection power of BA. The dots show data, the solid histogram shows total MC, the blue hatched shows the $K_L \rightarrow \pi^0 \pi^0$ MC and the red hatched shows the $K_L \rightarrow \pi^0 \pi^0 \pi^0$ MC. Bottom: The ratio of the data to the MC.

Another case for $K_L \rightarrow \gamma\gamma$ background was the events whose P_T became larger as shown in Fig. 6.17 because of mis-measured photon energy. To have a large transverse momentum satisfying the P_T cut, $P_T \geq 0.12$ (GeV/c), we considered a case where photon's energy was mis-measured due to the photo-nuclear interactions¹. The probability of such reaction for photons had been measured by the experiments for the CsI crystal and it was less than 10^{-4} for 200 MeV photons and 10^{-6} for 1 GeV photons [25, 26]. Therefore, the number of background events in such a case was negligible.

7.1.3 Other K_L backgrounds

The inefficiency of the plastic scintillator for the charged particles caused $K_L \rightarrow \pi^+ \pi^- \pi^0$ background. If two photons from the π^0 decay hit the CsI calorimeter and the remaining charged particles went through the beam hole, the inefficiency of BHCV would determine the background level. The inefficiency of the BHCV for the charged particle was slightly larger than other detectors; due to its thin thickness (~ 1 mm), the light yield was smaller and the energy deposit had a larger fluctuation. We estimated the inefficiency of the BHCV for charged particles using the distribution of the energy deposit collected during the calibration (muon) run as shown in Fig. 7.7. We fitted this distribution for a function:

$$f(x) = p1 \cdot \exp\left(-\frac{(x - p2)^2}{\sqrt{2}[p3 + p4(x - p2)]^2}\right), \quad (7.2)$$

(asymmetric-gaussian) and estimated the fraction of the number of events below the threshold of 0.1 MeV to be 1.6×10^{-3} .

¹The photo-nuclear interaction is a reaction in which an incident photon was absorbed by the nucleus and this nucleus emits only neutrons.

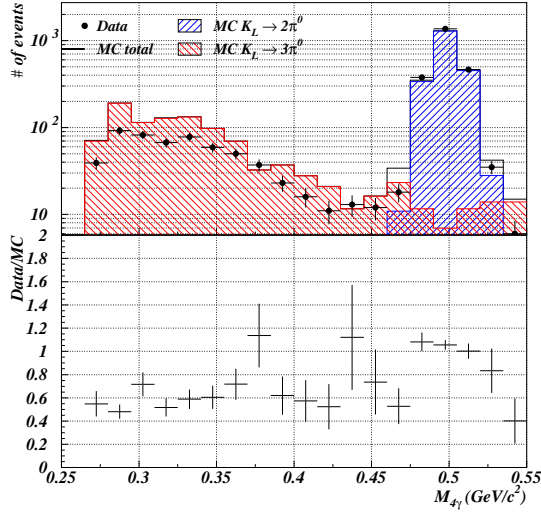


Figure 7.5: Top: $M_{4\gamma}$ with the cuts on the photon identification and the shower shape in addition to the cuts on the photon veto detectors. The dots show data, the solid histogram shows total MC, the blue hatched shows the $K_L \rightarrow \pi^0\pi^0$ MC and the red hatched shows the $K_L \rightarrow \pi^0\pi^0\pi^0$ MC. Bottom: The ratio of the data to the MC.

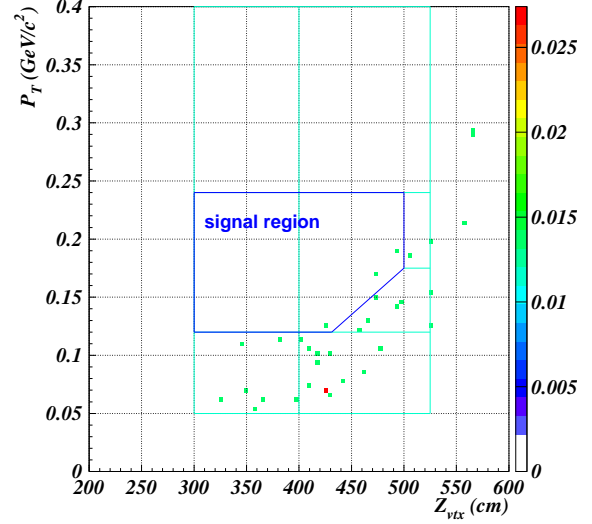


Figure 7.6: The distribution of Z_{vtx} versus P_T for the $K_L \rightarrow \pi^0\pi^0$ MC with all the event selection cuts.

The number of the $K_L \rightarrow \pi^+\pi^-\pi^0$ background was estimated as follows:

$$N_{\pi^+\pi^-\pi^0}^{bkg} = N_{decay} \times Br(K_L \rightarrow \pi^+\pi^-\pi^0) \times A \times (\text{Inefficiency for charged particles})^2, \quad (7.3)$$

where $A = 7.4 \times 10^{-8}$ is the acceptance with all the selection cuts except for the BHCV cut². Based on those parameters, the remaining number of $K_L \rightarrow \pi^+\pi^-\pi^0$ background was estimated to be negligible.

In case of $K_L \rightarrow \pi^-e^+\nu$, the inefficiency of the CV for charged particles increased the number of background events. In particular, if following three things happened at the same time, it became a background event.

- (1) the π^- went through $\pi^- + p \rightarrow \pi^0 + n$ and the two photons decayed from the π^0 overlapped in the electromagnetic calorimeter,

²The maximum momentum of the π^0 from the $K_L \rightarrow \pi^+\pi^-\pi^0$ decay in the center-of-mass system of K_L is 133 MeV/c. It caused a large suppression.

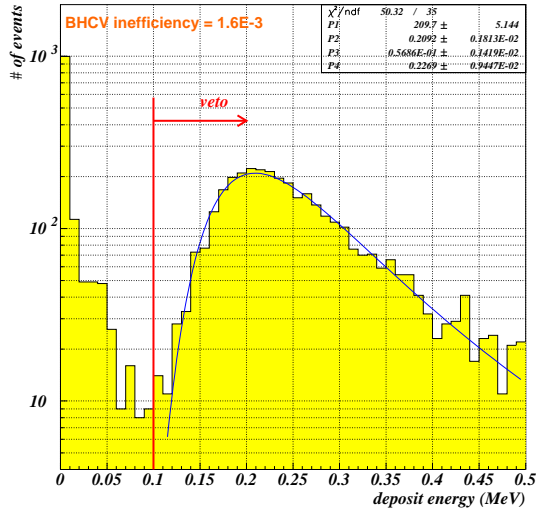


Figure 7.7: The distribution of energy deposit in the BHCV collected during the calibration (muon) run. The curve shows the fitted asymmetric-gaussian.

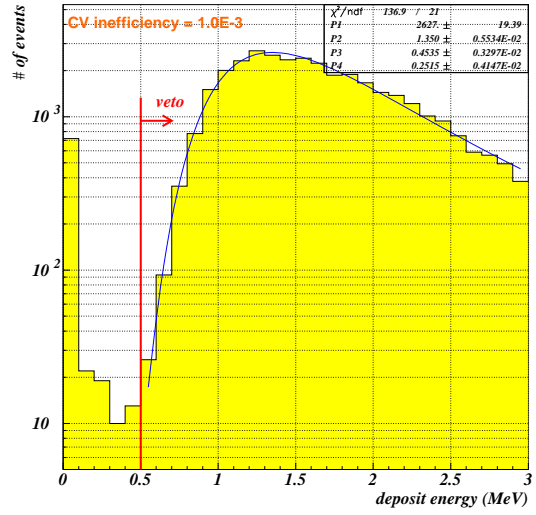


Figure 7.8: The distribution of energy deposit in the CV collected during the calibration (muon) run. The curve shows the fitted asymmetric-gaussian.

- (2) the e^+ went through a pair annihilation ($e^+ + e^- \rightarrow \gamma + \gamma$), and these two photons also overlapped, and
- (3) the energy deposit in the CV was too low to be detected.

The number of $K_L \rightarrow \pi^- e^+ \nu$ background events was conservatively estimated assuming the probability of overlapping photons to be 1 :

$$\begin{aligned}
 N_{ke3}^{bkg} &= N_{decay} \times Br(K_L \rightarrow \pi^- e^+ \nu) \times A \\
 &\quad \times (\text{Inefficiency for } \pi^-) \\
 &\quad \times (\text{Inefficiency for } e^+), \tag{7.4}
 \end{aligned}$$

where $A = 2.5 \times 10^{-5}$ is the acceptance where π^- and e^+ hit the CV and passed all the selection cuts except for the CV cut. We estimated the inefficiency of the CV due to the fluctuation of its light yield using the distribution of the energy deposit collected during the calibration (muon) run. As shown in Fig. 7.8, the inefficiency of the CV was estimated as 1.0×10^{-3} . The inefficiency due to the reactions (1) and (2) was measured as 3.0×10^{-4} for π^- and 1.6×10^{-4} for e^+ [31]. Combining these inefficiencies, we obtained the inefficiency for π^- and e^+ to be 1.3×10^{-3} and 1.2×10^{-3} , respectively. Based on these parameters, 0.01 $K_L \rightarrow \pi^- e^+ \nu$ background events were expected.

7.2 Backgrounds associated with the neutron interaction

We estimated the number of background events associated with neutron interactions using the real data, because the amount of the membrane in the beam was not surely known.

Figure 7.9 shows the Z_{vtx} versus P_T for events after applying all the event selection cuts. The region, $300 \leq Z_{\text{vtx}}(\text{cm}) \leq 525$ and $0.05 \leq P_T(\text{GeV}/c) \leq 0.4$, was masked in order to avoid any biases in this background study. The masked region was categorized into eight regions because it was expected that the contamination of each background source depended on the $Z_{\text{vtx}} - P_T$ plane. The signal region defined in the previous chapter corresponds to the region (3) and (4).

The “halo neutron CC02” events were located upstream of the signal region. The “core neutron η ” events were also located around the same region but most of those events were eliminated by the η cut. The “core neutron single π^0 ” events and the “halo neutron CV” events were located downstream of the signal region.

In subsection 7.2.1, we will estimate the number of “core neutron multiple π^0 ” background events. In subsection 7.2.2, we will estimate the number of other background events.

7.2.1 Core neutron multiple π^0

We estimated the number of “core neutron multiple π^0 ” background events³ as follows.

We first made the events dominated by the “core neutron multiple π^0 ” background events by removing following cuts.

- cuts on CV and the photon veto detector: MB, CC03, CC04, CC06, CC07 and BA, and
- cuts on the photon energy and the photon hit position in the CsI calorimeter,

Hereafter, we call the combined cuts of the first item as “PV” cut and the second item as “EH” cut. We first checked how many other background events contaminate in the data without the PV cut and the EH cut. The number of $K_L \rightarrow \pi^0\pi^0$ background events was estimated with the MC by removing the PV cut and the EH cut. In each $Z_{\text{vtx}} - P_T$ region, the fraction of $K_L \rightarrow \pi^0\pi^0$ background events was less than 0.5 %. We estimated the number of background events associated with the neutron interactions after removing the PV cut and the EH cut with the method that will be described in Section 7.2.2. In the regions, (3) and (7), the fraction of the “core neutron η background” events was $[2 \pm 1]$ %, and the fraction of the “halo neutron CC02” background events was $[0.24 \pm 0.07]$ %. Since we removed the photon energy cut, an additional background source, in which two accidental photons were reconstructed, could increase. In the regions, (2), (4), (5), (6) and (8), there were $[3 \pm 3]$ % of such background events⁴.

Now, let us consider the number of background events for the four combinations of the PV cut and the EH cut, as shown in Fig. 7.10.

³The halo neutron background events where two photons came from the multiple π^0 produced at the CV were also reconstructed in the signal region, but its rate would be smaller than the “core neutron multiple π^0 ” background because the rate of halo neutron was 10^5 times smaller than the core neutron.

⁴We estimated the number of background events from two accidental photons were reconstructed as follows. First, using the accidental trigger, the rate of one accidental cluster with energy deposit greater than 10 MeV was estimated as 15 kHz. We applied ± 4 nsec timing window in the event selection. Therefore, during 1.8×10^5

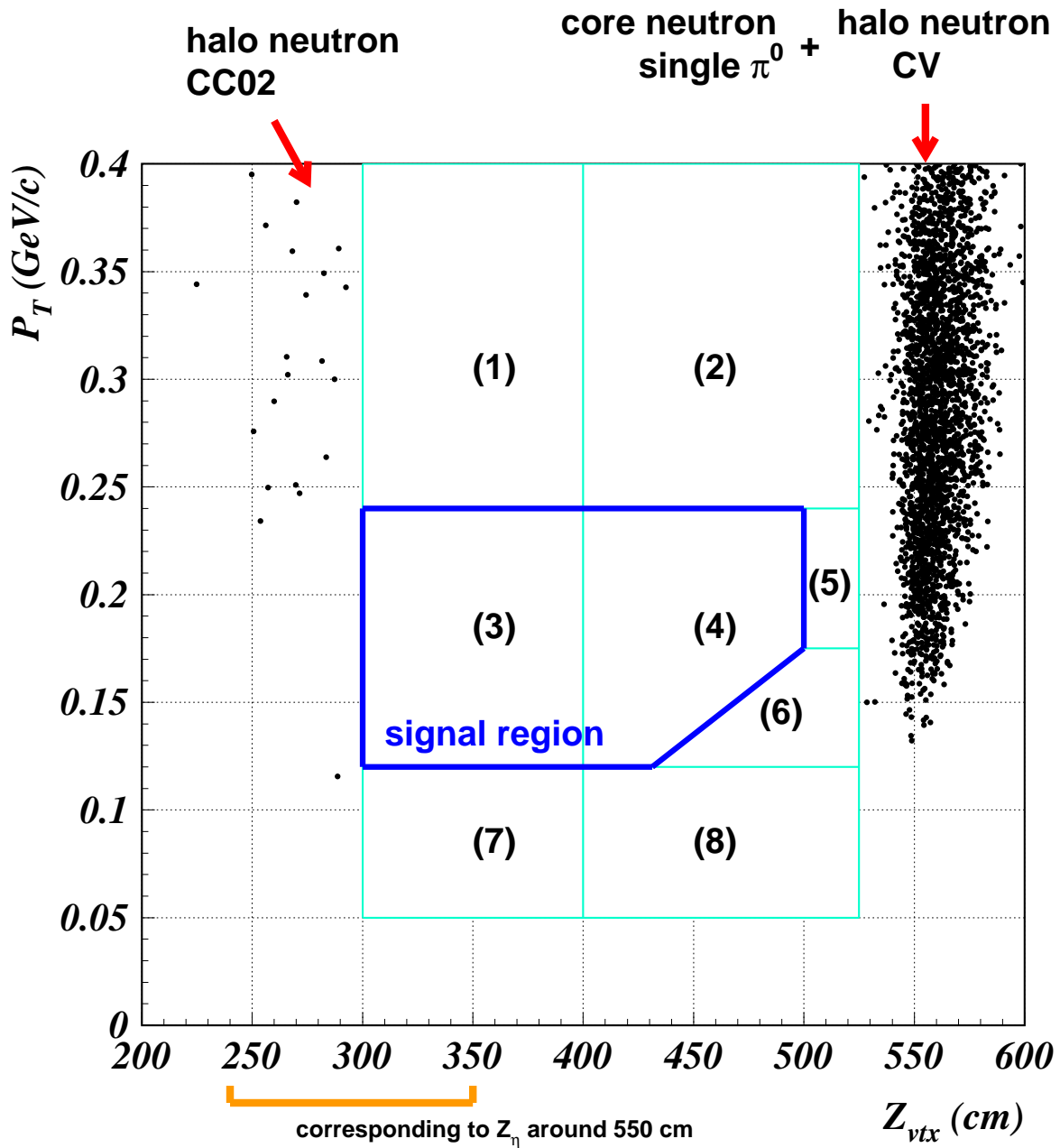


Figure 7.9: Z_{vtx} versus P_T with all the event selection cuts. The region with $300 \leq Z_{vtx}(\text{cm}) \leq 525$ and $0.05 \leq P_T(\text{GeV}/c) \leq 0.4$ was masked, and divided into eight regions for a background study.

1. combination A : N_A events passed the EH cut, but failed the PV cut,
2. combination B : N_B events failed both the EH cut and the PV cut,
3. combination C : N_C events passed the PV cut, but failed the EH cut, and
4. combination S : N_{bkg} events passed both the EH cut and the PV cut.

The final number of the “core neutron multiple π^0 ” background was determined by applying both the PV cut and the EH cut, hence it was N_{bkg} . If the PV cut and the EH cut were independent of each other, then we get:

$$\frac{N_{bkg}}{N_C} = \frac{N_A}{N_B}, \quad (7.6)$$

and

$$\frac{N_{bkg}}{N_A} = \frac{N_C}{N_B}. \quad (7.7)$$

Therefore, the final number of the background events is:

$$N_{bkg} = \frac{N_A \times N_C}{N_B}. \quad (7.8)$$

We confirmed the independence of the PV cut and the EH cut as follows. For each selection cut in the EH cut, we examined the ratio of the number of events passing the cut and the number of events failing the cut. If both ratios did not vary with and without the PV cut, the EH cut and the PV cut were independent of each other. Figure 7.11 shows the distribution of the photon energy and the photon hit position on the CsI calorimeter with and without the PV cut. The ratio for the photon energy cut was 0.73 ± 0.03 without the PV cut and 0.79 ± 0.12 with the PV cut. The ratio for the photon hit position cut was $[5.2 \pm 0.6] \times 10^{-2}$ without the PV cut and $[5.1 \pm 2.6] \times 10^{-2}$ with the PV cut. These results indicated that the EH cut and the PV cut were independent.

Table 7.1 shows the estimated number of the “core neutron multiple π^0 ” background events in each region on the $Z_{\text{vtx}} - P_T$ plane with the method described above. In this table, if $N_C = 0$, we defined the number of background events according to the Bayesian method⁵.

seconds data taking time, the number of events in which two accidental photons were observed was:

$$N_{acc}^{total} = (15 \times 10^3 [\text{s}])^2 \times (8 \times 10^{-9} [\text{s}]) \times (1.8 \times 10^5 [\text{s}]) = 3.2 \times 10^5. \quad (7.5)$$

Next, we reconstructed π^0 from two accidental photons. These background events were reconstructed all over in the region (2), (4), (5), (6) and (8). We then estimated the survival probability of all the selection cuts except for the PV cut and the EH cut using the real data. It was $[1.1 \pm 1.1] \times 10^{-4}$. Therefore, the estimated number of the such background events was $[35 \pm 35]$ events in the regions (2), (4), (5), (6) and (8) and it corresponded to $[3 \pm 3] \%$.

⁵Let H be the unknown probability that an event passes the PV cut. The probability that we get a set of data, {data}, with N_C (N_B) events passing (failing) the PV cut for an assumed H is:

$$P(H|\{\text{data}\}) \propto H^{N_C} (1 - H)^{N_B}. \quad (7.9)$$

If $N_C = 0$, the most probable H is zero. We then calculated the number of background events according to Equation 7.8 and took the 90 % confidence interval as an uncertainty in the estimated number of background events.

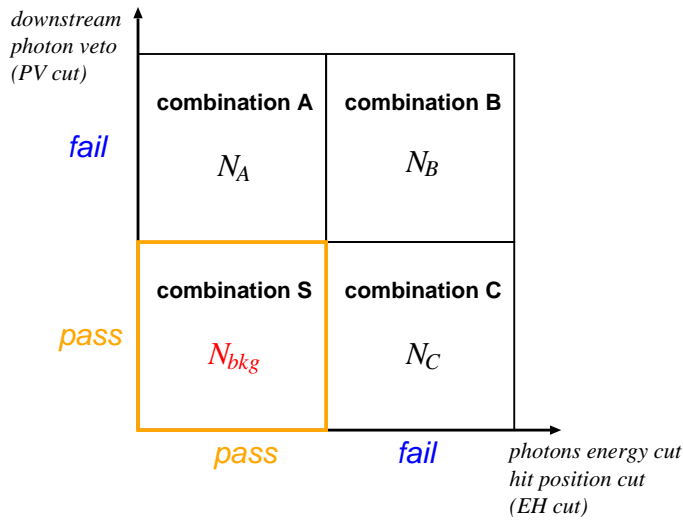


Figure 7.10: An illustration of the four cut combinations.

The numbers of the remaining “core neutron multiple π^0 ” background events in the signal region were $0.0^{+0.7}_{-0.0}$ and 1.5 ± 0.7 for the regions (3) and (4), respectively.

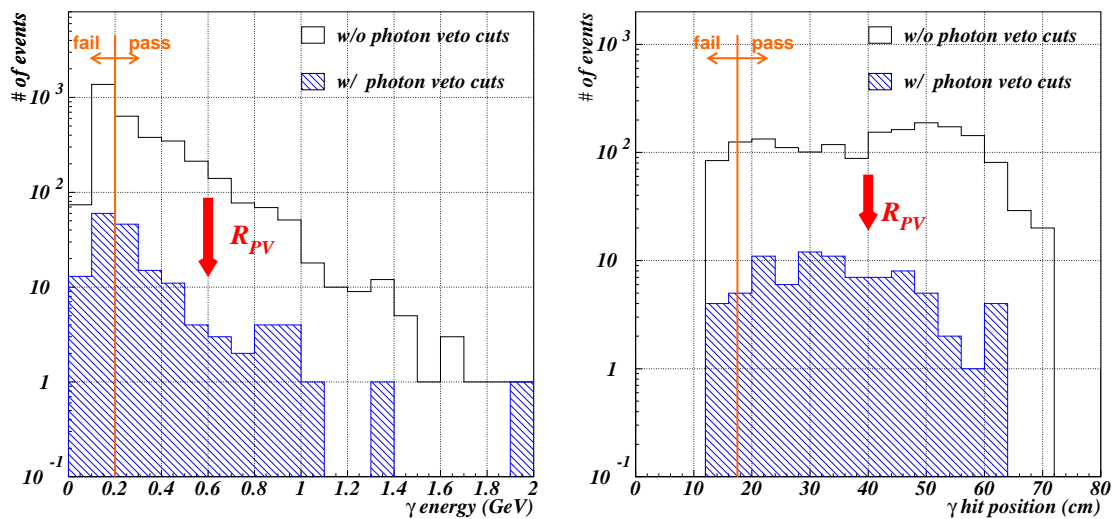


Figure 7.11: The distributions of the photon energy (left) and the hit position (right). Solid (dashed) shows the distribution before (after) the PV cut. The shape of both distributions did not depend on the PV cut.

Table 7.1: The list of the number of events in each cut combinations measured by the real data.

Region	N_A	N_B	N_C	N_{bkg}
(2)	52	103	8	4.0 ± 1.6
(3)	39	129	0	$0.0^{+0.7}_{-0.0}$
(4)	53	183	5	1.5 ± 0.7
(5)	24	48	6	3.0 ± 1.4
(6)	39	165	13	3.1 ± 1.0
(7)	58	187	0	$0.0^{+0.7}_{-0.0}$
(8)	75	470	34	5.4 ± 1.1

7.2.2 Other backgrounds associated with neutron interactions

The decay vertex of the “core neutron single π^0 ” events and the “halo neutron CV” events were properly reconstructed at $Z_{\text{vtx}} = 550$ cm as shown in Fig. 7.12. Their contamination in the signal region was negligible assuming a Gaussian.

The number of the “core neutron η ” events was similarly estimated by extrapolating the distribution of Z_η , the decay vertex calculated by assuming the η mass. As a result, the number of the “core neutron η ” background events was estimated to be 0.4 ± 0.2 in the signal region.

The contamination of the “halo neutron CC02” events in the signal region was estimated as follows. First, we estimated the fraction of the two photons produced at CC02 reconstructed in the fiducial region, $300 \leq Z_{\text{vtx}}(\text{cm}) \leq 500$, using the data collected in the π^0 run with an Al plate inserted in the beam. Figure 7.14 shows the distributions of the reconstructed vertex, Z_{vtx} , assuming the π^0 mass, and P_T after applying the cuts on the photon veto detector as for the $K_L \rightarrow \pi^0 \nu \bar{\nu}$ analysis. Taking the ratio of the number of events in the region: $200 \leq Z_{\text{vtx}}(\text{cm}) \leq 300$, to the number of events in the fiducial region, the fraction of the events contaminating the fiducial region was $A = [3.5 \pm 0.4] \%$. We then estimated the number of events in the region (1) and (3).

region(1): there were 25 events in the side band region, $200 \leq Z_{\text{vtx}}(\text{cm}) \leq 300$ and $P_T \geq 0.24$ (GeV/c). Using the fraction A , the number of events in the region (1) was estimated as 0.88 ± 0.20 .

region(3): there was 1 event in the side band region, $200 \leq Z_{\text{vtx}}(\text{cm}) \leq 300$ and $0.12 \leq P_T(\text{GeV}/c) \leq 0.24$. Using the fraction A , the number of events in the region (3) was estimated as 0.04 ± 0.04 .

7.3 Summary of background estimation

In this section, we summarize the background estimation described so far. Table 7.2 lists the number of background events in each region. Here we only considered the $K_L \rightarrow \pi^0 \pi^0$

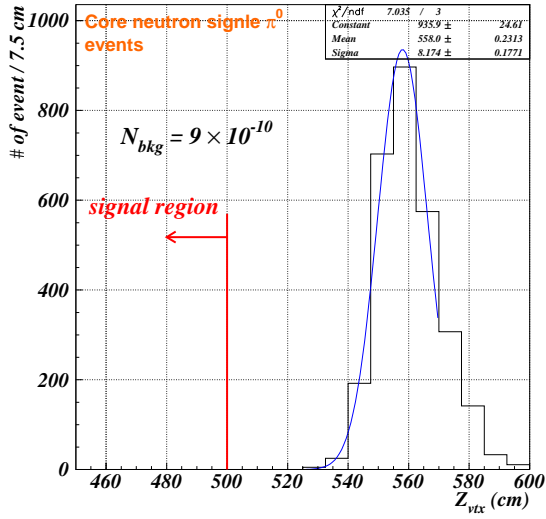


Figure 7.12: The Z_{vtx} distribution for the “core neutron single π^0 ” events and the “halo neutron CV” events where the Z_{vtx} was properly reconstructed. The contamination in the signal region was estimated by assuming a Gaussian shape.

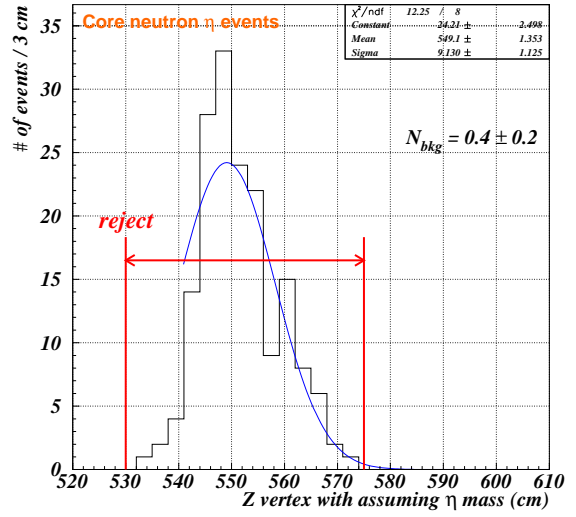


Figure 7.13: The distribution of the decay vertex assuming the η mass. Events in the region: $530 \leq Z_{\eta}(\text{cm}) \leq 575$ were removed by the η cut.

background for the K_L background because each background level from other K_L decay modes were less than 0.01.

The total number of background events in the signal region was estimated to be $0.4^{+0.7}_{-0.2}$ events in the region (3) and 1.5 ± 0.7 events in the region (4). The largest source came from the “core neutron η ” events in the region (3) and the “core neutron multiple π^0 ” events in the region (4). In almost all the regions, the contamination from the $K_L \rightarrow \pi^0\pi^0$ background was ~ 30 times smaller than the background associated with the neutron interactions.

7.4 The number of background events outside the signal region

In order to confirm our understanding of the background and the background estimation, we compared the number of events outside the signal region.

Figure 7.15 shows the distribution of the Z_{vtx} versus the P_T with all the selection cuts along with the observed and estimated number of events in each region. The estimated number of events in each region was consistent with the observed number of events.

Therefore, we conclude that we understand the backgrounds and their contributions. We will discuss the comparisons in the signal region in Chapter 9.

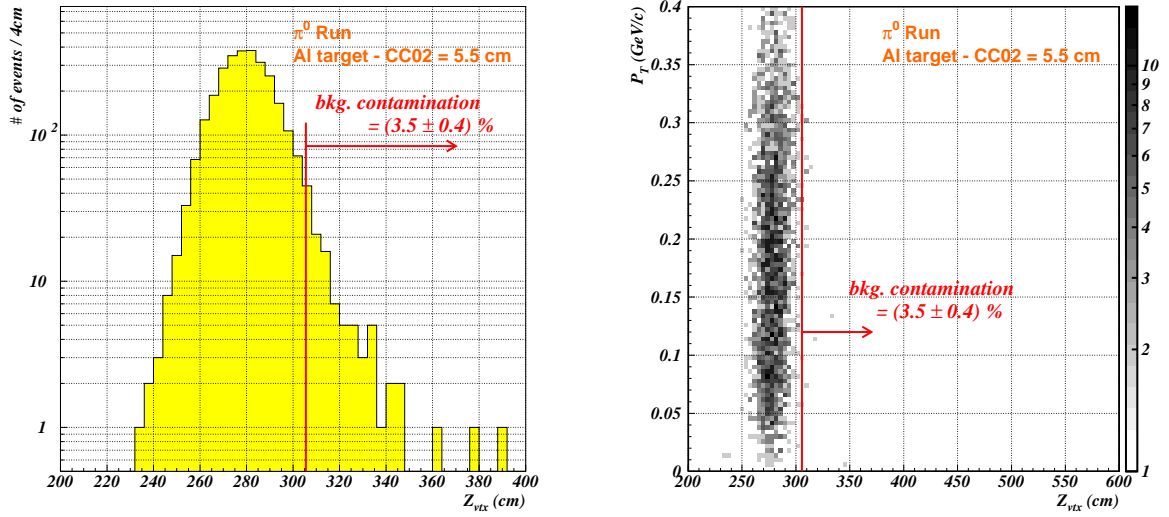


Figure 7.14: The distribution of the reconstructed vertex, Z_{vtx} , (left) and the transverse momentum, P_T (right) measured in the π^0 run with the Al target. We estimated the fraction of the event contamination in the fiducial region to be 3.5 ± 0.4 %.

Table 7.2: The list of the estimated number of background events in each region.

Background source	# of events	Background source	# of events
Region (1)		Region(2)	
halo neutron CC02	0.9 ± 0.2	core neutron multi. π^0	4.0 ± 1.6
Total	0.9 ± 0.2	Total	4.0 ± 1.6
Region (3)		Region(4)	
core neutron η	0.4 ± 0.2	core neutron multi. π^0	1.5 ± 0.7
core neutron multi. π^0	$0.0^{+0.7}_{-0.0}$	$K_L \rightarrow \pi^0\pi^0$	0.04 ± 0.03
halo neutron CC02	0.04 ± 0.04	Total	1.5 ± 0.7
Total	$0.4^{+0.7}_{-0.2}$	Total	1.5 ± 0.7
Region (5)		Region(6)	
core neutron multi. π^0	3.0 ± 1.4	core neutron multi. π^0	3.1 ± 1.0
$K_L \rightarrow \pi^0\pi^0$	0.01 ± 0.01	$K_L \rightarrow \pi^0\pi^0$	0.07 ± 0.05
Total	3.0 ± 1.4	Total	3.2 ± 1.0
Region (7)		Region(8)	
core neutron multi. π^0	$0.0^{+0.7}_{-0.0}$	core neutron multi. π^0	5.4 ± 1.1
$K_L \rightarrow \pi^0\pi^0$	0.1 ± 0.1	$K_L \rightarrow \pi^0\pi^0$	0.2 ± 0.1
Total	$0.1^{+0.7}_{-0.1}$	Total	5.6 ± 1.1

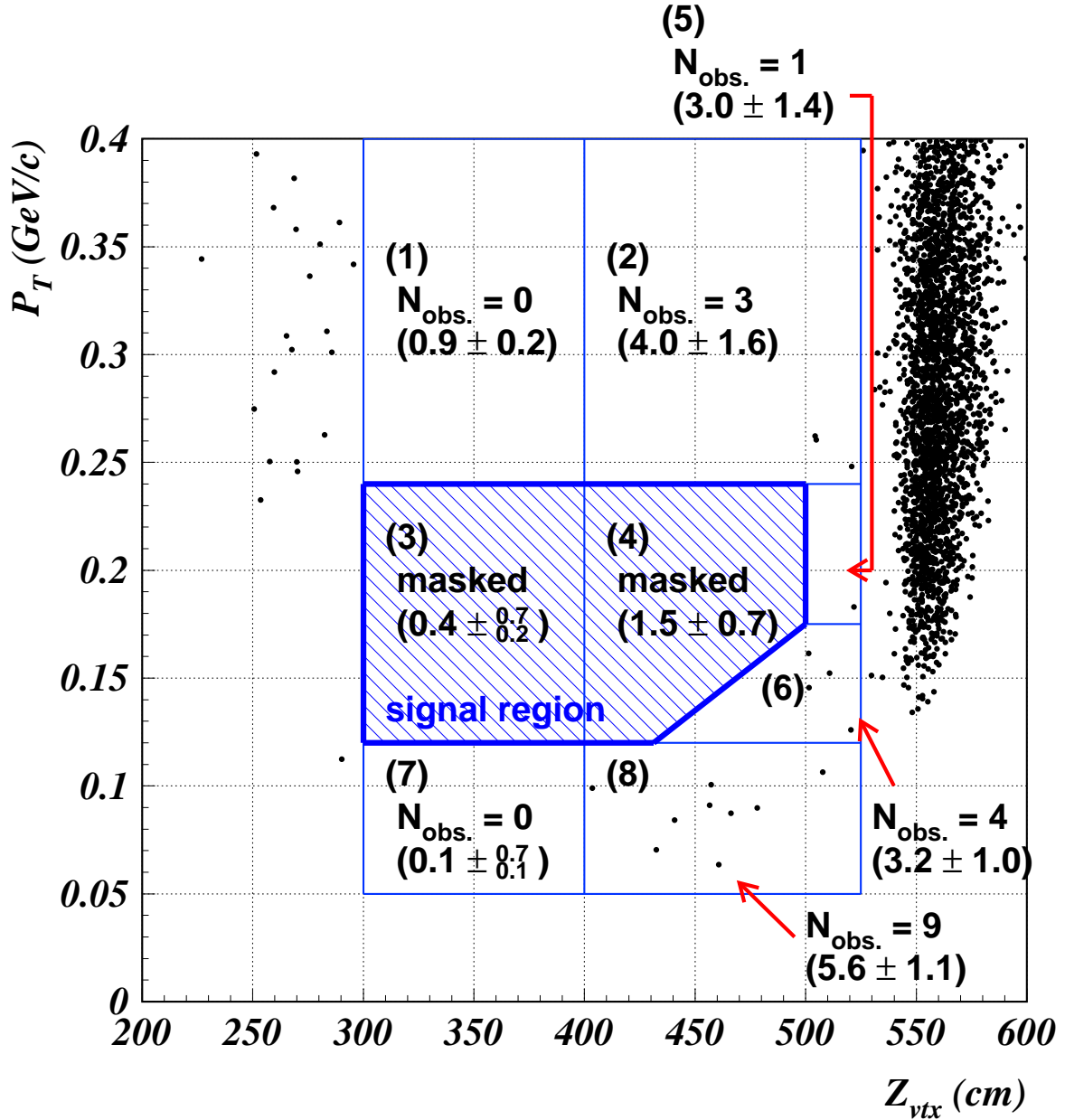


Figure 7.15: The Z_{vtx} versus P_T with all the event selection cuts. The number of events observed ($N_{obs.}$) and expected (in bracket) for the all the regions except for the signal region are shown.

Chapter 8

Systematic Errors

Before discussing the final result, we will summarize the systematic uncertainties on the Single Event Sensitivity (SES) in this search.

Using the variables defined so far,

$$\text{SES} = Br(K_L \rightarrow \pi^0 \pi^0) \times \frac{A_{2\pi^0}}{A_{sig}} \times \frac{1}{n_{2\pi^0}^{obs}}. \quad (8.1)$$

The uncertainties on the SES came from three components:

1. systematic uncertainties on the branching ratio of the $K_L \rightarrow \pi^0 \pi^0$,
2. systematic uncertainties on the acceptance ratio, $A_{2\pi^0}/A_{sig}$, and
3. statistical uncertainty in the observed number of the normalization mode, $n_{2\pi^0}^{obs}$.

For the first item, we will summarize the branching ratio and its error in Section 8.1. The second item was caused by a discrepancy between data and MC. A detailed description for the second item is given in Section 8.2. In addition, we defined the statistical error in the acceptances as a part of the systematic error in the SES, as explained in Section 8.3. Finally, we will summarize the systematic uncertainties in Section 8.4.

8.1 Branching ratio

The branching ratio of the $K_L \rightarrow \pi^0 \pi^0$ are [5]:

$$Br(K_L \rightarrow \pi^0 \pi^0) = [8.83 \pm 0.08] \times 10^{-4}. \quad (8.2)$$

We thus assigned 0.9 % as systematic uncertainty in the SES.

8.2 Acceptance ratio

The acceptance for both the $K_L \rightarrow \pi^0 \nu \bar{\nu}$ signal mode (A_{sig}) and the $K_L \rightarrow \pi^0 \pi^0$ normalization mode ($A_{2\pi^0}$) mode were evaluated with the MC. Therefore, the discrepancy between the data

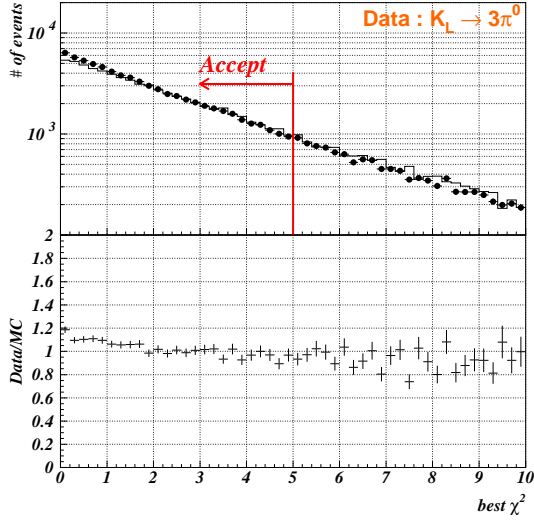


Figure 8.1: Top: The distribution of the vertex χ^2 of $K_L \rightarrow \pi^0 \pi^0 \pi^0$ decays. Dots show data and histogram shows MC. Bottom: The ratio of data and MC.

and the MC in the distributions of quantities used in the selection cuts can introduce an error in the acceptances. In order to keep the systematic uncertainty in the $A_{2\pi^0}/A_{sig}$ small, we made the event selection cuts for the signal and the normalization mode as similar as possible, so that many of the effects of the discrepancy cancel out in the ratio. However, the different final states, two photons for the $K_L \rightarrow \pi^0 \nu \bar{\nu}$ signal mode vs. four photons for the $K_L \rightarrow \pi^0 \pi^0$ normalization mode, caused some systematic uncertainties in $A_{2\pi^0}/A_{sig}$.

8.2.1 Different reconstruction methods

We reconstructed K_L vertexes for the normalization mode¹, while we reconstructed π^0 vertexes for the signal mode. In the $K_L \rightarrow \pi^0 \pi^0$ reconstruction, we applied a cut on the vertex χ^2 . However, since there is a small discrepancy in the vertex χ^2 distribution between data and MC, we could not correctly estimate the signal survival probability for the vertex χ^2 cut using the MC.

We evaluate the systematic uncertainty caused by this difference using the distribution of the vertex χ^2 measured with $K_L \rightarrow \pi^0 \pi^0 \pi^0$ decays because this samples had no background contamination. Figure 8.1 shows the distribution of the vertex χ^2 for $K_L \rightarrow \pi^0 \pi^0 \pi^0$ decays in data and MC. We found 3 % difference in the fraction of events that passed the vertex χ^2 cut between MC and data. We assumed that the same fraction for $K_L \rightarrow \pi^0 \pi^0$ decays also has an uncertainty of 3 %, and then assigned it as a systematic uncertainty in the SES.

¹A detailed description is given in Appendix B.

Table 8.1: The shift in the Γ_{00}/Γ_{000} due to the energy fluctuation of MB detector.

What is changed	Change	Shift in Γ_{00}/Γ_{000}
MB inner thr.	-10 %	-4.2 %
MB inner thr.	+10 %	+1.5 %
MB outer thr.	-10 %	-0.1 %
MB outer thr.	+10 %	+0.2 %

8.2.2 Discrepancy in Γ_{00}/Γ_{000}

The discrepancy in the ratio of the number of $K_L \rightarrow \pi^0\pi^0$ decays to the $K_L \rightarrow \pi^0\pi^0\pi^0$ decays, Γ_{00}/Γ_{000} , mostly came from the mismatch between data and MC in the transverse shower shape of the photon and the energy distribution in MB detector. We considered these effects on the SES.

Transverse shower shape of photons

We required that the transverse shower shape is consistent with a photon by using several quantities in the photon identification and the shower shape cut. However, some signal survival probabilities for these selection cuts were different from the MC estimation. For example, the probability for the shower shape cut measured with $K_L \rightarrow \pi^0\pi^0\pi^0 \rightarrow 6\gamma$ decays differed by 4.53 ± 0.05 %.

Even though we applied almost the same selection cuts on the signal and normalization modes, and took the acceptance ratio, the differences in the signal survival probabilities for the photon identification and the shower shape cut could arise because of the different number of photons in the final states. The Γ_{00}/Γ_{000} shifted by 4 % if the photon identification and the shower shape cuts were applied. Therefore, we assumed that the uncertainty in $A_{2\pi^0}/A_{sig}$ is also 4 % due to the photon identification and the shower shape cuts.

Energy distribution of MB detector

We found the mismatch between data and MC in the energy distribution in MB detector. This caused some errors in the acceptance of $K_L \rightarrow \pi^0\pi^0$ and $K_L \rightarrow \pi^0\pi^0\pi^0$ decays because there were some activities in the MC due to the shower-splash-back from the CsI calorimeter. Even though we applied the same cut on both decay modes, this difference did not cancel out in the Γ_{00}/Γ_{000} .

We varied the energy threshold by ± 10 % to cover accuracy of calibrations. Table 8.1 summarizes the variation in the Γ_{00}/Γ_{000} when we changed the threshold on the inner MB module and the outer MB module. By adding each shift in quadrature, we get a 4.2 % uncertainty in Γ_{00}/Γ_{000} . Assuming that the same effect applies to $A_{2\pi^0}/A_{sig}$, we assigned a systematic uncertainty of 4.2 % in $A_{2\pi^0}/A_{sig}$.

8.2.3 The energy measurement by the CsI calorimeter

Furthermore, we consider a systematic uncertainty in the acceptance ratio caused by the accuracy of the energy measurement with the CsI calorimeter. The photon energy was used in several variables: the decay vertex, the transverse momentum, the π^0 projection length etc.. Uncertainty in the energy calibration of CsI crystals produces an uncertainty in the signal survival probabilities of those selection cuts.

We estimated that we understand the CsI energy calibration to $\pm 3\%$, based on the monitoring of MIP peaks. When we shifted the energy scale by $\pm 3\%$ in MC, the $A_{2\pi^0}/A_{sig}$ changed by 1.4%. We assigned it as a systematic uncertainty in the $A_{2\pi^0}/A_{sig}$.

8.3 Statistical uncertainty

The additional uncertainty in the acceptance ratio was the statistical uncertainty. The error on the A_{sig} consists of the statistical uncertainty of the MC and the data. The statistical uncertainty of the MC was 1.2%. We used data to evaluate the survival probabilities for the particular three selection cuts: (a) cut on the timing dispersion on the photons, (b) cut on the hit timing difference between two photons, and (c) photon veto cut on the BA. The statistical uncertainties were 0.8%, 0.5% and 1.9% for the cut (a),(b) and (c), respectively. Adding these uncertainties in quadrature, we assigned a SES systematic uncertainty of 2.4%.

The statistical uncertainty of 0.5% in the $A_{2\pi^0}$ came from the MC statistics error and it was assigned a SES systematic uncertainty.

The statistical uncertainty came from the observed number of events of the normalization mode. We observed 2081 $K_L \rightarrow \pi^0\pi^0$ decays as described in Section 6.4, hence the statistical uncertainty was 2.2%.

Table 8.2 lists the statistical uncertainties in the $K_L \rightarrow \pi^0\nu\bar{\nu}$ signal, $K_L \rightarrow \pi^0\pi^0$ normalization mode and the observed normalization mode events.

8.4 Summary

The systematic uncertainties in the SES are summarized in Table 8.3. We assigned the total systematic uncertainty of 7.0% on the SES.

The large source of the systematic uncertainty came from the mismatch between data and MC in the transverse shower shape of the photon and the energy distribution in MB detector.

Table 8.2: The list of the statistical uncertainty in the acceptance estimation and the observed number of normalization mode, $K_L \rightarrow \pi^0 \pi^0$ decay. A detailed description of the acceptance estimation is given in Section 6.3.

source	size
$K_L \rightarrow \pi^0 \nu \bar{\nu}$ MC statistics	1.2 %
$\epsilon_{(a)}$ (Data stat.)	0.8 %
$\epsilon_{(b)}$ (Data stat.)	0.5 %
$\epsilon_{(c)}$ (Data stat.)	1.9 %
A_{sig} total statistical uncertainty	2.4 %
$K_L \rightarrow \pi^0 \pi^0$ MC statistics	0.5 %
$A_{2\pi^0}$ total statistical uncertainty	0.5 %
the observed number of $K_L \rightarrow \pi^0 \pi^0$ decays ($n_{2\pi^0}^{obs}$)	2.2 %

Table 8.3: The systematic and statistical uncertainties in the SES.

source	size (%)
$Br(K_L \rightarrow \pi^0 \pi^0)$ branching ratio	0.9
different reconstruction	3.0
transverse shower shape	4.0
MB energy distribution	4.2
stat. error for the A_{sig}	2.4
stat. error for the $A_{2\pi^0}$	0.5
Total systematic error	7.0
Statistical error	2.2

Chapter 9

Result and Discussion

All the analysis procedures have been carried out so far. In this chapter, we will describe the result of this search for the $K_L \rightarrow \pi^0 \nu \bar{\nu}$ decay. Section 9.1 describes the comparison of the remaining events with all the selection cuts between the data and the MC. Section 9.2 gives the result of this search. We will discuss this result in Section 9.3.

9.1 Data with all event selection cuts

All the event selection cuts described in Chapter 6 were performed on the two-photon event samples to suppress the number of background events. We estimated the remaining number of background events in both the signal region and outside the signal region. The expected number of background events outside the signal region was consistent with the observed number of background events. The number of background events in the signal box was estimated to be $1.9_{-0.7}^{+1.0}$ events in total, which mostly came from the core neutron background.

Figure 9.1 shows the distribution between the Z_{vtx} and the P_T with the all selection cuts. We observed no events in the signal box. This result was consistent with the background estimation.

9.2 Result

The Single Event Sensitivity (SES) in this search is:

$$\text{SES} = [9.11 \pm 0.20_{(\text{stat.})} \pm 0.64_{(\text{syst.})}] \times 10^{-8} . \quad (9.1)$$

Since no $K_L \rightarrow \pi^0 \nu \bar{\nu}$ events were observed, we set a new upper limit of the branching ratio:

$$\text{Br}(K_L \rightarrow \pi^0 \nu \bar{\nu}) < 2.10 \times 10^{-7} , \quad (9.2)$$

at the 90 % confidence level (C.L.)¹. We improved the current limit on the branching ratio [20] with a factor 2.8.

¹We calculated Equation 9.2 with the Poisson mean for the 90 % confidence level upper limit, $\mu = 2.3$ without regard for the number of background events. On the other hand, we calculated another upper limit with taking

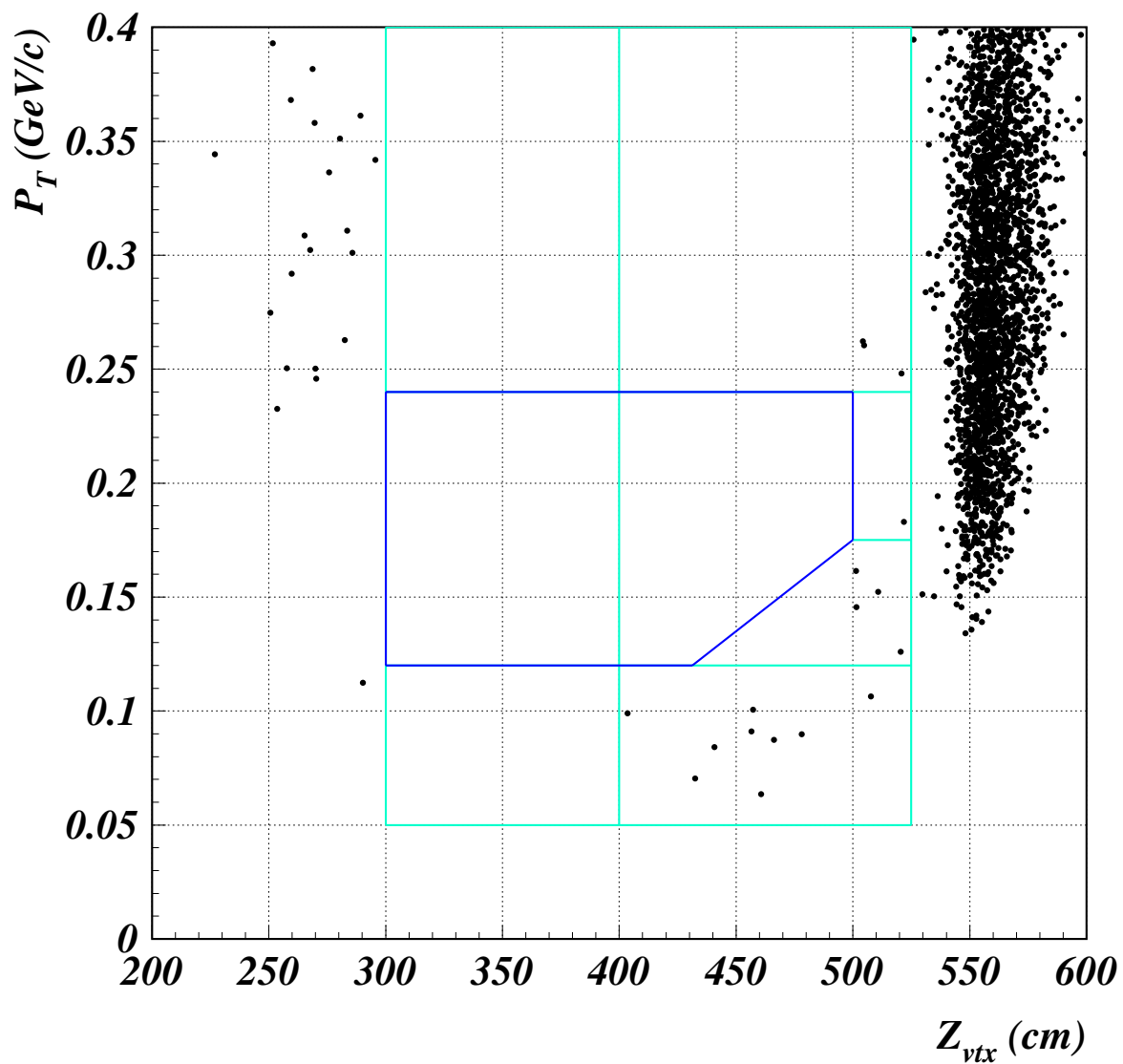


Figure 9.1: The 2-dimensional plot between Z_{vtx} and P_T with all the event selection cuts.

9.3 Discussion on physics

Observing no $K_L \rightarrow \pi^0 \nu \bar{\nu}$ events with the SES of 9×10^{-8} is consistent with the Standard Model prediction. This result did not play an important role to constrain the interesting CP violation phase in the Standard Model because it only led an upper limit, $\eta < 28$ at the 90 % C.L., according to Equation 1.34 while the current value is $\eta = 0.34$ [5].

We came closer to the Grossman-Nir limit improving the upper limit on $Br(K_L \rightarrow \pi^0 \nu \bar{\nu})$ with a factor 2.8 using only 10 % of data taken in the first period of E391a experiment. The SES is 64 times larger than the Grossman-Nir limit. As we will describe below, we can improve this difference in further analysis in the E391a experiment and future experiments.

9.4 Discussion on the model in Monte Carlo simulation

To estimate the signal acceptance, we used a Monte Carlo simulation (MC) as described in Chapter 4. In MC, we assumed V-A interaction in $K_L \rightarrow \pi^0 \nu \bar{\nu}$ decay. The π^0 energy is according to Equation 4.3. If we did not assume V-A interaction, the π^0 energy is according to three body phase space. As shown in Fig. 9.2, the distributions of π^0 energy is different. Since we selected higher P_T , the signal acceptance without V-A interaction decrease 10 %. If we use the signal acceptance without V-A interaction, $Br(K_L \rightarrow \pi^0 \nu \bar{\nu}) < 2.33 \times 10^{-7}$ at 90 % C.L.

9.5 Discussion from experimental point of view

We carried out the first dedicated search for the $K_L \rightarrow \pi^0 \nu \bar{\nu}$ decay. The purpose of this search was to establish the experimental method for the next higher sensitivity experiment to observe the $K_L \rightarrow \pi^0 \nu \bar{\nu}$ decay. As described in Chapter 2, the new detection methods were:

- require two and only two photons in the final state,

and with mainly three approaches:

- detect all extra photons with the hermetic detector system,
- make the neutral beam clean and narrow, and
- place detector in the vacuum.

In this section, we will discuss our experimental approaches and conclude that it is possible to search for $K_L \rightarrow \pi^0 \nu \bar{\nu}$ decay in future experiments with our approaches.

the estimated number of background events into account:

$$Br(K_L \rightarrow \pi^0 \nu \bar{\nu}) < 1.03 \times 10^{-7}, \quad (9.3)$$

at the 90 % C.L. using Feldman-Cousins prescription [37]. However, we finally set the upper limit as Equation 9.2 because the uncertainty of the estimated number of background events was large. A detailed discussion of this limit is given in Appendix C.

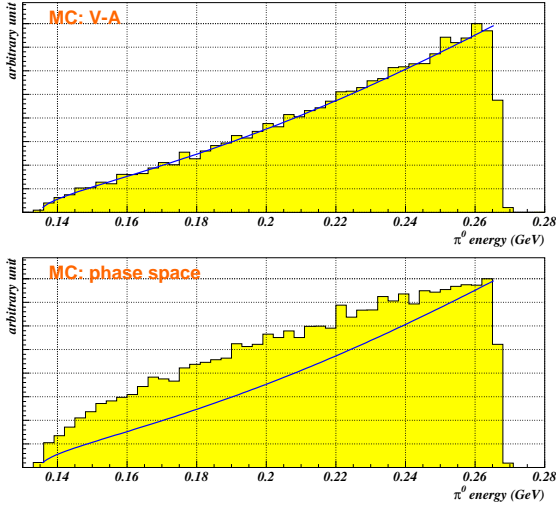


Figure 9.2: Top : The distribution of π^0 energy in MC when we assumed V–A interaction in $K_L \rightarrow \pi^0 \nu \bar{\nu}$ decay. The blue line shows Equation 4.3. Bottom : The distribution of π^0 energy in MC when we did not assume V–A interaction. The π^0 energy is according to three body phase space.

9.5.1 Detection method

In this search, we defined the signal of $K_L \rightarrow \pi^0 \nu \bar{\nu}$ decay as the event where two photons and no other particles are detected in the final state. Although there were unexpected single π^0 background from the core neutron interaction, we were able to reject it by the vertex cut. $K_L \rightarrow \gamma\gamma$ decay was the only other K_L decay with only two photons in the final state, but we were able to discriminate $K_L \rightarrow \pi^0 \nu \bar{\nu}$ decay from $K_L \rightarrow \gamma\gamma$ decay by requiring a finite P_T . Other background sources we found in this search had extra photons and/or charged particles, thus we were able to suppress them by applying the cuts on the photon veto detectors and the charged veto detectors, except for the core neutron background. As will be described later, we fixed the membrane to remove the core neutron background in the subsequent E391a runs.

Therefore, we found no problem with this detection method requiring only two photons with high P_T .

9.5.2 Background

For the core neutron background, we fixed the membrane to the correct position and ran the second and third period of data taking in E391a experiment (E391a Run-II and Run-III). Although the analysis of this data is still on going, in Fig. 9.3, we show the Z_{vtx} distributions after online trigger requirements for both the data used in this search and Run-II. The number of events are normalized by the number of K_L decays. The events in the upstream section, $200 \simeq Z_{\text{vtx}}(\text{cm}) \simeq 400$, consist of the $K_L \rightarrow \gamma\gamma$ decays because we reconstructed Z_{vtx} assuming the π^0 mass, and their amounts are more or less consistent with each other. On the other hand, the number of events at $z = 550$ cm decreased by a factor 4. We expect that the core neutron backgrounds will not be a big issue in the data from the Run-II.

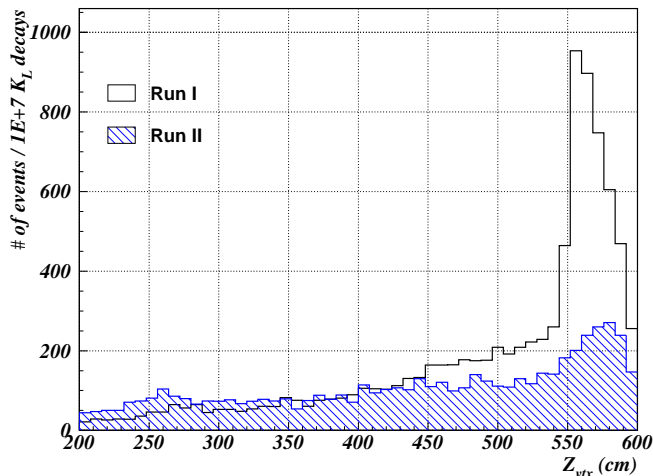


Figure 9.3: The distribution of the reconstructed decay vertex (Z_{vtx}) after online requirements for data taken in the first period (solid) and taken in the second period (dashed). The distributions are normalized by the expected number of K_L decay.

Furthermore, with no core neutron background, we can remove several event selection cuts applied to suppress the core neutron background. For example, if we remove the η cut, the π^0 projection length cut, and the $P_T - Z_{\text{vtx}}$ correlation cut, we gain 55 % in the signal acceptance.

We will discuss the halo neutron background and the $K_L \rightarrow \pi^0\pi^0$ background in following subsections.

9.5.3 Hermetic photon veto

Since the remaining number of $K_L \rightarrow \pi^0\pi^0$ background events was estimated to be 0.04 events, we conclude that the hermetic photon veto worked well in this search.

Based on the MC study, we can suppress the $K_L \rightarrow \pi^0\pi^0$ background furtherly improving the photon detection inefficiency of MB and BA in future experiments. For example, we can improve the photon detection inefficiency caused by the punch through effect by increasing the detector thickness. Considering Equation 2.5, additional $3 X_0$ for the MB detector improves the photon inefficiency with a factor 10. Moreover, we are now studying several types of BA detector in order to improve photon inefficiency.

On the other hand, only 36 % of the signal remained after the cuts on the photon veto detector, as described in Section 6.2.1. The largest loss was caused by the cut on MB detector, in which only 60 % of the signal remained after the cut. Based on the MC study, we found that the cut on MB removed 18 % of the signal because shower-splash-back from the CsI calorimeter deposited their energies in the MB. In addition, a 27 % of signal was lost due to the accidental activities in MB detector because we did not apply any timing window cut. Based on data, the accidental rate in the overall MB is 1.6 MHz with the energy deposit greater than 1 MeV. Moreover, we expect that the accidental rate will increase as the K_L flux increases in future experiments. In order to reduce those signal loss, we need a good timing resolution for MB, and apply a narrow timing window cut such as ± 5 nsec.

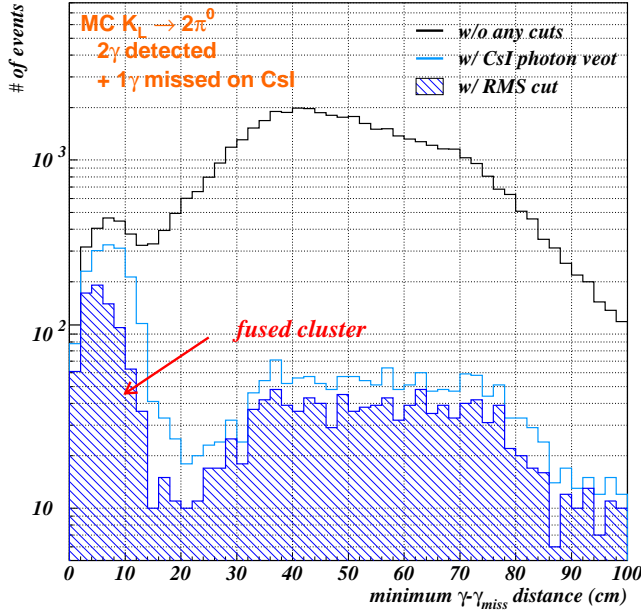


Figure 9.4: The MC distribution of the distance between a missed photon and the nearest photon cluster for two photon-cluster event samples in $K_L \rightarrow \pi^0\pi^0$ decays. The histograms show the events without any cuts (solid), with the photon veto cut on CsI (blue solid), and with the shower shape cut, “RMS cut”, (blue dashed).

In terms of the $K_L \rightarrow \pi^0\pi^0$ background, we also considered the probability of having fused clusters in the CsI calorimeter. Figure 9.4 shows the MC distribution of the distance between a missed photon and the nearest two photon-cluster event samples in $K_L \rightarrow \pi^0\pi^0$ decays. Even though we applied the cut on the shower shape (“RMS cut”), there are events in which the distance is less than 14 cm.

In order to suppress the probability of having fused clusters, we should use CsI crystals with a smaller cross section to see detailed transverse shower shape and identify fused clusters with such as “RMS”.

Neutral beam

A new technique in the experiment is the very narrow and small halo (clean) K_L beam, and it worked well. The beam size was 8 cm at 16 m downstream from the target. Even with such narrow K_L beam, the number of K_L 's per 2.5×10^{12} protons² was 7×10^5 .

We also succeeded in making a clean beam whose rate is 10^{-5} times the core component. The number of background events where a π^0 was produced by halo neutrons hitting CC02, was negligible in this search. In the future experiments, we can suppress the number of halo neutron background events in two ways. One is to add more collimators to suppress the beam halo. Another is to move CC02 farther from the fiducial region. For example, assuming the same background shape as shown in Fig. 7.14, if we move the CC02 40 cm upstream, we can

²This number typically corresponds to one pulse deliver from the KEK-PS.

Table 9.1: Summary of the E391a experiment. Run-I, Run-II and Run-III are the first, second and third period of the data taking, respectively. “abs.” means a short of the absorber. We fixed the membrane before stating the Run-II.

	period	# of K_L decay	abs.	comments
Run-I	Feb., '04 – Jul., '04	1.6×10^{10}	Pb abs.	same condition
Run-II	Mar., '05 – Apr., '05	3×10^9	Be,Pb abs.	CC00 + fixed TDC stop
Run-III	Nov., '05 – Dec., '05	3×10^9	Be,Pb abs.	+ new BA

reduce the halo neutron background events to 0.2 events at the sensitivity as of the Standard Model prediction.

Detector in the vacuum

We put most of the detector components in vacuum. The detector worked well without any serious troubles. We also achieved the high vacuum of 10^{-5} Pa in the fiducial region. A fact that the membrane was partially hanging in the beam was an error, and we fixed this problem by changing the support for the membrane. Therefore, the use of the membrane, which is new idea, also worked well.

9.6 Further $K_L \rightarrow \pi^0 \nu \bar{\nu}$ search

The new result was obtained from 10 % of data taken in the first period of E391a experiment. In following paragraphs, we first describe a prospect of the result from E391a experiment. Next, we describe $K_L \rightarrow \pi^0 \nu \bar{\nu}$ experiments in the future.

Prospect of E391a experiment

The E391a experiment ran until December 2005 in three data taking periods, Run-I, Run-II and Run-III, as shown in Table 9.1.

Run-I was carried out with completely the same condition as this search. We need further background suppression for the analysis of the remaining data taken in the Run-I, because there still are core neutron backgrounds.

Before starting Run-II, we fixed the membrane to the correct position. In addition, we also made following changes based on what learned in this search.

1. Installed a new detector, CC00, at the end of the neutral beam line in order to reduce the number of halo neutrons.
2. Installed a Be absorber in the beam in order to reduce accidental activities on BA.
3. Shortened TDC stop signal from 80 nsec to 20 nsec to reduce losing photon hits in the cut on BA, etc..

For Run-III, we installed a new BA with additional transverse segmentation to improve the photon identification in the BA.

For the data taken in the Run-II and Run-III, we expect smaller background. Also we expect to improve the signal acceptance up to a few % by improving selection cuts.

As a prospect of the E391a experiment, we expect the final single event sensitivity with all the collected data to be close to the Grossman-Nir limit.

Future $K_L \rightarrow \pi^0 \nu \bar{\nu}$ experiment

As described in Chapter 1, our final goal is to discover $K_L \rightarrow \pi^0 \nu \bar{\nu}$ decay and explore new origin of the CP violation. Based on things we learned in this search, and will be learned from further analysis in the E391a experiment, we take the next step to achieve the goal. We will start an experiment at Japan Proton Accelerator Research Complex (J-Parc).

The high power proton accelerator at J-Parc enables us to generate a high intensity K_L beam. The generated number of K_L is expected to be $\sim 1 \times 10^8$ per a pulse. Each pulse contains 3×10^{14} protons with a 30 GeV/c in kinetic energy. One of the features of the J-Parc $K_L \rightarrow \pi^0 \nu \bar{\nu}$ experiment is a cleaner K_L beam with the ratio of neutron to K_L ratio (n/K_L) of 10, compared to 60 in the E391a. This small n/K_L ratio can be made by the high energy proton beam and a larger target angle. It would reduce contaminations of the beam neutron backgrounds.

In the beginning of the J-Parc $K_L \rightarrow \pi^0 \nu \bar{\nu}$ experiment, the E391a detector will be used again with some modifications. One of them is the CsI calorimeter. We plan to use long CsI crystals ($25X_0$ in longitudinal length) instead of current one ($16X_0$). It reduces the photon inefficiency due to the punch through effect where the photon passes through the detector without any interaction. Also we will have fine segmentation. The size of new CsI crystals is $2.5 \times 2.5 \text{ cm}^2$ ($5 \times 5 \text{ cm}^2$ for outer region of the calorimeter) instead of the current $7 \times 7 \text{ cm}^2$. It enables us to identify fused-clusters because we can know a detailed transverse distribution of the photon's shower. Another modification is to increase the thickness of the MB detector by $3 \sim 5X_0$ in order to reduce the photon inefficiency due to the punch through effect.

With these modifications, we expect the sensitivity to be $O(10^{-12})$ with the signal to background ratio of 1.1. Furthermore, we plan to build new beam line and a detector in order to study the $K_L \rightarrow \pi^0 \nu \bar{\nu}$ decay with a sensitivity of $O(10^{-13})$.

Chapter 10

Conclusion

We performed the first dedicated experiment to search for the $K_L \rightarrow \pi^0 \nu \bar{\nu}$ decay. We analyzed 10 % of data taken in the first period of E391a experiment. The Single Event Sensitivity of this search was $[9.11 \pm 0.20_{(\text{stat.})} \pm 0.64_{(\text{syst.})}] \times 10^{-8}$. No signal candidate events were observed while the expected number of background events was $1.9_{-0.7}^{+1.0}$. We set a new upper limit on the branching ratio of $K_L \rightarrow \pi^0 \nu \bar{\nu}$ decay:

$$Br(K_L \rightarrow \pi^0 \nu \bar{\nu}) < 2.10 \times 10^{-7} ,$$

at the 90 % confidence level. This represents an improvement of a factor 2.8 over the current limit [20].

We searched for the $K_L \rightarrow \pi^0 \nu \bar{\nu}$ decay requiring two photons and no other particles detected in the final state, and introduced new experimental methods to suppress several background sources. Based on this search, we led new understanding.

First, we understood the backgrounds. The core neutron background was a big issue in this search, but it would be suppressed by fixing the membrane. In the future experiments, we have to suppress the $K_L \rightarrow \pi^0 \pi^0$ background with two missing photons by improving detection inefficiency of the detector. The background by halo neutrons interacting with the detector material and producing one or more π^0 's must be reduced by modifying the beamline and detector configuration in the future experiments.

Second, we found several issues which we have to solve in the future experiments. One is “shower-splash-back” from the CsI calorimeter to the MB detector. Since it caused some signal loss, we must solve this issue by utilizing timing information. Another is “fused photon cluster” where two nearby photons overlap in the CsI calorimeter and are misidentified as one photon. We must solve this issue by using a fine segmented calorimeter to see the detailed transverse shower shape and identify such overlapping photons.

We conclude that, in the future high sensitive experiments, some modifications are necessary to search for $K_L \rightarrow \pi^0 \nu \bar{\nu}$ decay. Now, based on this new result, we will start next high sensitive experiment at J-Parc. We expect that this new result would be a large step on the path to discover $K_L \rightarrow \pi^0 \nu \bar{\nu}$ decay and explore new origin of the CP violation.

Appendix A

Identification of photon cluster

Some of the clusters found with the cluster finding process were accidental hits, charged particles, electronic noises, etc.. In order to identify clusters consistent with photon showers (“photon cluster”) from them, we applied the following four selection cuts on clusters:

1. cluster size,
2. cluster shape,
3. energy dispersion, and
4. timing dispersion.

Each selection cut was studied with $K_L \rightarrow \pi^0\pi^0\pi^0$ decays in data with six detected photons. The samples had no background contamination so that clusters on the CsI calorimeter were actual photons from the K_L decay.

A.1 Cluster size

In order to identify photons using the transverse cluster shape of the photon cluster, we cut on the size of the cluster. We defined two kinds of cluster sizes.

- *csize-5* : The number of CsI crystals with the energy deposit greater than 5 MeV,
- *csize-1* : The number of CsI crystals with the energy deposit greater than 1 MeV touching the cluster plus the number of CsI crystals with the energy deposit greater than 5 MeV.

An illustration of the *csize-5* and the *csize-1* is shown in Fig. A.1.

Figure A.2 and A.3 show the distributions of the *csize-5* and the *csize-1* as a function of the total energy deposit in the cluster, respectively, for the $K_L \rightarrow \pi^0\pi^0\pi^0$ decays. On the other hand, Fig. A.4 and A.5 show the distributions for events collected with a trigger requiring at least one hardware cluster. These data mostly consists of accidental hits, charged particles, electronic noises, etc.. There were small *csize-5* (*csize-1*) clusters in lower energy region. Therefore, We defined a threshold on the *csize-5* (*csize-1*) depending on the total energy deposit in the cluster, as listed in Table A.1.



$\text{csize-5} = 7$
 $\text{csize-1} = 10$

Figure A.1: A schematic drawing of the csize-5 and the csize-1.

Table A.1: The list of the requirements on the csize-5 and the csize-1 to identify clusters as photons.

Cluster energy region (GeV)	csize-5	csize-1
0.0 – 0.1	≥ 2	≥ 2
0.1 – 0.2	≥ 2	≥ 3
0.2 – 0.3	≥ 2	≥ 4
0.3 – 0.4	≥ 3	≥ 5
0.4 – 0.5	≥ 3	≥ 5
0.5 – 0.7	≥ 4	≥ 6
0.7 – 1.0	≥ 4	≥ 8
1.0 – 1.5	≥ 6	≥ 9
1.5 – 2.0	≥ 7	≥ 11
2.0 – 3.0	≥ 8	≥ 12
3.0 –	≥ 8	≥ 12

The 71 % of the $K_L \rightarrow \pi^0\pi^0\pi^0$ decays in data satisfied the cut on csize-5 and csize-1, which was consistent with the MC expectation. The MC study showed that 87 % of $K_L \rightarrow \pi^0\nu\bar{\nu}$ signal passes these cut.

A.2 Cluster shape

We defined a cluster-shape as the number of crystals sharing edges with the crystal with a maximum energy deposit. An illustration of the cluster-shape is shown in Fig. A.6. Crystals were required to have an energy deposit greater than 1 MeV.

Figure A.7 shows the distributions of the cluster-shape as a function of the csize-1. We defined a threshold on the cluster-shape depending on the csize-1, as listed in Table A.2. We

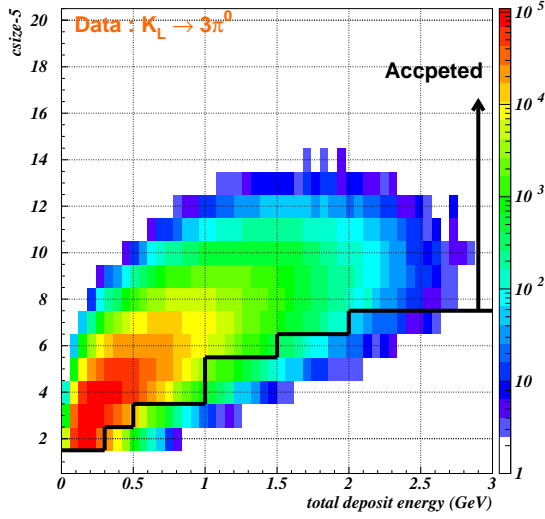


Figure A.2: The distribution of the csize-5 (horizontal axis) versus the cluster energy (vertical axis) for the $K_L \rightarrow \pi^0\pi^0\pi^0$ decays in data.

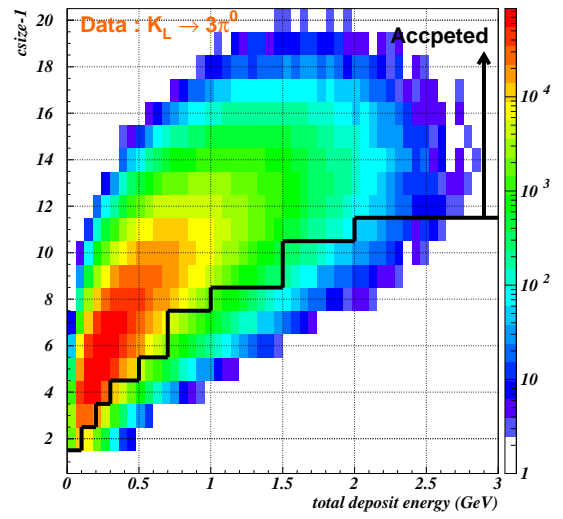


Figure A.3: The distribution of the csize-1 (horizontal axis) versus the cluster energy (vertical axis) for the $K_L \rightarrow \pi^0\pi^0\pi^0$ decays in data.

required the cluster-shape to accept more than 90 % of events in each bin.

The 91 % of the $K_L \rightarrow \pi^0\pi^0\pi^0$ decays in data satisfied the cut on the cluster-shape, which was consistent with the MC expectation. The MC showed that 97 % of the $K_L \rightarrow \pi^0\nu\bar{\nu}$ signal passes this cut.

A.3 Energy dispersion

We defined the energy dispersion, E_R , as:

$$E_R = \begin{cases} \frac{e_1}{E_{dep}} & N \leq 2 \\ \frac{e_1 + e_2}{E_{dep}} & N = 3 \\ \frac{e_1 + e_2 + e_3}{E_{dep}} & N \geq 4 \end{cases} \quad (\text{A.1})$$

where N is the number of the crystals with energies greater than 1 MeV in the cluster (equal to the csize-1), and E_{dep} is the total energy deposit in the cluster. The e_1 , e_2 and e_3 are

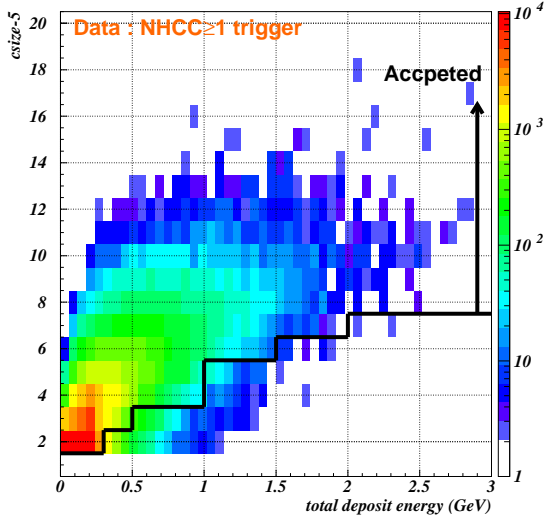


Figure A.4: The distribution of the $csize-5$ (horizontal axis) versus the cluster energy (vertical axis) for events collected with the trigger requiring at least one hardware cluster.

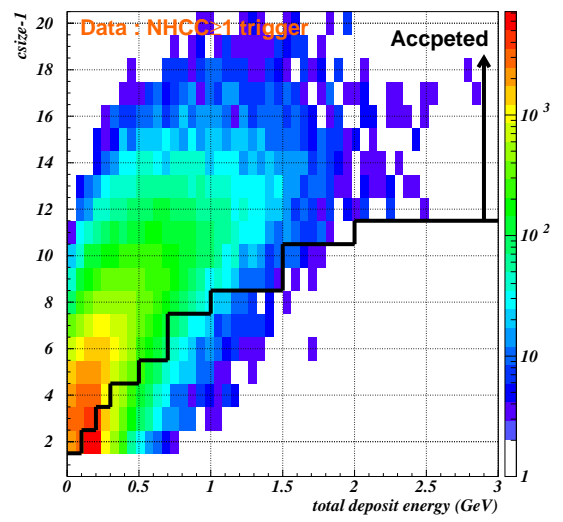


Figure A.5: The distribution of the $csize-1$ (horizontal axis) versus the cluster energy (vertical axis) for events collected with the trigger requiring at least one hardware cluster.

the largest, the second largest and third largest energy deposits in the crystals in the cluster, respectively.

Figure A.8 shows the distributions of the E_R as a function of the $csize-1$. We defined a threshold on the E_R depending on the $csize-1$, as listed in Table A.3, to accept more than 90 % of events in each $csize-1$ bin.

The 78 % of the $K_L \rightarrow \pi^0\pi^0\pi^0$ decays in data satisfied the cut on the E_R , which was consistent with the MC expectation. The MC showed the 93 % of the $K_L \rightarrow \pi^0\nu\bar{\nu}$ signal passes this cut.

A.4 Timing dispersion

We defined the timing dispersion, TDI:

$$TDI = \frac{1}{N} \sqrt{\sum_{\substack{i=1 \\ (e_i > 1\text{MeV})}}^N (T_i - T_m)^2}, \quad T_m \equiv \frac{1}{n} \sum_{\substack{i=1 \\ (e_i > 5\text{MeV})}}^n T_i \quad (\text{A.2})$$

where e_i is the energy deposit in each CsI crystal, n and N are the $csize-5$ and the $csize-1$, respectively, and T_m is the mean timing among the crystals in the cluster.

Table A.2: The list of the requirements on the cluster size: csize-5 and csize-1 to identify clusters as photons.

csize-1	cluster-shape	csize-1	cluster-shape
2	≥ 1	12	≥ 3
3	≥ 1	13	≥ 4
4	≥ 2	14	≥ 4
5	≥ 2	15	≥ 4
6	≥ 2	16	≥ 4
7	≥ 2	17	≥ 4
8	≥ 2	18	≥ 4
9	≥ 3	19	≥ 4
10	≥ 3	20	≥ 4
11	≥ 3	≥ 21	≥ 4

Table A.3: The list of the requirements on the energy dispersion, E_R , to identify clusters as photons.

csize-1	E_R	csize-1	E_R
2	≥ 0.53	12	≥ 0.89
3	≥ 0.56	13	≥ 0.89
4	≥ 0.62	14	≥ 0.89
5	≥ 0.72	15	≥ 0.89
6	≥ 0.82	16	≥ 0.89
7	≥ 0.87	17	≥ 0.89
8	≥ 0.89	18	≥ 0.88
9	≥ 0.89	19	≥ 0.87
10	≥ 0.90	20	≥ 0.88
11	≥ 0.89	≥ 21	≥ 0.88

Figure A.9 shows the distribution of the TDI obtained by the $K_L \rightarrow \pi^0\pi^0\pi^0$ data. We required the TDI to be less than 3. The 90 % of the $K_L \rightarrow \pi^0\pi^0\pi^0$ event samples passed this requirement.

Since the MC did not reproduce the TDI distribution, we estimated the signal loss with the real data. The number of reconstructed $K_L \rightarrow \pi^0\pi^0\pi^0$ ($K_L \rightarrow \pi^0\pi^0$) decays was reduced to 90 % (94%) with the TDI cut. Thus, the efficiency of the TDI cut per photon was $0.983 \pm 0.004_{(\text{stat.})}$ on average. Based on this value, we estimated the signal acceptance for the TDI cut to be 0.966 ± 0.008 . On the other hand, the TDI cut reduced the two photon event samples in the region, $300 \leq Z_{\text{vtx}}(\text{cm}) \leq 500$, by a factor of 0.778 ± 0.005 .

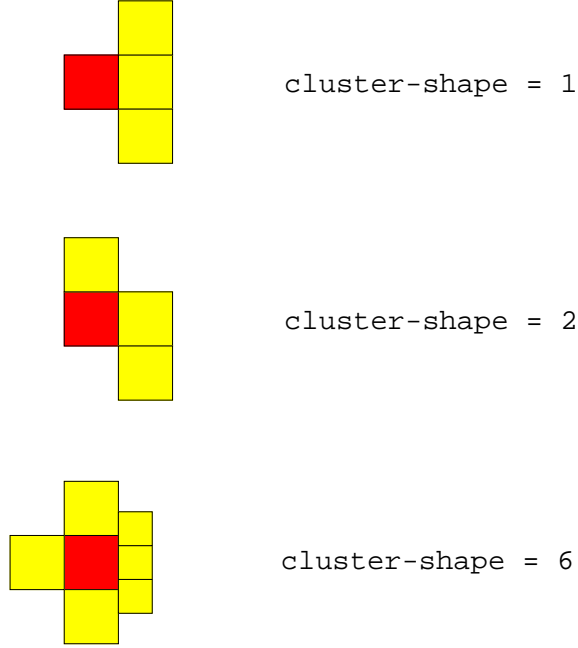


Figure A.6: A sketch of the cluster-shape. The red square indicates the crystal which had the maximum energy deposit in the cluster. Cluster-shape is the number of crystals sharing the edge with the crystal shown in red.

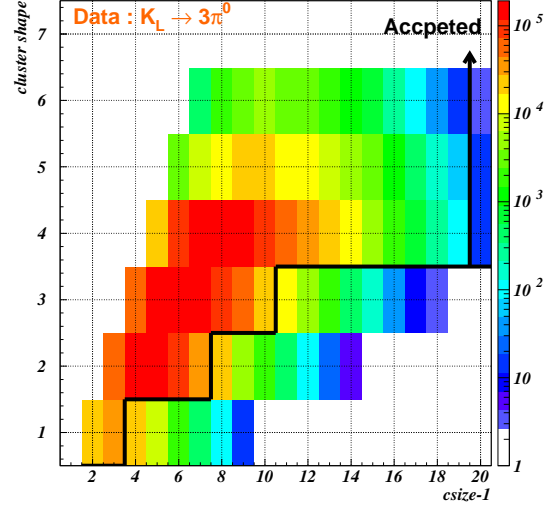


Figure A.7: The distribution of the cluster-shape versus the csz-1.

A.5 Summary

Table A.4 summarizes the survival probability for the $K_L \rightarrow \pi^0\pi^0\pi^0$ data, the $K_L \rightarrow \pi^0\pi^0\pi^0$ MC and the $K_L \rightarrow \pi^0\nu\bar{\nu}$ MC. In this table, we defined events in the region, $300 \leq \text{decay vertex (cm)} \leq 500$ and $0.47 \leq \text{invariant mass (GeV}/c^2) \leq 0.53$, as $K_L \rightarrow \pi^0\pi^0\pi^0$ decays. Also we defined two photon events in the region, $300 \leq Z_{\text{vtx}}(\text{cm}) \leq 500$ and $0.12 \leq P_T(\text{GeV}/c) \leq 0.25$, as the $K_L \rightarrow \pi^0\nu\bar{\nu}$ in the MC. Each cut efficiency by the $K_L \rightarrow \pi^0\pi^0\pi^0$ data was consistent with the MC prediction.

The result after applying these selection cuts on the two cluster data is also summarized in the Table A.4. In total, 70 % of two cluster events were removed by the photon identification cuts, while the signal loss was 22 %.

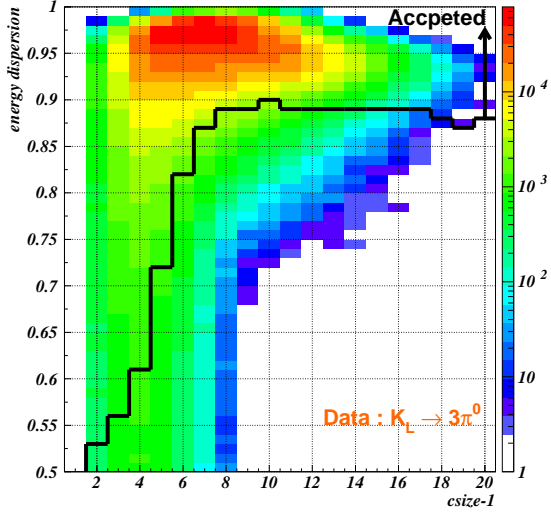


Figure A.8: The distribution of the energy dispersion versus the csizel-1.

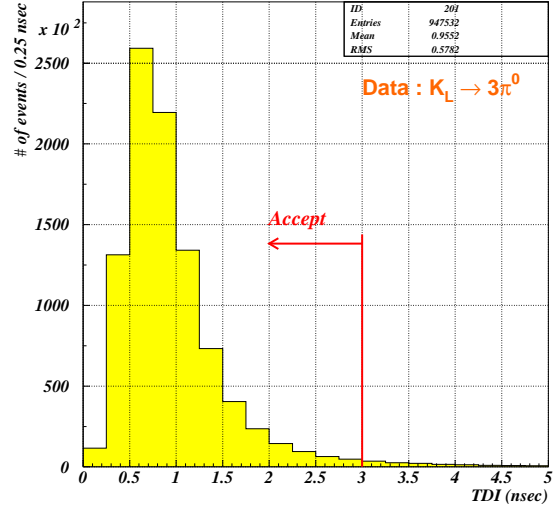


Figure A.9: The distribution of the timing dispersion for the $K_L \rightarrow \pi^0\pi^0\pi^0$ data.

Table A.4: The summary of the cut efficiency for each photon identification cut except for the cut on the TDI. The number for each cut in the upper two columns is the ratio: $N(\text{all cuts})/N(\text{all cuts except for the specific cut})$ for $K_L \rightarrow \pi^0\pi^0\pi^0$ events. The numbers in the column “ $K_L \rightarrow \pi^0\nu\bar{\nu}$ MC” are the ratio for $K_L \rightarrow \pi^0\nu\bar{\nu}$ MC events. The numbers in the last column show the ratio for two photon event samples in the region, $300 \leq Z_{\text{vtx}}(\text{cm}) \leq 500$.

data set	cluster-size and csizel	conn. pattern	E_R	Total
$K_L \rightarrow \pi^0\pi^0\pi^0$ data	0.707 ± 0.003	0.911 ± 0.004	0.785 ± 0.004	0.497 ± 0.003
$K_L \rightarrow \pi^0\pi^0\pi^0$ MC	0.703 ± 0.005	0.905 ± 0.005	0.780 ± 0.005	0.488 ± 0.005
$K_L \rightarrow \pi^0\nu\bar{\nu}$ MC	0.869 ± 0.005	0.970 ± 0.005	0.925 ± 0.005	0.776 ± 0.005
2γ data	0.524 ± 0.006	0.863 ± 0.007	0.592 ± 0.007	0.289 ± 0.006

Appendix B

$K_L \rightarrow \pi^0 \pi^0 \pi^0$ ($\pi^0 \pi^0$) reconstruction

In this appendix, we will describe the reconstruction method for $K_L \rightarrow \pi^0 \pi^0 \pi^0$ decays and $K_L \rightarrow \pi^0 \pi^0$ decays. We reconstructed both decay modes with the same method. We will explain the reconstruction of the $K_L \rightarrow \pi^0 \pi^0 \pi^0$ decay.

When we reconstructed K_L in six-photon event samples, there were fifteen possible photon pairings to form three π^0 's, as shown in Table B.1 (Table B.2 for $K_L \rightarrow \pi^0 \pi^0$ reconstruction). For each photon pair, we calculated the π^0 decay vertex, $Z_{\text{vtx}}(i)$, and calculated a quantity (vertex χ^2) :

$$\chi^2 = \sum_{i=1}^3 \frac{[Z_{K_L} - Z_{\text{vtx}}(i)]^2}{\sigma_{\text{vtx}}(i)}, \quad (\text{B.1})$$

where the Z_{K_L} is the z component of the decay vertex of the K_L defined as a weighted mean of the three π^0 vertices:

$$Z_{K_L} = \frac{\sum_{i=1}^3 [Z_{\text{vtx}}(i)/\sigma_{\text{vtx}}(i)^2]}{\sum_{i=1}^3 [1/\sigma_{\text{vtx}}(i)^2]}, \quad (\text{B.2})$$

where $\sigma_{\text{vtx}}(i)$ is the error on $Z_{\text{vtx}}(i)$.

For each event, we selected the photon pairing with the smallest χ^2 (so-called best χ^2 combination). We then calculate the following quantities.

- K_L energy :

$$E_{K_L} = \sum_{i=1}^6 E_{\gamma}(i), \quad (\text{B.3})$$

where $E_{\gamma}(i)$ is the i th photon's energy.

- K_L decay vertex :

$$\begin{pmatrix} X_{K_L} \\ Y_{K_L} \\ Z_{K_L} \end{pmatrix} = \begin{pmatrix} s \times \sum_{i=1}^6 E_\gamma X_\gamma(i)/E_{K_L} \\ s \times \sum_{i=1}^6 E_\gamma Y_\gamma(i)/E_{K_L} \\ Z_{K_L} \text{ [see Eq. B.2]} \end{pmatrix}, \quad (\text{B.4})$$

$$s = \frac{Z_{K_L} - Z_{target}}{Z_{CsI} - Z_{target}}, \quad (\text{B.5})$$

where $(X_\gamma(i), Y_\gamma(i))$ is the hit position of the i th photon on the CsI calorimeter, Z_{target} is the position of the production target (-1180 cm) and Z_{CsI} is the position of the CsI calorimeter (614.8 cm).

- Invariant mass :

$$M_{6\gamma} = \sqrt{[E_{K_L}]^2 - \left[\sum_{i=1}^6 P_{X_\gamma(i)} \right]^2 - \left[\sum_{i=1}^6 P_{Y_\gamma(i)} \right]^2 - \left[\sum_{i=1}^6 P_{Z_\gamma(i)} \right]^2}, \quad (\text{B.6})$$

where $P_{X_\gamma(i)}$, $P_{Y_\gamma(i)}$ and $P_{Z_\gamma(i)}$ are x , y and z components of the momentum vector of the i th photon calculated with the K_L vertex and the photon's energy and hit position on the CsI calorimeter.

In order to remove mis-reconstructed K_L 's, we required the χ^2 of the K_L candidate to be less than 5 (best χ^2 cut). Figure B.1 shows the distribution of the χ^2 of the K_L candidate for the six-photon-event samples in data, which was consistent with the MC.

Moreover, we required additional condition in order to make sure that we have selected the correct photon pairing. Sometimes, the photon pairing with the next smallest χ^2 (so-called second χ^2 pairing) had the invariant mass closer to the K_L mass than the photon pairing with the minimum χ^2 . Since events with such the second χ^2 pairing had a potential to be mis-reconstructed, we rejected events in which the invariant mass of the second χ^2 pairing ($M_{6\gamma-2nd-\chi^2}$) was in the region: $0.47 \leq M_{6\gamma-2nd-\chi^2}(\text{GeV}/c^2) \leq 0.54$, and the difference ($\Delta\chi^2$) between the smallest χ^2 and the next smallest χ^2 was less than 15 (second best χ^2 cut). Figure B.2 shows the distribution $M_{6\gamma-2nd-\chi^2}$ versus $\Delta\chi^2$. Figure B.3 shows the distribution of the next smallest χ^2 . The distribution of the next smallest χ^2 measured with the real data was also consistent with the MC.

As shown in Fig. B.4, the second best χ^2 cut reduced the number of mis-reconstructed K_L , appearing as the events in the side band region. The 35 % of signal was lost due to these requirements, which was consistent with the MC study within 3 %.

Table B.1: The fifteen possible photon pairings to form three π^0 's from six photons. In the table, $[i, j]$ means that a π^0 is formed with two photons with indexices, i and j .

comb. tag	photon pairing	comb. tag	photon pairing
comb[0]	[0,1], [2,3], [4,5]	comb[8]	[0,3], [1,5], [2,4]
comb[1]	[0,1], [2,4], [3,5]	comb[9]	[0,4], [1,2], [3,5]
comb[2]	[0,1], [2,5], [3,4]	comb[10]	[0,4], [1,3], [2,5]
comb[3]	[0,2], [1,3], [4,5]	comb[11]	[0,4], [1,5], [2,3]
comb[4]	[0,2], [1,4], [3,5]	comb[12]	[0,5], [1,2], [3,4]
comb[5]	[0,2], [1,5], [3,4]	comb[13]	[0,5], [1,3], [2,4]
comb[6]	[0,3], [1,2], [4,5]	comb[14]	[0,5], [1,4], [2,3]
comb[7]	[0,3], [1,4], [2,5]		

comb. tag	photon pairing
comb[0]	[0,1], [2,3]
comb[1]	[0,2], [1,3]
comb[2]	[0,3], [1,2]

Table B.2: The three possible photon pairings to form two π^0 's from four photons. In the table, $[i, j]$ means that a π^0 is formed with two photons with indexices, i and j .

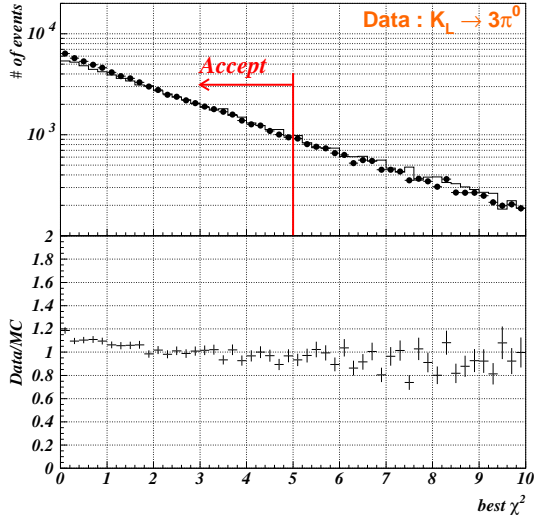


Figure B.1: The distribution of the smallest vertex χ^2 for the six-photon-event samples. In the top plot, the dots show the real data and the histogram shows the MC. The bottom plot shows the ratio of the data to the MC.

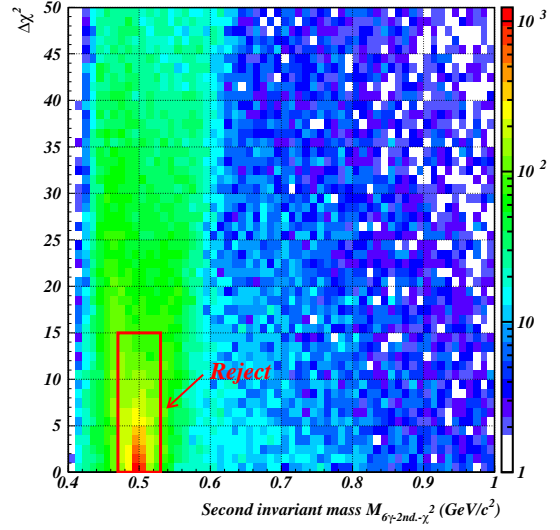


Figure B.2: The 2-dimensional distribution of the $M_{6\gamma-2nd.-\chi^2}$ versus $\Delta\chi^2$ for the six-photon-event samples measured with the real data. The events in the red box: $0.47 \leq M_{6\gamma-2nd.-\chi^2}(\text{GeV}/c^2) \leq 0.54$ and $\Delta\chi^2 < 15$ had a potential to be mis-reconstructed K_L , and thus were rejected.

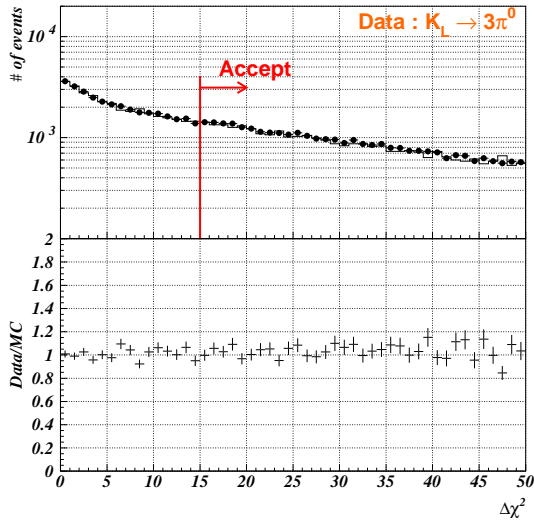


Figure B.3: The distribution of the difference between the smallest vertex χ^2 and the next smallest χ^2 for the six-photon-event samples. In the top plot, the dots show the real data and the histogram shows the MC. The bottom plot shows the ratio of the data to the MC.

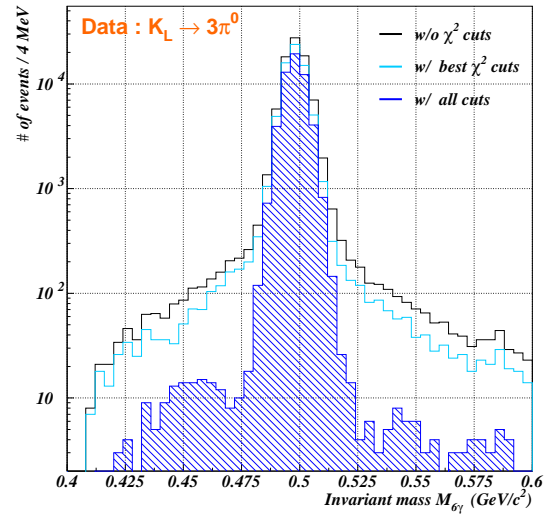


Figure B.4: The distribution of the invariant mass ($M_{6\gamma}$) for the best χ^2 combination without any χ^2 cut (black histogram), with only best χ^2 cut (light blue), and with both χ^2 cuts (blue dashed), for data.

Appendix C

Upper limit with another statistics model

Even though the total estimated number of background events was $1.9_{-0.7}^{+1.0}$, we set the new upper limit on the $Br(K_L \rightarrow \pi^0 \nu \bar{\nu})$ without taking it into account. In this appendix, we will discuss another upper limit considering the number of background events.

The observed number of events, n , follows as a Poisson distribution:

$$P(n|\mu) = \frac{(\mu + b)^n \exp[-(\mu + b)]}{n!} \quad (\text{C.1})$$

where μ is the expected mean number of signal events and b is the known number of background events. The Feldman-Cousins prescription [37] provides an unified confidence intervals. Table C.1 lists the 90 % confidence level intervals for the Poisson signal mean, $[\mu_1, \mu_2]$, for the observed number of events, n_0 , with 1.9 expected background events¹. Since we observed no events, the 90 % confidence level upper bound was 1.13. This sets

$$Br(K_L \rightarrow \pi^0 \nu \bar{\nu}) < 1.03 \times 10^{-7} \quad (90 \% \text{ C.L.}). \quad (\text{C.2})$$

This upper limit is 2.3 times better than the upper limit in Equation 9.2. However, the uncertainty of the estimated number of background events was large and thus the uncertainty of the upper limit in Equation C.2 was also large. Therefore, we conservatively set the upper limit, $Br(K_L \rightarrow \pi^0 \nu \bar{\nu}) < 2.10 \times 10^{-7}$, in Equation 9.2.

¹We performed the Feldman-Cousins method for $\mu_{\text{check}} = [0, 50]$ in steps of 0.005, which were the same parameter as in the reference [37]. We also confirmed our results using a public code `TFeldmanCousins` class in ROOT library[38].

Table C.1: 90 % confidence level intervals for the Poisson signal mean, $[\mu_1, \mu_2]$, for the observed number of events, n_0 , with 1.9 expected background events.

n_0	μ_1, μ_2
0	0.00, 1.13
1	0.00, 2.61
2	0.00, 4.02
3	0.00, 5.53
4	0.00, 6.70

Bibliography

- [1] C. S. Wu, E. Ambler, R. W. Hayward, D. D. Hoppes and R. P. Hudson, *Phys. Rev.* **105**, 1413 (1957).
- [2] J. H. Christenson, J. W. Cronin, V. L. Fitch and R. Turlay, *Phys. Rev. Lett.* **13**, 138 (1964).
- [3] A. D. Sakharov, *Pisma Zh. Eksp. Teor. Fiz.* **5**, 32 (1967), [*JETP Lett.* **5**, 24 (1967) SOPUA,34,392-393.1991 UFNAA,161,61-64.1991)].
- [4] S. M. Barr, G. Segre and H. A. Weldon, *Phys. Rev. D* **20**, 2494 (1979).
- [5] S. Eidelman *et al.* [Particle Data Group], *Phys. Lett. B* **592**, 1 (2004).
- [6] M. Kobayashi and T. Maskawa, *Prog. Theor. Phys.* **49**, 652 (1973).
- [7] N. Cabibbo, *Phys. Rev. Lett.* **10**, 531 (1963).
- [8] L. Wolfenstein, *Phys. Rev. Lett.* **51**, 1945 (1983).
- [9] C. Jarlskog, *Phys. Rev. Lett.* **55**, 1039 (1985).
- [10] B. Winstein and L. Wolfenstein, *Rev. Mod. Phys.* **65**, 1113 (1993).
- [11] A. J. Buras, arXiv:hep-ph/9905437.
- [12] Y. Grossman and Y. Nir, *Phys. Lett. B* **398**, 163 (1997).
- [13] W. J. Marciano and Z. Parsa, *Phys. Rev. D* **53**, 1 (1996).
- [14] V. V. Anisimovsky *et al.* [E949 Collaboration], *Phys. Rev. Lett.* **93**, 031801 (2004).
- [15] A. J. Buras, F. Schwab and S. Uhlig, arXiv:hep-ph/0405132.
- [16] T. Inami and C. S. Lim, *Prog. Theor. Phys.* **65**, 297 (1981).
- [17] A. J. Buras, R. Fleischer, S. Recksiegel and F. Schwab, *Nucl. Phys. B* **697**, 133 (2004).
- [18] A. J. Buras, R. Fleischer, S. Recksiegel and F. Schwab, *Phys. Rev. Lett.* **92**, 101804 (2004).
- [19] A. J. Buras, T. Ewerth, S. Jager and J. Rosiek, *Nucl. Phys. B* **714**, 103 (2005).

- [20] A. Alavi-Harati *et al.* [The E799-II/KTeV Collaboration], Phys. Rev. D **61**, 072006 (2000).
- [21] L. S. Littenberg, Phys. Rev. D **39**, 3322 (1989).
- [22] J. W. Cronin *et al.*, Phys. Rev. Lett. **18**, 25 (1967).
- [23] P.C. Wheeler, PhD thesis, Princeton University (1968).
- [24] J. Adams *et al.* [KTeV Collaboration], Phys. Lett. B **447**, 240 (1999).
- [25] S. Ajimura *et al.*, Nucl. Instrum. Meth. A **552**, 263 (2005).
- [26] K. Sakashita, Master thesis, Osaka University (2002).
- [27] H. Watanabe *et al.*, Nucl. Instrum. Meth. A **545**, 542 (2005).
- [28] H. Watanabe, PhD thesis, Saga University (2002).
- [29] M. Doroshenko *et al.*, Nucl. Instrum. Meth. A **545**, 278 (2005).
- [30] M. Doroshenko, PhD thesis, SOKENDAI (2004).
- [31] T. Inagaki, H. Hirayama, T. Sato, T. Shinkawa and Y. Yoshimura, Nucl. Instrum. Meth. A **359**, 478 (1995).
- [32] T. Ikei, Master thesis, Osaka University (2004), in Japanese.
- [33] M. Itaya *et al.*, Nucl. Instrum. Meth. A **522**, 477 (2004).
- [34] CERN Application Software Group, GEANT-Detector Description and Simulation Tool, W5013, CERN, 1993.
- [35] N. G. Deshpande and G. Eilam, Phys. Rev. Lett. **53**, 2289 (1984).
- [36] Y. Akune, Master thesis, Saga University (2004), in Japanese.
- [37] G. J. Feldman and R. D. Cousins, Phys. Rev. D **57**, 3873 (1998).
- [38] An Object-Oriented Data Analysis Framework, <http://root.cern.ch> .